Étude des processus physiques de la formation d'étoiles par effondrement gravo-turbulent

Pierre Marchand

To cite this version:

Pierre Marchand. Étude des processus physiques de la formation d'étoiles par effondrement gravo-turbulent. Astrophysique [astro-ph]. Université de Lyon, 2017. Français. NNT : 2017LYSE1154 . tel-01677949

HAL Id: tel-01677949
https://theses.hal.science/tel-01677949v1

Submitted on 8 Jan 2018

N° d'ordre NNT : 2017LYSE1154

THÈSE DE DOCTORAT DE L'UNIVERSITÉ DE LYON
opérée au sein de
l'Université Claude Bernard Lyon 1

École Doctorale ED52
Physique & Astrophysique de Lyon

Spécialité de doctorat : Astrophysique

Soutenue publiquement le 21/09/2017, par :
Pierre Marchand

Etude des processus physiques de la formation d'étoiles par effondrement gravo-turbulent

---

Devant le jury composé de :

Cabrit Sylvie, Astronome 1ère classe, LERMA	Présidente
Ferreira Jonathan, Professeur, IPAG	Rapporteur
Terquem Caroline, Professeur, Oxford University	Rapporteure
Blaizot Jérémy, Astronome, CRAL	Examinateur
Commerçon Benoît, Chargé de recherche, CRAL	Examinateur
Chabrier Gilles, Directeur de recherche, CRAL	Directeur de thèse

UNIVERSITE CLAUDE BERNARD - LYON 1

Président de l’Université	**M. le Professeur Frédéric FLEURY**
Président du Conseil Académique	M. le Professeur Hamda BEN HADID
Vice-président du Conseil d’Administration	M. le Professeur Didier REVEL
Vice-président du Conseil Formation et Vie Universitaire	M. le Professeur Philippe CHEVALIER
Vice-président de la Commission Recherche	M. Fabrice VALLÉE
Directrice Générale des Services	Mme Dominique MARCHAND

COMPOSANTES SANTE

Faculté de Médecine Lyon Est – Claude Bernard	Directeur : M. le Professeur G.RODE
Faculté de Médecine et de Maïeutique Lyon Sud – Charles Mérieux	Directeur : Mme la Professeure C. BURILLON
Faculté d’Odontologie	Directeur : M. le Professeur D. BOURGEOIS
Institut des Sciences Pharmaceutiques et Biologiques	Directeur : Mme la Professeure C. VINCIGUERRA
Institut des Sciences et Techniques de la Réadaptation	Directeur : M. X. PERROT
Département de formation et Centre de Recherche en Biologie Humaine	Directeur : Mme la Professeure A-M. SCHOTT

COMPOSANTES ET DEPARTEMENTS DE SCIENCES ET TECHNOLOGIE

Faculté des Sciences et Technologies	Directeur : M. F. DE MARCHI
Département Biologie	Directeur : M. le Professeur F. THEVENARD
Département Chimie Biochimie	Directeur : Mme C. FELIX
Département GEP	Directeur : M. Hassan HAMMOURI
Département Informatique	Directeur : M. le Professeur S. AKKOUCHE
Département Mathématiques	Directeur : M. le Professeur G. TOMANOV
Département Mécanique	Directeur : M. le Professeur H. BEN HADID
Département Physique	Directeur : M. le Professeur J-C PLENET
UFR Sciences et Techniques des Activités Physiques et Sportives	Directeur : M. Y.VANPOULLE
Observatoire des Sciences de l’Univers de Lyon	Directeur : M. B. GUIDERDONI
Polytech Lyon	Directeur : M. le Professeur E.PERRIN
Ecole Supérieure de Chimie Physique Electronique	Directeur : M. G. PIGNAULT
Institut Universitaire de Technologie de Lyon 1	Directeur : M. le Professeur C. VITON
Ecole Supérieure du Professorat et de l’Education	Directeur : M. le Professeur A. MOUGNIOTTE
Institut de Science Financière et d'Assurances	Directeur : M. N. LEBOISNE

Résumé

L'une des questions les plus étudiées concernant la formation d'étoiles est la régulation du moment cinétique : comment caractériser la rotation du gaz lors de l'effondrement gravitationnel qui donnera vie à l'étoile ? Cette question est reliée à de nombreux phénomènes, comme la formation de planètes ou la création d'un système binaire. Du nuage de gaz pré-stellaire à l'étoile finale, le système perd la grande majorité de son moment cinétique, et plusieurs processus sont avancés pour expliquer ce phénomène. Nous nous concentrons sur la magnéto-hydrodynamique (MHD) non-idéale, un formalisme qui permet de décrire le couplage entre un fluide et un champ magnétique. De nombreuses études suggèrent que l'inclure dans les modèles théoriques et numériques permet de reproduire de façon réaliste les observations, qui sont, avec les simulations numériques, les seuls moyens de tester les modèles théoriques en astrophysique.

Dans un premier temps, nous développons un code qui calcule l'équilibre chimique des éléments composant le gaz de la future étoile. Nous pouvons ainsi retrouver les résistivités de la MHD non-idéale qui sont ensuite utilisées dans nos simulations numériques. Nous étudions également l'influence de plusieurs paramètres sur ces valeurs, notamment concernant la population de grains de poussière.

Nous nous intéressons ensuite à l'effet Hall, un des trois processus de la MHD non-idéale et encore peu étudié dans ce contexte. Nous l'implémentons dans le code eulérien `RAMSES`, puis nous effectuons des simulations numériques pour quantifier son impact pendant un effondrement gravitationnel. L'effet Hall influence grandement la taille du disque protoplanétaire, dans lequel se forment les planètes, et crée des enveloppes de gaz tournant en sens inverse du reste du système.

Abstract

The regulation of angular momentum is widely studied in star formation: how to characterize the gas rotation during the gravitational collapse that forms the star ? This question is related to several phenomena, such as planet formation or the creation of a binary system. From the pre-stellar cloud to the final star, the system loses most of its angular momentum, and several mechanisms have been proposed to explain this phenomena. We focus on non-ideal magneto-hydrodynamics (MHD), which describes the behaviour of a magnetised fluid. Several studies suggest that including it into the theoretical and numerical models leads to results coherent with observations, which are, with the numerical simulations, the only ways to test the theoretical models in astrophysics.

First, we develop a code computing the chemical equilibrium of elements composing the gas of the future star. This way, we retrieve the values of the resistivities determining the strength of several MHD processes. We also study the influence of several parameters on these values, the grain population or the cosmic-rays ionisation rate for instance.

We then focus on the Hall effect, one of the three processes of non-ideal MHD and still scarcely studied in this context. We implement it into the eulerian code `RAMSES`, and perform numerical simulations to quantify its impact on a gravitational collapse. As predicted by theory, the Hall effect has a great influence on the size of the protoplanetary disk, in which planets form, and creates envelopes of gas rotating in the opposite direction from the rest of the system.

Remerciements

Tout d'abord, un énorme merci à Gilles et Benoît. Ils m'ont donné l'opportunité de réaliser un rêve vieux de 20 ans. Ils m'ont guidé pendant ces trois ans et j'ai beaucoup appris à leur côté.

Merci aussi à Patrick pour avoir suivit de près mon travail, et Jacques pour ses bonnes idées (et son morbier !).

Je remercie également Sylvie Cabrit, Jonathan Ferreira, Caroline Terquem et Jérémy Blaizot d'avoir accepté de faire partie de mon jury et de venir jusqu'à Lyon pour ma soutenance.

Je pense aux enseignants qui m'ont aidé tout au long de mes études et avec qui apprendre a été un vrai plaisir. Je pense en particulier à Mme Leblanc en première, JAC en prépa, Ségolène Callard à Centrale, et toute l'équipe du master de Paris pour cette superbe année.

Merci aux relecteurs et à la relectrice de ce manuscrit ! Adrien (on échange pour cette fois), Alise (coin coin), Jérémy (chacun son tour), Nathou (pense à ta stratégie) et Paul (noob).

Il y a aussi mes camarades du bureau des thésards: Pierre et nos machines tout à fait physiquement réalisables, son antithèse Florian le mangeur de légumes, Ugo promis à un bel avenir (en commun), et Adrien désormais à l'autre bout de la France pour enseigner les stratégies pokémon en prépa.

Je pense aussi au reste du labo et aux gens que j'ai le plaisir de croiser régulièrement: Guillaume (ça marche !), Neil désormais à Copenhague, Christophe, Rolf, Gérard, Thomas, Martin, Isabelle, et ceux perchés par delà les montagnes à St Genis-Laval: JF, Guillaume, Floriane, Anthony, Mohammed, Peter... Et puis Stéphanie, sans qui le labo ne serait pas le même et qui mérite amplement la gratitude de tout le monde ! Je passe le coucou à tout le reste de Plop et bon courage aux Suisses pour la fin de leurs thèses !

Je remercie ceux qui m'ont motivé: John Williams, Nobuo Uematsu, Joe Hisaishi, Hans Zimmer, Ludwig Van Beethoven, Wolgang Amadeus Mozart, Piötr Ilyich Tchaikovsky, Serguei Rachmaninov, Dire Straits, Babymetal, Ghost... Et puis ceux qui m'ont bien aidé du début à la fin: Stack Overflow et Thesaurus.

Merci à mes parents qui m'ont soutenu et m'ont donné toutes les chances d'accomplir mon rêve.

Enfin, merci à Marjorie et Hana, sources intarissables de mon bonheur.

Prelude

When I was writing the fourth chapter of this manuscript, I started to lack synonyms and periphrases to express the ideas of "rotation" and "velocity". I then wondered two things. First, will the thesis be pleasant to read (science is cool, but is cooler when nicely written) ? Second, what will the Zipf law looks like ?

This law was popularized several decades ago by the linguist George Kingsley Zipf (Zipf 1936, 1949). It stipulates that in any text in any language, the nth most common word have n times less occurences than the first. Its accuracy is astonishing and I decided to examine its validity in this work.

Figure 1 presents the occurences of the 15 most common words in this manuscript. We fit[1] an inverse law $\mathrm{occurence(n)} = \frac{\alpha}{\mathrm{n}}$ on the 100 first points of this data, represented as the red curve on the plot, with a correlation coefficient of $R \approx 0.991$.

When we compare these 15 words to the British National Corpus (BNC), thanks to the website www.wordcount.org, we note that the 8 first words are in the top 12 of the corpus, in roughly the same order ("The", "Of" and "And" being the same top 3). The only one standing out in this plot is "Times", ranked 287 in the corpus but 15 in my thesis with 189 occurences. If we look in the top 100, we find even more peculiar words. In table 1, we list them, with an arbitary criterion for their selection: their rank must be greater than 2000 in the BNC. The words with * have been associated with their plural form, and the displayed BNC ranking is the highest between both. We retrieve most of the thematics of this thesis, except "star", which is, unfortunately for the argument, a word a bit too common. I was nicely surprised to discover that the two words that worried me, "rotation" and "velocity", had about the same number of occurences.

As you will find out, these words are not homogeneously distributed across the manuscript, but I guess that is why I have divided it into several chapters.

I wish you a good reading.

---

[1] Using the least squared method.

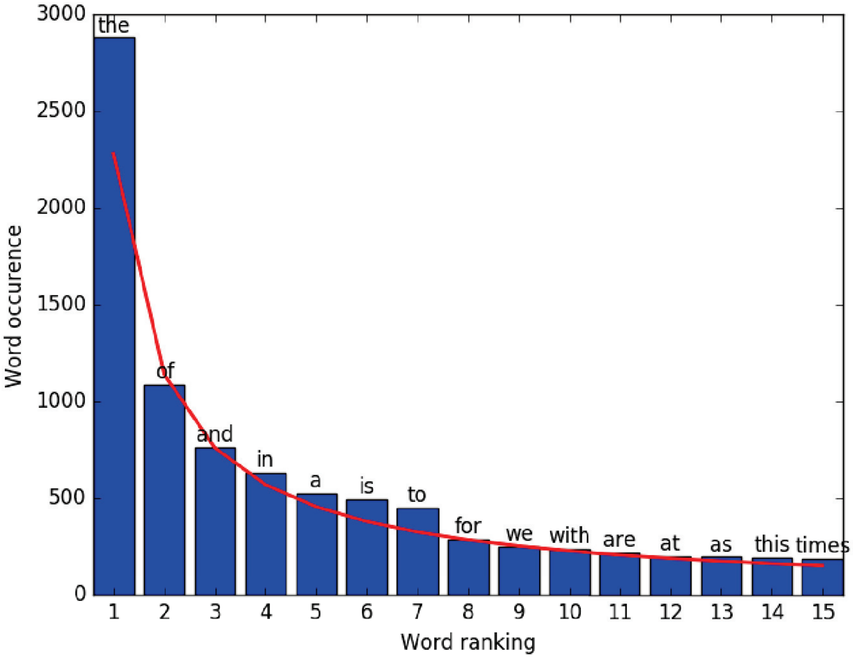

Figure 1: Occurences of the 15 most common words of this manuscript.

Table 1: Peculiar words of this manuscript (in the top 100).

Word	Occurences	Rank	BNC rank	Word	Occurences	Rank	BNC rank
Grain*	154	17	4649	Formation	58	51	2510
Magnetic	139	21	5228	Fluid	49	64	4950
Density	109	24	5067	Abundances	48	65	44096
Core	97	27	2884	MHD	46	71	Not listed
Resistivity*	92	28	37970	Evolution	41	76	3659
Angular	75	29	12189	Chemical	40	80	2261
Momentum	85	31	7260	Ionisation	39	83	60804
Disk	82	34	3501	Thermal	36	91	9226
Velocity	78	36	7630	Radius	36	92	9579
Angular	76	38	12189	Azimuthal	35	94	82703
Rotation	74	39	8251	Resolution	35	95	2677
Collapse	72	41	3561	Cloud	34	98	4020
Equation	61	48	3688	Numerical	34	87	8957
Simulations	58	50	19697				

Contents

Chapter 1

Introduction

From galaxies to planets, the universe is all about stars. During their life, they transform Hydrogen and Helium into heavier atoms. At their death, these elements are released in the interstellar medium with a large amount of energy, which can trigger the formation of new stars and planets enriched with the products of older generations. Stars are the motor of the galactic evolution and the source of life. Understanding the process by which they form is therefore of prime scientific importance for understanding the universe.

The broad picture has been known for decades. Interstellar matter gathers itself into cold molecular clouds in which dense cores form due to gravitational instabilities and turbulent motion. If a core is gravitationally unstable, it collapses under its own weight. The collapse proceeds until the gas becomes dense and hot enough to ignite nuclear reactions, burning Hydrogen into Helium during what is called their *main sequence* phase. The energy production eventually becomes high enough to perfectly counterbalance gravity and stop the collapse. This state of equilibrium is what we call a star. The details of this process are still actively debated because the physics at stake is an entanglement of complex mechanisms: the clouds in which star forms are magnetised, agitated by turbulent motions, they react to their own radiative emissions, and their composition is altered by cosmic-rays, chemical reactions and the feedback of supernovae explosions. Additionally, observations show that most stars have a companion, in systems called *Binary Stars* and their formation is still matter to debate.

In this manuscript, we study the first stages of star formation through the prism of non-ideal magnetohydrodynamics (MHD), which describes the behaviour of a magnetised fluid, and its effect on the regulation of angular momentum. We describe some of the major issues of star formation and the associated theory in this chapter. In chapter 2, we focus on chemistry in both a theoretical and numerical way, with a code that solves the chemical equilibrium of several species in protostellar collapse conditions, in order to compute the non-ideal MHD resistivity coefficients. Chapter 3 is dedicated to the numerical methods of eulerian codes and non-ideal MHD. Finally, we present the application of these tools to star formation simulations in chapter 4.

1.1 The formation of low-mass stars

For a long time, the formation of stars stayed a theoretical field. While populating galaxies by billions, their formation is a process of several millions years, making impossible any observation in a civilisation life-time. Additionally, it involves a colossal quantity of matter and energy, therefore being hardly reproducible in a laboratory experiment. Fortunately, the technological progress allowed the development of powerful instruments able to seek and observe the forming stars in our galaxy. Their large number provided numerous snapshots of the process at different phases, from which a precise idea of an evolution scenario was constructed.

1.1.1 The interstellar medium

Stars are the most visible objects in galaxies. Between them lies the interstellar medium (ISM), filled with sparse cold gas, slowly evolving. Despite its low density, barely 10^3 particles per cubic centimeter, its mass is enormous because of the huge space it occupies. The ISM structures itself into molecular clouds, that are regions often several light-years wide, harbouring thousands of solar masses and creating necessary conditions for star formation. The world "molecular" qualifies the Hydrogen, mostly in its H_2 form at $10 - 20$ K, the temperature of the clouds. Although Hydrogen is their main component ($\sim$74% by mass), they also host a large number of other species. Previous generations of stars have formed heavier elements by nuclear fusion and have released them in their environment, thus enriching the ISM. The second most abundant species in molecular clouds is Helium ($\sim$25%). Other molecules, such as CO, NH_3 or HCO^+, are present in far lower numbers but play nonetheless a major role in star formation as will be explained in further sections.

1.1.2 Collapse of a dense core - Theory

The turbulent motion of the gas within the molecular cloud and the feedback from nearby stars (particles, radiation) creates overdense regions called *dense cores* that dynamically decouple from the surrounding cloud. If a core is gravitationally unstable, it collapses under its own weight and eventually becomes a stellar system. The stability analysis of a dense core is described in section 1.2.

Larson (1969) performed the first numerical simulations of low-mass star formation. Despite the simplicity of his model, the results delivered a general picture of the process that is still relevant today. The first stages can be divided into four phases.

- *The isothermal phase.* The gas has a temperature of 10 K because it is transparent to its own thermal radiation. It free-falls towards the center of mass and structures itself with a density profile $\rho \sim r^{-2}$.
- *The first Larson core.* When the density reaches $\rho = 10^{-13}$ g cm^{-3} after several tens of kyr[1], the gas becomes opaque to its own black body thermal radiation. The light-matter interaction increases the temperature, which provides enough support to slow the collapse and form an object in a quasi-hydrostatic equilibrium called the *first Larson core*. The core undergoes a slow adiabatic contraction while its temperature rises and its mass increases by the accretion of the surrounding matter. The first core have a typical radius of few tens of au[2] and a mass of $\sim 10^{-2}$ $M_\odot$ [3] (Vaytet et al. 2013).
- *The second collapse.* At about 2000 K, the H_2 molecules dissociate. This transformation requires an amount of energy that is provided by the temperature of the gas. The thermal support then decreases and the inner part of the core collapses onto itself until all H_2 molecules are depleted, at densities lower than ~ 1 g cm^{-3}.
- *The second Larson core.* When only atomic Hydrogen remains, the gas resumes its slow adiabatic contraction. It is the *second Larson core*, with a radius of several 10^{10} cm and a mass of 10^{-3} $M_\odot$.

This evolution is summarized in the density-temperature plot of figure 1.1. For a perfect gas, the polytropic index γ defines each phase with $T \propto \rho^{\gamma-1}$.

The second core may be qualified as a "protostar". During its contraction, which can last several million years, it accretes the major part of its mass from its surrounding medium. Outflows (collimated jets of matter) launched from its poles have been observed. They carry away angular momentum (see 1.2.3 for more details).

---

[1] kilo year = 1000 years.

[2] Astronomical Units, the Earth Sun distance $\approx 1.5 \times 10^13$ cm.

[3] $1\ M_\odot = 1$ solar mass $\approx 2 \times 10^{33}$ g.

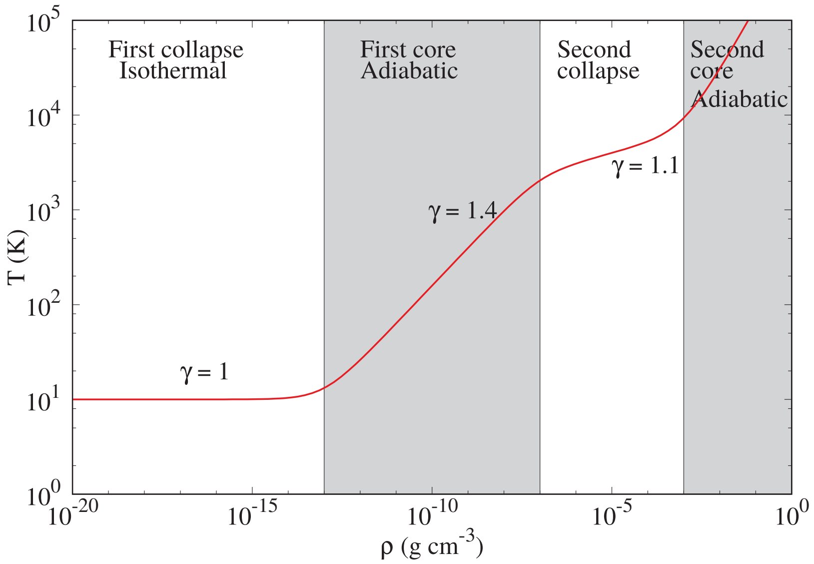

Figure 1.1: Density-temperature evolution of the gas through the 4 early phases of the collapse.

1.1.3 The protoplanetary disk and the young star

During the first Larson core contraction, a fraction of the surrounding (rotating) gas is submitted to a centrifugal force able to counter-act gravity, and structures itself into the so-called *protoplanetary disk*, in which planets form. The disk size varies from one system to another and may reach a few hundreds of au in radius. One of the most famous protoplanetary disks is certainly HL Tau with its rings of dust, represented in figure 1.2.

Both structures, the core and the disk, evolve and interact for a long time (up to several millions years). The core accretes from the disk, heats up and contracts until the Hydrogen atoms can overcome their repulsive electric barrier and start nuclear fusion. The chain of nuclear reactions is complex, but the outcome mostly consists in Helium and radiative energy. This extra amount of energy generates more heat and stops the contraction of the core. This system, in equilibrium between gravitational collapse and thermal support by fusion reactions, is a newborn star which enters in its *main-sequence* phase. The matter that has not fallen into the star generally forms planets, asteroids and comets within the disk.

1.1.4 Grains

Some of the ISM molecules aggregate themselves into *dust grains*. Grains are composed of more than a hundred molecules that are essentially based on Carbon, Silicon or Aluminium. Their size may vary from a few nanometers to a micrometer in these regions, and they represent about 1% of the mass of the gas (Savage & Jenkins 1972). They are at the core of planet formation. Indeed, around young stars, grains gather and aggregate by collisional sticking. They become macroscopic rocks, then planetesimals able to gravitationally pull the surrounding matter and grow even larger. Ultimately, most grains form terrestrial planets like Earth, the core of giants gaseous planets like Jupiter, or simply asteroids. They are opaque to the visible wavelengths because of their large size, and their black body thermal emission is an important source of infrared radiation. Both properties makes them excellent for observations as they are used to track the presence of matter sometimes difficult to detect. The telescopes ALMA, Spitzer and Herschel have been widely used to observe them at several wavelengths (infrared

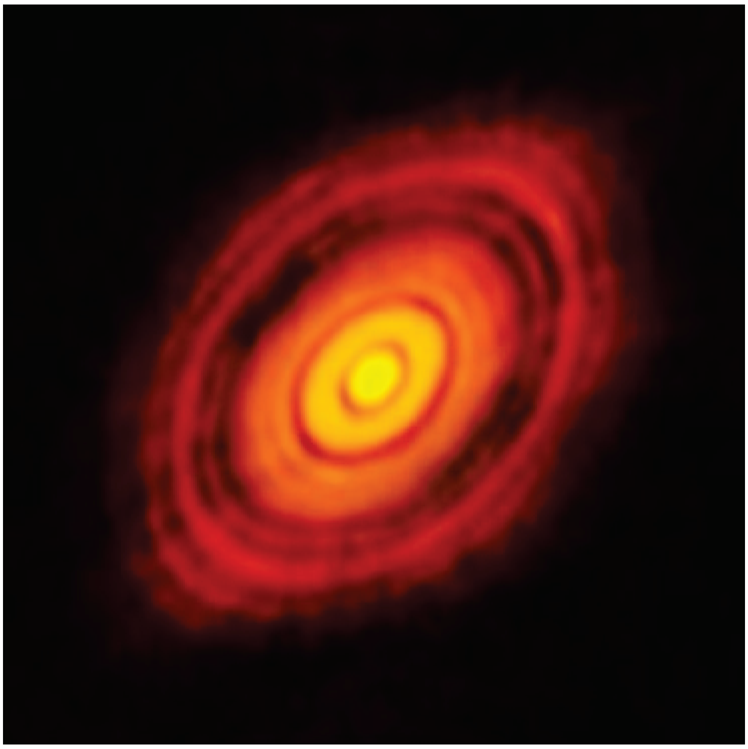

Figure 1.2: HL Tau protoplanetary disk observed by ALMA (ALMA Partnership et al. 2015)

and submillimeter radiation). In particular, the ISM has been surveyed for decades, either by direct observations or using its effect on the light coming from stars on its background (Bless & Savage 1972; York et al. 1973). The analysis of the extinction and polarization of light in these observations has been interpreted as a non-homogeneous grain population, both in composition (Krishna Swamy & O'dell 1968; Gillett et al. 1973) and in size (Mathis et al. 1977).

1.1.5 Observations

Light is the only information at our disposal to study space bodies[4]. This is why the Spectral Energy Distribution (SED) is a very convenient tool for observations. It is a decomposition of the electromagnetic waves across all wavelengths. From the amount of energy carried by each wavelength, observers can deduce the distance, temperature, velocity distribution and composition of the object.

Physical properties of dense cores Observations have revealed several characteristics of the dense cores from the analysis of their SED.

- *The mass distribution.* The dust continuum emission and absorption of infrared radiation reveals a flat density profile at the center ($r \leq 500$ au), with a density of $\rho \approx 10^{-18}$ g cm^{-3}. At larger radius, the density decreases as r^{-2} (André et al. 1996), fitting remarkably well the Bonnor-Ebert profile (Ebert 1955; Bonnor 1956) (see more details in 1.2.1).

- *The gas velocity.* Goodman et al. (1993) found that dense cores generally undergo a solid body rotation around an axis, with a rotational over gravitational energy ratio of $\beta \approx 0.02$. For an homogeneous sphere of radius R, mass M, in solid body rotation at angular velocity Ω, the calculation gives $\beta = \frac{R^3\Omega^2}{3GM}$. The typical angular velocity of dense cores is then $\Omega \approx 10^{-13}$ rad s^{-1}.

---

[4] And gravitational waves in specific cases since recently.

- *The magnetic field.* The Zeeman effect (splitting of the atomic emission lines) and the polarisation of dust radiation are evidences of magnetic fields in the interstellar medium (Hiltner 1951; Troland & Crutcher 2008). In dense cores, they may be strong enough to prevent a gravitational collapse (see section 1.3).

- *Turbulence.* Feedback from the external medium and random perturbations leads to velocity distributions following the laws of turbulence (Kolmogorov 1941). These turbulent motions have been widely observed in the ISM (Larson 1981; Kleiner & Dickman 1985; Kitamura et al. 1993). The speeds at stake can rise up to several km s^{-1}, but low-mass dense cores remains mostly coherent and not fully turbulent (Goodman et al. 1998).

The empirical evolutionary sequence The Young Stellar Objects (YSO) are classified according to their SED, which corresponds to different stages of the star formation process (Lada & Wilking 1984; André 2002), that are summarized in figure 1.3.

The SED of the early stages of star formation (the Larson phases described in 1.1.2) is well approximated by a simple black body spectrum. In the far infrared region, it is assumed that most of the light comes from the grain thermal emission. The bolometric temperature[5] ranges from 10 K for the dense cores to $\sim$ 70 K for the early protostar. A YSO in its Larson cores phases, accreting its surrounding envelope of gas, is called a Class 0 protostar (André et al. 1993). Observationally, they are also characterized by collimated CO outflows.

At later stages, extra infrared radiation is added to the black-body spectrum, when the emission of both the disk and the young protostar contribute to the SED. The central object concentrates most of the mass of the system. This is a Class I protostar. The transition between Class 0 and Class I is still ill-known, partly because it involves the debated formation of the disk.

In Class II objects, the gas in the envelope has been accreted on the protostar or has settled in the disk. The protostar emission heats the disk and the resulting SED is a superposition of the black body emissions of both the star and the disk, in the near and mid infrared. The near IR spectrum gives information concerning the inner structure of the disk. Class II protostars are also named "Classical T Tauri stars".

Finally, Class III objects, or "Weak-lined T Tauri stars", correspond to protostars about to enter their main-sequence phase. They are surrounded by gas at low density and rocky fragments, but since most of the light originates from the photosphere, it is difficult to probe their environment. Ultimately, when the disk has completely disappeared (either by falling onto the star or by forming large objects), the SED transforms into a classical stellar black body.

1.2 Theory of gravitational collapses

The gravitational collapse of dense cores is not systematic. Gravity is a dominant force at this scale, but there are mechanisms able to support the gas under its own weight. The first studies on this subject compared the balance between the gravitational and the thermal energy, and derived criteria to determine if the thermal pressure could prevent a gravitational collapse. While we now know that the picture is a bit more complex, involving rotation, magnetic fields, turbulence and supernovae energy input, these formulae are still widely used for their fair approximation of reality.

---

[5] i.e. the equivalent temperature of a black body emitting the same amount of energy (integrated over the whole spectrum).

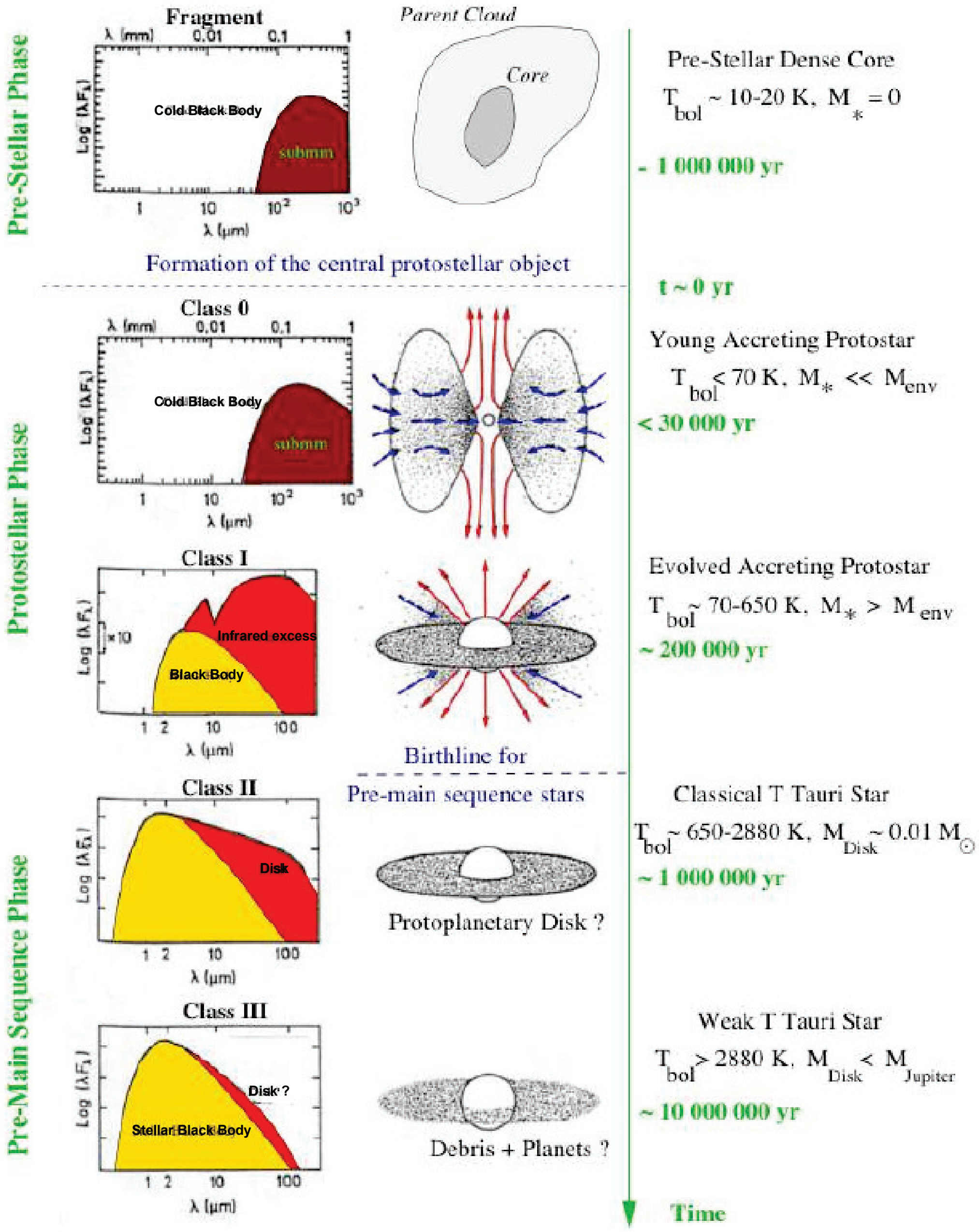

Figure 1.3: Empirical evolution sequence of a protostar (from André 2002).

1.2.1 Clouds at equilibrium: a self-similar solution

Bonnor (1956) and Ebert (1955) investigated the density profile of a sphere of gas at equilibrium with gravity. The equations at stake are

$$\frac{\partial \mathbf{u}}{\partial t} = -\frac{1}{\rho}\nabla P - \nabla\Phi, \tag{1.1}$$

$$\Delta\Phi = 4\pi G\rho, \tag{1.2}$$

$$P = \rho c_{\mathrm{s}}^2. \tag{1.3}$$

$\mathbf{u}$[6] represents the velocity of the gas, ρ its density, P its thermal pressure, Φ the gravitational potential and $c_{\mathrm{s}} = \sqrt{\gamma P/\rho}$ is the sound speed. $G = 6.67\times10^{-8}$ cm^{-3} g^{-1} s^{-2} is the gravitational constant. The first equation is the equivalent to the second Newton's law and rules the dynamics of the fluid. In our case, at equilibrium, $\mathbf{u} = 0$. The second is the Poisson equation that describes the gravitational potential as a function of the spatial distribution of mass. Finally, the third equation is an equation of state (EOS) linking the pressure and the density in an isothermal medium. The typical value of c_{s} in dense cores is $c_{\mathrm{s}} \approx 0.19$ km s^{-1} with $\gamma = 1$ during the isothermal phase.

We take the divergence of equation (1.1) and replace the pressure by density using the EOS to obtain

$$c_{\mathrm{s}}^2\nabla\cdot\left(\frac{1}{\rho}\nabla\rho\right) + \Delta\Phi = 0. \tag{1.4}$$

The Laplacian of Φ is then replaced with the Poisson equation. The derivatives are expressed for a spherically symmetric cloud, i.e.

$$\nabla f = \frac{\partial f}{\partial r}\mathbf{e_r} \quad ; \qquad\qquad \nabla\cdot\mathbf{g} = \frac{1}{r^2}\frac{\partial}{\partial r}(r^2 g_r),$$

for any function f and $\mathbf{g}$. Using the dimensionless variables $D = \frac{\rho}{\rho_{\mathrm{c}}}$ and $x = r\frac{\sqrt{4\pi G\rho_{\mathrm{c}}}}{c_{\mathrm{s}}}$, where ρ_{c} is the maximum density, we get

$$\frac{1}{x^2}\frac{d}{dx}\left(\frac{x^2}{D}\frac{dD}{dx}\right) + D = 0, \tag{1.5}$$

or

$$\Delta(\ln(D)) = -D, \tag{1.6}$$

which is equivalent in spherical coordinates. Combining with the Poisson equation

$$\Delta\left(\ln(D) + \frac{\Phi}{4\pi G\rho_{\mathrm{c}}}\right) = -D + \frac{\rho}{\rho_{\mathrm{c}}} = 0. \tag{1.7}$$

Therefore, $D \propto e^{-\Phi}$. Replacing this relation into equation (1.5) yields the famous Lane-Emden equation

$$\frac{d^2\Phi}{dx^2} + \frac{2}{x}\frac{d\Phi}{dx} = e^{-\Phi}. \tag{1.8}$$

This equation has no analytical solution in the isothermal case, but can be numerically integrated. It describes a family of self-similar solutions[7] pictured in figure 1.4. The inner region of the density profile is flat, then the density decreases as r^{-2} for $x > 1$.

By studying the behaviour of such a cloud to small pressure perturbations, through the sign of $\frac{\partial P}{\partial V}$, Bonnor (1956) and Ebert (1955) found that the stability of the cloud depends on its dimensionless radius x_{max}. For $x_{\mathrm{max}} > 6.451$, the cloud is unstable and collapses in a self-similar manner. x_{max} increases as the collapse proceeds, meaning that the cloud can not recover stability.

---

[6] Bold font represent vectors, generally in 3 dimensions.

[7] i.e. scale invariant

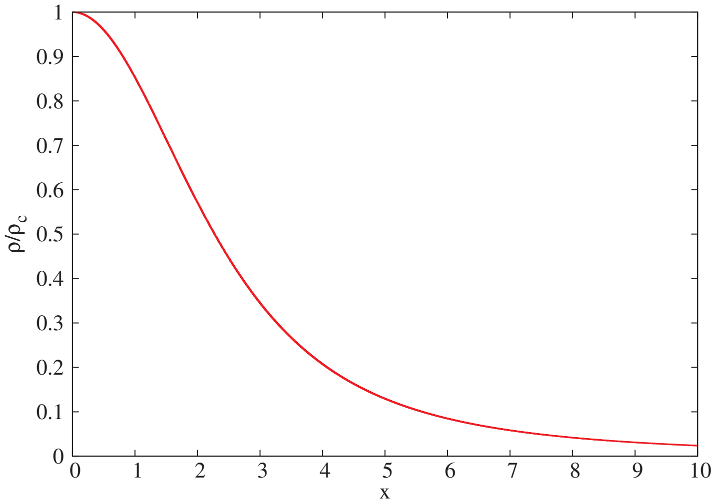

Figure 1.4: Generic density profile of a Bonnor-Ebert sphere.

The degenerated case of a Bonnor-Ebert sphere, and the limit of the collapse at $x_{\max} \to \infty$, is the singular sphere of Shu (1977), whose density follows $\rho(r) \propto r^{-2}$ and is infinite in the center. While the Bonnor-Ebert profile fits remarkably well the observations (see figure 1.5), the Shu limit is unrealistic as other physical processes prevent the formation of a singularity. It is, however, a simpler model to include in an analysis.

1.2.1.1 The Virial theorem

The Virial theorem is a popular tool used to describe the equilibrium of self-gravitating systems. It is more general than the Bonnor-Ebert calculation since it applies to molecular clouds and dense cores, but also globular clusters and galaxies. The system does not need to be continuous.

The second Newton law for a particle of mass m_i submitted to a force $\mathbf{F}_i$ is $m_i \frac{\partial^2 \mathbf{r_i}}{\partial t^2} = \mathbf{F_i}$. The Virial is the quantity $\mathbf{F_i} \cdot \mathbf{r_i}$. Introducing it into the Newton's law yields

$$m_i \frac{\partial^2 \mathbf{r_i}}{\partial t^2} \cdot \mathbf{r_i} = \mathbf{F_i} \cdot \mathbf{r_i}. \tag{1.9}$$

Using $\frac{\partial^2 \mathbf{r_i}}{\partial t^2} \cdot \mathbf{r_i} = \frac{\partial}{\partial t}\left(\mathbf{r_i} \cdot \frac{\partial \mathbf{r_i}}{\partial t}\right) - \left(\frac{\partial \mathbf{r_i}}{\partial t}\right)^2$ and $\frac{\partial}{\partial t}\left(\mathbf{r_i} \cdot \frac{\partial \mathbf{r_i}}{\partial t}\right) = \frac{1}{2}\frac{\partial^2 (\mathbf{r_i}^2)}{\partial t^2}$, we have

$$\frac{1}{2} m_i \frac{\partial^2 (\mathbf{r_i}^2)}{\partial t^2} = m_i (\partial_t \mathbf{r_i})^2 + \mathbf{F_i} \cdot \mathbf{r_i}. \tag{1.10}$$

In this equality, we recognize two known quantities. First, the left hand side can be rewritten $\frac{1}{2} m_i \frac{\partial^2 (\mathbf{r_i}^2)}{\partial t^2} = \frac{1}{2}\ddot{I}_i$, where $I_i = m_i \mathbf{r_i}^2$ is the inertia momentum of a particle of mass m_i. Then, the first term on the right-hand side is twice the kinematic energy $\mathcal{U}_i = \frac{1}{2} m_i \dot{\mathrm{r}}_\mathrm{i}^2$ of the particle. Therefore

$$\frac{1}{2}\ddot{I}_i = 2\mathcal{U}_i + \mathbf{F_i} \cdot \mathbf{r}_i. \tag{1.11}$$

By summing this equality over a group of particles we obtain the expression of the Virial theorem

$$\frac{1}{2}\ddot{I} = 2\mathcal{U} + \Omega, \tag{1.12}$$

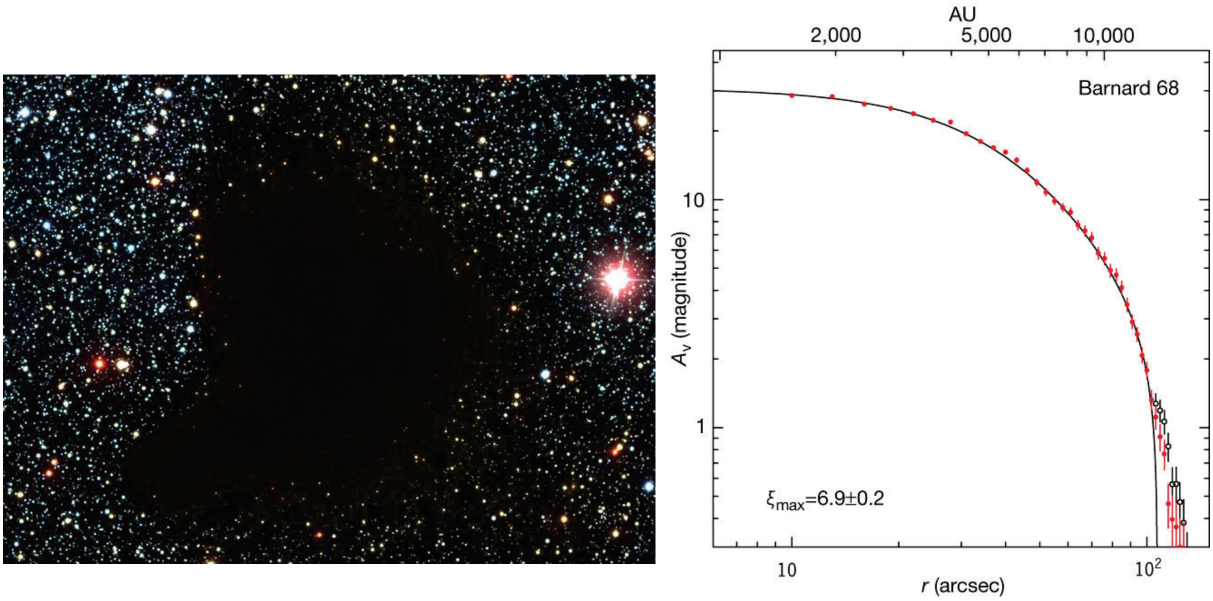

Figure 1.5: Image of the cloud Barnard 68 (left panel) and its luminosity profile (right panel): comparison between the observation (red dots) and the theoretical Bonnor-Ebert profile (solid line). Image credit: NASA, plot from Alves et al. (2001).

where I and $\mathcal{U}$ are the total inertia momentum and the total kinetic energy, and $\Omega = \sum_i \mathbf{F_i} \cdot \mathbf{r_i}$. In our system, the only force $\mathbf{F}$ is gravity Ω writes

$$\Omega = \sum_i \sum_{j \neq i} \frac{G m_i m_j}{|\mathbf{r_j} - \mathbf{r_i}|^3} (\mathbf{r_j} - \mathbf{r_i}) \cdot \mathbf{r_i}. \tag{1.13}$$

In this double sum, we can consider that each term is counted twice. For any distinct i and j, the following terms appear

$$\begin{aligned} &\frac{G m_i m_j}{|\mathbf{r_j} - \mathbf{r_i}|^3} (\mathbf{r_j} - \mathbf{r_i}) \cdot \mathbf{r_i}, \text{ and} \\ &\frac{G m_j m_i}{|\mathbf{r_i} - \mathbf{r_j}|^3} (\mathbf{r_i} - \mathbf{r_j}) \cdot \mathbf{r_j}. \end{aligned}$$

Their addition yields

$$\frac{G m_i m_j}{|\mathbf{r_j} - \mathbf{r_i}|^3} (\mathbf{r_j} - \mathbf{r_i}) \cdot (\mathbf{r_i} - \mathbf{r_j}).$$

On this basis, equation (1.13) can be simplified to

$$\Omega = -\sum_{i \neq j} \frac{G m_i m_j}{|\mathbf{r_j} - \mathbf{r_i}|}. \tag{1.14}$$

We then recognize in Ω the gravitational potential energy.

For a system at equilibrium, the Virial theorem gives

$$2\mathcal{U} + \Omega = 0. \tag{1.15}$$

In other words, a self-gravitating system is at equilibrium only if its gravitational potential energy is twice its kinetic energy in absolute value. The kinetic energy represents the motion of celestial bodies (planets, stars...) for large structures, but in our case it accounts for the thermal agitation of gas particles. This means that an interstellar cloud cannot collapse onto itself if the thermal support is too high, and the Virial theorem gives the limiting value. We can derive a critical mass and radius from equation (1.15) above which the thermal support is not sufficient to prevent a gravitational collapse. For an homogeneous spherical cloud of mass M and radius R, the gravitational potential energy is

$$\Omega = -\int_R \frac{Gm}{r} dm = -\frac{3GM^2}{5R}, \tag{1.16}$$

and the thermal energy is

$$\mathcal{U} = \frac{3}{2} n k_{\mathrm{B}} T = \frac{3 M k_{\mathrm{B}} T}{2 \mu m_{\mathrm{H}}}. \tag{1.17}$$

In this last equation, we sum the thermal energy of the n particles in the cloud. $k_{\mathrm{B}} = 1.38065 \times 10^{-16}$ erg K^{-1} is the Boltzmann constant, $m_{\mathrm{H}} = 1.67262 \times 10^{-24}$ g is the mass of a proton, and μ is the mean weight of interstellar particles in proton mass. In protostellar collapse conditions, $\mu = 2.31$. Replacing 1.16 and 1.17 in equation (1.15) yields, after rearranging the terms,

$$R_{\mathrm{crit}} = \sqrt{\frac{15 k_{\mathrm{B}} T}{4\pi G \rho \mu m_{\mathrm{H}}}}, \quad M_{\mathrm{crit}} = \frac{4}{3}\pi R_{\mathrm{crit}}^3 \rho. \tag{1.18}$$

Above these values of radius and mass, the temperature of a cloud cannot counter-balance gravity and a collapse is possible.

1.2.1.2 The Jeans length

In 1902, James Jeans (Jeans 1902) proposed another approach to measure the gravitational stability of interstellar clouds, by performing a perturbation analysis on the Euler equations. This technique is widely used in physics to examine the response of a system to a small (a priori unavoidable) perturbation. We consider an infinite and homogeneous medium in its gravitational field

$$\frac{\partial \rho}{\partial t} + \nabla \cdot [\rho \mathbf{u}] = 0, \tag{1.19}$$

$$\frac{\partial \rho \mathbf{u}}{\partial t} + \nabla \cdot [\rho \mathbf{u} \otimes \mathbf{u} + P\mathbb{I}] = -\rho \nabla \Phi, \tag{1.20}$$

$$\frac{\partial E}{\partial t} + \nabla \cdot [\mathbf{u}(E + P)] = -\rho \mathbf{u} \nabla \Phi, \tag{1.21}$$

$$\Delta \Phi = 4\pi \rho G, \tag{1.22}$$

with $E = \rho\epsilon + \rho\frac{u^2}{2}$ the total energy density. The first three equations represent the conservation of mass, momentum and energy in the system. We examine the propagation of a small perturbation in this medium. The flow variables are decomposed into two terms

$$\rho = \rho_0 + \rho_1, \tag{1.23}$$

$$\mathbf{u} = \mathbf{u}_1, \tag{1.24}$$

$$\Phi = \Phi_0 + \Phi_1, \tag{1.25}$$

where the subscript 0 represents the equilibrium state and 1 the perturbed quantity. In our infinite homogeneous system, the spatial derivatives of ρ_0 and Φ_0 are zero. Keeping only the first order terms yields[8]

$$\frac{\partial \rho_1}{\partial t} + \nabla \cdot [\rho_0 \mathbf{u}_1] = 0, \tag{1.26}$$

$$\rho_0 \frac{\partial \mathbf{u}_1}{\partial t} + \nabla P = -\rho_0 \nabla \Phi_1, \tag{1.27}$$

$$\Delta \Phi_1 = 4\pi \rho_1 G. \tag{1.28}$$

We then differentiate the first equation with respect to time. We can swap the time-derivative and the divergence, and combine the result with the other two equations to obtain

$$\frac{\partial^2 \rho_1}{\partial t^2} = 4\pi \rho_0 G \rho_1 + c_\mathrm{s}^2 \Delta \rho_1. \tag{1.29}$$

Let the perturbation be a wave propagating at a frequency ω with a wave number k along the x-coordinate: $\rho_1 = \rho e^{i(\omega t - kx)}$. Replacing this formula in equation (1.29) gives the following dispersion relation

$$\omega^2 = k^2 c_\mathrm{s}^2 - 4\pi \rho_0 G. \tag{1.30}$$

The modes of this wave are unstable if $\omega^2 < 0$, or

$$k < \sqrt{\frac{4\pi \rho_0 G}{c_\mathrm{s}^2}}. \tag{1.31}$$

The corresponding length $\lambda = \frac{2\pi}{k}$ then verifies

$$\lambda > \lambda_\mathrm{J} = c_\mathrm{s} \sqrt{\frac{\pi}{\rho_0 G}}. \tag{1.32}$$

Therefore, a gas cloud larger than λ_J, called the *Jeans length*, is gravitationally unstable. In both the Virial and Jeans analysis, the critical length and mass scale as $\rho^{-\frac{1}{2}}$. If a collapse is triggered, then both the density and the Jean mass $M_\mathrm{J} = \frac{4}{3}\pi \lambda_\mathrm{J}^3 \rho_0$ increase and the gas collapses indefinitely.

In reality, the gas does not remain isothermal at high densities, as seen in the Larson core phases. For a polytropic law $P \propto \rho^n$, in association with the perfect gas law $P = \frac{\rho k_\mathrm{B} T}{\mu m_\mathrm{H}}$, we find $M_\mathrm{J} \propto \rho^{\frac{3}{2}n-2}$. $n = \frac{4}{3}$ is then a critical value below which nothing stops the collapse, and above which the collapse eventually stops, as the gas can provide its own support via thermal energy. When n equals the adiabatic index γ, the process is adiabatic, which is the case in the first and second Larson cores.

1.2.2 The free-fall time

Each physical mechanism plays its role in its own time-scale. In the case of self-gravitating systems, the *free-fall* time indicates the typical time taken by a particle to reach the center of mass.

Let us consider a particle on the outer edge of a spherical cloud at rest of mass M at a distance r_0 of the center (or a spherical shell with the same properties). The Gauss theorem certifies that the particle or shell is subject to the attraction of the enclosed mass. Newton's second law is expressed as

$$\ddot{r} = -\frac{GM}{r^2}. \tag{1.33}$$

Multiplying by $\dot{r}$ on each side and integrating over time yields

$$\frac{\dot{r}^2}{2} = GM \left(\frac{1}{r} - \frac{1}{r_0} \right),$$

---

[8] The zeroth order terms are solution of the equations, so their sum is zero. The solution of the Poisson equation gives $\rho_0 = 0$ g cm^{-3} for a constant Φ_0, but the calculus remains correct.

and with some re-arrangement

$$\frac{\dot{r}}{\sqrt{\frac{r_0}{r}-1}} = \sqrt{2\frac{GM}{r_0}}.$$

By using the variable $\cos(\beta)^2 = r/r_0$ and $M = \frac{4\pi r_0^3\rho_0}{3}$, a second integration gives the following result

$$\beta + \frac{1}{2}\sin(2\beta) = \left(\frac{8\pi G\rho_0}{3}\right)^{\frac{1}{2}} t. \tag{1.34}$$

The free-fall time is defined when the particle/shell reaches the center ($r = 0$, or $\beta = \frac{\pi}{2}$)

$$t_{\mathrm{ff}} = \sqrt{\frac{3\pi}{32G\rho_0}}. \tag{1.35}$$

We notice that the only parameter here is the density. The initial radius does not intervene, which means that all the particles in the sphere reach the center at the same time. This formula can also be found by using the third Kepler's law, that relates the period t_{orb} and the semi-major axis a of the orbit of an object around a massive body,

$$\frac{t_{\mathrm{orb}}^2}{a^3} = \frac{4\pi^2}{GM}, \tag{1.36}$$

and considering a degenerated ellipse of eccentricity 1 and semi-major axis $a = r_0/2$.

This result relies on very simple hypotheses, yet it provides a useful approximation of the time needed for a dense core to reach the Larson core stages.

1.2.3 The angular momentum in star formation

The angular momentum is a useful quantity to characterize the rotation of a system. It is calculated as

$$\mathbf{L} = \int \rho\mathbf{r} \times \mathbf{u} d\tau, \tag{1.37}$$

with $d\tau$ the volume element, and $\mathbf{r} \times \mathbf{u}$ the vectorial product between the position vector and the velocity vector. It increases if the rotation involves more mass, or is faster, or if the mass is distributed further from the center. For an isolated system, it is conserved through time. The specific angular momentum is sometimes used instead. It corresponds to the angular momentum normalized by the mass of the system M

$$\mathbf{J} = \frac{\mathbf{L}}{M}. \tag{1.38}$$

The dense cores have a non-zero angular momentum, due to their own turbulence which random motions do not average at zero, and the global turbulent motions of the parent molecular cloud that sets up a rotation. Let us consider a uniform sphere of gas of radius R_0 in a solid rotation around the z-axis with an angular velocity of Ω_0. The specific angular momentum along this axis is $J = \Omega_0 R_0^2$. The conservation of J gives, at any time t,

$$\Omega(t) = \Omega_0 \left(\frac{R_0}{R(t)}\right)^2. \tag{1.39}$$

In other words, while the cloud shrinks, its angular velocity increases as the square of the factor of contraction of its size. The diameter of a dense core is typically one tenth of a light-year, so the contraction factor when the star starts its main sequence phase is[9] $\frac{R_0}{R_\odot} \approx 6 \times 10^5$, which results in an increase of the angular velocity of $\frac{\Omega}{\Omega_0} \approx 4 \times 10^{11}$. A star with the size of the sun with such an angular momentum would be rotating near the speed of light ! This is of course both

---

[9] $R_\odot \approx 1.5 \times 10^{10}$ cm is the radius of the sun.

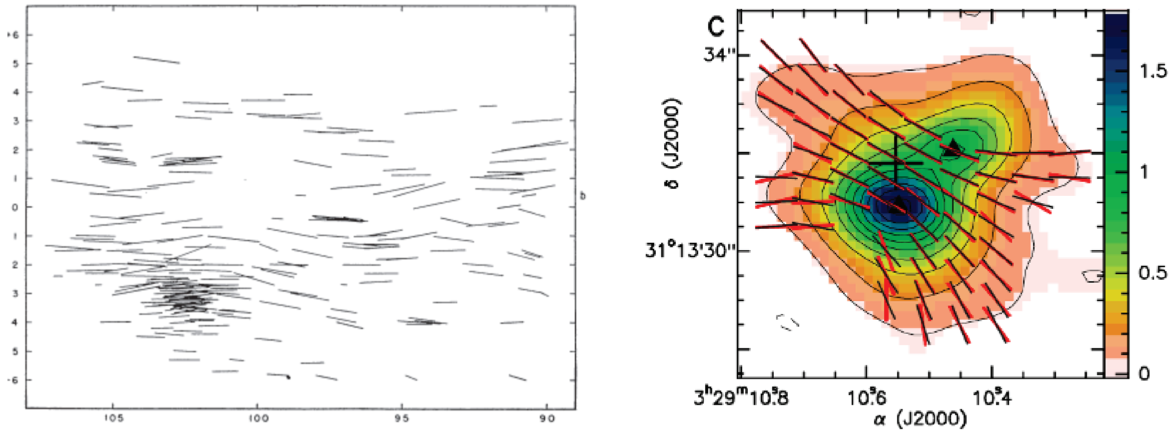

Figure 1.6: Left : observation of the polarization of the interstellar medium in the regions of Cassopeia and Perseus (Hiltner 1951). Right : observation of the magnetic field threading a dense core (Girart et al. 2006).

unobserved and unphysical given that the centrifugal force would dominate gravitation by several orders of magnitude and would tear the star apart. Actually, the specific angular momentum of a T Tauri star is 1000 times smaller than the dense core (typically 10^{18} cm^2 s^{-1} and 10^{21} cm^2 s^{-1} respectively). It means that there must exist mechanisms able to dissipate or carry away this angular momentum.

The formation of a binary system or a massive planet is an efficient way to distribute the angular momentum. The rotation of a massive object far away from the center of mass, like Jupiter in the solar system, concentrates a great portion of the system's angular momentum. But this is generally not sufficient and more physical processes are needed to describe star formation, such as the contribution of the magnetic field, which is one of the main points of this study.

1.3 The role of magnetic fields

Hiltner (1951) and Hall (1951) observed the polarization of light from distant stars by dust grains in the interstellar medium (see figure 1.6), making them the firsts to highlight the presence of large-scale magnetic fields. Such fields have been shown to play a significant role at the scale of the galaxy, notably in the acceleration of cosmic-rays (Fermi 1949) and in the support of galactic spiral arms (Chandrasekhar & Fermi 1953). Magnetised clouds have later been theorized by Mestel & Spitzer (1956) in the context of star formation. They addressed several issues arising from this new framework. First, the magnetic pressure is an additional support against gravity and can prevent the collapse of a cloud. A more general form of the Virial theorem leads to a criterion on the mass and the strength of the magnetic field for a cloud to be able to collapse. The second issue is the *magnetic braking* and is addressed further. Please note that in this work, the equations are expressed in the electromagnetic CGS convention, i.e. the electromagnetic permeability μ_0 is equal to 1.

1.3.1 The ideal MHD

The physics describing the behaviour of a magnetised fluid is called *magnetohydrodynamics* (MHD). In ideal MHD, the equations of the fluid are

$$\frac{\partial \rho}{\partial t} + \nabla \cdot [\rho \mathbf{u}] = 0, \tag{1.40}$$

$$\rho \frac{\partial \mathbf{u}}{\partial t} + \rho(\mathbf{u} \cdot \nabla)\mathbf{u} = -\nabla P + \mathbf{J} \times \mathbf{B}, \tag{1.41}$$

$$\frac{\partial E}{\partial t} + \nabla \cdot [(E + P_{\text{tot}})\mathbf{u} - (\mathbf{u} \cdot \mathbf{B})\mathbf{B}] = 0, \tag{1.42}$$

$$\frac{\partial \mathbf{B}}{\partial t} = \nabla \times (\mathbf{u} \times \mathbf{B}), \tag{1.43}$$

$$\nabla \cdot \mathbf{B} = 0. \tag{1.44}$$

The first three equations are the usual conservation of mass, momentum and energy, where $\mathbf{J} \times \mathbf{B}$ is the Lorentz force. The total energy is expressed as $E = \frac{1}{2}\rho u^2 + \rho\epsilon + \frac{1}{2}B^2$ and the total pressure is $P_{\text{tot}} = P + \frac{1}{2}B^2$. Equation (1.43) is the Maxwell-Faraday equation, also called the *induction equation.* $\mathbf{u} \times \mathbf{B}$ represents the electric field induced by the motion of electric charges in the fluid. Finally, the last equation is the well-known solenoidal constraint of the magnetic field. Ideal MHD is an approximation which do not take into account the diffusive processes of charged particles.

1.3.2 Magnetised Virial theorem

We use the same approach as in section 1.2.1.1 by adding the magnetic forces. In this context, the Navier-Stokes equation can be written as

$$\rho \frac{d\mathbf{u}}{dt} + \rho(\mathbf{u} \cdot \nabla)\mathbf{u} = -\nabla P - \nabla \left(\frac{B^2}{2}\right) - (\mathbf{B} \cdot \nabla)\mathbf{B} - \rho \mathbf{g}. \tag{1.45}$$

This is the same equation as (1.41) with the addition of the gravitational field $\mathbf{g}$. The Lorentz force has been decomposed into two terms using vectorial identities and the Maxwell-Ampère equation $\nabla \times \mathbf{B} = \mathbf{J}$. $B^2/2$ is the magnetic pressure and $(\mathbf{B} \cdot \nabla)\mathbf{B}$ represents the magnetic tension. Similarly to the simplified Virial theorem, we multiply the equation by $\cdot\mathbf{r}$ and integrate over the whole volume V. We obtain once more

$$\int_V \rho \frac{d\mathbf{u}}{dt} \cdot \mathbf{r} \mathrm{d}V = \frac{1}{2}\ddot{I} - 2\mathcal{T}, \tag{1.46}$$

$$\int_V \rho \mathbf{g} \cdot \mathbf{r} \mathrm{d}V = \Omega, \tag{1.47}$$

with $\mathcal{T}$ the total kinetic energy of the fluid. The pressure is expressed with the ideal gas equation of state $P = (\gamma - 1)e$, where e is the energy density. From here, we use the Ostrogradsky's theorem : $\int_V \nabla \cdot \mathbf{A} \mathrm{d}V = \int_\Sigma \mathbf{A} \cdot \mathbf{dS}$ where Σ is the surface that encloses the volume V. We obtain

$$\begin{aligned}
\int_V \nabla P \cdot \mathbf{r} \mathrm{d}V &= \int_V \nabla \cdot (P\mathbf{r})\mathrm{d}V - (\gamma - 1)\int_V e\nabla \cdot \mathbf{r} \mathrm{d}V \\
&= \int_\Sigma P\mathbf{r} \cdot \mathbf{dS} - 3(\gamma - 1)\int_V e \mathrm{d}V \\
&= \int_\Sigma P\mathbf{r} \cdot \mathbf{dS} - 3(\gamma - 1)\mathcal{U} && (1.48) \\
& && (1.49)
\end{aligned}$$

where $\mathcal{U}$ is the total internal energy.
We use a vectorial identity to express the magnetic pressure term

$$\begin{aligned}\nabla\left(\frac{B^2}{2}\right)\cdot\mathbf{r} &= \nabla\cdot\left(\frac{B^2}{2}\mathbf{r}\right)-(\nabla\cdot\mathbf{r})\frac{B^2}{2}\\ &= \nabla\cdot\left(\frac{B^2}{2}\mathbf{r}\right)-3\frac{B^2}{2}. \qquad (1.50)\\ & \qquad (1.51)\end{aligned}$$

For the magnetic tension, it is easier to adopt the Einstein notations: expressing the components and dropping the sum signs[10]

$$\begin{aligned}((\mathbf{B}\cdot\nabla)\mathbf{B})\cdot\mathbf{r} &= B_i x_j \partial_i B_j\\ &= B_i(\partial_i(B_j x_j)-B_j\partial_i x_j)\\ &= \partial_i(B_iB_jx_j)-B_jx_j\partial_iB_i-B_iB_j\delta_i^j\\ &= \nabla\cdot((\mathbf{B}\cdot\mathbf{r})\mathbf{B})-(\mathbf{B}\cdot\mathbf{r})\nabla\cdot\mathbf{B}-(B_x^2+B_y^2+B_z^2)\\ &= \nabla\cdot((\mathbf{B}\cdot\mathbf{r})\mathbf{B})-B^2, \qquad (1.52)\\ & \qquad (1.53)\end{aligned}$$

where we used the solenoidal condition on magnetic field $\partial_iB_i=\nabla\cdot\mathbf{B}=0$. Adding both integrated terms yields

$$\int_V\left[-\nabla\left(\frac{B^2}{2}\right)\cdot\mathbf{r}+((\mathbf{B}\cdot\nabla)\mathbf{B})\cdot\mathbf{r}\right]\mathrm{d}V=\mathcal{M}+\int_\Sigma\left[(\mathbf{B}\cdot\mathbf{r})\mathbf{B}-\left(\frac{B^2}{2}\mathbf{r}\right)\right]\cdot\mathbf{dS}, \tag{1.54}$$

with $\mathcal{M}=\int_V B^2/2\mathrm{d}V$ the total magnetic energy. The Virial theorem is then written

$$3(\gamma-1)\mathcal{U}+\mathcal{M}+\Omega+2\mathcal{T}=\frac{1}{2}\ddot{I}-\int_\Sigma\left[(\mathbf{B}\cdot\mathbf{r})\mathbf{B}-\left(P+\frac{B^2}{2}\right)\mathbf{r}\right]\cdot\mathbf{dS}. \tag{1.55}$$

In a simple situation, for an isolated spherical cloud at rest, the theorem reads

$$3(\gamma-1)\mathcal{U}+\mathcal{M}+\Omega=0. \tag{1.56}$$

The magnetic energy is added to the thermal pressure to support the cloud against its self-gravity. From this expression, Mouschovias & Spitzer (1976) express the minimal mass required for the collapse of a cloud solely supported by magnetic fields

$$M_{\text{crit}}=\frac{0.53}{3\pi}\left(\frac{5}{G}\right)^{\frac{1}{2}}\phi, \tag{1.57}$$

where $\phi=\pi BR^2$ is the magnetic flux. The strength of the magnetic field in a cloud is often defined using this value in the *mass-to-flux ratio* μ

$$\mu=\frac{\left(\frac{M}{\phi}\right)}{\left(\frac{M}{\phi}\right)_{\text{crit}}}=\frac{\frac{\int dM}{\int d\phi}}{\frac{0.53}{3\pi}\left(\frac{5}{G}\right)^{\frac{1}{2}}}. \tag{1.58}$$

It represents the ratio of gravitational on magnetic energy compared to the critical value. The cases $\mu<1$ and $\mu>1$ are respectively called sub-critical and super-critical. Only super-critical cores can collapse, and observations show that dense cores show typical values of $\mu\in[2-5]$ (Crutcher et al. 1999).

---

[10] e.g., we remove the sum sign in the ith component of the vector: $B_i\sum_{j=1,3}B_ix_j\partial_iB_j$.

1.3.3 The magnetic field during the collapse

In ideal MHD, the induction equation (1.43) can be interpreted as a freezing of the magnetic field lines into the fluid. In other words, the field lines are dragged by the motion of the matter. As a result, they get "pinched" where the density increases, and "twisted" by rotation. The situation for a collapse is represented in figure 1.7.

The bending of the field lines creates a magnetic tension that acts to straighten them. This force generates perturbations of the magnetic field, the Alfvén waves, that propagate along the field lines at the Alfvén speed $c_\mathrm{A} = B/\sqrt{\rho}$.

The pseudo-disk The "pinching" of the field lines induces a strong radial component of the magnetic field. The gas is falling almost radially even in rotating cores, as the infall velocity is much greater than the rotation velocity. It is then deviated because the Lorentz force is perpendicular to the field. The encounters of symmetrically deviated gas particles cancel their speed component parallel to the magnetic field, which leads to an accumulation of matter perpendicular to the field known as the "pseudo-disk" (Galli & Shu 1993; Tsukamoto et al. 2017). Contrarily to the circumstellar disk, the pseudo-disk is not stable against collapse. It is much denser than the surrounding medium, and reaches a radius of several hundreds of au.

Angular momentum transport As seen previously, the rotation of the fluid entangles the field lines around the rotation axis. The toroidal component of the momentum equation (1.41) can be reformulated as

$$\frac{\partial \rho u_\theta}{\partial t} + \nabla \cdot \left[\rho u_\theta \mathbf{u} + \left(P + \frac{B^2}{2} \right) \mathbf{e}_\theta - B_\theta \mathbf{B} \right] = 0. \tag{1.59}$$

The magnetic tension $B_\theta \mathbf{B}$ then generates an azimuthal acceleration $\partial u_\theta / \partial t$ if $B_\theta \neq 0$ in order to straighten the field lines[11]. As a consequence, a toroidal magnetic field induced by the twisting of the field lines produces a force resisting the rotation that created it. Through this process, the magnetic field redistributes the angular momentum from the dense regions to the exterior of the cloud via Alfvén waves (Mestel & Spitzer 1956; Gillis et al. 1974; Mouschovias 1977, 1991; Joos et al. 2012). This is known as the *magnetic braking* and is one of the most serious candidate to remove the angular momentum from the star. However, in the ideal MHD approximation, the magnetic flux becomes so intense in the core that the majority of the angular momentum is removed. The lack of rotational support leads to protostars with small or no disk (Allen et al. 2003; Matsumoto & Tomisaka 2004; Galli et al. 2006; Price & Bate 2007; Hennebelle & Teyssier 2008; Hennebelle & Fromang 2008; Commerçon et al. 2010; Masson et al. 2016). The large number of protoplanetary disks observed around protostars proves that ideal MHD does not accurately describe the reality of protostellar collapses.

Another issue concerns the magnetic flux itself. The magnetic fluxes observed in dense cores are much larger than in young stars (Nakano 1984; Li 1998). However, the flux is conserved through the collapse in the framework of ideal MHD. Non-ideal MHD describes more accurately the interplay between the fluid and the magnetic field, and gives answers to these problems.

1.3.4 Non-ideal Magnetohydrodynamics

1.3.4.1 The generalized Ohm's law

Non-ideal MHD is a more complete description of reality than its ideal counter-part. It considers fluids of electrons, ions and neutrals, and describes their behaviour and their interaction. Neglecting specific terms is possible depending on the physical situation. In proto-stellar collapses, we use the fact that the medium is weakly ionised. As Balbus & Terquem (2001) and in agreement with the one-fluid hydrodynamical code `RAMSES` (Teyssier 2002) (see chapter 3), we

---

[11] Note that this is also true for the other components.

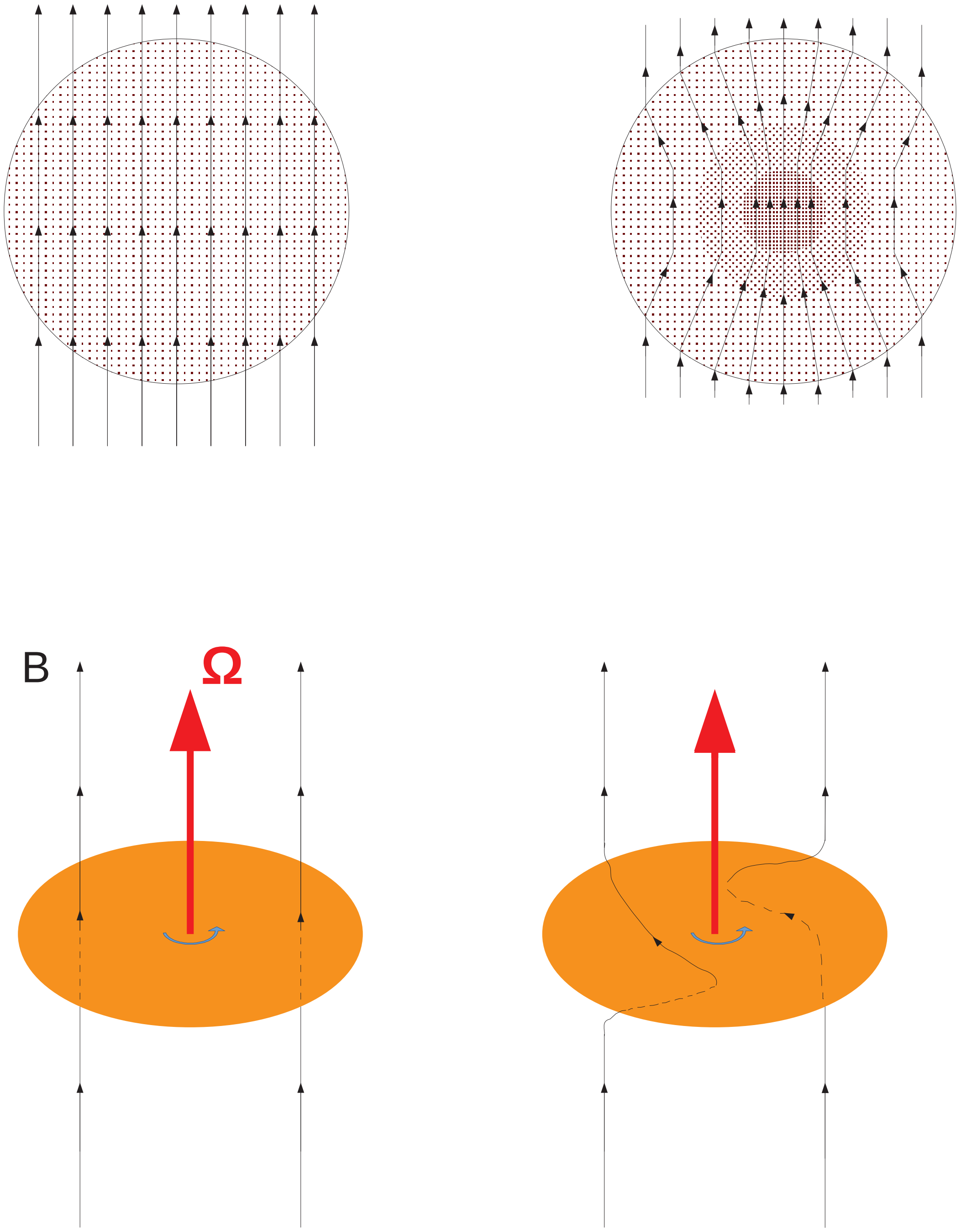

Figure 1.7: Representation of the frozen flux in ideal MHD. Top Left: uniform magnetic field in a uniform cloud, top Right: collapsed cloud and "pinching" of the field lines. Bottom left: rotating disk threaded by field lines, bottom right: twisting of the field lines by the rotation.

adopt the single fluid approximation (see Toth (1994) for the two-fluid approximation and Pinto & Galli (2009); Pinto et al. (2008) for a three-fluid description).

We start from the momentum equation of ions and electrons

$$\begin{aligned} Zen_{\mathrm{i}}\,(\mathbf{E}+\mathbf{u_i}\times\mathbf{B})-\rho_{\mathrm{i}}\nu_{\mathrm{ie}}(\mathbf{u_i}-\mathbf{u_e})-\rho_i\nu_{\mathrm{in}}(\mathbf{u_i}-\mathbf{u}) &= 0, & (1.60)\\ -en_{\mathrm{e}}\,(\mathbf{E}+\mathbf{u_e}\times\mathbf{B})-\rho_{\mathrm{e}}\nu_{\mathrm{ei}}(\mathbf{u_e}-\mathbf{u_i})-\rho_e\nu_{\mathrm{en}}(\mathbf{u_e}-\mathbf{u}) &= 0. & (1.61)\\ & & (1.62) \end{aligned}$$

The low ionisation ensures a quasi-equilibrium between the Lorentz force (first term) and the collisions with the two other species (two other terms). We have assimilated the neutral velocity $\mathbf{u}_{\mathrm{n}}$ to the fluid velocity $\mathbf{u}$. Z is the mean ionisation degree, and n represents the number density of the species in particle/cm^3, so $Zn_{\mathrm{i}}=n_{\mathrm{e}}$ ensures the charge equilibrium. e is the elementary electric charge, ρ is the mass density of the species and $\mathbf{E}$ the electric field. ν_{ab} is a coupling term between species a and b and reads

$$\nu_{ab}=\rho_b\frac{<\sigma v>_{ab}}{m_a+m_b}, \tag{1.63}$$

where $<\sigma v>_{ab}$ is the mean collision rate coefficient between a and b, and m is their mass. Replacing these expressions into (1.60)-(1.61) then adding the two equations yields

$$\mathbf{J}\times\mathbf{B}+\frac{\rho_{\mathrm{i}}\rho_{\mathrm{n}}<\sigma v>_{\mathrm{in}}}{m_{\mathrm{i}}+m_{\mathrm{n}}}(\mathbf{u}-\mathbf{u_i})+\frac{\rho_{\mathrm{e}}\rho_{\mathrm{n}}<\sigma v>_{\mathrm{en}}}{m_{\mathrm{e}}+m_{\mathrm{n}}}(\mathbf{u_e}-\mathbf{u})=0, \tag{1.64}$$

where we have introduced the electric current $\mathbf{J}=en_{\mathrm{e}}(\mathbf{u_i}-\mathbf{u_e})$. The last term is small compared to the others, so we can write

$$\mathbf{J}\times\mathbf{B}=\frac{\rho_i\rho_n<\sigma v>_{\mathrm{in}}}{m_{\mathrm{i}}+m_{\mathrm{n}}}(\mathbf{u_i}-\mathbf{u}). \tag{1.65}$$

Now, we make the ions and neutrals velocities appear in the electron equation (1.61)

$$\begin{aligned} &\mathbf{E}+[\mathbf{u}+(\mathbf{u_e}-\mathbf{u_i})+(\mathbf{u_i}-\mathbf{u})]\times\mathbf{B}-\frac{\rho_{\mathrm{e}}\rho_{\mathrm{i}}<\sigma v>_{\mathrm{ei}}}{en_{\mathrm{e}}(m_{\mathrm{e}}+m_{\mathrm{i}})}(\mathbf{u_i}-\mathbf{u_e})\\ &+\frac{\rho_{\mathrm{e}}\rho_{\mathrm{n}}<\sigma v>_{\mathrm{en}}}{en_{\mathrm{e}}(m_{\mathrm{e}}+m_{\mathrm{n}})}\left[(\mathbf{u_e}-\mathbf{u_i})+(\mathbf{u_i}-\mathbf{u})\right]=0. \end{aligned} \tag{1.66}$$

We can neglect the term in $\boldsymbol{\rho_e\rho_i}$ because of the low ionisation, as well as the last term (refer to Balbus 2009, for more details about the approximations used in this calculation). Replacing the velocity differences with $\mathbf{J}$ and equation (1.65) expressions and using $\rho_a=m_an_a$, we finally get

$$\mathbf{E}=-\left[\mathbf{u}\times\mathbf{B}-\frac{\mathbf{J}}{\sigma}-\frac{\mathbf{J}\times\mathbf{B}}{en_{\mathrm{e}}}+\frac{(\mathbf{J}\times\mathbf{B})\times\mathbf{B}}{\gamma_{\mathrm{AD}}\rho\rho_{\mathrm{i}}}\right], \tag{1.67}$$

with $\sigma=\frac{n_{\mathrm{e}}e^2}{n_{\mathrm{n}}m_{\mathrm{e}}<\sigma_{\mathrm{en}}v_{\mathrm{e}}>}$ and $\gamma_{\mathrm{AD}}=\frac{\sigma_{\mathrm{in}}v_i}{m_{\mathrm{i}}+m_{\mathrm{n}}}$. We then replace the electric field into the Maxwell-Faraday equation to obtain the induction equation

$$\frac{\partial\mathbf{B}}{\partial t}=\nabla\times(\mathbf{u}\times\mathbf{B}+\mathbf{E}_{\mathrm{NIMHD}}). \tag{1.68}$$

$\mathbf{E}_{\mathrm{NIMHD}}$ is the electric field associated to the non-ideal MHD effects and corresponds to the last three terms of equation (1.67). In the presence of multiples charged species, it can also be written (Nakano et al. 2002)

$$\mathbf{E}_{\mathrm{NIMHD}}=-\eta_\Omega\mathbf{J}-\frac{\eta_{\mathrm{H}}}{||\mathbf{B}||}(\mathbf{J}\times\mathbf{B})+\frac{\eta_{\mathrm{AD}}}{||\mathbf{B}||^2}((\mathbf{J}\times\mathbf{B})\times\mathbf{B}), \tag{1.69}$$

The three effects are, in order

- the *Ohmic diffusion*, i.e. the diffusion of electrons by neutral particles,
- the *Hall effect*, an electric field created by the speed difference between the electron and the ion fluids,
- the *ambipolar diffusion*, representing the diffusion of ions by neutral particles.

The strength of each process is governed by its resistivity η (see more details in chapter 2).

1.3.4.2 Energy transport

Non-ideal MHD effects do not only affect the magnetic field evolution. The conservation of the system's total energy reads

$$\frac{\partial E_{\mathrm{tot}}}{\partial t} + \nabla \cdot \left[(E_{\mathrm{tot}} + P_{\mathrm{tot}})\mathbf{u} - (\mathbf{u} \cdot \mathbf{B})\mathbf{B} - \mathbf{E}_{\mathrm{NIMHD}} \times \mathbf{B} \right] = 0, \tag{1.70}$$

Replacing $E_{\mathrm{tot}} = \rho\epsilon + \frac{1}{2}\rho u^2 + \frac{B^2}{2}$ in the time derivative of equation (1.70) yields

$$\frac{\partial \rho\epsilon}{\partial t} + \frac{1}{2}\frac{\partial \rho u^2}{\partial t} + \mathbf{B} \cdot \frac{\partial \mathbf{B}}{\partial t} + \nabla \cdot \left[(E_{\mathrm{tot}} + P_{\mathrm{tot}})\mathbf{u} - (\mathbf{u} \cdot \mathbf{B})\mathbf{B} + \mathbf{E}_{\mathrm{NIMHD}} \times \mathbf{B} \right] = 0.$$

The energy equation is coupled with the induction equation (1.68). Replacing the time-derivative of $\mathbf{B}$ then gives

$$\begin{aligned} &\frac{\partial \rho\epsilon}{\partial t} + \frac{1}{2}\frac{\partial \rho u^2}{\partial t} + \nabla \cdot \left[(E_{\mathrm{tot}} + P_{\mathrm{tot}})\mathbf{u} - (\mathbf{u} \cdot \mathbf{B})\mathbf{B} + E_{\mathrm{NIMHD}} \times \mathbf{B} \right] \\ &+ \mathbf{B} \cdot \left[\nabla \times (\mathbf{u} \times \mathbf{B}) \right] - \mathbf{B} \cdot (\nabla \times \mathbf{E}_{\mathrm{NIMHD}}) = 0. \end{aligned}$$

The NIMHD contribution in the energy equation is thus

$$\Delta E_{\mathrm{mag}} = \mathbf{B} \cdot (\nabla \times \mathbf{E}_{\mathrm{NIMHD}}) - \nabla \cdot (\mathbf{E}_{\mathrm{NIMHD}} \times \mathbf{B}). \tag{1.71}$$

The vectorial identity $\nabla \cdot (\mathbf{A} \times \mathbf{B}) = \mathbf{B} \cdot (\nabla \times \mathbf{A}) - \mathbf{A} \cdot (\nabla \times \mathbf{B})$ simplifies the expression as some terms cancel out

$$\Delta E_{\mathrm{mag}} = \mathbf{E}_{\mathrm{NIMHD}} \cdot (\nabla \times \mathbf{B}). \tag{1.72}$$

Replacing $\mathbf{E}_{\mathrm{NIMHD}}$ by its expression (1.69)

$$\Delta E_{\mathrm{mag}} = \eta_{\Omega} \left[\mathbf{J} \cdot \mathbf{J} \right] + \frac{\eta_{\mathrm{H}}}{||\mathbf{B}||} \left[(\mathbf{J} \times \mathbf{B}) \cdot \mathbf{J} \right] - \frac{\eta_{\mathrm{AD}}}{||\mathbf{B}||^2} \left[((\mathbf{J} \times \mathbf{B}) \times \mathbf{B}) \cdot \mathbf{J} \right] \tag{1.73}$$

Finally, the contribution of each non-ideal MHD term is

$$\Delta E_{\mathrm{mag}_{\Omega}} = \eta_{\Omega} ||\mathbf{J}||^2, \tag{1.74}$$

$$\Delta E_{\mathrm{mag}_{\mathrm{H}}} = 0, \tag{1.75}$$

$$\Delta E_{\mathrm{mag}_{\mathrm{AD}}} = \eta_{\mathrm{AD}} \frac{||\mathbf{J} \times \mathbf{B}||^2}{||\mathbf{B}||^2} \tag{1.76}$$

Whereas ideal MHD lacked dissipative processes, the non-ideal description involves the Ohmic and ambipolar diffusions that fill that role. On the other hand, the Hall effect has no direct influence on the fluid and its energy, only on the magnetic field. Taking into account either of these three effects, or all of them, breaks the freezing of the field lines, which is why non-ideal MHD is a serious candidate to solve the angular momentum and magnetic flux problem (Wurster et al. 2016; Masson et al. 2016).

1.3.4.3 The Hall effect

Several studies have shown that the Hall effect may have a serious impact on star formation (Li et al. 2011; Krasnopolsky et al. 2011; Tsukamoto et al. 2015, 2017; Wurster et al. 2016, 2017). Yet, it is still rarely included in recent works. We introduce here some elements on the theory about the Hall effect and its influence on star formation.

A dispersive term We first perform a perturbation analysis to characterize the role of the Hall effect. We neglect all forces but the Lorentz force. Let us consider a fluid in an almost-equilibrium state, with a magnetic field $\mathbf{B} = B\mathbf{e}_z$. We introduce small perturbations δu_x, δu_y, δB_x, δB_y of the speed and magnetic field in the x and y-directions, propagating along the $z-$direction at the frequency ω. Each perturbation is then proportional to $\exp(i\omega t - ikz)$. Considering only the Hall effect, the induction equation is simply

$$\frac{\partial \mathbf{B}}{\partial t} = \nabla \times \left[\mathbf{u} \times \mathbf{B} - \frac{\eta_{\mathrm{H}}}{||\mathbf{B}||}\mathbf{J} \times \mathbf{B}\right]. \tag{1.77}$$

It is coupled with the momentum equation

$$\rho \frac{\partial \mathbf{u}}{\partial t} = \mathbf{J} \times \mathbf{B}. \tag{1.78}$$

We replace the variables in equations (1.77) and (1.78), and cancel out the zeroth and second order terms.

$$\rho i\omega \delta u_x = -ikB\delta B_x \tag{1.79}$$
$$\rho i\omega \delta u_y = -ikB\delta B_y \tag{1.80}$$
$$i\omega \delta B_x = ikB\delta u_x + \eta_{\mathrm{H}} k^2 \delta B_y \tag{1.81}$$
$$i\omega \delta B_y = ikB\delta u_y - \eta_{\mathrm{H}} k^2 \delta B_x \tag{1.82}$$
$$\tag{1.83}$$

The system of equation is linear and can be written in matrix form

$$\begin{pmatrix} \rho i\omega & 0 & ikB & 0 \\ 0 & \rho i\omega & 0 & ikB \\ -ikB & 0 & i\omega & -\eta_{\mathrm{H}}k^2 \\ 0 & -ikB & \eta_{\mathrm{H}}k^2 & i\omega \end{pmatrix} \begin{pmatrix} \delta u_x \\ \delta u_y \\ \delta B_x \\ \delta B_y \end{pmatrix} = 0 \tag{1.84}$$

A non-trivial solution is possible if the matrix determinant is zero. We obtain

$$\omega^4 - \omega^2(2k^2c_{\mathrm{A}}^2 + \eta_{\mathrm{H}}^2 k^4) + k^4 c_{\mathrm{A}}^4 = 0. \tag{1.85}$$

This equation can also be written as

$$(\omega^2 - k^2c_{\mathrm{A}}^2)^2 - (\eta_{\mathrm{H}}k^2\omega)^2 = 0, \text{ then} \tag{1.86}$$
$$(\omega^2 - \eta_{\mathrm{H}}k^2\omega - k^2c_{\mathrm{A}}^2)(\omega^2 + \eta_{\mathrm{H}}k^2\omega - k^2c_{\mathrm{A}}^2) = 0. \tag{1.87}$$

We only keep the positive solutions for ω, which yields the following dispersion relation (Balbus & Terquem 2001)

$$\omega = \pm\frac{\eta_{\mathrm{H}}k^2}{2} + \sqrt{\left(\frac{\eta_{\mathrm{H}}k^2}{2}\right)^2 + k^2c_{\mathrm{A}}^2}. \tag{1.88}$$

Contrarily to the ambipolar and the Ohmic diffusions, the Hall effect is purely dispersive. Any perturbation creates two waves whose frequencies ω are linked to their wavelength $\lambda = 2\pi/k$.

They are called *whistler waves*. They propagate the magnetic field perturbations along the field lines at the whistler speed

$$c_{\mathrm{w}} = \frac{\omega}{k} = \pm\frac{\eta_{\mathrm{H}} k}{2} + \sqrt{\left(\frac{\eta_{\mathrm{H}} k}{2}\right)^2 + c_{\mathrm{A}}^2}. \tag{1.89}$$

One of these two waves is always faster than the Afvén speed, and can theoretically travel at an unbound speed for very high frequencies. In practice, it is physically limited by the ion cyclotron frequency (Srinivasan & Shumlak 2011).

Influence on star formation Expressing the three components of the vectorial equation (1.77) is not difficult, but long and fastidious. We only write here the azimuthal component in cylindrical coordinates, assuming axisymmetry (so $\partial/\partial\theta = 0$) and a constant η_{H}

$$\begin{aligned}\frac{\partial B_\theta}{\partial t} &= [\nabla \times (\eta_{\mathrm{H}}(\nabla \times \mathbf{B}) \times \mathbf{B})]_\theta \\ &= \eta_{\mathrm{H}} \left[\frac{\partial}{\partial z}\left[B_z\left(\frac{\partial B_r}{\partial z} - \frac{\partial B_z}{\partial r}\right) - \frac{B_\theta}{r}\frac{\partial (r B_\theta)}{\partial r}\right] + \frac{\partial}{\partial r}\left[B_\theta \frac{\partial B_\theta}{\partial z} + B_r \frac{\partial B_r}{\partial z} + B_r \frac{\partial B_z}{\partial r}\right]\right].\end{aligned} \tag{1.90}$$

This expression reveals that the Hall effect generates a toroidal magnetic field B_θ provided that B_r and B_z are not constant. It even happens without the need of B_θ as setting $B_\theta = 0$ does not reduce the right term at zero. In other words, the vertical and radial components of the field are transposed in the azimuthal direction through time, creating a twisting of the field lines, similarly to the rotation in the frozen flux approximation. Remembering equation (1.59), the consequence is clear: an azimuthal acceleration is created.

When submitted to the Hall effect, the field lines move at the Hall speed

$$\mathbf{u}_{\mathrm{H}} = -\eta_{\mathrm{H}} \frac{\mathbf{J}}{\|\mathbf{B}\|}. \tag{1.91}$$

The induction equation then becomes

$$\frac{\partial \mathbf{B}}{\partial t} = \nabla \times [(\mathbf{u} + \mathbf{u}_{\mathrm{H}}) \times \mathbf{B}]. \tag{1.92}$$

A reasoning similar to ideal MHD can be held: the magnetic tension acts to straighten the field lines and creates an acceleration to counter-act their motion. This time however, the fluid does not converge toward $\mathbf{u} = 0$ but $\mathbf{u} + \mathbf{u}_{\mathrm{H}} = 0$. If this condition is met, the fluid velocity perfectly compensates the motion of the field lines due to the Hall effect. $\mathbf{u}_{\mathbf{H}}$ is parallel to the electric current $\mathbf{J}$, which is mostly azimuthal in the pseudo-disk (Tsukamoto 2016). Therefore, the fluid in the pseudo-disk is expected to converge towards the velocity $\mathbf{u} = -u_{\mathrm{H},\theta}\mathbf{e}_\theta$. The central region accretes its matter from the pseudo-disk, so the Hall effect impacts the dynamics of the circumstellar disk and the core. Depending on the sign of η_{H} (see chapter 2), the Hall effect can therefore enhance, prevent or even induce the rotation of a fluid through the creation of B_θ. Hence, it may play a major role in the redistribution of the angular momentum.

1.3.4.4 Non-ideal MHD in litterature

The first non-ideal MHD effects studied in numerical simulations were the ambipolar and the Ohmic diffusion, starting with Black & Scott (1982) (see more details about the numerical implementation in section 3.1.7). Subsequent studies have determined that ambipolar diffusion does weaken the magnetic braking, allowing the formation of larger disks, and redistributes the magnetic flux, reducing the magnetic field in the core (Duffin & Pudritz 2008; Mellon & Li 2009; Kunz & Mouschovias 2010; Tomida et al. 2015; Masson et al. 2016). Ohmic diffusion is also able to decrease the magnetic flux in high density regions, resulting in a weakened magnetic braking at the scale of the first Larson core and a modified dynamics of protostellar jets (Machida et al. 2006, 2007, 2008, 2009). However, as shown in chapter 2, the Hall resistivity has the same order of magnitude as the ambipolar resistivity, so its effects can be similar in strength. It is therefore necessary to implement it for studying in what extent the dynamics and outcome of the collapse is affected.

Krasnopolsky et al. (2011) were the first to study the Hall effect in the context of star formation, in simple configurations (homogeneous core, no rotation or rotation axis parallel to the magnetic field and constant resistivity). They found that the Hall effect does indeed generate rotation in the middle plane, in either direction depending on the sign of the magnetic field, and counter-rotating envelopes form on each side of the disk by conservation of the angular momentum. These results were later confirmed by Tsukamoto et al. (2015), and extended to several values and inclinations of the magnetic field in Wurster et al. (2016) and Tsukamoto et al. (2017). Wurster et al. (2017) then performed simulations in the context of binary star formation, and showed that the Hall effect had a major influence on the outcome of the system (number of fragments, distance), by either enhancing or inhibiting the fragmentation.

Given that these results are still young and mostly produced by the same kind of SPH code and implementation (see more details in section 3.4), they need to be confirmed by additional studies using other numerical methods. Additionally, the chemical models employed to compute the non-ideal MHD resistivities in these studies differ from ours, described in chapter 2. As shown in a further section, the resistivities may be extremely sensitive to several parameters, meaning that using another model could lead to different results. Finally, no study has addressed the point of turbulence yet.

1.3.4.5 Outline

In the next chapter, I focus on chemistry in order to compute the non-ideal MHD resistivities η during star formation. I then present my implementation of the Hall effect in the eulerian code `RAMSES` in chapter 3. Finally, I present my results on the influence of the Hall effect during the protostellar collapse in chapter 4.

Chapter 2

Chemistry

2.1 Introduction

Stars form in a chemically complex environment. While most of the interstellar gas is composed of Hydrogen ($\sim 74\%$ by mass) and Helium ($\sim 25\%$), heavier elements coming from star remnants and supernovae feedbacks add a large diversity of chemical species. These elements are essentially under molecular form, but a fraction aggregates to form dust grains. The grains are composed of up to several hundred carbon or silicate-based molecules, and can reach 1 μm size in the first steps of star formation. Both dust and gas are coupled to the magnetic field because they are partially ionised. The repartition of electric charges in the medium determines the response of the fluid to the magnetic effects. In the non-ideal MHD regime, the relative abundances and the degree of ionisation of the grains and molecules in the collapsing cloud determine the resistivities η_{Ω}, $\eta_{\rm H}$ and $\eta_{\rm AD}$. Numerical simulations including non-ideal MHD require precise values of these resistivities. In this section, we present a reduced chemical network that we designed to compute the resistivities in the star forming environment. This network significantly extends over previous prescriptions(Umebayashi & Nakano 1990; Nishi et al. 1991; Nakano et al. 2002; Kunz & Mouschovias 2009), by including new pieces of physics, necessary for a precise description of the chemical evolution of the interstellar gas.

Our reduced chemical network allows us to test the impact of various parameters, such as the evolution of grains of different sizes and the cosmic-ray ionisation rate, on the equilibrium abundances of chemical species and the non-ideal MHD diffusion coefficients. This work was published in Astronomy and Astrophysics (Marchand et al. 2016).

2.2 Theory

2.2.1 The magnetic resistivities

The resistivities of the non-ideal MHD effects are defined in terms of the conductivities of the gas-dust mixture as

$$\eta_{\Omega} = \frac{1}{\sigma_{\parallel}}, \tag{2.1}$$

$$\eta_{\rm H} = \frac{\sigma_{\rm H}}{\sigma_{\perp}^2 + \sigma_{\rm H}^2}, \tag{2.2}$$

$$\eta_{\rm AD} = \frac{\sigma_{\perp}}{\sigma_{\perp}^2 + \sigma_{\rm H}^2} - \frac{1}{\sigma_{\parallel}}. \tag{2.3}$$

If we neglect the inelastic collisions contribution on resistivities (see section 2.4.8), the parallel, perpendicular and Hall conductivities are in turn expressed, respectively, as

$$\sigma_{\parallel} = \sum_i \sigma_i, \tag{2.4}$$

$$\sigma_{\perp} = \sum_i \frac{\sigma_i}{1 + (\omega_i \tau_{\text{in}})^2}, \tag{2.5}$$

$$\sigma_{\text{H}} = -\sum_i \frac{\sigma_i \omega_i \tau_{\text{in}}}{1 + (\omega_i \tau_{\text{in}})^2}. \tag{2.6}$$

with $\sigma_i = \dfrac{n_i q_i^2 \tau_{\text{in}}}{m_i}$ the conductivity, $\omega_i = \dfrac{q_i B}{m_i c}$ the cyclotron frequency, and

$$\tau_{\text{in}} = \frac{1}{a_{i\text{He}}} \frac{m_i + m_{\text{H}_2}}{m_{\text{H}_2}} \frac{1}{n_{\text{H}_2} \langle \sigma_{\text{coll}} w \rangle_i}$$

the characteristic time between elastic collisions between a charged species and a neutral gas particle. Here i stands for any particle of charge q_i, with a charge particle number-density n_i, m_i denotes the mass of a particle, and c is the speed of light. The factor $a_{i\text{He}}$ accounts for collisions with Helium atoms and is equal to 1.14 for ions, 1.16 for electrons and 1.28 for grains (Desch & Mouschovias 2001). $\langle \sigma_{\text{coll}} w \rangle_i$ is the rate constant for collisions between a particle i and H_2 molecules (Desch & Mouschovias 2001; Pinto & Galli 2008). Please note that these rates have been calculated in a three-fluid formalism, and we use them in a multifluid context. ω_i can be negative, depending on the charge q_i. This is important when calculating the conductivities, since the Hall conductivity σ_{H} can be either positive or negative. This implies that the Hall resistivity can be negative, since it is of the same sign as σ_{H}. On the other hand, the Ohmic and ambipolar diffusion resistivities are always positive.

The dimension of the resistivities is cm^2 s^{-1}, with a typical value of $\eta \approx 10^{20}$ cm^2 s^{-1}. We however use the reduced value of resistivities in this chapter by dividing them by $c^2/4\pi \approx 10^{20}$ cm^2 s^{-2}. They are thus expressed in seconds.

2.2.2 Chemical Network

Umebayashi & Nakano (1990) proposed a chemical network containing the elements : H, He, C, O, heavy metal elements such as Na, K, Mg, Al, Si, Ca, Fe, Ni, and grains. In dense molecular clouds, the temperature is low enough to allow these species to exist in their molecular forms : H_2, H_2O, OH, O_2, CO. In our network, we consider the following charged particles: electrons, H^+, H_3^+, He^+, C^+, K^+, Na^+, heavy metals M^+, molecular ions m^+ (mostly represented by HCO^+), and charged dust grains. We note α_{ij} the reaction of the ionisation of species j into species i

$$j \rightarrow i + e^-, \tag{2.7}$$

and ζ the ionisation rate of Hydrogen molecules. In our context, UV and radionucleides contributions to the ionisation rate are negligible compared to the cosmic rays that can penetrate deeply into dense cores (Kunz & Mouschovias 2009; Padovani et al. 2014). Therefore, we write $\zeta = \zeta_{\text{CR}}$. Let β_{ijk} represent the reactions between j and k to form i

$$j + k \rightarrow i + *, \tag{2.8}$$

and β_{*jk} (where $*$ denotes any other species which might be present) the reactions between j and k to form another species. Note that $\beta_{ijk} = \beta_{ikj}$. We also define γ_{jk} to represent the reactions between j and k to form another species, as β_{*jk}, but γ_{jk} specifically characterizes the destruction of j and k rather than the creation of a given species

$$j + k \rightarrow *. \tag{2.9}$$

Table 2.1: Chemical reactions and rate coefficients of the chemical network.

Reaction	α_0 (cm^3 s^{-1})	β_0	γ_0
$H^+ + O \rightarrow H + O^+$	6.86×10^{-10}	0.26	0
$H^+ + O_2 \rightarrow H + O_2^+$	2.00×10^{-9}	0.00	0
$H^+ + M \rightarrow H + M^+$	1.10×10^{-9}	0.00	0
$He^+ + H_2 \rightarrow He + H^+ + H$	3.70×10^{-14}	0.00	35
$He^+ + CO \rightarrow He + C^+ + O$	1.60×10^{-9}	0.00	0
$He^+ + O_2 \rightarrow He + O^+ + O$	1.10×10^{-9}	0.00	0
$H_3^+ + CO \rightarrow H_2 + HCO^+$	1.36×10^{-9}	-0.14	0
$H_3^+ + O \rightarrow H_2 + OH^+$	7.98×10^{-10}	-0.16	0
$H_3^+ + O_2 \rightarrow H_2 + O_2H^+$	9.30×10^{-10}	0.00	0
$H_3^+ + M \rightarrow H_2 + H + M^+$	1.10×10^{-9}	0.00	0
$C^+ + H_2 \rightarrow CH_2^+ + h\nu$	2.00×10^{-16}	0.00	0
$C^+ + O_2 \rightarrow CO^+ + O$	3.42×10^{-10}	0.00	0
$C^+ + O_2 \rightarrow CO + O^+$	4.54×10^{-10}	0.00	0
$C^+ + M \rightarrow C + M^+$	1.10×10^{-9}	0.00	0
$m^+ + M \rightarrow m + M^+$	2.90×10^{-9}	0.00	0
$H^+ + e^- \rightarrow H + h\nu$	3.50×10^{-12}	-0.75	0
$He^+ + e^- \rightarrow He + h\nu$	5.36×10^{-12}	-0.5	0
$H_3^+ + e^- \begin{array}{l} \rightarrow H + H + H \\ \rightarrow H_2 + H \end{array}$	2.34×10^{-8}	-0.52	0
$C^+ + e^- \rightarrow C + h\nu$	2.36×10^{-12}	-0.29	0
$m^+ + e^- \rightarrow m_1 + m_2$	2.40×10^{-7}	-0.69	0
$M^+ + e^- \rightarrow M + h\nu$	2.78×10^{-12}	-0.68	0
$H_2 \rightarrow H_2^+ + e^-$	0.98ζ		
$H_2 \rightarrow H^+ + H + e^-$	0.02ζ		
$He \rightarrow He^+ + e^-$	0.53ζ		
$K \rightarrow K^+ + e^-$	see below		
$Na \rightarrow Na^+ + e^-$	see below		
$H \rightarrow H^+ + e^-$	see below		

Here $\gamma_{jk} = \gamma_{kj}$. All the reactions considered are summarized in table 2.1 and their rate coefficients are given by the UMIST Database (McElroy et al. 2013).

The reaction rates are calculated from the parameters $\alpha_0,\ \beta_0,\ \gamma_0$ as

$$k = \alpha_0 * (T/300)^{\beta_0} e^{-\frac{\gamma_0}{T}}. \tag{2.10}$$

The ionisation rates for Potassium, Sodium and Hydrogen are given by Pneuman & Mitchell (1965):

$$\frac{dn_{\mathrm{K}^+}}{dt} = 6.5 \times 10^{-15} n_{\mathrm{H}_2} T^{\frac{1}{2}} \times e^{-\frac{5.1\times10^4\,\mathrm{K}}{T}} \quad \mathrm{cm}^{-3}\,\mathrm{s}^{-1}, \tag{2.11}$$

$$\frac{dn_{\mathrm{Na}^+}}{dt} = 1.4 \times 10^{-15} n_{\mathrm{H}_2} T^{\frac{1}{2}} \times e^{-\frac{6.0\times10^4\,\mathrm{K}}{T}} \quad \mathrm{cm}^{-3}\,\mathrm{s}^{-1}, \tag{2.12}$$

$$\frac{dn_{\mathrm{H}^+}}{dt} = 2.0 \times 10^{-10} n_{\mathrm{H}_2} T^{\frac{1}{2}} \times e^{-\frac{15.8\times10^4\,\mathrm{K}}{T}} \quad \mathrm{cm}^{-3}\,\mathrm{s}^{-1}. \tag{2.13}$$

We consider recombination reactions at the surface of the grains. We use the collision rates of Draine & Sutin (1987) and the interactions described in Umebayashi & Nakano (1990), Ilgner & Nelson (2006) and Kunz & Mouschovias (2009):

- Neutral grains: when hit by an electron, the electron sticks onto the grain with a probability of $P_{\mathrm{e}} = 60\%$, while an ion always sticks.
- Negatively charged grains: when hit by an ion, the ion recombines and becomes neutral.
- Positively charged grains: when hit by an electron, the grain becomes neutral.
- Charged grains: if two grains with opposite charges collide, one charge is transfered.
- Neutral grains: if hit by a charged grain, one charge is transfered to the neutral grain.

The mean collision rate $\langle\sigma v\rangle$ between a grain with a radius a and a charge q_{g} and another species with a mass m and a charge q_{s} is

$$\langle\sigma v\rangle = \pi a^2 \left(\frac{8k_{\mathrm{B}}T}{\pi m}\right)^{\frac{1}{2}} \left(1 - \frac{q_{\mathrm{s}} q_{\mathrm{g}}}{a k_{\mathrm{B}} T}\right) \left(1 + \left(\frac{2}{\frac{a k_{\mathrm{B}} T}{e^2} - \frac{q_{\mathrm{g}}}{q_{\mathrm{s}}}}\right)^{\frac{1}{2}}\right) \tag{2.14}$$

for $q_{\mathrm{s}} q_{\mathrm{g}} < 0$,

$$\begin{aligned} \langle\sigma v\rangle = \pi a^2 \left(\frac{8k_{\mathrm{B}}T}{\pi m}\right)^{\frac{1}{2}} &\left(1 + \left(\frac{4 a k_{\mathrm{B}} T}{e^2} + 3\frac{q_{\mathrm{g}}}{q_{\mathrm{s}}}\right)^{-\frac{1}{2}}\right)^2 \\ &\times \exp\left(-\frac{q_{\mathrm{g}} e^2}{(q_{\mathrm{s}} a k_{\mathrm{b}} T)\left(1 + \left(\frac{q_{\mathrm{s}}}{q_{\mathrm{g}}}\right)^{\frac{1}{2}}\right)}\right) \end{aligned} \tag{2.15}$$

for $q_{\mathrm{s}} q_{\mathrm{g}} > 0$ and

$$\langle\sigma v\rangle = \pi a^2 \left(\frac{8k_{\mathrm{B}}T}{\pi m}\right)^{\frac{1}{2}} \left(1 + \left(\frac{\pi e^2}{2 a k_{\mathrm{B}} T}\right)^{\frac{1}{2}}\right). \tag{2.16}$$

for $q_{\mathrm{g}} = 0$.

For two grains of opposite charges q and $q^{'}$ with radii a and $a^{'}$ and a reduced mass $\mu_{\mathrm{g}} = \frac{mm^{'}}{m+m^{'}}$, the collision rate is

$$\langle\sigma v\rangle = \pi(a + a^{'})^2 \left(\frac{8k_{\mathrm{B}}T}{\pi \mu_{\mathrm{g}}}\right)^{\frac{1}{2}} \left(1 - \frac{qq^{'}}{(a + a^{'}) k_{\mathrm{B}} T}\right), \tag{2.17}$$

Table 2.2: Abundances of neutrals relatively to H.

Species	Relative abundance
H_2	0.5
He	8.5×10^{-2}
C	8.4×10^{-5}
O	4.1×10^{-5}
O_2	4.8×10^{-5}
M	1.7×10^{-6}
K	2.2×10^{-10}
Na	3.1×10^{-9}

and the collision rate between a charged and a neutral grain is

$$\langle \sigma v \rangle = \pi (a + a^{'})^2 \left(\frac{8 k_{\mathrm{B}} T}{\pi \mu_{\mathrm{g}}} \right)^{\frac{1}{2}} \left(1 + \left(\frac{\pi e^2}{2(a + a') k_{\mathrm{B}} T} \right)^{\frac{1}{2}} \right) P_a. \tag{2.18}$$

$P_a = \frac{a^2}{a^2 + a'^2}$ denotes the probability of a charge transfer to the neutral grain of radius $a^{'}$.

The initial abundances of neutral species (relatively to H) are given in table 2.2.2.

2.2.3 Dust grain model

The interstellar medium is fed by the matter ejected from dying stars. It is thus not only composed of Hydrogen and Helium, but also of Carbon, Silicon and other heavy elements. This complicates the chemistry at stake in this environment, especially with some of the elements aggregating into grains. While reacting with other species, their surface act as a catalyst for other reactions to happen. Grains are then major actors of the chemical environment, but large uncertainties on their structure, abundance, size distribution and evolution still remain and approximate models need to be used. In this section, we describe the size and number density of grains, because these two quantities determine the surface area available for chemical reactions. Additionally, we need to account for their thermal evaporation, because it occurs at temperatures close to the second collapse, after the first core formation.

2.2.3.1 Grain size

The grain reaction rates and the conductivity of the dust-gas mixture depend on the grain cross section. In our calculations, we include a power-law grain size distribution by considering a finite number N_{bins} of size bins with equal width in log space. We define a minimum and maximum grain sizes a_{min} and a_{max}, respectively, with a number density of grains of radius between a and $a + da$

$$dn_{\mathrm{g,tot}}(a) = \mathcal{C}\, a^{\lambda}\, da\ , \tag{2.19}$$

where the subscript g denotes the grains and $\mathcal{C}$ is a normalization constant. Unless otherwise stated, we have used throughout this work $\lambda = -3.5$, which is the MRN size distribution (Mathis et al. 1977). However, for the sake of generality, we write here the equations for any power-law index λ. Following Kunz & Mouschovias (2009), we choose for the minimum and maximum radii $a_{\mathrm{min}} = 0.0181\,\mu$m and $a_{\mathrm{max}} = 0.9049\,\mu$m. Each size bin α is defined by a lower $a_{l,\alpha}$ and an upper radius $a_{u,\alpha}$, with $a_{u,\alpha} = a_{l,\alpha+1}$. The bin boundaries are entirely defined by the minimum radius, the maximum radius and the number of bin N_{bins}

$$a_{l,\alpha} = \frac{a_{\mathrm{min}}}{\chi^{\frac{\alpha-1}{N_{\mathrm{bins}}}}}, \quad a_{u,\alpha} = \frac{a_{\mathrm{min}}}{\chi^{\frac{\alpha}{N_{\mathrm{bins}}}}}. \tag{2.20}$$

where $\chi = \frac{a_{\mathrm{min}}}{a_{\mathrm{max}}}$.

The conservation of number density and surface yields

$$n_{\mathrm{g,tot}} = \int_{a_{\min}}^{a_{\max}} dn_{\mathrm{g,tot}}, \tag{2.21}$$

$$n_{\mathrm{g}}^{\alpha} = \int_{a_{l,\alpha}}^{a_{u,\alpha}} dn_{\mathrm{g,tot}}, \tag{2.22}$$

$$n_{\mathrm{g},\alpha} a_{\alpha}^2 = \int_{a_{l,\alpha}}^{a_{u,\alpha}} a^2 dn_{\mathrm{g,tot}}. \tag{2.23}$$

The integration yields

$$n_{\mathrm{g}}^{\alpha} = n_{\mathrm{g,tot}} \chi^{\frac{-(\lambda+1)(\alpha-1)}{N_{\mathrm{bins}}}} \left(\frac{1 - \chi^{\frac{-(\lambda+1)}{N_{\mathrm{bins}}}}}{1 - \chi^{-(\lambda+1)}} \right), \tag{2.24}$$

$$a_{\alpha} = a_{\min} \chi^{\frac{-\alpha}{N_{\mathrm{bins}}}} \left[\left(\frac{\lambda+1}{\lambda+3} \right) \left(\frac{1 - \chi^{\frac{\lambda+3}{N_{\mathrm{bins}}}}}{1 - \chi^{\frac{\lambda+1}{N_{\mathrm{bins}}}}} \right) \right]^{\frac{1}{2}}. \tag{2.25}$$

The total number density of dust $n_{\mathrm{g,tot}}$ is determined by constraining the total grain mass density in the size distribution to be

$$\rho_{\mathrm{g,tot}} = \int_{a_{\min}}^{a_{\max}} \frac{4}{3} \pi \rho_s a^3 \mathcal{C} a^{\lambda} da \ , \tag{2.26}$$

which yields

$$n_{\mathrm{g,tot}} = \left(\frac{\rho_{\mathrm{g,tot}}}{\frac{4}{3} \pi \rho_s a_{\min}^3} \right) \left(\frac{\lambda+4}{\lambda+1} \right) \left(\frac{1 - \chi^{-(\lambda+1)}}{\chi^{\lambda+4} - 1} \right) \chi^{\lambda+4}. \tag{2.27}$$

Finally, we constrain the factor $\mathcal{C}$ by choosing the total grain density $\rho_{\mathrm{g,tot}}$ to obtain the same total surface area as a fiducial uniform distribution with a grain size a_0 (see Kunz & Mouschovias 2009), which, using the fact that

$$n_{\mathrm{g,tot}} = \frac{a_{\max}^{\lambda+1} \mathcal{C}}{\lambda+1} \left(1 - \chi^{\lambda+1} \right) \ , \tag{2.28}$$

yields

$$\rho_{\mathrm{g,tot}} = \rho_{\mathrm{g,tot}}^{\mathrm{fiducial}} \left(\frac{a_{\min}}{a_0} \right) \left(\frac{\lambda+3}{\lambda+4} \right) \left(\frac{1 - \chi^{-(\lambda+4)}}{1 - \chi^{-(\lambda+3)}} \right), \tag{2.29}$$

where for a dust to gas ratio of 1%, $\rho_{\mathrm{g,tot}}^{\mathrm{fiducial}} = 0.01 \ \rho_{\mathrm{n,tot}}$ ($\rho_{\mathrm{n,tot}}$ represents the density of neutral gas). In the MRN distribution, small grains vastly outnumber the big ones, contributing dominantly to the total surface area. The total grain density is then $\rho_{\mathrm{g,tot}}^{(\mathrm{MRN})} = 0.0341 \rho_{\mathrm{n,tot}}$.

2.2.3.2 Grains at high temperature

Grain evaporation The three main constituents of grains are carbon (essentially amorphous), silicates (here represented by the molecule $(\mathrm{MgFe})\mathrm{SiO}_4$) and aluminium oxyde ($\mathrm{Al}_2\mathrm{O}_3$) (Lenzuni et al. 1995). For simplicity, we suppose that each grain is composed of only one of these three materials, instead of considering a layered structure, as suggested by various studies (e.g. Semenov et al. 2003). The precise evolution of the grain population is a complex issue, but we know grains evaporate around 1000 K, during the first core contraction, before the second collapse. Lenzuni et al. (1995) proposed two main processes of grain destruction: thermal evaporation (destruction due to the thermal agitation), and chemisputtering (reactions between dust and gas). They found that carbon evaporates between 750 K and 1100 K, silicates between 1200 K and 1300

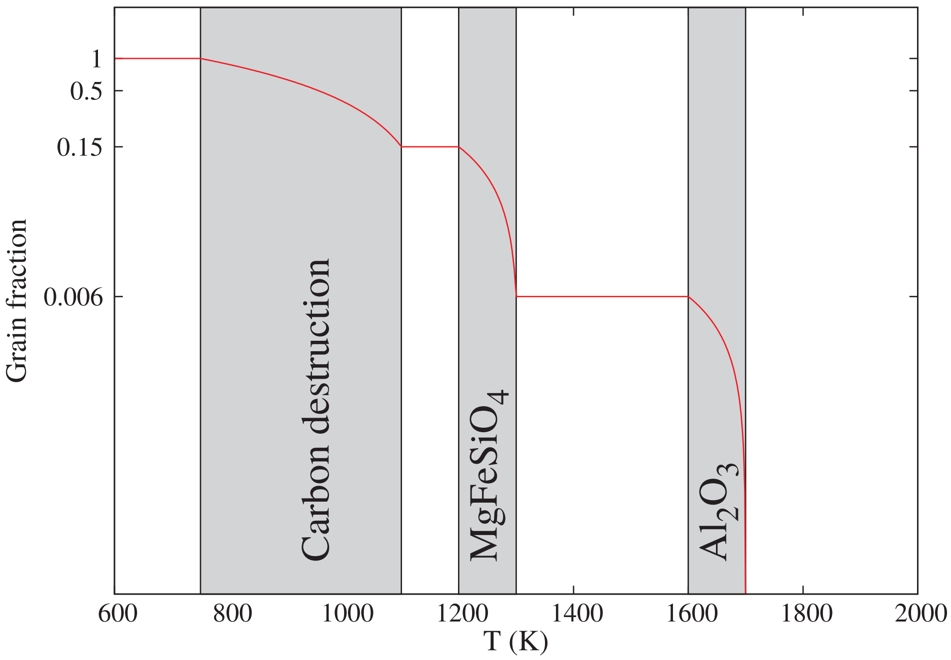

Figure 2.1: Abundance of grains (relative to their value at T $<$ 750 K) as a function of temperature. The most abundant species (C, $MgFeSiO_4$ and Al_2O_3) evaporate during the three represented main destruction stages.

K and aluminium oxydes between 1600 K and 1700 K. In this work, we suppose that for each material, the quantity of evaporated grains grows linearly with temperature until total depletion of this kind of grain. Additionally, we assume that once evaporated, the grain material disappears completely from the chemical network[1]. Given the relative fractional abundances of each material calculated from the Table 2 in Lenzuni et al. (1995): C 85%, $(MgFe)SiO_4$ 14.4%, Al_2O_3 0.6%, we consider the three steps evolution curve displayed in figure 2.1.

Thermionic emission Thermal agitation on grains induces spontaneous emission of electrons adsorbed on grain surface (Desch & Turner 2015). The Richardson's law gives the rate of emission

$$\phi = 4\pi a^2 \lambda_{\mathrm{R}} \frac{4\pi m_{\mathrm{e}}(k_{\mathrm{B}}T)^2}{h^2} \exp\left(\frac{W + \frac{Ze^2}{a}}{k_{\mathrm{B}}T}\right) \tag{2.30}$$

with $\lambda_{\mathrm{R}} = 0.5$, $W = 5\mathrm{eV}$, Z the grain charge and a its radius.

Grain charges Grains can hold several electric charges (Draine & Sutin 1987). However, multiply charged grains are weakly abundant in comparison to the single-charge or neutral grains (Sano et al. 2000). Including these grains means handling abundances ranging over 20 orders of magnitude, which is difficult to achieve accurately. Furthermore, current analytical models do not correctly describe the charge distribution when grain-grain reactions dominate (see section 2.4.6 for more details). Most of our results consider grains holding only one electric charge but we do take into account the grain-grain reactions.

2.2.4 Temperature and magnetic field

Our chemical network was used to compute conductivities for a density range spanning 10^2 cm^{-3} $<$ n $<$ 10^{26} cm^{-3}. This covers typical (parent) molecular cloud conditions (low temperature and

---

[1] In real life, dust material remains in the gas and participates to the chemistry and the optical opacity of the medium.

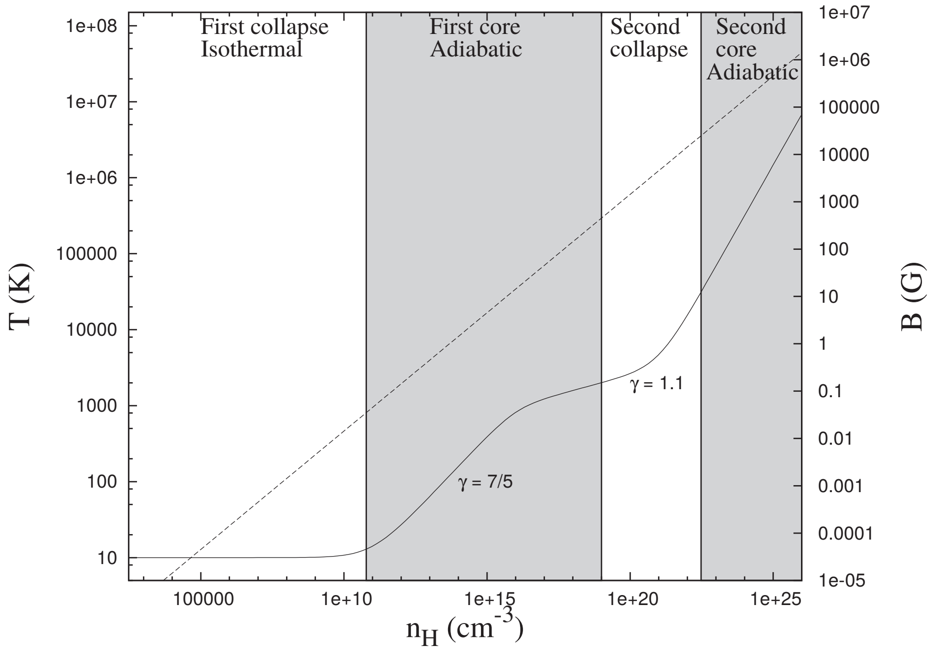

Figure 2.2: Solid line : Temperature as a function of density for the equation of state. Dashed line : Magnetic field prescription following Li et al. (2011)

density) as well as the interior of first and second Larson cores, where densities and temperatures have increased by many orders of magnitude, as a result of the strong gravitational compression of the gas. However, for clarity as well as for comparison with previous studies, the majority of the results are presented only as a function of density. To mimic the natural temperature evolution as a function of density in a collapsing dense core (as opposed to using a single constant temperature), we used the piecewise barotropic equation of state (EOS) from Machida et al. (2006)

$$T = T_0 \sqrt{1 + \left(\frac{n}{n_1}\right)^{2g_1}} \left(1 + \left(\frac{n}{n_2}\right)\right)^{g_2} \left(1 + \left(\frac{n}{n_3}\right)\right)^{g_3}, \tag{2.31}$$

with n the total number density,

$$\begin{array}{ll} n_1 = 10^{11}\ \mathrm{cm}^{-3}\ ; & g_1 = 0.4; \\ n_2 = 10^{16}\ \mathrm{cm}^{-3}\ ; & g_2 = -0.3; \\ n_3 = 10^{21}\ \mathrm{cm}^{-3}\ ; & g_3 = 0.56667, \end{array} \tag{2.32}$$

and $T_0 = 10$ K. This EOS successively characterises the isothermal phase of the collapse, the adiabatic phase during the first Larson core evolution, the second collapse and the second Larson core evolution. It s represented in figure 2.2.

Computing the resistivities also requires a knowledge of the magnetic field intensity. To present our magnetic resistivities as a function of density alone, we assumed that the magnetic intensity scales as $B(n_{\mathrm{H}}) = 1.43 \times 10^{-7} \sqrt{n_{\mathrm{H}}}$ (Li et al. 2011) (also shown in figure 2.2), which corresponds to the magnetic flux conservation (flux-freezing approximation). Although the scaling in real collapse calculations is more complex, the magnetic field here is only used to illustrate the behaviour of the resistivities and has no influence on the chemistry. In detailed protostellar collapse calculations, the temperature and the magnetic field evolutions are properly calculated and the resistivities are computed consistently during the collapse (see Masson et al. 2016; Hennebelle et al. 2016).

2.3 Implementation

2.3.1 The network

We solve the complete set of equations for each charged species (written in dimensionless form)

$$\begin{cases} \cdots \\ \frac{dx_i}{\tilde{dt}} = \sum_{j=1}^{N} \left[\alpha_{ij}x_j + \frac{n_{\mathrm{H}}}{2\zeta}\sum_{k=1}^{N}\beta_{ijk}x_jx_k - \frac{n_{\mathrm{H}}}{\zeta}\gamma_{ij}x_jx_i\right] \\ \cdots \end{cases} \tag{2.33}$$

where N is the total number of species (both neutrals and charged particles), n_{H} is the density of neutrals (here the density of Hydrogen molecules), x_i denotes the fractional abundances of various particles, $x_i = \frac{n_i}{n_{\mathrm{H}}}$, and $\tilde{dt} = dt\zeta$.

We consider that neutral abundances are constant, except K, Na and H, and we solve for the 8 above mentioned cations (H^+, H_3^+, He^+, C^+, K^+, Na^+, M^+, and m^+), plus electrons and grains.

2.3.2 Numerical method

Our resolution method is a semi-implicit scheme. It is unconditionally stable and either permits an accurate following of the temporal evolution of the solution (using a stringent constraint on the time step), or a fast calculation of the equilibrium abundances (using a larger time step). In that latter case, we lose precision on the temporal evolution of the network, but the convergence towards equilibrium is unconditional, which is our prime interest.

We write $F_i(\mathbf{x}) = \sum_{j=1}^{N}\left[\alpha_{ij}x_j + \frac{n_{\mathrm{H}}}{2\zeta}\sum_{k=1}^{N}\beta_{ijk}x_jx_k - \frac{n_{\mathrm{H}}}{\zeta}\gamma_{ij}x_jx_i\right]$, and Taylor-expand the right-hand side of equations (2.33). This yields

$$\begin{aligned} x_i^{n+1} &= x_i^n + \tilde{dt}F_i(\mathbf{x}^{n+1}), \\ &= x_i^n + \tilde{dt}\left[F_i(\mathbf{x}^n) + \sum_{j=1}^{N}\mathbb{J}_{ij}^n\delta x_j + \mathcal{O}(||\delta\mathbf{x}||)\right], \end{aligned} \tag{2.34}$$

where $\mathbb{J}$ is the jacobian matrix, and δx_i denotes the variation in abundance of the species i between the time steps n and $n+1$. In matrix form, this reads

$$\left(\mathbb{I} - \tilde{dt}\mathbb{J}^n\right)\delta\mathbf{x} = \tilde{dt}\,\mathbf{F}(\mathbf{x^n}), \tag{2.35}$$

where $\mathbb{I}$ is the identity matrix, and $\mathbf{F}(\mathbf{x}) = (F_1(\mathbf{x}), \ldots, F_n(\mathbf{x}))$.

The Jacobian general expression (for charged particles only, neutral grains are taken care of separately) reads

$$\begin{aligned} \mathbb{J}_{ij} &= \frac{\partial F_i}{\partial x_j} \\ &= \alpha_{ij} + \frac{n_{\mathrm{H}}}{2\zeta}\sum_{k=1}^{N}\beta_{ijk}x_k - \frac{n_{\mathrm{H}}}{\zeta}\gamma_{ij}x_i - \frac{n_{\mathrm{H}}}{\zeta}\delta_{ij}\sum_{k=1}^{N}\gamma_{ik}x_k. \end{aligned} \tag{2.36}$$

The Jacobian expression for neutral grains in the bin α is

$$\mathbb{J}_{g_0^\alpha j} = -\mathbb{J}_{g_+^\alpha j} - \mathbb{J}_{g_-^\alpha j}. \tag{2.37}$$

This makes the Jacobian matrix $\mathbb{J}$ singular, which is a major issue when solving the system using Newton-Raphson iterations. In this case, a simple solution consists on reducing the calculated species to charged particles only, then updating with the neutral grains at the end of the iteration.

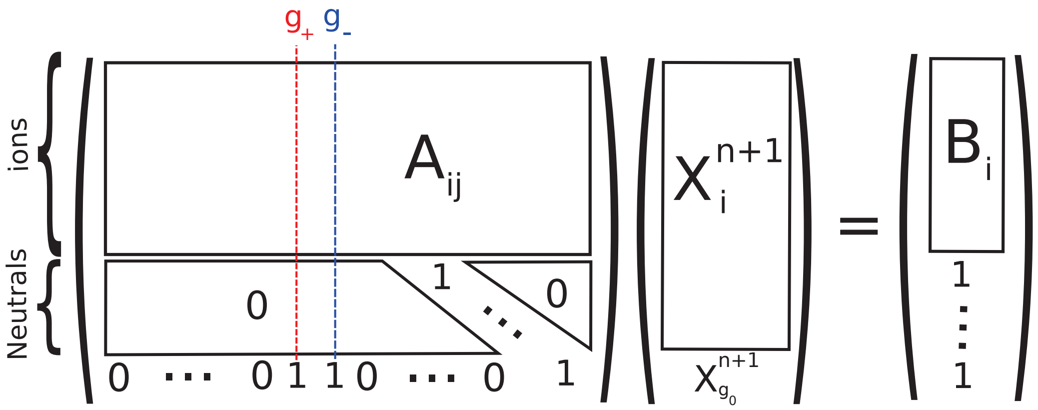

Figure 2.3: Matrix visualisation of the system to be solved after linearisation in time.

A schematic diagram of the system is shown in figure 2.3, with

$$\mathbb{A}_{ij} = \delta_{ij} - \tilde{dt}\left[\alpha_{ij} - \frac{n_{\mathrm{H}}}{\zeta}\gamma_{ij}x_i^n + \frac{n_{\mathrm{H}}}{\zeta}\sum_{k=1}^{N}(\beta_{ijk} - \gamma_{ik}\delta_{ij})x_k^n\right], \tag{2.38}$$

$$\mathbb{B}_i = \frac{n_{\mathrm{H}}}{\zeta}\left[\sum_{j=1}^{N}\gamma_{ij}x_j^n x_i^n - \frac{1}{2}\sum_{j=1}^{N}\sum_{k=1}^{N}\beta_{ijk}x_j^n x_k^n\right]\tilde{dt} + x_i^n. \tag{2.39}$$

While the system has nearly reached equilibrium, the abundances of the least abundant species may still be varying significantly, in relative values, for a long time. For this reason, we choose to stop the calculations when the time-step $\tilde{dt}$ reaches a final, roughly constant value. The least abundant species may continue to evolve, but this is inconsequential to evaluate the equilibrium abundances of the dominant species. With t the time during which the species have evolved, our stopping criteria is

$$\frac{\tilde{dt}}{t} < 10^{-5}. \tag{2.40}$$

We limit $\tilde{dt}$ by constraining the maximum allowed relative variation during one time step

$$\frac{||\Delta\mathbf{x}||}{||\mathbf{x}||} < \epsilon, \tag{2.41}$$

with the control parameter $\epsilon = 10^{-2}$. This permits equilibrium to be rapidly reached and with good precision. The matrix on the left-hand side of equation (2.35) is singular, or numerically very close to singular[2]. We use the SVD decomposition (Singular Value Decomposition) (Golub & van Loan 1983), described in Press et al. (2007), to solve system (2.35).

We impose $F_i(\mathbf{x}) = 0$ for species whose abundances are more than 20 orders of magnitude smaller than the most abundant one, because their variations have a negligible influence on the chemical evolution, and this avoids unnecessary small time steps. For $T > 1700$ K, we also set up the fractional abundance of grains to 10^{-40} rather than to 0 to avoid numerical issues.

2.3.3 Code validation

In order to test the code with the most simple parameter set, we try to reproduce the results of Umebayashi & Nakano (1990). We consider the basic case of 1 bin of grains, with a size a_0. Let δ_1 be the fraction of C and O in the gas phase, and δ_2 the fraction of metals, so that $n_{\mathrm{C}} = \delta_1 n_{\mathrm{C},0}$,

---

[2] Because of the neutral grains, although it is very close to singular even without them, due to the presence of very scarce species.

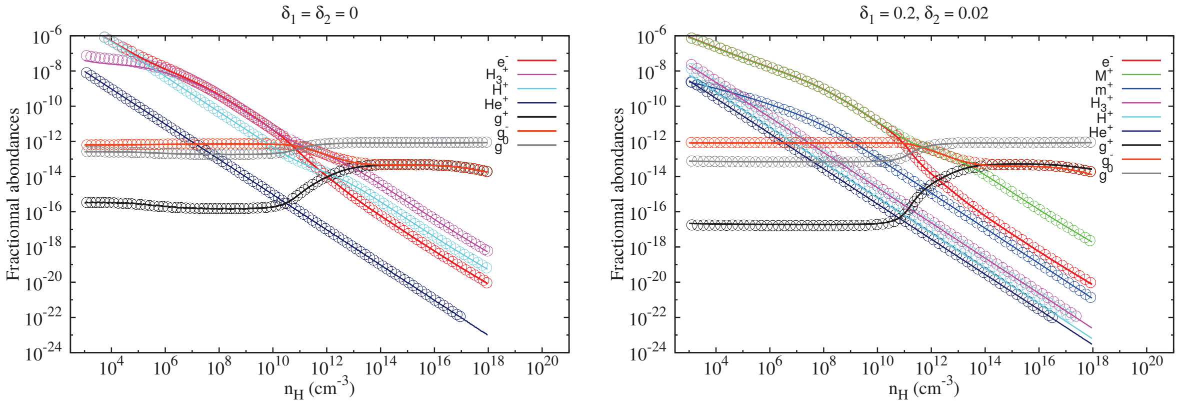

Figure 2.4: Evolution of the abundances of various charged particles as a function of the number-density of Hydrogen atoms, at $T = 10$ K. Solid lines are our results, and circles are taken from figures 2 and 4 of Umebayashi & Nakano (1990). Left: $\delta_1 = \delta_2 = 0$, right: $\delta_1 = 0.2$, $\delta_2 = 0.02$.

$n_{\mathrm{O}} = \delta_1 n_{\mathrm{O},0}$, $n_{\mathrm{O}_2} = \delta_1 n_{\mathrm{O}_2,0}$ and $n_{\mathrm{M}} = \delta_2 n_{\mathrm{M},0}$, where $n_{i,0}$ is the abundance of the neutral species i as given in table 2.2.2. We do not follow the evolution of Na and K, and we do not account for the dust evaporation, the thermionic emission and the thermal ionisation.

Our results are shown in figure 2.4, which represents the evolution of the relative abundances with the density at $T = 10$ K, compared with data from Umebayashi & Nakano (1990) for two different cases ($\delta_1 = \delta_2 = 0$ for the left plot and $\delta_1 = 0.2$ and $\delta_2 = 0.02$ for the right plot). The two are in very good agreement. For $n_{\mathrm{H}} < 10^{10}$ cm^{-3}, most of the grains have a negative charge and electrons and ions are the dominant species. For $n_{\mathrm{H}} > 10^{13}$ cm^{-3}, charged grains are more abundant than electrons and ions.

2.4 Results

2.4.1 Fiducial case

Our fiducial case includes 10 bins of grain sizes and a standard cosmic-ray ionisation rate of 10^{-17} s^{-1} (as in Umebayashi & Nakano 1990). All the physical effects described above are taken into account with the help of the barotropic EOS (2.32). The evolution of the various abundances of charged species as a function of density along the global collapse of a prestellar core is presented in figure 2.5.

Electrons and metallic ions are the dominant charged species at low densities. For $n_{\mathrm{H}} > 10^8$ cm^{-3}, grains take over while the abundances of all other species decrease by several orders of magnitude. At 10^{16} cm^{-3}, the thermionic emission of grains becomes non-negligible and a lot of electrons are released in the fluid. Meanwhile, grain evaporation begins through the three stages of destruction that are clearly visible up to $n_{\mathrm{H}} = 10^{18}$ cm^{-3}. This affects the abundances of other species, especially M^+, K^+, Na^+ and e^-. Immediately after the complete destruction of the grains, the thermal ionisations of K, Na and H become relevant, and their ionised counterparts become the dominant species along with M^+ and e^-. Eventually, all neutral K, Na and M atoms disappear, leaving H^+ as the most abundant ionised species. Grain evaporation takes place at the end of the first core phase, and the thermal ionisations essentially happen during the second collapse.

The corresponding conductivities and resistivities are plotted in figure 2.6 and 2.7. Ohmic and ambipolar conductivities are positive, but Hall conductivities and resistivities have negative values at low densities (light blue curves), before becoming positive (dark blue curves). For $n_{\mathrm{H}} < 10^{15}$ cm^{-3}, these figures are qualitatively comparable to Figure 7 of Kunz & Mouschovias (2010). There is a peak in resistivities at $n_{\mathrm{H}} \approx 10^{18}$ cm^{-3}, due to grain evaporation, where all three resistivities have similar values (but are still dominated by Ohmic diffusion). The peak

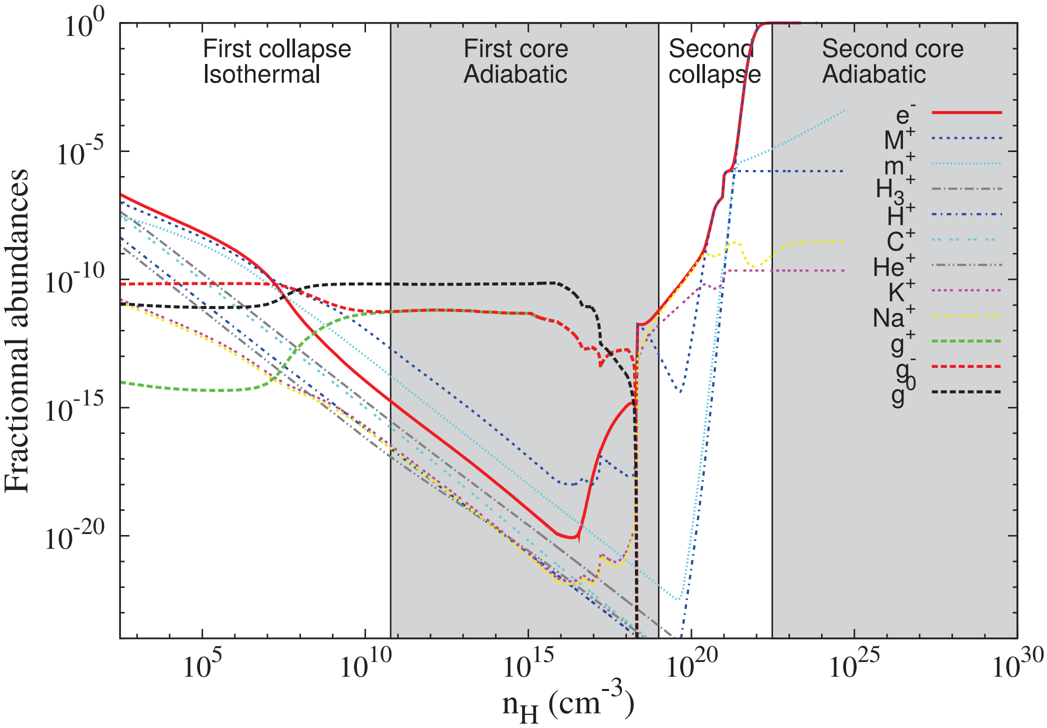

Figure 2.5: Evolution of the fractional abundances for the charged species with density for our fiducial case: 10 bins of grains, barotropic equation of state and a cosmic-ray ionisation rate $\zeta_{\rm CR} = 10^{-17}$ s^{-1}.

does not extend over a large range of densities, as the number density of charged species increases again as soon as thermal ionisations begin, drastically decreasing the resistivities. After the peak, the resistivity is dominated by the Ohmic and Hall contributions, which remain comparable, until Ohmic resistivity eventually prevails. Figure 2.7 also clearly highlights the differences, in the evolution of the various resistivities, between the present calculations and the results of previous studies. For the ambipolar resistivity, Duffin & Pudritz (2008) used the simple analytical expression $\eta_{\rm AD} \propto \frac{B^2}{n_{\rm H}\sqrt{n_{\rm H}}}$, so their resistivity scales as $\frac{1}{\sqrt{n_{\rm H}}}$ (since we consider $B \propto \sqrt{n_{\rm H}}$). Our ambipolar resistivity is close to theirs at low densities, but the two values diverge around $n_{\rm H} = 10^{10}$ cm^{-3}. This is due to their assumption that ions are perfectly coupled to the magnetic field, and that the ion-neutral collision time is much smaller than the other characteristic physical times of the system. They acknowledge that their model fails for dense regions, with $n_{\rm H} > 10^{10}$ cm^{-3}. The model of Ohmic resistivity from Machida et al. (2007) also matches ours for $n_{\rm H} \leq 10^{15}$ cm^{-3}. The chemical network they consider (Nakano et al. 2002), however, does not include as many physical processes, such as grain evaporation. At low density ($n_{\rm H} \leq 10^{[15-16]}$ cm^{-3} for the Ohmic resistivity and $n_{\rm H} \leq 10^{10}$ cm^{-3} for ambipolar resistivity), these two commonly used models are then in agreement with our results, but the additional physics included in our work significantly improves the situation for the conditions inside the first and second cores.

2.4.2 Magnetic field variations

The magnetic field only influences the resistivities and the conductivities but has no impact on the chemistry. Figure 2.8 shows the resistivities for the fiducial case and for magnetic fields three times lower and higher. Hall and ambipolar resistivities are slightly shifted, while the Ohmic resistivity is not impacted. The greatest shift is in the first collapse density range, but it is not the most critical. The density at which Hall resistivity changes its sign, during the first

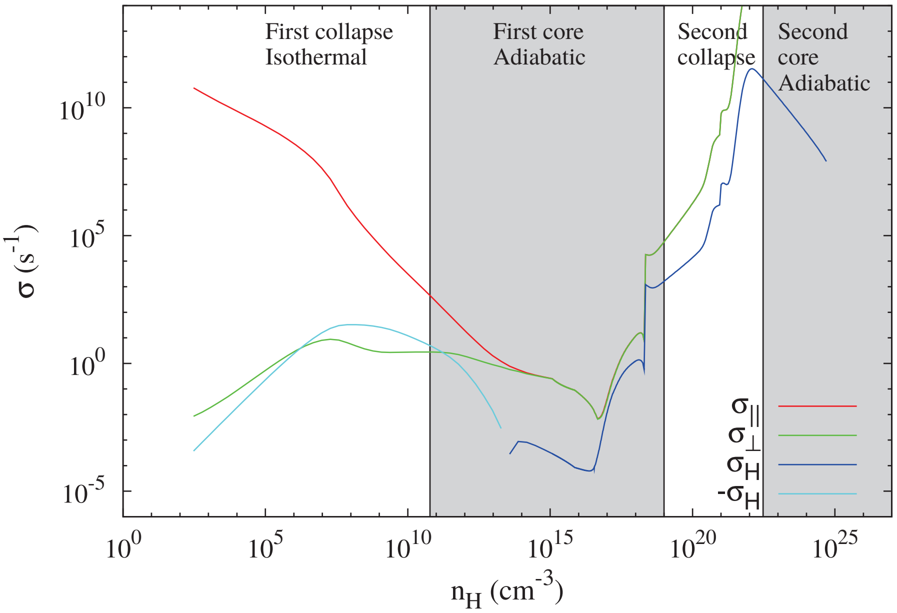

Figure 2.6: Conductivities as a function of density for the fiducial case. Light blue: negative Hall conductivity, Dark blue : positive Hall conductivity, Red: parallel conductivity, Green: perpendicular conductivity.

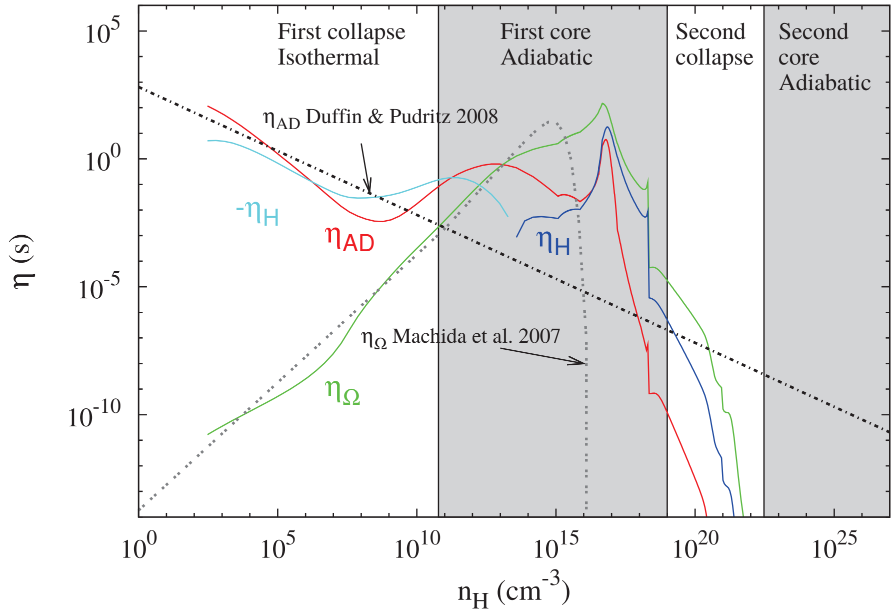

Figure 2.7: Resistivities as a function of density for the fiducial case. Light blue: negative Hall resistivity, Dark blue: positive Hall resistivity, Red: ambipolar diffusion resistivity, Green: Ohm resistivity.

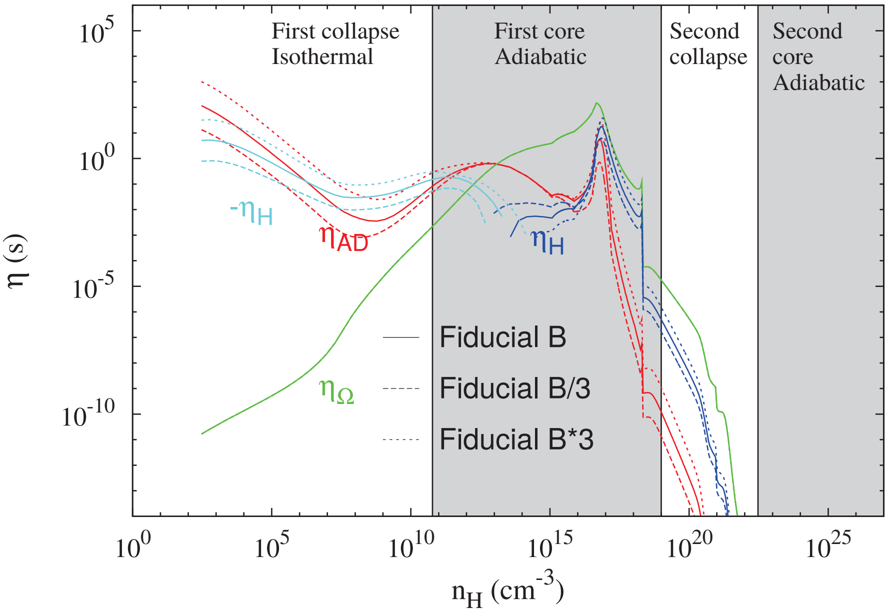

Figure 2.8: Resistivities as a function of density for the fiducial case, and a magnetic field 3 times higher and lower. Same color coding as figure 2.7.

core contraction, is also shifted, and the ratio between the three resistivities is highly impacted, especially in the $10^{16} - 10^{18}$ cm^{-3} density range. Since we compute the resistivities on the fly, using the magnetic field of the simulation, it could be interesting to study this ratio in that context.

2.4.3 Impact of grain evaporation

Figure 2.9 presents the same calculations as for the fiducial case, but *without* grain evaporation. There are substantial changes for $n_{\rm H} > 10^{16}$ cm^{-3}, at the onset of grain destruction. Both electrons and metallic ions abundances increase due to the thermionic emission of the grains and the thermal ionisations. They are the dominant species along with negatively charged grains, more prone to form because of the large number of free electrons released by K, Na and H atoms. Consequently, both the abundances of neutral and positive grains drop, while the abundances of other species remain very small. Figure 2.10 shows the effect of removing grain evaporation on the resistivities. At high densities ($> 10^{20}$ cm^{-3}) the resistivities still decrease, as the number of ionised particles increases in the medium. The most notable differences lie in the density range typical of the first Larson core and the second collapse, $10^{15} < n_{\rm H} < 10^{22}$cm^{-3}, where the Hall and the Ohmic resistivities show large differences with the fiducial case. Hall resistivity is lower then higher, while the Ohmic resistivity is tremendously higher in this range of density. At $n_{\rm H} \approx 10^{22}$ cm^{-3}, the excessive abundance of electrons in the medium nullify the difference between the two cases. An accurate description of grains evaporation is thus mandatory to study the possible transformation of the first core into a disk around the second Larson core (as described in Machida et al. 2006).

2.4.4 Cosmic ray ionisation rates

Cosmic-rays (CR) are charged particles traveling through space at relativistic velocities. They compose a third of the ISM energy density and are the main source of ionisation in molecular clouds (Padovani & Galli 2013), thus being of prime importance in astrophysical processes. Nonetheless, their origin is still matter to debate. They interact with both matter and magnetic

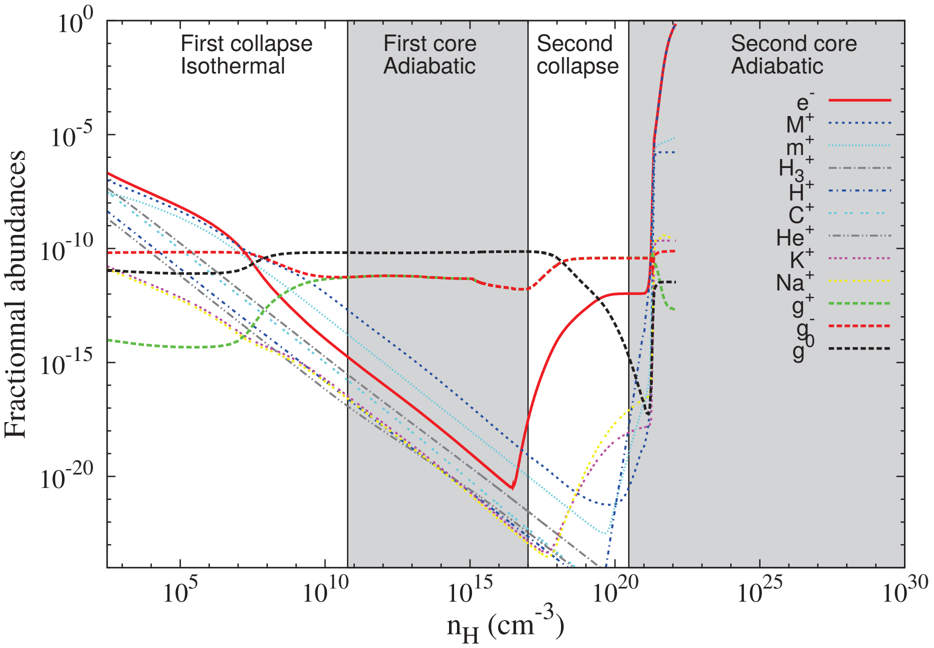

Figure 2.9: Fractional abundances, using 10 bins, without grain evaporation.

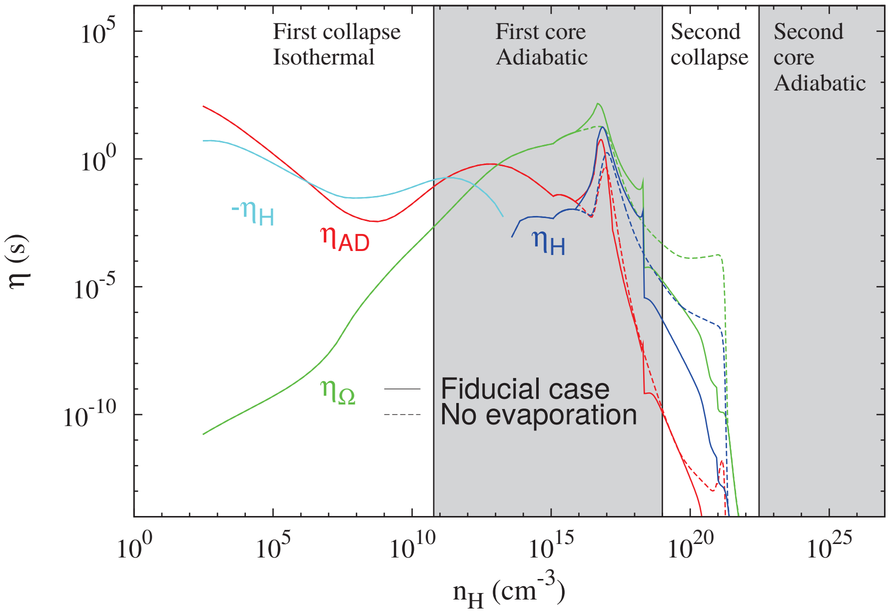

Figure 2.10: Comparison of the resistivities with and without grain evaporation. Same color coding as in figure 2.7. Dashed lines represent the absence of evaporation, whereas solid lines stand for the fiducial case.

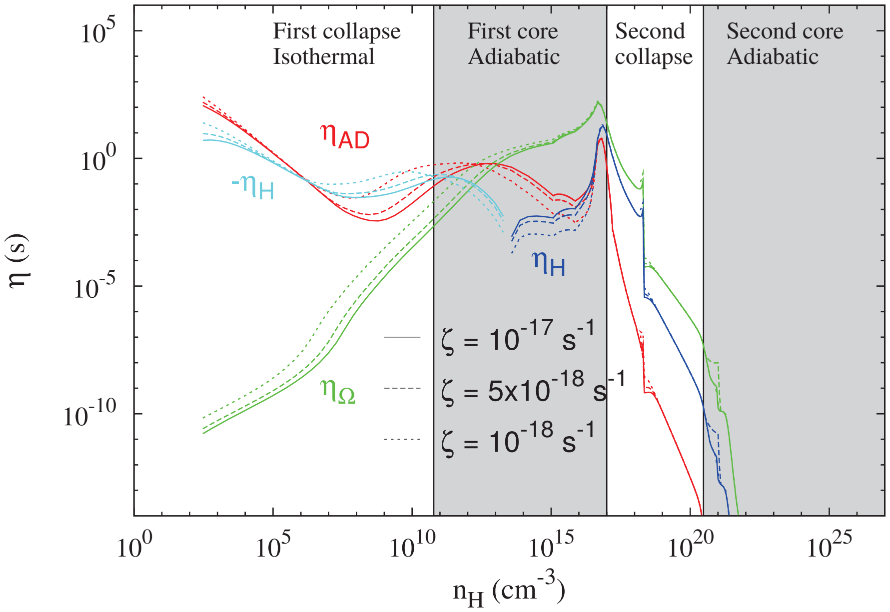

Figure 2.11: Resistivities for different cosmic ray ionisation rates, with the barotropic EOS. Solid lines: fiducial value $\zeta_{\mathrm{CR_{ref}}} = 1 \times 10^{-17}\mathrm{s}^{-1}$. Long dashed lines: $\zeta_{\mathrm{CR}} = \frac{\zeta_{\mathrm{CR_{ref}}}}{2} = 5 \times 10^{-18}\mathrm{s}^{-1}$. Short dashed lines: $\zeta_{\mathrm{CR}} = \frac{\zeta_{\mathrm{CR_{ref}}}}{10} = 1 \times 10^{-18}\mathrm{s}^{-1}$. Same color coding as figure 2.7

fields. CR propagation along field lines is affected by two competing effects: magnetic focusing, which increases the ionisation rate, and magnetic mirroring, which prevents CRs to reach deep parts of the cloud. Padovani et al. (2014) found that mirroring always dominates over focusing for a field topology obtained by ideal-MHD simulations of collapsing rotating clouds, and that the ionisation rate could vary by up to a factor 50, depending on the mass-to-flux ratio and the magnetic flux tube considered. In addition, CR are partly absorbed by the dense medium, lowering the CR ionisation rate (Padovani & Galli 2011).

To quantify the impact of such uncertainties on the CR ionisation rate in a protostellar environment with a complex magnetic field topology (twisted field lines, misalignement, turbulence...), we have computed abundances and resistivities for two CR values beside our standard case, namely $\zeta_{\mathrm{CR}} = 5 \times 10^{-18}\,\mathrm{s}^{-1}$ and $\zeta_{\mathrm{CR}} = 1 \times 10^{-18}\,\mathrm{s}^{-1}$. The resulting resistivities are shown in figure 2.11 (we do not show the abundances, as they are similar to the fiducial case). The Hall and ambipolar diffusion contributions are alternatively increased and decreased. In comparison, for $\zeta_{\mathrm{CR}} = 1 \times 10^{-17}\,\mathrm{s}^{-1}$ the Ohmic dissipation is one order of magnitude smaller, before the resistivities decrease at $n_{\mathrm{H}} \approx 10^{17}$ cm^{-3}. Minor deviations are to be seen in the second collapse density range, but the overwhelming contribution of electrons and Hydrogen compensates most of the variations. See appendix 2.B for more discussion about the ionisation rate in collapsing cores.

2.4.5 Grain size distribution

Because most of the grain surface is due to the smallest grains, a large enough number of grain bins is necessary for a proper evaluation of the final conductivity. As Kunz & Mouschovias (2009), we find that 5 size-bins seem to be sufficient to reach a relative precision of the order of 1% for every considered species. In this part, our reference case includes 10 size-bins. Figure 2.12 shows the error on the abundances, calculated as $\frac{||\mathbf{x}_\alpha - \mathbf{x}_{\mathrm{ref}}||}{||\mathbf{x}_{\mathrm{ref}}||}$, where $||\ ||$ is the L_2 norm of the abundances vector $\mathbf{x}$, $\mathbf{x}_\alpha$ corresponds to the number of bins α considered, and $\mathbf{x}_{\mathrm{ref}}$ stands for the 10 bins case. To calculate the error on grains for the different values of α, we compared

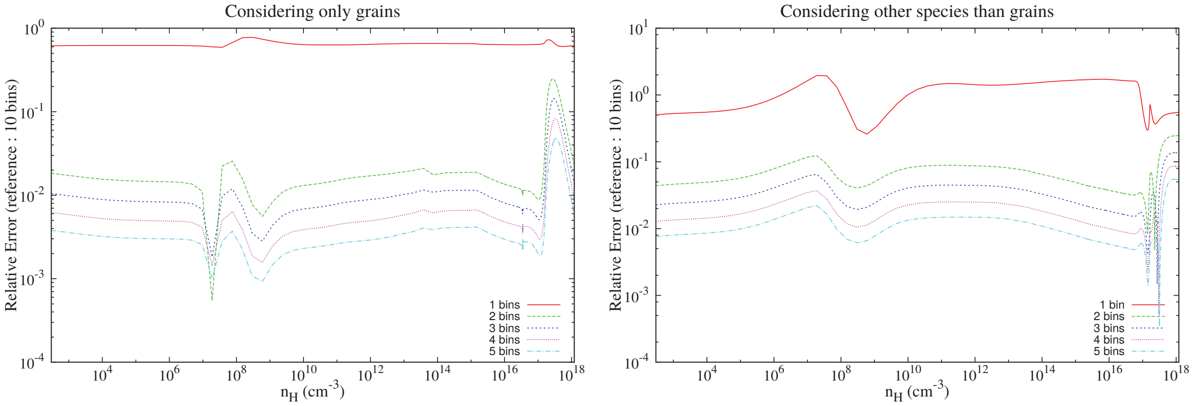

Figure 2.12: Relative error in the species abundances ($= \frac{||\mathbf{x}_\alpha - \mathbf{x}_{\mathbf{ref}}||}{||\mathbf{x}_{\mathbf{ref}}||}$) for different numbers of size-bins (relatively to the 10 bins results), for the grains only (top panel), or for other species (bottom panel) in the density range before grain evaporation.

the total abundance of positive, negative and neutral grains. The relative error on the least abundant gas molecules becomes fairly high when grains start to evaporate at 10^{18} cm^{-3}, but this is inconsequential since these species hardly contribute to the resistivity at this stage. We see that 5 bins abundances yield a small error in comparison to the 10 bin case, which shows that our fiducial calculations have a good precision. The resistivities for different numbers of bins (1, 5 and 10) are plotted in figure 2.13. When considering only one bin, resistivities are shifted up and down by about one order of magnitude, and strongly overestimated in the $10^{12} - 10^{17}$ cm^{-3} density range. However, the 5 bins and 10 bins cases are extremely close to each other. A large enough number of bins is thus necessary to properly describe this highly dynamic phase of the prestellar core evolution.

Even though the MRN grain size distribution is reasonable when considering interstellar dust, it becomes of questionable validity for denser media like molecular clouds or Larson cores, for which the knowledge of a precise grain size distribution is still lacking. We have examined the impact of this uncertainty by conducting calculations with another distribution: $\lambda = -2.8$ (instead of $\lambda = -3.5$ for the MRN distribution), as suggested by Compiègne et al. (2011) for amorphous carbon grains between ~ 5 and a few hundreds nanometers radius. The result for the resistivities is shown in figure 2.14. Despite the similarity of the resistivities' behaviour between 10^5 cm^{-3} and 10^{17} cm^{-3}, there is a slight difference concerning the partitioning for the dominant effect. For example, around $n_{\rm H} = 10^{14}$ cm^{-3}, Ohmic diffusion takes the lead upon the ambipolar diffusion for a density ten times higher than compared to the MRN distribution. This is a typical density range in protostellar discs, whose evolution may be impacted by various size distributions, with effects difficult to control (grain coalescence, premature destruction...). Several authors proposed their own size distribution. Compiègne et al. (2011) also suppose a lognormal distribution for the smallest grains (PAH and small amorphous carbon), and a power law with an exponential cut-off for larger amorphous carbon grains and amorphous silicate grains, to reproduce observed emission and extinction spectra (see their Fig. 2).

2.4.6 Influence of grains charges

Multiply charged grains are part of the chemical network (Nishi et al. 1991). Figure 2.15 shows the abundances of species in a simplified case (only one bin of size, without Na, the thermionic emission and thermal ionisation of H) but with grains holding two electric charges. Although they are generally less abundant than single-charge grains, they impact the charge distribution, especially for $n_{\rm H} > 10^{12}$ cm^{-3}. The main effect is that single-charge grains, the main charge carriers, seem to form more neutral grains and are less numerous than in the fiducial case (see the right panel of the figure). This of course impacts the resistivities, as shown in figure 2.16.

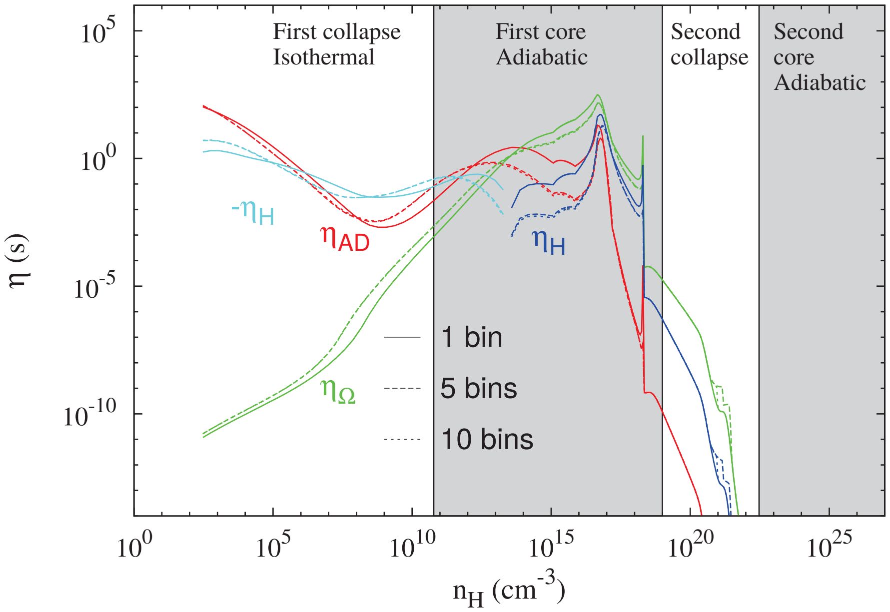

Figure 2.13: Resistivities for different numbers of size-bins. Solid line: 1 bin, dashed line: 5 bins, short-dashed line: 1 bins. Same color coding as figure 2.7.

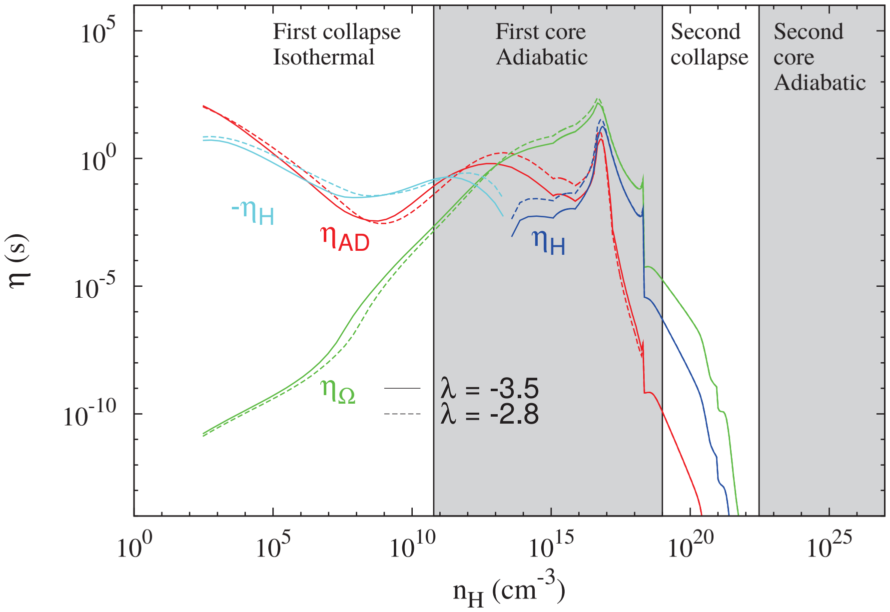

Figure 2.14: Ambipolar diffusion resistivity for the MRN ($\lambda = -3.5$, solid line) and another size distribution ($\lambda = -2.8$, dashed line), with our same barotropic EOS.

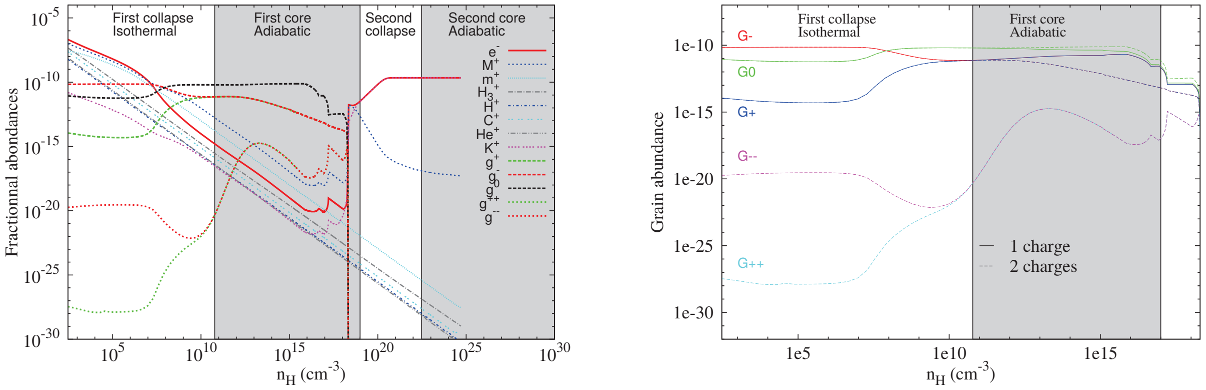

Figure 2.15: Left panel: abundances of the chemical species with double-charge grains, without Na, thermal ionisation of H and thermionic emission. Right panel: abundances of the grains with and without double-charged grains presence.

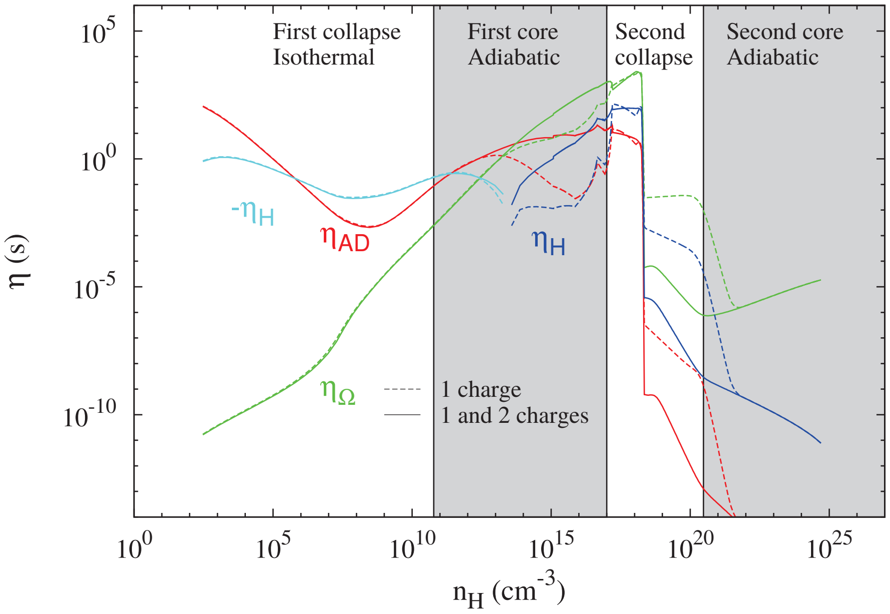

Figure 2.16: Resistivities comparison for the simplified case. Dashed line: network with only 1-charge grains, solid line: network with 1 and 2-charges grains.

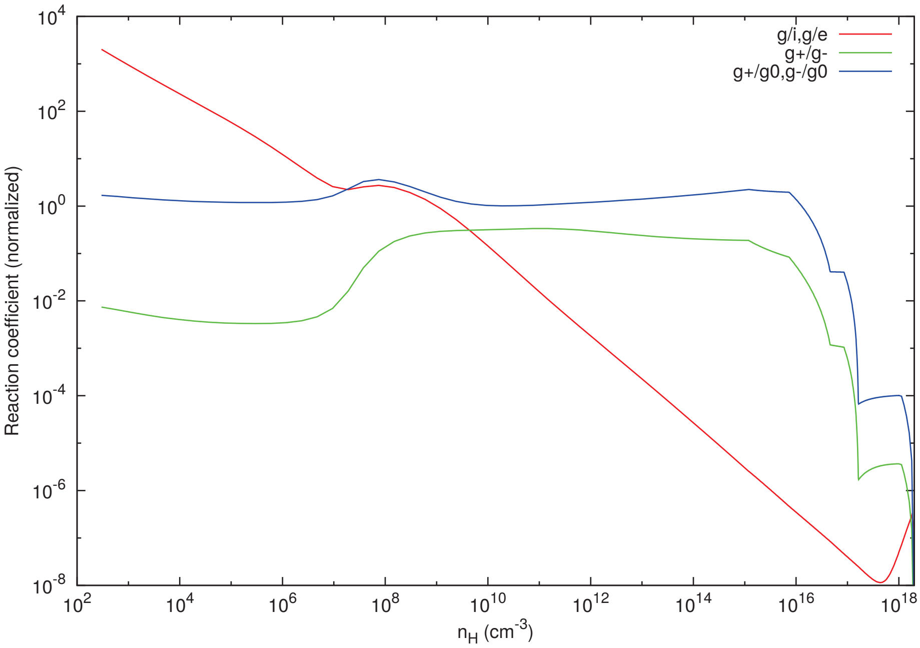

Figure 2.17: Maximum reaction rates for grain/ion and grain/electron reactions (red curve), positively charged grain/negatively charged grain reactions (green curve) and neutral grain/charged grain reactions (blue curve).

We could produce such a result only for one bin of size with the current method of resolution. The abundance gap between the 2-charge holding grains and the rest of the species spans over 20 orders of magnitude (especially at low densities in this case). This gap widens for several number of bins, as small grains tend to hold a smaller number of charges, and large grains are less abundant. Dealing with so many orders of magnitude is problematic as numerical round-off errors may artificially change the contribution of the less abundant species. Several authors use analytical expressions of charge distribution to avoid this numerical difficulty (Draine & Sutin 1987; Okuzumi 2009; Fujii et al. 2011). These models, however, do not take into account the charge transfer between grains. Figure 2.17 shows the maximum reaction rates of grain-ion, grain-electron and grain-grain reactions. Reaction rates between grains are largely dominant for $n_{\mathrm{H}} > 10^{12}\mathrm{cm}^{-3}$, and not taking them into account leads to large discrepancies concerning the grains abundances in this density range (see figure 2.18), with, in turn, an impact on the resistivities (see figure 2.19).

On the other hand, using the analytical expressions of Draine & Sutin (1987) with the ion and electron abundances calculated in our simplified case, with only 1 charge and without considering grain-grain reactions, enables us to predict the grain abundances for one and two charges with good precision. Figure 2.20 depicts such predicted abundances of grains, compared to those computed with our code, for 1 and 2 charges. The predicted abundances of the 2-charge grains are slightly overestimated for $10^{14} < n_{\mathrm{H}} < 10^{17}\mathrm{cm}^{-3}$, but the agreement is very good otherwise. Figure 2.21 shows the relative error $\frac{||\mathbf{x}_{\mathrm{predict}} - \mathbf{x}_{\mathrm{num}}||}{||\mathbf{x}_{\mathrm{num}}||}$ of the model prediction upon the numerical run with two charges allowed. All abundances agree within roughly 10%, except for g^{++} at low densities and g^{-} and g^{++} for $n_{\mathrm{H}} > 10^{12}\mathrm{cm}^{-3}$. Figure 2.22 shows the corresponding resistivities. Both models are relatively close except in the density range mentioned above. For $10^{14} < n_{\mathrm{H}} < 10^{17}\mathrm{cm}^{-3}$, resistivities of the prediction are slightly underestimated, but the differences with the numerical results remain similar. At low densities, the errors on the abundances result in a sign change of the Hall resistivity, as even a small change allows the positive contribution of η_{H} to overcome the negative contribution. However, the Hall effect is not expected to play a role at these early stages of protostellar collapse. Therefore, even though we could not verify

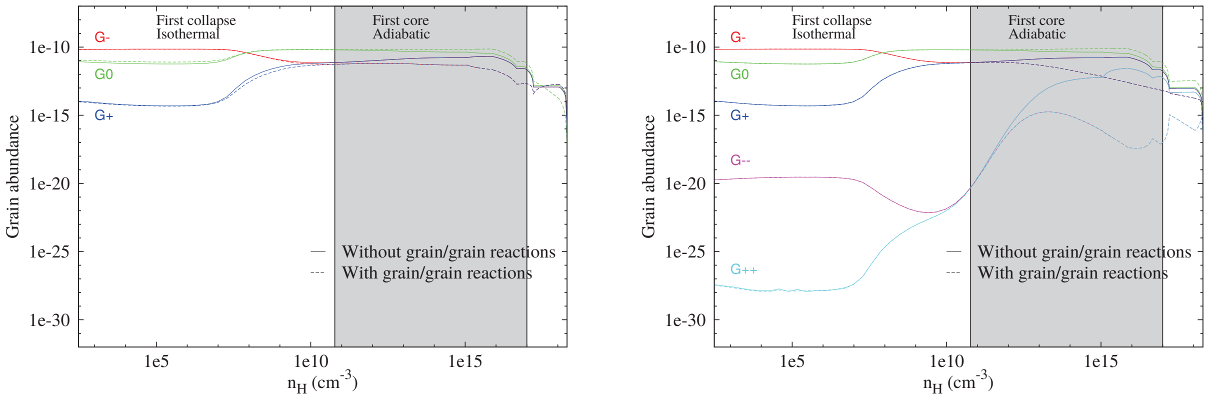

Figure 2.18: Comparison of the grains abundances with (dashed lines) and without (solid lines) charge transfer between grains, for 1-charged grains (left figure) and 1 and 2-charged grains (right figure).

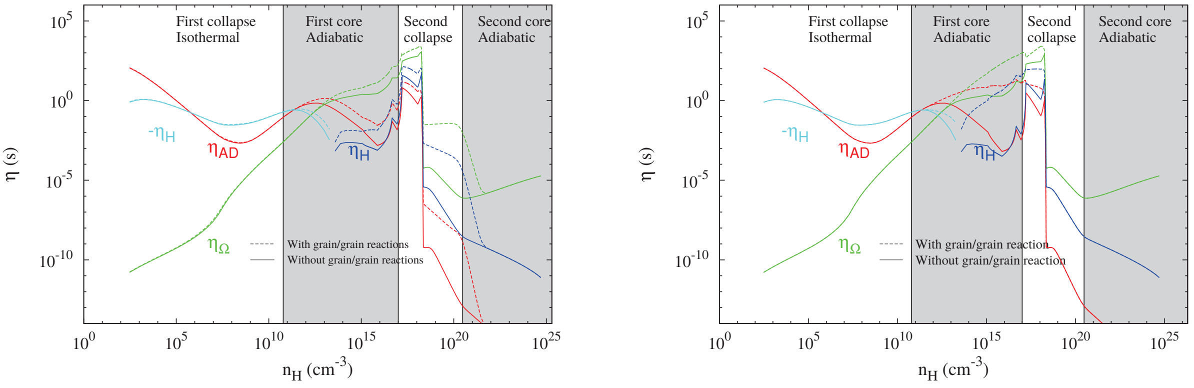

Figure 2.19: Comparison of the resistivities with (dashed lines) and without (solid lines) charge transfer between grains, for 1-charged grains (left figure) and 1 and 2-charged grains (right figure).

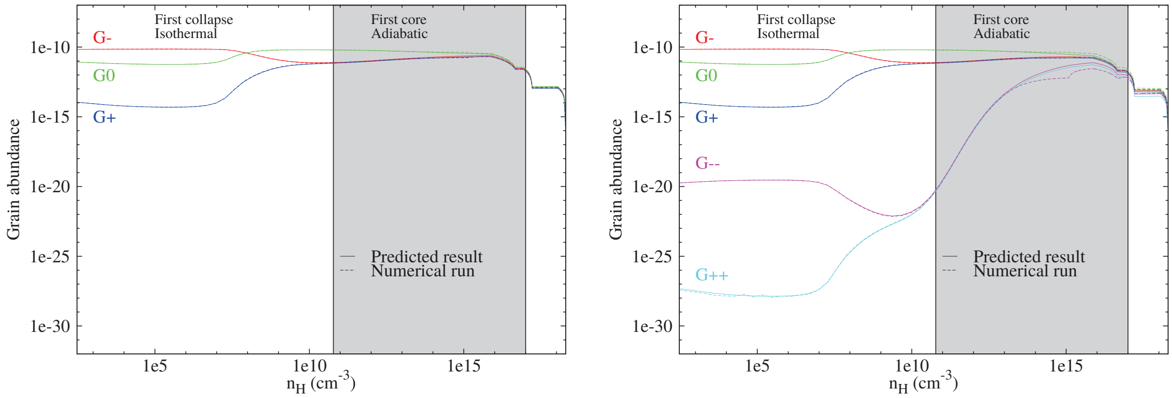

Figure 2.20: Comparison of the abundances of grains computed with our code (dashed lines) and predicted from the ion and electron abundances (solid lines), for 1-charged grains (left figure) and 1 and 2-charged grains with 1 bin (right figure).

the exactitude of the prediction for grains holding a larger number of charges (due to numerical difficulties), it seems reasonable to say that our method gives satisfying results at least in the case of a small number of charges, which is the relevant case, as grains holding more than 3 charges are not expected to be abundant enough to significantly modify the resistivities (Sano et al. 2000).

2.4.7 Non-equilibrium chemistry

In this study, all the species abundances were calculated at chemical equilibrium. In real situations, the chemical reaction time-scale could be greater than the dynamical (collapse) one. In that case, the environment conditions (density, temperature...) can change significantly before a chemical equilibrium is reached. We have explored this issue by comparing the time-scale required for our chemical network to reach equilibrium with the typical free-fall time for a self-gravitating spherical cloud, $t_{\rm ff} = \sqrt{\frac{3\pi}{32G\bar{\rho}}}$ (with $\bar{\rho}$ the mean density of the cloud). The results are portrayed in figure 2.23. Clearly, the free-fall time is far larger than the chemical equilibrium time for all densities. Furthermore, the above free-fall time estimate is likely to be underestimated since real clouds are additionally supported by thermal, turbulent and magnetic pressures. Therefore, assuming chemical equilibrium seems to be valid in the context of collapsing prestellar cores, with the limitation that we do not consider the history of the chemical species during the collapse. Indeed, particles may be transported from one specific environment to another one (e.g. from the core region to the outflow then to the disk). The only way to properly account for this complicated pattern is to calculate non-equilibrium chemical reactions on the fly during the dynamical collapse. Additionally, the flow of the fluid should also be taken into account as it changes the dynamics and statistics of the collisions. This task, for now, remains computationally prohibitive.

2.4.8 Inelastic collisions

Up to this point, we did not consider the influence of inelastic collisions on the magnetic resistivities. In formulae (2.4), (2.5) and (2.6), the inelastic contributions have been neglected. A more realistic description reads[3]

---

[3] see Kunz & Mouschovias (2009) for more details on the calculations.

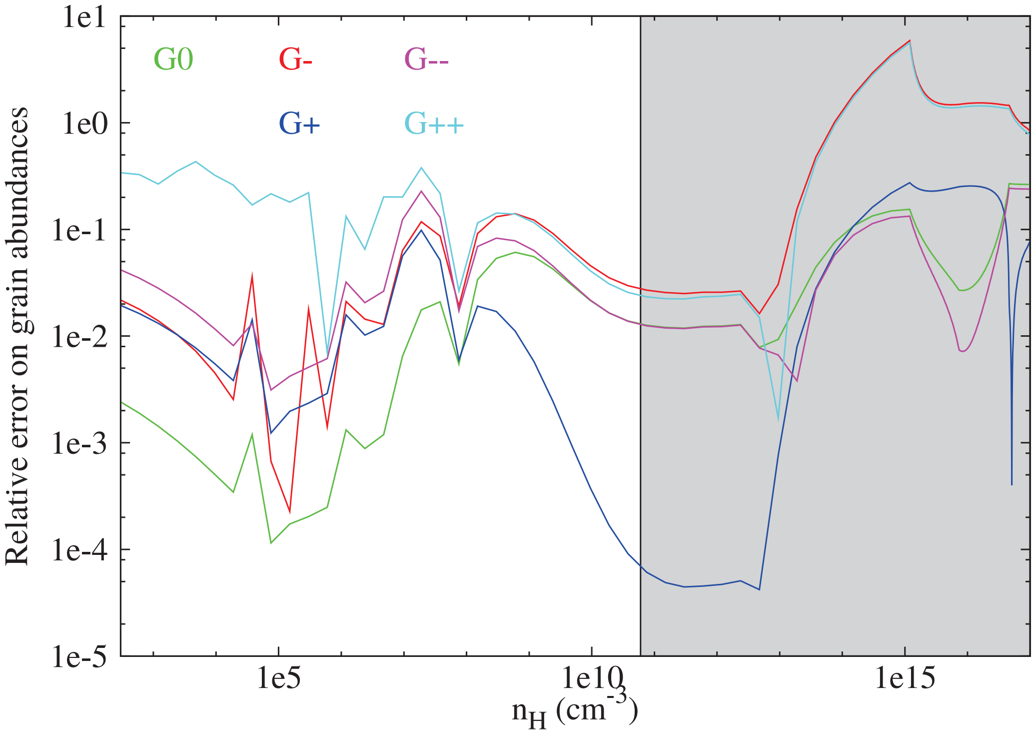

Figure 2.21: Relative error $\frac{||\mathbf{x}_{\text{predict}} - \mathbf{x}_{\text{num}}||}{||\mathbf{x}_{\text{num}}||}$ between the numerical abundances of grains and the predicted results of figure 2.20 for 1 and 2-charged grains.

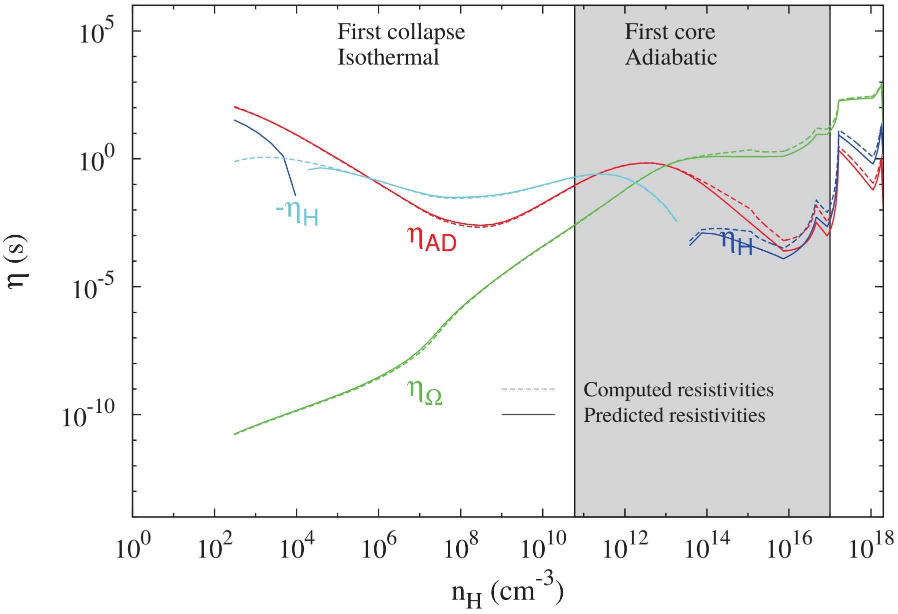

Figure 2.22: Comparison of the resistivities using abundances computed with our code (dashed lines) and abundances predicted with Draine & Sutin (1987) formulae (solid lines), for 1 and 2-charged grains, without charge transfer between grains.

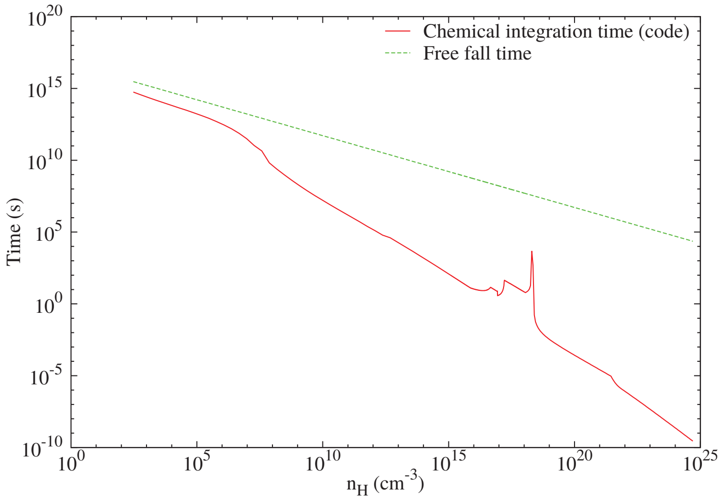

Figure 2.23: Characteristic time for reaching chemical equilibrium (solid red line) and free-fall time (dashed green line) as a function of density.

$$\sigma_{\parallel} = \sum_i \sigma_i (1 - \zeta_i), \tag{2.42}$$

$$\sigma_{\perp} = \sum_i \frac{\sigma_i (1 - \zeta_i)}{1 + (\omega_i \tau_{\text{in}})^2 (1 - \varphi_i)} \Upsilon_i(\zeta), \tag{2.43}$$

$$\sigma_{\text{H}} = -\sum_i \frac{\sigma_i \omega_i \tau_{\text{in}} (1 - \varpi_i)}{1 + (\omega_i \tau_{\text{in}(1-\varphi_i)})^2} \Upsilon(\varpi). \tag{2.44}$$

The calculation of the inelastic terms ζ_i, φ_i, ϖ_i and Υ uses the inelastic collision time $\tau_{i,\text{inel}}$ involving species i. It represents the typical timescale for this species to be created or destroyed by an inelastic collision (in this case, by a charge transfer). As mentioned in Kunz & Mouschovias (2009) (from which we take our notations), the elastic collisions of ions and electrons with the neutral fluid occur at a much higher rate than the inelastic collisions (i.e. $(\tau_{i,\text{inel}}/\tau_{\text{in}}) >> 1$), meaning that we only need to take in account the grains contribution. For positively and negatively charged grains of bin α, the inelastic collision time is given by

$$\frac{1}{\tau_{\text{g}^\alpha_+,\text{inel}}} = \frac{1}{\tau_{\text{g}^\alpha_+/\text{ions},\text{inel}}} + \frac{\rho_{\text{g}^\alpha_+}}{\rho_{\text{g}^\alpha_0}} \frac{1}{\tau_{\text{g}^\alpha_+/\text{e},\text{inel}}} + \sum_{\alpha'} \left[\frac{1}{\tau_{\text{g}^\alpha_0/\text{g}^{\alpha'}_+,\text{inel}}} + \frac{\rho_{\text{g}^\alpha_+}}{\rho_{\text{g}^\alpha_0}} \left(\frac{1}{\tau_{\text{g}^\alpha_+/\text{g}^{\alpha'}_0,\text{inel}}} + \frac{1}{\tau_{\text{g}^\alpha_+/\text{g}^{\alpha'}_-,\text{inel}}} \right) \right], \tag{2.45}$$

$$\frac{1}{\tau_{\text{g}^\alpha_-,\text{inel}}} = \frac{1}{\tau_{\text{g}^\alpha_0/\text{e},\text{inel}}} + \frac{\rho_{\text{g}^\alpha_-}}{\rho_{\text{g}^\alpha_0}} \frac{1}{\tau_{\text{g}^\alpha_-/\text{ions},\text{inel}}} + \sum_{\alpha'} \left[\frac{1}{\tau_{\text{g}^\alpha_0/\text{g}^{\alpha'}_-,\text{inel}}} + \frac{\rho_{\text{g}^\alpha_-}}{\rho_{\text{g}^\alpha_0}} \left(\frac{1}{\tau_{\text{g}^\alpha_-/\text{g}^{\alpha'}_0,\text{inel}}} + \frac{1}{\tau_{\text{g}^\alpha_-/\text{g}^{\alpha'}_+,\text{inel}}} \right) \right]. \tag{2.46}$$

$\tau_{i_1/i_2,\text{inel}}$ is the inelastic collision time of species i_1 on species i_2, i.e.

$$\tau_{i_1/i_2,\text{inel}} = \frac{1}{n_{i_1} \langle \sigma v \rangle_{i_1/i_2}}, \tag{2.47}$$

where $\langle \sigma v \rangle_{i_1/i_2}$ is the reaction rate coefficient between the two species and follows the formulae of section 2.2.2. From this, we define two quantities

$$\varrho_s = \frac{\rho_{\mathrm{g}_0}}{\rho_s}\frac{\tau_{\mathrm{in}}}{\tau_{i,\mathrm{inel}}},$$
$$\frac{1}{\tau_0} = \frac{1}{\tau_{\mathrm{g}_0\mathrm{n}}} + \sum_i \frac{1}{\tau_{i,\mathrm{inel}}}.$$

Finally, the expressions of the inelastic terms are the following

$$\zeta_{\mathrm{g}_\pm} = \frac{\varrho_{\mathrm{g}_\pm}}{1+\varrho_{\mathrm{g}_\pm}} \frac{\frac{\tau_0}{\tau_{\mathrm{g}_0\mathrm{n}}} + \frac{2}{1+\varrho_{\mathrm{g}_\mp}}\frac{\tau_0}{\tau_{\mathrm{g}_\mp,\mathrm{inel}}}}{\frac{\tau_0}{\tau_{\mathrm{g}_0\mathrm{n}}} + \frac{1}{1+\varrho_{\mathrm{g}_+}}\frac{\tau_0}{\tau_{\mathrm{g}_+,\mathrm{inel}}} + \frac{1}{1+\varrho_{\mathrm{g}_-}}\frac{\tau_0}{\tau_{\mathrm{g}_-,\mathrm{inel}}}}, \tag{2.48}$$

$$\varpi_{\mathrm{g}_\pm} = \frac{\zeta_{\mathrm{g}_\pm}}{1+\varrho_{\mathrm{g}_\pm}} + \frac{\varrho_{\mathrm{g}_\mp}}{1+\varrho_{\mathrm{g}_\mp}} \frac{\frac{\tau_0}{\tau_{\mathrm{g}_0\mathrm{n}}} + \frac{\zeta_{\mathrm{g}_+}}{1+\varrho_{\mathrm{g}_+}}\frac{\tau_0}{\tau_{\mathrm{g}_+,\mathrm{inel}}} + \frac{\zeta_{\mathrm{g}_-}}{1+\varrho_{\mathrm{g}_-}}\frac{\tau_0}{\tau_{\mathrm{g}_-,\mathrm{inel}}}}{\frac{\tau_0}{\tau_{\mathrm{g}_0\mathrm{n}}} + \frac{1}{1+\varrho_{\mathrm{g}_+}}\frac{\tau_0}{\tau_{\mathrm{g}_+,\mathrm{inel}}} + \frac{1}{1+\varrho_{\mathrm{g}_-}}\frac{\tau_0}{\tau_{\mathrm{g}_-,\mathrm{inel}}}} \tag{2.49}$$

$$\varphi_{\mathrm{g}_\pm} = \frac{\varrho_{\mathrm{g}_\pm}}{1+\varrho_{\mathrm{g}_\pm}} \frac{2+\varrho_{\mathrm{g}_\pm}}{1+\varrho_{\mathrm{g}_\pm}} \frac{\frac{\tau_0}{\tau_{\mathrm{g}_0\mathrm{n}}} + \frac{1}{1+\varrho_{\mathrm{g}_\mp}}\frac{\tau_0}{\tau_{\mathrm{g}_\mp,\mathrm{inel}}}}{\frac{\tau_0}{\tau_{\mathrm{g}_0\mathrm{n}}} + \frac{1}{1+\varrho_{\mathrm{g}_+}}\frac{\tau_0}{\tau_{\mathrm{g}_+,\mathrm{inel}}} + \frac{1}{1+\varrho_{\mathrm{g}_-}}\frac{\tau_0}{\tau_{\mathrm{g}_-,\mathrm{inel}}}} \tag{2.50}$$

$$+ \frac{\tau_0}{\tau_{\mathrm{g}_\pm,\mathrm{inel}}} \frac{\varrho_{\mathrm{g}_\pm}}{(1+\varrho_{\mathrm{g}_\pm})^2} \frac{\frac{\varrho_{\mathrm{g}_\pm}}{1+\varrho_{\mathrm{g}_\pm}}\frac{\tau_0}{\tau_{\mathrm{g}_0\mathrm{n}}}\left(\frac{\varrho_{\mathrm{g}_+}}{1+\varrho_{\mathrm{g}_+}} + \frac{\varrho_{\mathrm{g}_-}}{1+\varrho_{\mathrm{g}_-}}\right)\frac{1}{1+\varrho_{\mathrm{g}_\mp}}\frac{\tau_0}{\tau_{\mathrm{g}_\mp,\mathrm{inel}}}}{\frac{\tau_0}{\tau_{\mathrm{g}_0\mathrm{n}}} + \frac{1}{1+\varrho_{\mathrm{g}_+}}\frac{\tau_0}{\tau_{\mathrm{g}_+,\mathrm{inel}}} + \frac{1}{1+\varrho_{\mathrm{g}_-}}\frac{\tau_0}{\tau_{\mathrm{g}_-,\mathrm{inel}}}} \tag{2.51}$$

$$\Upsilon_{\mathrm{g}_\pm}(X) = \frac{1 + \frac{\omega^2_{\mathrm{g}_\mp}\tau^2_{\mathrm{g}_\mp}\vartheta_\pm}{1+\omega^2_{\mathrm{g}_\mp}\tau^2_{\mathrm{g}_\mp\mathrm{n}}(1-\varphi_{\mathrm{g}_\mp})}\frac{1-X_{\mathrm{g}_\mp}}{1-X_{\mathrm{g}_\pm}}}{1 - \frac{\omega^2_{\mathrm{g}_+}\tau^2_{\mathrm{g}_+}\vartheta_-}{1+\omega^2_{\mathrm{g}_+}\tau^2_{\mathrm{g}_+\mathrm{n}}(1-\varphi_{\mathrm{g}_+})}\frac{\omega^2_{\mathrm{g}_-}\tau^2_{\mathrm{g}_-}\vartheta_+}{1+\omega^2_{\mathrm{g}_-}\tau^2_{\mathrm{g}_-\mathrm{n}}(1-\varphi_{\mathrm{g}_-})}} \tag{2.52}$$

with $X_{\mathrm{g}_\pm} = \zeta_{\mathrm{g}_\pm}$ or $\varpi_{\mathrm{g}_\pm}$, and

$$\vartheta_\pm = \frac{\varrho_{\mathrm{g}_\pm}}{(1+\varrho_{\mathrm{g}_\pm})^2}\frac{\tau_0}{\tau_{\mathrm{g}_\mp,\mathrm{inel}}} \frac{\frac{1}{1+\varrho_{\mathrm{g}_\mp}}\left(1 - \frac{\varrho_{\mathrm{g}_\pm}}{1+\varrho_{\mathrm{g}_\pm}}\frac{\tau_0}{\tau_{\mathrm{g}_\pm,\mathrm{inel}}}\right) - \frac{1}{1+\varrho_{\mathrm{g}_\pm}}\left(1 - \frac{\varrho_{\mathrm{g}_\mp}}{1+\varrho_{\mathrm{g}_\mp}}\frac{\tau_0}{\tau_{\mathrm{g}_\mp,\mathrm{inel}}}\right)}{\left(\frac{\tau_0}{\tau_{\mathrm{g}_0\mathrm{n}}} + \frac{1}{1+\varrho_{\mathrm{g}_+}}\frac{\tau_0}{\tau_{\mathrm{g}_+,\mathrm{inel}}} + \frac{1}{1+\varrho_{\mathrm{g}_-}}\frac{\tau_0}{\tau_{\mathrm{g}_-,\mathrm{inel}}}\right)^2} \tag{2.53}$$

which represents the inelastic collisional coupling between pairs of charged grains.

Figure 2.24 displays the maximum value of the inelastic terms as a function of density for our fiducial case with 1 bin. In the ideal fully elastic collisions case, the numbers ζ, φ and ϖ (red curves) are equal to zero, and $\Upsilon(\zeta)$ and $\Upsilon(\varpi)$ (blue curves) are equal to one. Below $n_{\mathrm{H}} = 10^{10}$ cm^{-3}, the red terms are higher or of the order of 1, and at least one blue term is higher than unity, so the inelastic terms cannot be neglected in this density range. Figure 2.25 shows the comparison between the resistivities for the standard and inelastic cases. The main difference lies in the ambipolar diffusion coefficient at low density[4], dropping by two orders of magnitude for $n_{\mathrm{H}} \in [10^2; 10^6]$ cm^{-3}. Given the high values of the inelastic terms, we could expect a much higher difference. However, at such low density the inelastic contribution is tempered by the dominating abundances of ions and electrons over the grains. Above this point, the two models give almost identical results because, while the grains are the most abundant charged species, the inelastic terms are closer to the elastic case.

---

[4] Around $n_{\mathrm{H}} = 10^6$ cm^{-3}, the ambipolar resistivity is negative, which is unphysical despite being a mathematical posibility in the one fluid approximation. This is due to the finite numerical precision of our code, added to an unlucky set of coefficients that makes the denominator of $\sigma_\perp$ a little too close to 0 by negative value.

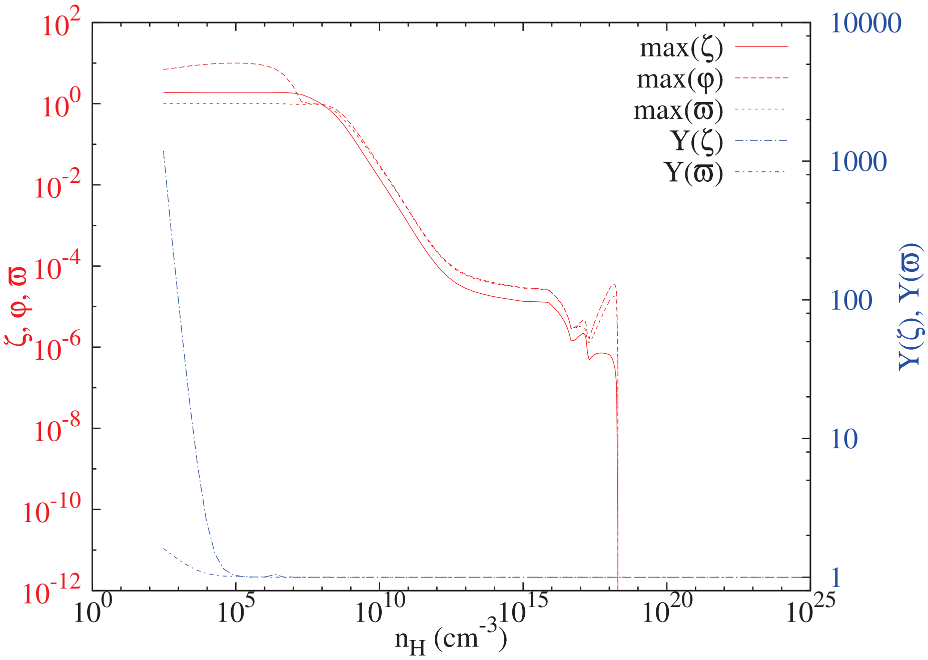

Figure 2.24: Maximum value of the inelastic terms in our fiducial case. The red curves: ζ, φ and ϖ need to be read on the left axis while the right axis corresponds to the blue curves $\Upsilon(\zeta)$ and $\Upsilon(\varpi)$.

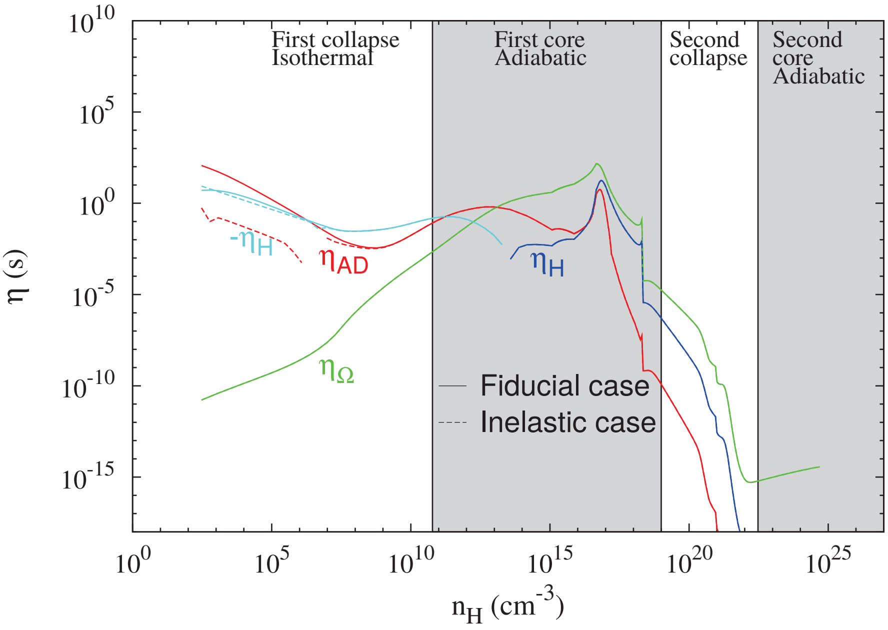

Figure 2.25: Comparison between the resistivities of the fiducial (solid lines) and inelastic (dashed lines) cases.

2.5 Conclusion

We have developed a solver which computes a detailed network of the main chemical reactions relevant to the first and second collapse of prestellar cores. The network is based on the work of Umebayashi & Nakano (1990) but extends significantly over this study by updating the reaction rates and by including the effects of dust evaporation, thermal ionisation of potassium and by exploring various cosmic ray ionisation rates. We have also used a distribution of grain sizes, the MRN distribution, and explored the impact of the number of size-bins on the results. The equilibrium abundances computed by the solver are used to calculate the non-ideal MHD resistivities, namely Ohmic, Hall and ambipolar resistivities, during the collapse, using a barotropic EOS to reproduce the typical density-temperature conditions. The resistivities determine the dynamics of the first and second collapse, and thus the properties of the first and second Larson cores.

Above a temperature of $T = 700$ K, the effects of grain evaporation and potassium ionisation become preponderant. An accurate description of these processes is mandatory for a proper characterization of the collapse, since they occur during the first core contraction and influence the initial conditions of the second collapse. Dust destruction has a double effect on the collapse. First, it modifies the opacity of the medium (see e.g. Lenzuni et al. 1995), which regulates the radiative cooling of the system. Evaporation increases the efficiency of this process, and the collapse accelerates as the gas is less thermally supported. Second, it affects the various resistivities of the non-ideal MHD terms, as does potassium ionisation, with direct impact on magnetic field topology and a diminution of the magnetic braking.

We have not included the molecular dissociation of elements in the chemical network, in particular the dissociation of H_2 at 2000 K, which leads to the second collapse. However, we do not expect the resistivities to be significantly affected by this process, as H^+ ions and electrons are dominant charged species at these temperatures. As mentioned in the text, our grain model is simplified, as we suppose that each grain is composed of only one material. A more realistic structure containing several layers of different materials, evaporating one after the other, will be included in future work.

Besides the general outcome of these calculations and their impact on prestellar core evolution, we wish to highlight the following points

- Using at least 5 bins for the grain size distribution is necessary for a reliable determination of the resistivities. As discussed in section 2.4.5, a precise knowledge of the grain size distribution would certainly improve the reliability of the results.
- As shown in §2.4.4, resistivities change by one order of magnitude when ionisation rates vary with a factor 10. This highlights the importance of shielding against cosmic rays in collapsing cores (Padovani et al. 2014).
- In the temperature range $750\ \mathrm{K} \lesssim T \lesssim 1700\ \mathrm{K}$, dust grains evaporate. This evaporation has tremendous consequences on the various chemical abundances and thus on the resistivities, since grains are the main contributors to the resistivities at these temperatures.
- Around 1500 K and above, thermal ionisation of metallic ions and Hydrogen occur, grains have been entirely destroyed, and H^+ and electrons become the main charge carriers, making the resistivities drop even further.
- Our chemical integration time is always lower than the free-fall time. We can thus assume equilibrium chemistry, less demanding than non-equilibrium chemistry, especially during hydrodynamics simulations.

The present solver allows us to compute a large, multi-dimensional multi-species equilibrium abundance table for large temperature, density and ionisation rate ranges. This table can be used during simulations of the first and second collapse of prestellar cores, allowing a consistent dynamical-chemical description of this process.

The table is available at https://bitbucket.org/pmarchan/chemistry.

2.A APPENDIX - Log-normal distribution

We consider a log-normal distribution centered around the size μ with a standard deviation σ. The number density is given by

$$dn_{\mathrm{g,tot}}(a) = \frac{\mathcal{C}}{a} e^{\frac{-log\left(\frac{a}{\mu}\right)^2}{2\sigma^2}} da. \tag{2.54}$$

In a similar manner than in section 2.2.3, we obtain

$$n_{\mathrm{g}}^{\alpha} = n_{\mathrm{g,tot}} \frac{\mathrm{erf}\left(\frac{\ln\left(\frac{a_{\min}}{\mu\chi^{\frac{\alpha}{N}}}\right)}{\sqrt{2}\sigma}\right) - \mathrm{erf}\left(\frac{\ln\left(\frac{a_{\min}}{\mu\chi^{\frac{\alpha-1}{N}}}\right)}{\sqrt{2}\sigma}\right)}{\mathrm{erf}\left(\frac{\ln\left(\frac{a_{\min}}{\mu\chi}\right)}{\sqrt{2}\sigma}\right) - \mathrm{erf}\left(\frac{\ln\left(\frac{a_{\min}}{\mu}\right)}{\sqrt{2}\sigma}\right)}, \tag{2.55}$$

$$a_{\alpha} = \mu e^{\sigma^2} \left[\frac{\mathrm{erf}\left(\frac{\ln\left(\frac{a_{\min}}{\mu\chi^{\frac{\alpha}{N}}}\right) - 2\sigma^2}{\sqrt{2}\sigma}\right) - \mathrm{erf}\left(\frac{\ln\left(\frac{a_{\min}}{\mu\chi^{\frac{\alpha-1}{N}}}\right) - 2\sigma^2}{\sqrt{2}\sigma}\right)}{\mathrm{erf}\left(\frac{\ln\left(\frac{a_{\min}}{\mu\chi^{\frac{\alpha}{N}}}\right)}{\sqrt{2}\sigma}\right) - \mathrm{erf}\left(\frac{\ln\left(\frac{a_{\min}}{\mu\chi^{\frac{\alpha-1}{N}}}\right)}{\sqrt{2}\sigma}\right)} \right]^{\frac{1}{2}}, \tag{2.56}$$

$$n_{\mathrm{g,tot}} = \frac{\rho_{\mathrm{g,tot}}}{\frac{4}{3}\pi\rho_{\mathrm{s}}\mu^2} e^{\frac{-9\sigma^2}{2}} \frac{\mathrm{erf}\left(\frac{\ln\left(\frac{a_{\min}}{\mu\chi}\right)}{\sqrt{2}\sigma}\right) - \mathrm{erf}\left(\frac{\ln\left(\frac{a_{\min}}{\mu}\right)}{\sqrt{2}\sigma}\right)}{\mathrm{erf}\left(\frac{\ln\left(\frac{a_{\min}}{\mu\chi}\right) - 3\sigma^2}{\sqrt{2}\sigma}\right) - \mathrm{erf}\left(\frac{\ln\left(\frac{a_{\min}}{\mu}\right) - 3\sigma^2}{\sqrt{2}\sigma}\right)}, \tag{2.57}$$

$$\rho_{\mathrm{g,tot}} = \frac{\rho_{\mathrm{g,0}}}{a_0} e^{\frac{\sigma^2}{2}} \frac{\mathrm{erf}\left(\frac{\ln\left(\frac{a_{\min}}{\mu\chi}\right) - 3\sigma^2}{\sqrt{2}\sigma}\right) - \mathrm{erf}\left(\frac{\ln\left(\frac{a_{\min}}{\mu}\right) - 3\sigma^2}{\sqrt{2}\sigma}\right)}{\mathrm{erf}\left(\frac{\ln\left(\frac{a_{\min}}{\mu\chi}\right) - 2\sigma^2}{\sqrt{2}\sigma}\right) - \mathrm{erf}\left(\frac{\ln\left(\frac{a_{\min}}{\mu}\right) - 2\sigma^2}{\sqrt{2}\sigma}\right)}. \tag{2.58}$$

2.B APPENDIX - Ionisation rate in a collapsing core

In figure 2.26, we show typical values of column density (left panel) and ionisation rate (right panel) as a function of density in a dense core at the first Larson core stage. These figures have been obtained through numerical simulations with `RAMSES`[5]. The extinction A, i.e. the absorption of a medium, is calculated at every location by tracing rays throughout the cloud (Valdivia & Hennebelle 2014). We then find the effective extinction by averaging on each direction with a harmonic mean. We choose this method because low extinction paths have a greater influence on the amount of radiation able to reach this location. We then retrieve the column density following the law given by Semenov et al. (2004)

$$N_{\mathrm{H_2}} = 1.59 \times 10^{21} \times A \text{ g cm}^2. \tag{2.59}$$

It represents the amount of particles by surface units a ray is "seeing" as projected along its path. Finally, we use the fit of Padovani et al. (2013) with an intermediate CR flux to obtain the CR ionisation rate. For the very high extinctions, the ionisation rate is kept at a minimum of $\zeta = 10^{-19}$ s^{-1} because the decays of radionucleides is another source of ionisation (Kunz & Mouschovias 2009). Throughout the cloud, the column density spans from 10^{21} to 10^{30} cm^{-2}, and the ionisation rate ranges across three orders of magnitude. Note that in most results presented

---

[5] see chapter 3 for more details on the code.

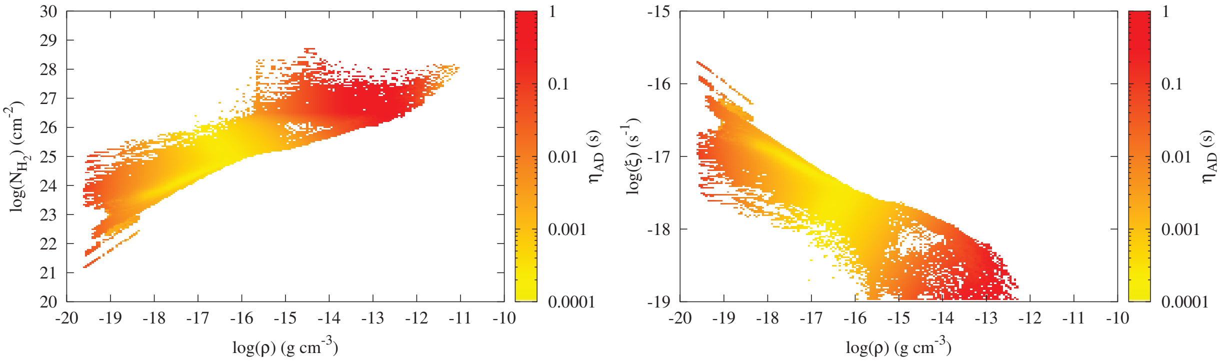

Figure 2.26: Column density (left panel) and CR ionisation rate (right panel) as a function of density, computed with `RAMSES`. The color coding corresponds to the ambipolar resistivity.

in this chapter, the ionisation rate is overestimated at higher densities since it takes the fiducial value of $\zeta = 10^{-17}$ s^{-1} (typically after the first Larson core formation). Hence, the resistivities are underestimated in these examples, but they properly evolve with the ionisation rate in `RAMSES`. The color represents the ambipolar diffusion resistivity η_{AD}. It undergoes variations by a factor 10 at a given density, hence justifying the need of a proper description of the ionisation rate.

Chapter 3

Numerical methods

3.1 The `RAMSES` code

Over the history of mankind, our understanding of nature has improved thanks to more and more accurate theories, and analytical calculus has always been a core tool for accurately describing physical phenomena. However, scientists quickly realized that describing a whole system taking into account all the physics at stake would be overwhelmingly difficult to do precisely with traditional methods. The apparition of computers in the 20th century allowed them to perform calculations much faster and simulate complex systems in a reasonable time. Nowadays, numerical simulations are widely used in most fields of science, and while they do not completely replace analytical calculus, they greatly help us verifying our understanding of the universe. By essence, computers are unable to describe perfectly our continuous world. All they do is storing and calculating numbers, and these operations demand a certain amount of processing time and memory. Consequently, a finite computer can not keep track of the infinite number of points in our 3D space and in time. Performing numerical simulations therefore requires a spatial and temporal discretization of reality. Inaccuracies arise from this imperfect description. Over the last decades, the power of computers (memory, speed) has increased exponentially, and sophisticated techniques have been developed to compensate this limited precision. Today, hydrodynamical codes in astrophysics also contain a lot of physical processes, like magnetisation or light-matter interaction, and are divided into two main categories. The *eulerian* codes use a grid whose cells contain information about their local environment (temperature, density...), whereas *lagrangean* codes describe the evolution of a set of particles.

`RAMSES` (Raffinement Adaptatif de Maillage Sans Effort Surhumain) is an explicit eulerian hydrodynamics code created by Romain Teyssier (Teyssier 2002), whose public version can be downloaded at https://bitbucket.org/rteyssie/ramses. It uses the Adaptative Mesh Refinement (AMR) technique (Berger & Oliger 1984) which consists in a local refinement of the grid where more precision is needed, to capture small-scale structures for example. The code is in 3D, but the explanations in this chapter are written in 1D in order to make the calculus clearer. We describe here state-of-the-art methods that are employed in many eulerian codes, including `RAMSES`. First, we explain how the code handles the discretization of the physical quantities onto the grid. Then we show how it makes them evolve through time by interpolating them and computing fluxes at cell interfaces.

3.1.1 Conservative methods

`RAMSES` uses the finite volume method, meaning that in each cell the flow variables are averaged over the volume of the cell. We have

$$u_{\mathrm{cell}} = \frac{1}{V_{\mathrm{cell}}} \int_{V_{\mathrm{cell}}} u(\mathbf{x}) \mathrm{d}\mathbf{x}, \tag{3.1}$$

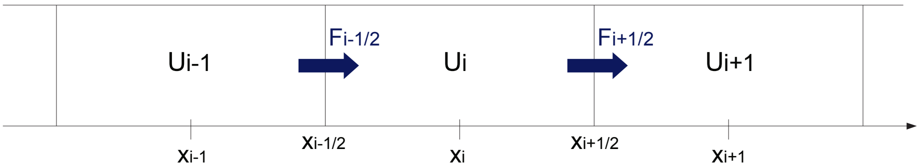

Figure 3.1: Schematic representation of a 1D discretized system, between cells $i-1$ and $i+1$.

for any flow variable u in a cell of size Δx. The variables are piecewise constant, and are ruled by the fluid equations in conservative form

$$\partial_t \mathbf{U} + \nabla \cdot \mathbf{F}(\mathbf{U}) = 0, \tag{3.2}$$

where $\mathbf{U}$ is the vector containing the conservative variables, and $\mathbf{F}(\mathbf{U})$ the corresponding fluxes. For example, in standard 1D-hydrodynamics, the Euler equations for an inviscid and compressible flow in conservative form are

$$\frac{\partial \rho}{\partial t} + \nabla \cdot (\rho u) = 0, \tag{3.3}$$

$$\frac{\partial \rho u}{\partial t} + \nabla \cdot (\rho u^2 + P) = 0, \tag{3.4}$$

$$\frac{\partial E}{\partial t} + \nabla \cdot (u(E+P)) = 0, \tag{3.5}$$

representing the conservation of mass, momentum and total energy respectively. ρ is the density, u the velocity, P the pressure and $E = \frac{1}{2}\rho u^2 + \rho\epsilon$ the total energy density of the fluid. The correspondence with equation (3.2) is straightforward; $\mathbf{U} = (\rho, \rho u, \rho E)$ and $\mathbf{F}(\mathbf{U}) = \big(\rho u, \rho u^2 + P, \rho u(E+P)\big)$. The set of equations is then closed by an equation of state. For a perfect gas, it reads $P = \frac{\rho k_{\mathrm{B}} T}{\mu m_{\mathrm{H}}} = \rho\epsilon(\gamma - 1)$, where T is the temperature, μ is the mean weight of fluid particles, m_{H} is the proton mass, ϵ is the specific internal energy and γ is the ratio of specific heats.

In this representation, the temporal evolution of the physical quantities is entirely determined by the corresponding fluxes between cells. It can be pictured as an exchange of information at cell interfaces in order to compute the quantities U_i^n, corresponding to the flow variable in the cell centered on x_i between $[x_{i-1/2}; x_{i+1/2}]$ (with $\Delta x = x_{i+1/2} - x_{i-1/2}$) at the nth time-step. We call $\mathbf{U}_i^n = \frac{1}{\Delta x}\int_{x_{i-1/2}}^{x_{i+1/2}} \tilde{\mathbf{U}}(x, t^n)dx$ the vector of variables U_i^n[1] The situation is represented on figure 3.1.

Integrating the equation 3.2 over a cell between two time-step yields

$$\int_{x_{i-1/2}}^{x_{i+1/2}} [\mathbf{U}(x, t^{n+1}) - \mathbf{U}(x, t^n)]dx = \int_{t^n}^{t^{n+1}} [\mathbf{F}(x_{i+1/2}, t) - \mathbf{F}(x_{i-1/2}, t)]dt. \tag{3.6}$$

`RAMSES` uses Godunov method (Godunov 1959) to approximate this equation. The first-order Godunov scheme is expressed as

$$\frac{U_i^{n+1} - U_i^n}{\Delta t} + \frac{F_{i+1/2}^n - F_{i-1/2}^n}{\Delta x} = 0, \tag{3.7}$$

---

[1] Here, we use the bold notation $\mathbf{U}$ for the variable vector, while the normal font U designates any component of $\mathbf{U}$ (e.g. $U = \rho$).

where $F^n_{i+1/2}$ and $F^n_{i-1/2}$ are the Godunov fluxes evaluated at their respective cell interfaces. At these locations, the flow variables are discontinuous due to the piecewise constant nature of the description. Dealing with the discontinuities is called a *Riemann problem*, and it is used to compute the flux.

3.1.2 Riemman problems

In order to solve a Riemann problem, one must determine the characteristic speeds of the system, as they determine how fast the information and perturbations travels. Equation (3.2) is equivalent to

$$\partial_t \mathbf{U} + \mathbb{J}\nabla \cdot \mathbf{U} = 0, \tag{3.8}$$

where $\mathbb{J}$ is the Jacobian matrix of $\mathbf{F}(\mathbf{U})$, $J_{ij} = \partial F_i / \partial U_j$. The characteristic speeds are simply the eigenvalues of $\mathbb{J}$. As it may be laborious to calculate the Jacobian matrix and its eigenvalues, it is often simpler to use the primitive variables $\mathbf{W}$ instead. Whereas the conservative variables allows to write the equations in conservative form ($\partial/\partial t + \nabla \cdot [\;] = 0$), which is useful for numerical schemes, the primitive variables corresponds to the physical quantities of the system and are more intuitive to handle. The equations in primitive form reads, in one dimension

$$\partial_t \mathbf{W} + \mathbb{A}\partial_x \mathbf{W} = 0. \tag{3.9}$$

$\mathbb{A}$ and $\mathbb{J}$ are similar matrix[2], so they have the same eigenvalues.

In our example of standard hydrodynamics, the primitive variables are $\mathbf{W} = (\rho, u, P)$, and we have

$$\mathbb{J} = \begin{pmatrix} 0 & 1 & 0 \\ \frac{\gamma-3}{2}u^2 & (3-\gamma)u & \gamma-1 \\ \frac{\gamma-2}{2}u^3 - \frac{\gamma u P}{\rho(\gamma-1)} & \frac{3-2\gamma}{2}u^2 - \frac{\gamma P}{\rho(\gamma-1)} & \gamma u \end{pmatrix}, \tag{3.10}$$

and

$$\mathbb{A} = \begin{pmatrix} u & \rho & 0 \\ 0 & u & \rho^{-1} \\ 0 & \gamma P & u \end{pmatrix}. \tag{3.11}$$

It is much easier to do calculation with the matrix $\mathbb{A}$ rather than with the Jacobian matrix. We quickly find the eigenvalues of $\mathbb{A}$ to be

$$\lambda^1 = u - c_\mathrm{s}, \quad \lambda^2 = u, \quad \lambda^3 = u + c_\mathrm{s},$$

where $c_\mathrm{s} = \sqrt{\frac{\gamma P}{\rho}}$ is the sound speed. In this case, three waves will propagate from the discontinuity. The situation is represented in a space-time diagram in the left panel of figure 3.2. The two initial states U_L and U_R are separated by the three waves, creating two additional constant states U_L^* and U_R^*. The wave λ^2 is called a contact discontinuity, λ^1 is a rarefaction wave and λ^3 is a shock wave. We want to compute the state U at the cell interfaces in $x = 0$ (in this case U_L^*).

It is possible to calculate the exact solution of a Riemann problem, but at heavy computational cost. Approximate Riemann solvers are more commonly used in hydrodynamical codes. The HLL (Harten Lax van Leer) (Harten et al. 1983) solver is one of the most famous. It approximates the Riemann fan of characteristic speeds by a constant state between the slowest and fastest waves of speed S_L and S_R emerging from the discontinuity, i.e. $S_L = \min(\lambda^i)$ and $S_R = \max(\lambda^i)$. It then supposes a constant state in-between (see right panel of Figure 3.2). The flux at the interface is given by

$$\mathbf{F}^{\mathrm{HLL}} = \begin{cases} \mathbf{F}_L & \text{if } 0 \leq S_L, \\ \frac{S_R \mathbf{F}_L - S_L \mathbf{F}_R + S_L S_R (\mathbf{U}_R - \mathbf{U}_L)}{S_R - S_L} & \text{if } S_L \leq 0 \leq S_R, \\ \mathbf{F}_R & \text{if } S_R \leq 0. \end{cases} \tag{3.12}$$

---

[2] There exists a matrix $\mathbb{P}$ so that $\mathbb{A} = \mathbb{P}\mathbb{J}\mathbb{P}^{-1}$

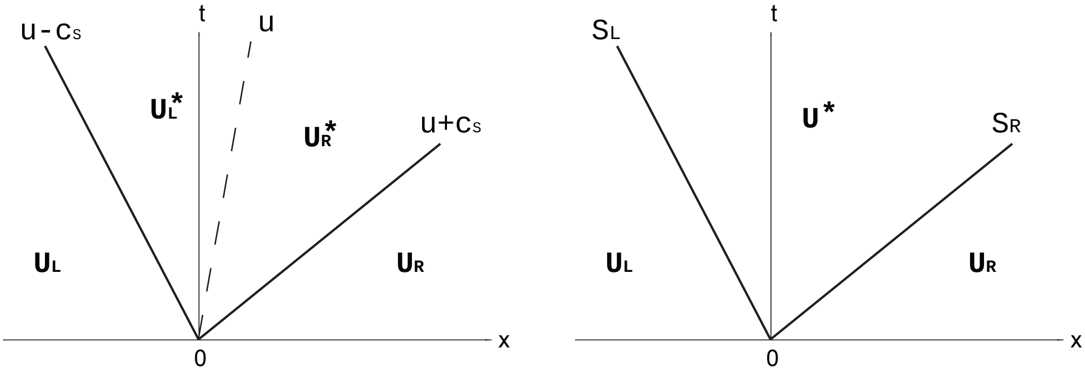

Figure 3.2: Wave propagation in the Riemann problem. Left panel: exact Riemann problem in the hydro case, right panel: approximation of the problem by the HLL solver.

This flux needs to be calculated at the left and right interfaces of the cell, to be directly input in the Godunov scheme (equation (3.7)) in order to update the flow variables for the next time-step. Lax-Friedrich and HLLC are other well-known Riemann solvers. The Lax-Friedrich scheme considers only the fastest wave, i.e. $S_L = -\max(\text{abs}(\lambda^i))$ and $S_R = \max(\text{abs}(\lambda^i))$, while HLLC describes two constant states between the standard HLL waves and the contact discontinuity wave (which would look like the left panel of figure 3.2). For more information about the resolution of Riemann problems, we strongly advise the reading of the chapters 4 and 10 of Toro (2009).

3.1.3 The predictor-corrector scheme MUSCL

The first order Godunov scheme is only first order in space and time, resulting in a high diffusivity. To tackle this problem, `RAMSES` uses the Monotone Upstream-centered Scheme for Conservative Laws (MUSCL) (van Leer 1976). The goal is to extrapolate the states at the interfaces to compute the fluxes. In this description, we consider that the flow variables vary linearly throughout the cell as

$$U_i(x) = U_i^n + \frac{x - x_i}{\Delta x}\Delta i. \tag{3.13}$$

The slope coefficient Δi is determined by using the neighboring cells. It ensures a second order accuracy in space, meaning that the numerical error due to the approximation scales as Δx^2. The choice of Δi is very important because we want the monotonicity to be preserved from one time-step to another. A slope too steep may generate new (unwanted) extrema in the system.

The Total Variation Diminishing (TVD) (Harten 1983) method has been introduced for this purpose. It limits the slope, and guarantees the monotonicity provided the Total Variation $TV = \sum_{i=0}^{N} |U_{i+1} - U_i|$ is a decreasing function over time. The most common slope limiters are

- *minmod* $= \begin{cases} 0 & \text{if } (U_i - U_{i-1})(U_{i+1} - U_i) < 0, \\ \min_{\text{mag}}(U_i - U_{i-1}, U_{i+1} - U_i) & \text{otherwise,} \end{cases}$
- *Van Leer* $= \begin{cases} 0 & \text{if } (U_i - U_{i-1})(U_{i+1} - U_i) < 0, \\ \min_{\text{mag}}\left(\beta(U_i - U_{i-1}), \beta(U_{i+1} - U_i), \frac{U_{i+1} - U_{i-1}}{2}\right) & \text{otherwise,} \end{cases}$

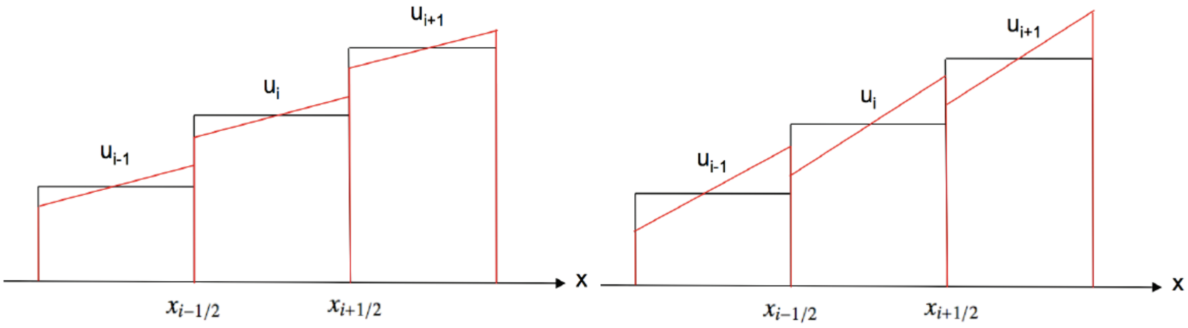

Figure 3.3: Visualisation of the *moncen* (left) and *minmod* (right) slope limiters. From a Romain Teyssier lecture.

- *moncen* $= \begin{cases} 0 & \text{if } (U_i - U_{i-1})(U_{i+1} - U_i) < 0, \\ \min_{\text{mag}}\left(2(U_i - U_{i-1}), 2(U_{i+1} - U_i), \frac{U_{i+1} - U_{i-1}}{2}\right) & \text{otherwise,} \end{cases}$

where $\min_{\text{mag}}$ returns the number with the smallest magnitude. Both slope limiters are implemented into `RAMSES`, in which the interpolation and the TVD are performed independently in each dimension. They are schematically represented in figure 3.3. We also sometimes use a 3D unsplit slope limiter. It first computes $v_{\min} = \min(U_{i',j',k'} - U_{i,j,k})$ and $v_{\max} = \max(U_{i',j',k'} - U_{i,j,k})$ where $m' \in [m-1, m+1]$, for $m = i, j, k$. The directional variations are calculated as $d_i = 0.5(U_{i+1,j,k} - U_{i-1,j,k})$, and the final slopes are given by

$$\Delta(U)_{i,j,k} = d_i \times \min(1, \frac{\min(\text{abs}(v_{\min}), \text{abs}(v_{\min}))}{\frac{\|d_i\| + \|d_j\| + \|d_k\|}{2}} \tag{3.14}$$

Once the slope $(\Delta(U))_i$ is known, the flow variables are predicted at the center of the cell by integrating the discretized Euler equations using these slopes. For instance, the mass conservation equation $\partial\rho/\partial t + \mathbf{u} \cdot \nabla\rho + \rho\nabla \cdot \mathbf{u} = 0$ becomes

$$\frac{\rho_i^{n+1/2} - \rho_i^n}{\Delta t} = u_i \frac{(\Delta(\rho))_i}{\Delta x} + \rho_i \frac{(\Delta(u))_i}{\Delta x}, \tag{3.15}$$

where $\rho_i^{n+1/2}$ is the predicted density at the center of the cell, and $\Delta_i(A)$ stands for the TVD slope of cell i for variable A. Once all equations have been integrated, the states at cell interfaces are calculated using equation (3.13)

$$U_{i-1/2}^{R,n+1/2} = U_i^{n+1/2} - \frac{(\Delta(U))_i}{2} \quad \text{and} \quad U_{i+1/2}^{L,n+1/2} = U_i^{n+1/2} + \frac{(\Delta(U))_i}{2}. \tag{3.16}$$

The subscripts L and R designate the left and right side of the interface. A Riemann problem is then solved at each interface using these values, which gives the predicted states $U_i^{L,n+1/2}$ and $U_i^{R,n+1/2}$. The fluxes are then evaluated

$$F_{i+1/2}^{n+1/2} = \frac{1}{\Delta t} \int_{t^n}^{t^{n+1}} F_{i+1/2} dt \approx F\left(U_i^R\left(\frac{\Delta t}{2}\right)\right) \tag{3.17}$$

and input in the Godunov scheme (equation (3.7)). In short, instead of computing fluxes as $F_{i+1/2}^n = F(\text{RP}(U_i, U_{i+1}))$, the MUSCL scheme calculate them as

$$F_{i+1/2}^{n+1/2} = F\left[\text{RP}(U_i^{R,n+1/2}, U_{i+1}^{L,n+1/2})\right]. \tag{3.18}$$

The different steps of a time-step in `RAMSES` are then

- Calculating the slope Δ_i for each cell using the TVD,
- Obtaining the predicted states at cell interfaces by integrating the Euler equations in primitive form with the slopes in place of the spatial derivatives,
- Solving the Riemann problem with the predicted values to compute the flux at the interfaces,
- Updating the conservative variables with these fluxes (eq. (3.7)).

`RAMSES` is a 3D code, but uses the dimensional splitting. The steps described above are done for every cell, once in each direction (x, y and z) independently[3].

3.1.4 A word on time-steps

As seen in Section 3.1.2, characteristic waves propagate the fluid perturbations over the system, and that is from one cell to another in the discretized world of the simulation. We do not want a perturbation to propagate too far and to 'jump' accross a cell during one timestep. For example, in Figure 3.1, if a perturbation is created in cell $i-1$ at the time-step n and is transported to cell $i+1$ at the time-step $n+1$, it is not accounted for because information is exchanged only between adjacent cells. Concretely, a wave with a speed c must travel a distance smaller than Δx in a time Δt. Hence the condition

$$\frac{\Delta x}{c\Delta t} > 1. \tag{3.19}$$

This is known as the CFL condition (Courant et al. 1928), which ensures the convergence and stability of explicit schemes[4]. `RAMSES` computes Δt at each time-step for every cell in the simulation box, using the local fastest wave speed, then takes the global minimum as the next value.

3.1.5 The Adaptative Mesh Refinement (AMR)

The precision of a simulation is deeply related to its spatial resolution, which is the size of the cell in an eulerian code. Smaller cells means higher precision. In cartesian grids, all the cells have the same size and to achieve more precision one needs to refine the whole grid with smaller cells. This is computationally prohibitive because the number of cells grows rapidly, especially in 3 dimensions. The AMR tackles this problem as it consists in automatically refining a grid at specific locations, rather than refining the whole grid. It is a common feature of modern astrophysical codes because it saves (expensive) computational time while allowing for a good precision on small-scale effects. In `RAMSES`, the AMR is "tree-based" as its data structure is organized in a "Fully Threaded Tree" (FTT) (Khokhlov 1998). The basic elements of the grid are *oct*s, that are groups of 2^{dim} cells. They are flagged as part of a refinement level ℓ. The code first creates a base grid that is cartesian and defined by the minimum level of refinement ℓ_{min}. At that point, each cell of size Δx from level ℓ can be independently refined in 2^{dim} cells of size $\Delta x/2$, creating a child oct at level $\ell+1$. The *split cells* are refined cells and do not take part in the hydrodynamics calculations, that are performed on cells without children called *leaf cells*. Figure 3.4 shows an example in 2D, with $\ell_{\text{min}} = 2$ and cells refined at $\ell = 3$. Blue cells 6 and 10 are refined once, becoming split cells by creating the red leaf cells $1-8$.

Sub-cycling The characteristic evolution times of the fluid in fine levels are often smaller than in the coarse level. Therefore, similarly to the spatial-domain, having a uniform time-step for the whole grid is constraining. That is where another big advantage of AMR intervenes, the sub-cycling. This method allows the coarser levels to evolve with a bigger time-step than the

---

[3] Except the slope calculation when using the 3D unsplit slope limiter

[4] In explicit schemes, the variable evolution between time steps n and $n+1$ only depends on variables at time step n, while in implicit schemes it only depends on variables at time step $n+1$. Implicit schemes are unconditionally stable but more difficult to handle numerically.

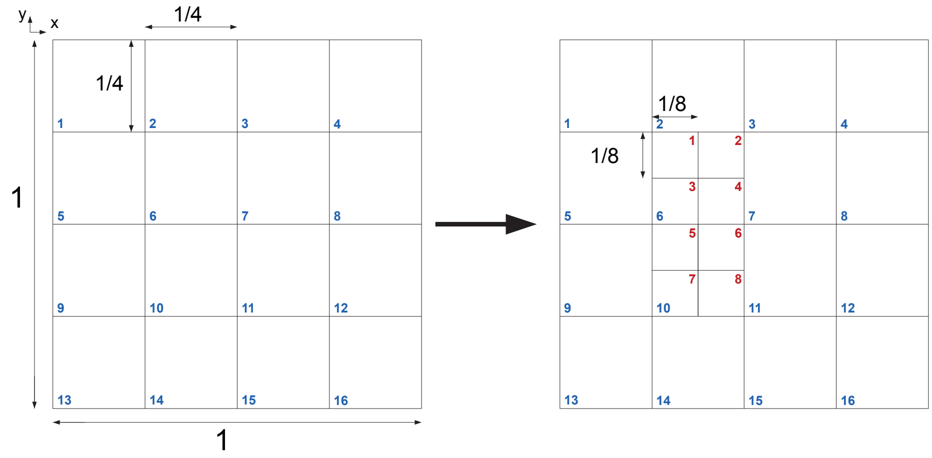

Figure 3.4: Illustration of the refinement method in `RAMSES`. Left panel represents the base grid with $\ell_{\min} = 2$ (so $2^2 \times 2^2$ cells), and right panel shows the same grid with cells 6 and 10 refined at $\ell = 3$. The blue numbers reference the cells of level $\ell = 2$, while the red numbers account for the $\ell = 3$ cells.

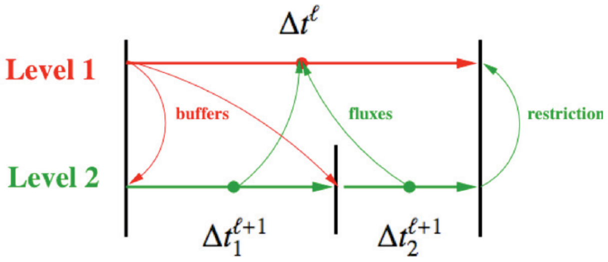

Figure 3.5: Schematic illustration of subcycling. Taken from Romain Teyssier lecture.

finer levels. Typically, cells at level ℓ perform two time-steps, while level $\ell - 1$ only performs one. At the end of each coarse time-step, every level is synchronized

$$\Delta t_1^{\ell} + \Delta t_2^{\ell} = \Delta t^{\ell-1}. \tag{3.20}$$

Fluxes at level interfaces are time-averaged for the hydrodynamics calculation at the coarser level (see figure 3.5).

AMR in star formation In star formation calculations, it is necessary to resolve the Jeans length to accurately describe the gravitational collapse and the potential fragmentation. We therefore use this criterion to refine our grid by imposing a minimum number of points N_{J} per Jeans length λ_{J}. We must have at every location

$$\lambda_{\mathrm{J}} > N_{\mathrm{J}} \times \Delta x, \tag{3.21}$$

where Δx is the size of the local cell. Truelove et al. (1997) showed that N_{J} should be at least 4 to avoid spurious gravitational effects.

3.1.6 The constrained transport

The magnetic field evolution is controlled by the induction equation

$$\frac{\partial \mathbf{B}}{\partial t} = \nabla \times \mathbf{E}, \tag{3.22}$$

with $\mathbf{E} = \mathbf{u} \times \mathbf{B}$ in ideal MHD. However, this is not the only constraint on the magnetic field, as its solenoidal nature needs to be conserved, i.e. $\nabla \cdot \mathbf{B} = 0$. The method of the *constrained transport* (Evans & Hawley 1988) exploits the Stokes theorem in the finite volume formalism and guarantees the preservation of $\nabla \cdot \mathbf{B}$ in ideal MHD. `RAMSES` uses this method (Fromang et al. 2006; Teyssier et al. 2006). The magnetic flux through a surface S is calculated as

$$\phi = \iint_S \mathbf{B} \cdot \mathrm{d}\mathbf{S}. \tag{3.23}$$

Using this definition in the induction equation (3.22) yields

$$\frac{\partial \phi}{\partial t} = \iint_S \frac{\partial \mathbf{B}}{\partial t} \cdot \mathrm{d}\mathbf{S} = \iint_S \nabla \times \mathbf{E} \mathrm{d}\mathbf{S} = \oint_C \mathbf{E} \cdot \mathrm{d}\mathbf{l}. \tag{3.24}$$

While the other flow variables are defined at the center of the cell, each component of the magnetic field is averaged on the corresponding orthogonal face (for example, B_y is defined in $i, j-1/2, k$). The magnetic flux through the surface is then calculated by adding the electromotive forces (emf) E on the four edges that compose the contour of the face (see figure 3.6). The finite volume form of equation (3.24) yields, for the x-direction,

$$\frac{B^{n+1}_{x,i-1/2,j,k} - B^{n}_{x,i-1/2,j,k}}{\Delta t} = \frac{E^{n+1/2}_{z,i-1/2,j+1/2,k} - E^{n+1/2}_{z,i-1/2,j-1/2,k} - E^{n+1/2}_{y,i-1/2,j,k+1/2} + E^{n+1/2}_{y,i-1/2,j,k-1/2}}{\Delta x}, \tag{3.25}$$

where the emfs are computed using the MUSCL scheme, then solving a Riemann problem. Because they are located at the intersection of 4, and not 2, cells, the fluxes of the Riemann problem (3.12) need to be adapted. Instead of using the left and right states of the interface, we need to use the corner left-bottom, left-top, right-bottom and right-top states. These states are calculated using the linear slopes in both directions $U_{i-1/2,j-1/2} = U_i - \frac{\Delta i}{2} - \frac{\Delta j}{2}$. Similarly to the 1D case, the HLL flux (here, the emfs) for this 2D Riemann problem is (Londrillo & del Zanna 2004)

$$\begin{aligned} E^{n+1/2}_{z,i-1/2,j-1/2,k} =& \frac{S_L S_B E_{z,LB} - S_L S_T E_{z,LT} - S_R S_B E_{z,RB} + S_R S_T E_{z,RT}}{(S_R - S_L)(S_T - S_B)} \\ & - \frac{S_T S_B}{S_T - S_B}(B_{x,T} - B_{x,B}) + \frac{S_R S_L}{S_R - S_L}(B_{y,R} - B_{y,L}), \end{aligned} \tag{3.26}$$

where S_L, S_R, S_B and S_T are the slowest and fastest waves in the x and y directions, and $E_z = v_x B_y - v_y B_x$ for each corner. All the other notations are defined on figure 3.7. This method is repeated independently in every direction.
In ideal MHD, there are 7 characteristic waves to account for

- 2 Alfvèn waves, that propagate the perturbations of the magnetic field, $\lambda = u \pm c_\mathrm{a}$.
- 2 fast magneto-sonic waves, representing the correlation between $\mathbf{B}$ and ρ by the coupling between Lorentz force and thermal pressure, $\lambda = v \pm \sqrt{\frac{1}{2}(c_\mathrm{s}^2 + c_\mathrm{a})^2 + \frac{1}{2}\sqrt{(c_\mathrm{s}^2 + c_\mathrm{a})^2 - 4c_\mathrm{s}^2 c_{\mathrm{a},x}^2}}$ (with $c_\mathrm{a,x}$ the component of the Alfvèn speed in the direction of propagation).
- 2 slow magneto-sonic waves, representing the anti-correlation between $\mathbf{B}$ and ρ by the coupling between Lorentz force and thermal pressure, $\lambda = v \pm \sqrt{\frac{1}{2}(c_\mathrm{s}^2 + c_\mathrm{a})^2 - \frac{1}{2}\sqrt{(c_\mathrm{s}^2 + c_\mathrm{a})^2 - 4c_\mathrm{s}^2 c_{\mathrm{a},x}^2}}$
- 1 contact discontinuity wave $\lambda = v$.

The HLLD Riemann solver (Miyoshi & Kusano 2005) uses 5 different waves to interpolate the interface states, and is therefore more suited to MHD than HLL.

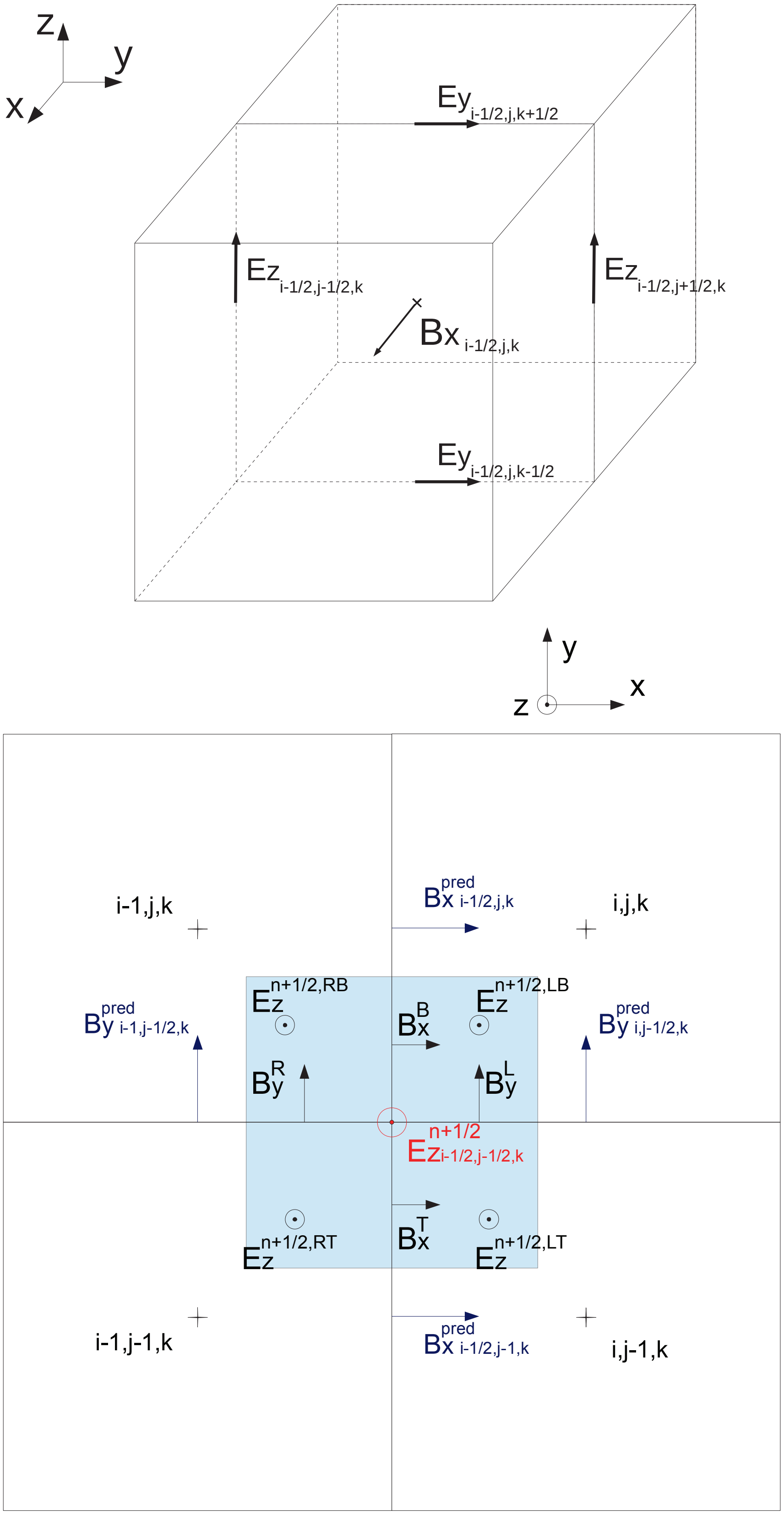

Figure 3.7: Scheme of a 2D Riemann problem in the z-direction. The blue area represents the states at the corner for each cell at $i-1/2, j-1/2, k$.

3.1.7 Non-ideal MHD

In ideal MHD, the electric field of equation (3.22) is simply $\mathbf{E} = \mathbf{u} \times \mathbf{B}$, but there are additional terms in the non-ideal MHD description. Including the ambipolar and Ohmic diffusion yields

$$\mathbf{E} = \mathbf{u} \times \mathbf{B} + \eta_\Omega \nabla \times \mathbf{B} - \eta_{\mathrm{AD}}((\nabla \times \mathbf{B}) \times \mathbf{B}) \times \mathbf{B}.$$

There are several different ways to treat non-ideal MHD effects (Black & Scott 1982; Stone & Norman 1992; Mac Low et al. 1995; Falle 2003; Machida et al. 2006; O'Sullivan & Downes 2006; Mellon & Li 2009; Choi et al. 2009; Li et al. 2011; Tilley & Balsara 2011). For example, Black & Scott (1982) were the first to attempt the implementation of ambipolar diffusion, exploiting the rapid collisional coupling between ions and neutrals to compute the drift velocity. Mac Low et al. (1995) simplified the equations by neglecting the ion pressure to incorporate the effect in the explicit ZEUS code (Stone & Norman 1992), while Machida et al. (2006) described both diffusions as a Laplace operator. In `RAMSES`, the one-fluid approximation is used (Shu et al. 1987) as in Mac Low et al. (1995) and Duffin & Pudritz (2008), and ambipolar and Ohmic diffusion are directly implemented in term of fluxes in the energy and induction equations (Masson et al. 2012). The emf (3.26) then becomes

$$\begin{aligned} E^{n+1/2}_{z,i-1/2,j-1/2,k} =& E^{\mathrm{ideal},n+1/2}_{z,i-1/2,j-1/2,k} \\ & - \eta_\Omega \left[\frac{B^n_{y,i,j-1/2,k} - B^n_{y,i-1,j-1/2,k}}{\Delta x} - \frac{B^n_{x,i-1/2,j,k} - B^n_{y,i-1/2,j-1,k}}{\Delta y} \right] \\ & + \eta_{\mathrm{AD}} \left[(u_{\mathrm{ad}})^n_{x,i-1/2,j-1/2,k} B^n_{y,i-1/2,j-1/2,k} - (u_{\mathrm{ad}})^n_{y,i-1/2,j-1/2,k} B^n_{x,i-1/2,j-1/2,k} \right], \end{aligned} \tag{3.27}$$

where $\mathbf{u_d} = \mathbf{J} \times \mathbf{B}$. In the ambipolar term, the quantities are not always naturally defined and are interpolated on faces, edges and corner of the cells. For instance,

$$B_{y,i-1/2,j-1/2,k} = \frac{1}{2}(B_{y,i,j-1/2,k} + B_{y,i-1,j-1/2,k}), \tag{3.28}$$

$$J_{x,i-1/2,j-1/2,k} = \frac{B_{z,i-1/2,j,k} - B_{z,i-1/2,j-1,k}}{\Delta y} - \frac{B_{z,i-1/2,j-1/2,k+1/2} - B_{z,i-1/2,j-1/2,k-1/2}}{\Delta z}. \tag{3.29}$$

All the other terms are calculated in the same way. A schematic visualization of these interpolations is pictured in figure 3.8.

3.2 Implementation of the Hall effect

The Hall effect is an electric field created by the difference between the speeds of the electron fluid and the ion fluid. Unlike the ambipolar and Ohmic diffusions, the Hall effect is purely dispersive, meaning that it does not carry mass nor momentum, and does not dissipate energy. It exclusively changes the topology of the magnetic field by propagating magnetic perturbations through the fluid via dispersive waves called 'whistler waves'. We describe here our implementation of the Hall effect in `RAMSES` and the tests of our scheme.

3.2.1 Principle of the implementation

The introduction of new waves in the system by the Hall effect modifies the Riemann problem at cell interfaces. For this reason, we choose to follow Lesur et al. (2014) and to directly modify the Riemann Solver instead of considering the Hall effect as a source term (as it is the case for ambipolar and Ohmic diffusions).

As defined in section 1.3.4.3, the Hall speed[5] is $\mathbf{u}_{\mathrm{H}} = -\eta_{\mathrm{H}} \frac{\nabla \times \mathbf{B}}{||\mathbf{B}||}$. The induction equation

---

[5] Not to be confused with the whistler speed !

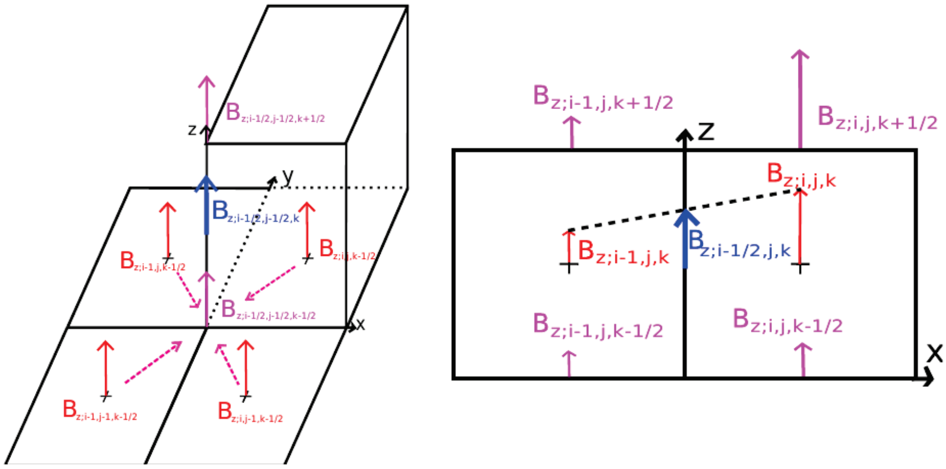

Figure 3.8: Visualization of the magnetic field interpolations on cell edges for the ambipolar diffusion. Taken from Jacques Masson thesis.

(1.77) yields

$$\frac{\partial \mathbf{B}}{\partial t} = -\nabla \times [(\mathbf{u} + \mathbf{u}_{\mathrm{H}}) \times \mathbf{B}]. \tag{3.30}$$

In the constrained transport method, the electromagnetic forces $\mathrm{E} = \mathbf{u} \times \mathbf{B}$ are computed on the four edges of the interface by using a 2D-Riemann solver for each edge. To implement the Hall effect, we have replaced $\mathbf{u}$ by an 'effective' speed $\mathbf{u} + \mathbf{u}_{\mathrm{H}}$ in the 2D-Riemann solver.

3.2.2 The Hall speed

We need to compute the Hall speed on cell edges. The first step is to determine the predicted states of the flow variables on cell faces and edges using a TVD slope (e.g. *minmod*) before computing the Hall term. The predicted state is computed using the induction equation without the Hall term coupled with the Stokes theorem

$$\frac{B^{n+\frac{1}{2}}_{x,i-\frac{1}{2},j,k} - B^{n}_{x,i-\frac{1}{2},j,k}}{\Delta t} = \frac{E^{n}_{z,i-\frac{1}{2},j+\frac{1}{2},k} - E^{n}_{z,i-\frac{1}{2},j-\frac{1}{2},k}}{\Delta x} - \frac{E^{n}_{y,i-\frac{1}{2},j,k+\frac{1}{2}} - E^{n}_{y,i-\frac{1}{2},j,k-\frac{1}{2}}}{\Delta x}, \tag{3.31}$$

$$\frac{B^{n+\frac{1}{2}}_{y,i,j-\frac{1}{2},k} - B^{n}_{x,i,j-\frac{1}{2},k}}{\Delta t} = \frac{E^{n}_{x,i,j-\frac{1}{2},k+\frac{1}{2}} - E^{n}_{x,i,j-\frac{1}{2},k-\frac{1}{2}}}{\Delta x} - \frac{E^{n}_{z,i+\frac{1}{2},j-\frac{1}{2},k} - E^{n}_{z,i-\frac{1}{2},j-\frac{1}{2},k}}{\Delta x}, \tag{3.32}$$

$$\frac{B^{n+\frac{1}{2}}_{z,i,j,k-\frac{1}{2}} - B^{n}_{z,i,j,k-\frac{1}{2}}}{\Delta t} = \frac{E^{n}_{y,i+\frac{1}{2},j,k-\frac{1}{2}} - E^{n}_{y,i-\frac{1}{2},j,k-\frac{1}{2}}}{\Delta x} - \frac{E^{n}_{x,i,j+\frac{1}{2},-+\frac{1}{2}} - E^{n}_{y,i,j-\frac{1}{2},k-\frac{1}{2}}}{\Delta x}, \tag{3.33}$$

where $\mathbf{E}^n = \mathbf{u}^n \times \mathbf{B}^n$ is the electric field calculated on cell edges using simple interpolations of $\mathbf{u}^n$ and $\mathbf{B}^n$ at these locations, e.g.

$$\mathbf{u}^{n}_{i-\frac{1}{2},j-\frac{1}{2},k} = \frac{1}{4}\left(\mathbf{u}^{n}_{i,j,k} + \mathbf{u}^{n}_{i-1,j,k} + \mathbf{u}^{n}_{i,j-1,k} + \mathbf{u}^{n}_{i-1,j-1,k}\right). \tag{3.34}$$

$$B^{n}_{x,i-\frac{1}{2},j-\frac{1}{2},k} = \frac{1}{2}\left(B^{n}_{x,i-\frac{1}{2},j,k} + B^{n}_{x,i-\frac{1}{2},j-1,k}\right), \tag{3.35}$$

$$B^{n}_{y,i-\frac{1}{2},j-\frac{1}{2},k} = \frac{1}{2}\left(B^{n}_{y,i,j-\frac{1}{2},k} + B^{n}_{x,i-1,j-\frac{1}{2},k}\right). \tag{3.36}$$

Only the perpendicular component of the magnetic field has been calculated on each face. We reconstruct the other two by interpolating the state at the cell center, and using the TVD slope. For instance, to obtain B_y on the face located at $(i-\frac{1}{2},j,k)$, we successfully calculate

$$B^{n+\frac{1}{2}}_{y,i,j,k} = \frac{1}{2}\left(B^{n+\frac{1}{2}}_{y,i,j-\frac{1}{2},k} + B^{n+\frac{1}{2}}_{y,i,j+\frac{1}{2},k}\right), \text{ then} \tag{3.37}$$

$$B^{n+\frac{1}{2}}_{y,i-\frac{1}{2},j,k} = B^{n+\frac{1}{2}}_{y,i,j,k} - \frac{\Delta_y(B_y)_{i,j,k}}{2}, \tag{3.38}$$

where $\Delta_y(B_y)_{i,j,k}$ is the slope of B_y in the $y-$direction for cell (i,j,k).

The slopes are computed in each direction and in each cell independently. As a consequence, the predicted state at a given cell interface is different whether it was extrapolated from the left or right cell, because $\mathbf{B}^{n+\frac{1}{2}}_{i-\frac{1}{2},j,k}$ can be obtained from either cell (i,j,k) or cell $(i-1,j,k)$. This discontinuity of $\mathbf{B}$ is a problem here, because the Hall effect relies on the electric current $\mathbf{J} = \nabla \times \mathbf{B}$. The jumps at cell interfaces may be assimilated as perturbations with an infinitely small wavelength that would propagate at an infinite speed, which is of course unphysical. To tackle this problem, we average $\mathbf{B}$ and consider that $\mathbf{J}$ is constant on cell faces and edges (Tóth et al. 2008; Lesur et al. 2014), at the price of a greater numerical diffusivity since we smooth discontinuities. We note B^{pred} the averaged magnetic field, therefore calculated as

$$\mathbf{B}^{\text{pred}}_{i-\frac{1}{2},j,k} = \frac{\mathbf{B}^{n+\frac{1}{2},L}_{i-\frac{1}{2},j,k} + \mathbf{B}^{n+\frac{1}{2},R}_{i-\frac{1}{2},j,k}}{2}. \tag{3.39}$$

$\mathbf{B}^{n+\frac{1}{2},L}_{i-\frac{1}{2},j,k}$ has been calculated using equations (3.37) & (3.38) for cell (i,j,k), and $\mathbf{B}^{n+\frac{1}{2},R}_{i-\frac{1}{2},j,k}$ from cell $(i-1,j,k)$.

We now interpolate $\mathbf{J}$ on cell edges. For this, we also need the magnetic field at the two ends of the edges, that we interpolate from $\mathbf{B}^{\text{pred}}$. On the edge located at $(i-\frac{1}{2},j-\frac{1}{2},k)$, this yields

$$\mathbf{B}^{\text{int}}_{i-\frac{1}{2},j-\frac{1}{2},k+\frac{1}{2}} = \frac{\mathbf{B}^{\text{pred}}_{i-\frac{1}{2},j-1,k} + \mathbf{B}^{\text{pred}}_{i-\frac{1}{2},j-1,k+1} + \mathbf{B}^{\text{pred}}_{i-\frac{1}{2},j,k+1} + \mathbf{B}^{\text{pred}}_{i-\frac{1}{2},j,k}}{4}. \tag{3.40}$$

$$\mathbf{B}^{\text{int}}_{i-\frac{1}{2},j-\frac{1}{2},k-\frac{1}{2}} = \frac{\mathbf{B}^{\text{pred}}_{i-\frac{1}{2},j-1,k-1} + \mathbf{B}^{\text{pred}}_{i-\frac{1}{2},j-1,k} + \mathbf{B}^{\text{pred}}_{i-\frac{1}{2},j,k} + \mathbf{B}^{\text{pred}}_{i-\frac{1}{2},j,k-1}}{4}. \tag{3.41}$$

Figure 3.9 depicts the magnetic fields used in the calculation of $\mathbf{J}$ on edge $(i-\frac{1}{2},j-\frac{1}{2},k)$. The faces represented are situated at $x=(i-\frac{1}{2})$ (see left picture).

We then compute $\mathbf{J}$ as $\nabla \times \mathbf{B}$

$$J_{x,i-\frac{1}{2},j-\frac{1}{2},k} = \frac{B^{\text{pred}}_{z,i-\frac{1}{2},j,k} - B^{\text{pred}}_{z,i-\frac{1}{2},j-1,k}}{dy} - \frac{B^{\text{int}}_{y,i-\frac{1}{2},j-\frac{1}{2},k+\frac{1}{2}} - B^{\text{int}}_{z,i-\frac{1}{2},j-\frac{1}{2},k-\frac{1}{2}}}{dz}, \tag{3.42}$$

$$J_{y,i-\frac{1}{2},j-\frac{1}{2},k} = \frac{B^{\text{int}}_{x,i-\frac{1}{2},j-\frac{1}{2},k+\frac{1}{2}} - B^{\text{int}}_{x,i-\frac{1}{2},j-\frac{1}{2},k-\frac{1}{2}}}{dz} - \frac{B^{\text{pred}}_{z,i,j-\frac{1}{2},k} - B^{\text{pred}}_{z,i-1,j-\frac{1}{2},k}}{dx}, \tag{3.43}$$

$$J_{z,i-\frac{1}{2},j-\frac{1}{2},k} = \frac{B^{\text{pred}}_{y,i,j-\frac{1}{2},k} - B^{\text{pred}}_{y,i-1,j-\frac{1}{2},k}}{dx} - \frac{B^{\text{pred}}_{x,i-\frac{1}{2},j,k} - B^{\text{pred}}_{x,i-\frac{1}{2},j-1,k}}{dy}. \tag{3.44}$$

The Hall resistivity η_{H} depends on the density, temperature, CR ionisation rate and magnetic field. These quantities are interpolated on cell edges from the cell-centered predicted states. For any of these variables A, we compute

$$\overline{A}_{i-\frac{1}{2},j-\frac{1}{2},k} = \frac{1}{4}\left(A^{n+\frac{1}{2}}_{i,j,k} + A^{n+\frac{1}{2}}_{i-1,j,k} + A^{n+\frac{1}{2}}_{i-1,j-1,k} + A^{n+\frac{1}{2}}_{i,j-1,k}\right). \tag{3.45}$$

Finally, the Hall speed is

$$\mathbf{u}_{\text{H},i-\frac{1}{2},j-\frac{1}{2},k} = -\frac{\eta_{\text{H}}(\overline{\rho},\overline{T},\overline{\zeta},\overline{B})}{\overline{B}}\mathbf{J}, \tag{3.46}$$

with every quantity calculated at $(i-\frac{1}{2},j-\frac{1}{2},k)$.

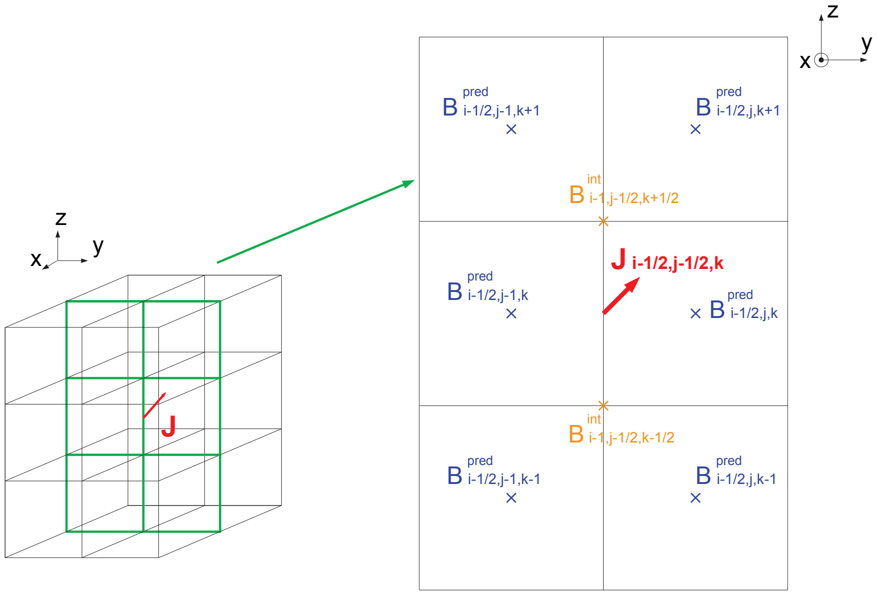

Figure 3.9: Magnetic fields used to calculate **J** on edge $(i-\frac{1}{2}, j-\frac{1}{2}, k)$. The right picture represents the cell faces at $(i-\frac{1}{2})$, as highlighted on the 12 cells block $(i-1..i, j-1..j, k-1..k+1)$ on the left (the front right middle cell is cell (i, j, k)).

3.2.3 The conservative update

The constrained transport method (Evans & Hawley 1988) is used to update the magnetic field. We then incorporate the Hall speed to the calculation of the electromotive forces, and then solve the 2D Riemann problem as in section 3.1.6. The notations are the same as figure 3.7. The blue area represents the corner states of the four cells at $(i-\frac{1}{2}, j-\frac{1}{2}, k)$, as calculated in equations (3.47) to (3.58), and the red label is the emf computed in equation (3.59).

The flow variables are extrapolated on edges from the predicted states at cell centers using the TVD slopes. Similarly to the magnetic field on cell faces, this process yields four different states at each corner

$$U^{n+\frac{1}{2},LB}_{i-\frac{1}{2},j-\frac{1}{2},k} = U^{n+\frac{1}{2}}_{i,j,k} - \frac{\Delta_x(U)_{i,j,k}}{2} - \frac{\Delta_y(U)_{i,j,k}}{2}, \tag{3.47}$$

$$U^{n+\frac{1}{2},RB}_{i-\frac{1}{2},j-\frac{1}{2},k} = U^{n+\frac{1}{2}}_{i-1,j,k} + \frac{\Delta_x(U)_{i-1,j,k}}{2} - \frac{\Delta_y(U)_{i-1,j,k}}{2}, \tag{3.48}$$

$$U^{n+\frac{1}{2},LT}_{i-\frac{1}{2},j-\frac{1}{2},k} = U^{n+\frac{1}{2}}_{i,j-1,k} - \frac{\Delta_x(U)_{i,j-1,k}}{2} + \frac{\Delta_y(U)_{i,j-1,k}}{2}, \tag{3.49}$$

$$U^{n+\frac{1}{2},RT}_{i-\frac{1}{2},j-\frac{1}{2},k} = U^{n+\frac{1}{2}}_{i-1,j-1,k} + \frac{\Delta_x(U)_{i-1,j-1,k}}{2} + \frac{\Delta_y(U)_{i-1,j-1,k}}{2}, \tag{3.50}$$

for any flow variable U, except the magnetic field that is averaged on the interfaces

$$\begin{aligned} B^{n+\frac{1}{2},B}_{x,i-\frac{1}{2},j-\frac{1}{2},k} &= \frac{B^{n+\frac{1}{2},LB}_{x,i-\frac{1}{2},j-\frac{1}{2},k} + B^{n+\frac{1}{2},RB}_{x,i-\frac{1}{2},j-\frac{1}{2},k}}{2} \\ &= \frac{\left[B^{n+\frac{1}{2},L}_{x,i-\frac{1}{2},j,k} - \frac{\Delta_y(B_x)_{i,j,k}}{2}\right] + \left[B^{n+\frac{1}{2},R}_{x,i-\frac{1}{2},j,k} - \frac{\Delta_y(B_x)_{i-1,j,k}}{2}\right]}{2}, \end{aligned} \tag{3.51}$$

$$B^{n+\frac{1}{2},T}_{x,i-\frac{1}{2},j-\frac{1}{2},k} = \frac{B^{n+\frac{1}{2},LT}_{x,i-\frac{1}{2},j-\frac{1}{2},k} + B^{n+\frac{1}{2},RT}_{x,i-\frac{1}{2},j-\frac{1}{2},k}}{2}$$
$$= \frac{\left[B^{n+\frac{1}{2},L}_{x,i-\frac{1}{2},j-1,k} + \frac{\Delta_y(B_x)_{i,j-1,k}}{2}\right] + \left[B^{n+\frac{1}{2},R}_{x,i-\frac{1}{2},j-1,k} + \frac{\Delta_y(B_x)_{i-1,j-1,k}}{2}\right]}{2}, \tag{3.52}$$

$$B^{n+\frac{1}{2},L}_{y,i-\frac{1}{2},j-\frac{1}{2},k} = \frac{B^{n+\frac{1}{2},LB}_{y,i-\frac{1}{2},j-\frac{1}{2},k} + B^{n+\frac{1}{2},LT}_{y,i-\frac{1}{2},j-\frac{1}{2},k}}{2}$$
$$= \frac{\left[B^{n+\frac{1}{2},B}_{y,i,j-\frac{1}{2},k} - \frac{\Delta_x(B_y)_{i,j,k}}{2}\right] + \left[B^{n+\frac{1}{2},T}_{y,i,j-\frac{1}{2},k} - \frac{\Delta_x(B_y)_{i,j-1,k}}{2}\right]}{2}, \tag{3.53}$$

$$B^{n+\frac{1}{2},R}_{y,i-\frac{1}{2},j-\frac{1}{2},k} = \frac{B^{n+\frac{1}{2},RB}_{y,i-\frac{1}{2},j-\frac{1}{2},k} + B^{n+\frac{1}{2},RT}_{y,i-\frac{1}{2},j-\frac{1}{2},k}}{2}$$
$$= \frac{\left[B^{n+\frac{1}{2},B}_{y,i-1,j-\frac{1}{2},k} + \frac{\Delta_x(B_y)_{i-1,j,k}}{2}\right] + \left[B^{n+\frac{1}{2},T}_{y,i-1,j-\frac{1}{2},k} + \frac{\Delta_x(B_y)_{i-1,j-1,k}}{2}\right]}{2}. \tag{3.54}$$

We now write these quantities B_x^B, B_x^T, B_y^L and B_y^R. The emfs are then computed at each corner-state, with the addition of the Hall speed (3.46), that is common for the four states, so that $\mathbf{E} = (\mathbf{u} + \mathbf{u}_\mathrm{H}) \times \mathbf{B}$. On the $(i-\frac{1}{2}, j-\frac{1}{2}, k)$ edge, we need the $z-$component

$$E_z^{n+\frac{1}{2},LB} = (u_x^{n+\frac{1}{2},LB} + u_{\mathrm{H},x})B_y^L - (u_y^{n+\frac{1}{2},LB} + u_{\mathrm{H},y})B_x^B, \tag{3.55}$$
$$E_z^{n+\frac{1}{2},LT} = (u_x^{n+\frac{1}{2},LT} + u_{\mathrm{H},x})B_y^L - (u_y^{n+\frac{1}{2},LT} + u_{\mathrm{H},y})B_x^T, \tag{3.56}$$
$$E_z^{n+\frac{1}{2},RB} = (u_x^{n+\frac{1}{2},RB} + u_{\mathrm{H},x})B_y^R - (u_y^{n+\frac{1}{2},RB} + u_{\mathrm{H},y})B_x^B, \tag{3.57}$$
$$E_z^{n+\frac{1}{2},RT} = (u_x^{n+\frac{1}{2},RT} + u_{\mathrm{H},x})B_y^R - (u_y^{n+\frac{1}{2},RT} + u_{\mathrm{H},y})B_x^T. \tag{3.58}$$

The resulting emf on the edge is obtained by solving the Riemann problem. In this case, the HLL flux has the same expression as (3.26)

$$E_z^{n+\frac{1}{2}} = \frac{S_L S_B E_z^{n+\frac{1}{2},LB} - S_L S_T E_z^{n+\frac{1}{2},LT} - S_R S_B E_z^{n+\frac{1}{2},RB} + S_R S_T E_z^{n+\frac{1}{2},RT}}{(S_R - S_L)(S_T - S_B)}$$
$$- \frac{S_T S_B}{S_T - S_B}(B_x^T - B_x^B) + \frac{S_R S_L}{S_R - S_L}(B_y^R - B_y^L), \tag{3.59}$$

where S_L, S_R, S_B and S_T are the slowest and fastest waves in the x and $y-$directions. Finally, the magnetic field is updated with the constrained transport method

$$\frac{B^{n+1}_{x,i-\frac{1}{2},j,k} - B^n_{x,i-\frac{1}{2},j,k}}{\Delta t} = \frac{E^{n+\frac{1}{2}}_{z,i-\frac{1}{2},j+\frac{1}{2},k} - E^{n+\frac{1}{2}}_{z,i-\frac{1}{2},j-\frac{1}{2},k}}{\Delta y} - \frac{E^{n+\frac{1}{2}}_{y,i-\frac{1}{2},j,k+\frac{1}{2}} - E^{n+\frac{1}{2}}_{y,i-\frac{1}{2},j,k-\frac{1}{2}}}{\Delta z}. \tag{3.60}$$

3.2.4 The CFL condition

In order to correctly propagate the perturbations caused by the Hall effect, the whistler waves need to be taken into account in the CFL condition. The speed of the whistler waves increases indefinitely as their wavelengths become small, but the Shannon-Nyquist theorem indicates that we cannot describe a wave having a wavelength smaller than twice our resolution. We use this limit to define the maximum allowed speed of whistler waves in our system. Using equation (1.89), we have

$$c_{\mathrm{w,max}} = \frac{\eta_{\mathrm{H}}\pi}{2\Delta x} + \sqrt{\left(\frac{\eta_{\mathrm{H}}\pi}{2\Delta x}\right)^2 + c_{\mathrm{A}}^2}, \tag{3.61}$$

where Δx is the smallest cell size in the simulation. At high resolution, we roughly have $c_{\mathrm{w}} \approx \frac{\eta_{\mathrm{H}}\pi}{\Delta x}$, and the corresponding time-step

$$dt_{\mathrm{Hall}} \approx \frac{\Delta x}{c_{\mathrm{w}}} \sim \Delta x^2. \tag{3.62}$$

The scaling of the time-step as Δx^2 is a dramatic limitation of current numerical simulation codes, because the fast diminution of the time-step with the resolution increases in the same extent the required processor time needed to run a simulation. Techniques that allow a faster integration such as Super Time-Stepping cannot be employed because a larger time-step would not satisfy the CFL condition and would cut-off the high-frequency whistler waves. At high resolution, these fast whistler waves are dominant in the calculation of the characteristic speeds of the Riemann problem. We then have $S_L = u_x - c_{\mathrm{w}}$, $S_R = u_x + c_{\mathrm{w}}$, $S_B = u_y - c_{\mathrm{w}}$ and $S_T = u_y + c_{\mathrm{w}}$.

3.2.5 Summary

The different steps of the Hall resolution are, in order

- Find the new time-step by taking into account the whistler speed (3.61)
- Compute the predicted states of the flow variables on cell faces (eq. (3.34) - (3.36)),
- Interpolate **B** on cell faces and corner with equations (3.37)-(3.41),
- Calculate the electric current **J** on edges with equations (3.42)-(3.44)),
- Average the flow variables on every edge with the corner-states to obtain the resistivity (eq. (3.45)),
- Calculate the Hall speed of the edges with the averaged quantities and the interpolated **J** (eq. (3.46)),
- Extrapolate the flow variables on cell corners (eq. (3.47)-(3.54)),
- Use the effective speed $\mathbf{u} + \mathbf{u}_{\mathrm{H}}$ instead of $\mathbf{u}$ to compute the HLL flux (eq. (3.55)-(3.58)),
- Solve the Riemann problem by considering the whistler waves in the calculation of S_L, S_R, S_B, and S_T, to get the electric fields $E^{n+1/2}$ with equation (3.59),
- Update the flow variable with the constrained transport scheme (3.60).

3.2.6 The cyclotron frequency limitations

Despite the dispersive nature of Hall effect, not all whistler waves are able to propagate in a real medium, because they are cut-off by the cyclotron frequency (Srinivasan & Shumlak 2011). The highest frequency of a whistler wave allowed in our system is given by the maximum resolution

$$\omega_{\max} \approx \frac{\eta_{\mathrm{H}}(2\pi)^2}{\Delta x^2}. \tag{3.63}$$

For a typical resolution of $\Delta x = 1$ au $= 1.5 \times 10^{13}$ cm, and a maximum resistivity $\eta_{\mathrm{H}} = 10 \times \frac{c^2}{4\pi}$ cm^2 s^{-1}, we obtain $\omega_{\max} \approx 1.3 \times 10^{-4}$ s^{-1}. The cyclotron frequency is defined as

$$\omega_{\mathrm{c}} = \frac{qB}{m}. \tag{3.64}$$

If we consider that the heaviest charge carrier is a 1 μm grain, with a bulk density of 2.3 g cm^{-3}, carrying one electric charge in a magnetic field of $B = 0.1$ G, we have $\omega_{\mathrm{c}} \approx 5$ s^{-1}. At the moment, we therefore do not need to take the cyclotron frequency into account in the propagation of the whistler waves, since their frequencies are several orders of magnitude lower.

3.3 Tests

In the following section, we test our implementation of the Hall effect, especially the propagation of the whistler waves.

The complete set of equations to solve is

$$\frac{\partial \rho}{\partial t} + \nabla \cdot [\rho \mathbf{u}] = 0, \tag{3.65}$$

$$\frac{\partial \rho \mathbf{u}}{\partial t} + \nabla \cdot \left[\rho \mathbf{u}\mathbf{u} + \left(P + \frac{B^2}{2}\right)\mathbb{I} - \mathbf{B}\mathbf{B}\right] = 0, \tag{3.66}$$

$$\frac{\partial \mathbf{B}}{\partial t} - \nabla \times (\mathbf{u} \times \mathbf{B} + \mathbf{E}_{\mathrm{NIMHD}}) = 0, \tag{3.67}$$

$$\frac{\partial E_{\mathrm{tot}}}{\partial t} + \nabla \cdot [(E_{\mathrm{tot}} + P_{\mathrm{tot}})\mathbf{u} - (\mathbf{u} \cdot \mathbf{B})\mathbf{B} - \mathbf{E}_{\mathrm{NIMHD}} \times \mathbf{B}] = 0. \tag{3.68}$$

$$\tag{3.69}$$

Except in the shock test, $\mathbf{E}_{\mathrm{NIMHD}}$ is always reduced to the Hall effect.

3.3.1 Dispersion relation test

We followed the test described in Kunz & Lesur (2013) to determine the accuracy of our implementation with the scheme previously described. The goal is to retrieve the dispersion relation (1.88) of whistler waves. In a box with a constant density and pressure, we set a whistler wave with a wave number k and study its propagation in the x-direction

$$\rho = 1 \text{ g cm}^{-3}, \qquad Bx = 0.1 \text{ G},$$
$$P = 1.5 \times 10^{-5} \text{ dyne cm}^{-2}, \qquad By = 10^{-3}\cos(2\pi k x) \text{ G},$$
$$\gamma = \frac{5}{3}, \qquad Bz = 0 \text{ G}.$$
$$\mathbf{u} = 0 \text{ cm s}^{-1},$$

The length of the simulation box is 1 cm, and we impose periodic boundary conditions, which forces k to be an integer to enforce continuity. We typically set its value between 5 and 20. η_{H} is constant and we adopt values from 5×10^{-4} to 0.1 cm^2 s^{-1} for our test. The slope limiter is moncen for now, with a resolution of 1/128 cm, but these points are discussed next section.

Two whistler waves propagate, with frequencies satisfying the dispersion relation 1.88 for the associated wave number k. The fluid is set into motion at the same frequencies (see figure 3.10). The Fourier transform of the temporal evolution of the magnetic field in the y direction contains two peaks corresponding to the frequencies at which the wave propagate. In figure 3.11, we clearly see the two peaks around $\omega \approx 2$ s^{-1} and $\omega \approx 0.3$ s^{-1}. The results are displayed in figure 3.12, where we have plotted the wave frequency normalized by the Hall frequency $\omega_{\mathrm{H}} = \frac{c_{\mathrm{A}}^2}{\eta_{\mathrm{H}}}$ as a function of kl_{H}, with $l_{\mathrm{H}} = \frac{\eta_{\mathrm{H}}}{c_{\mathrm{A}}}$ the Hall length. The agreement between our results and the theoretical dispersion relation is very good. We however could not extract good approximations of the low frequency waves at high kl_{H} because of the fast dissipation of the signal (see next section).

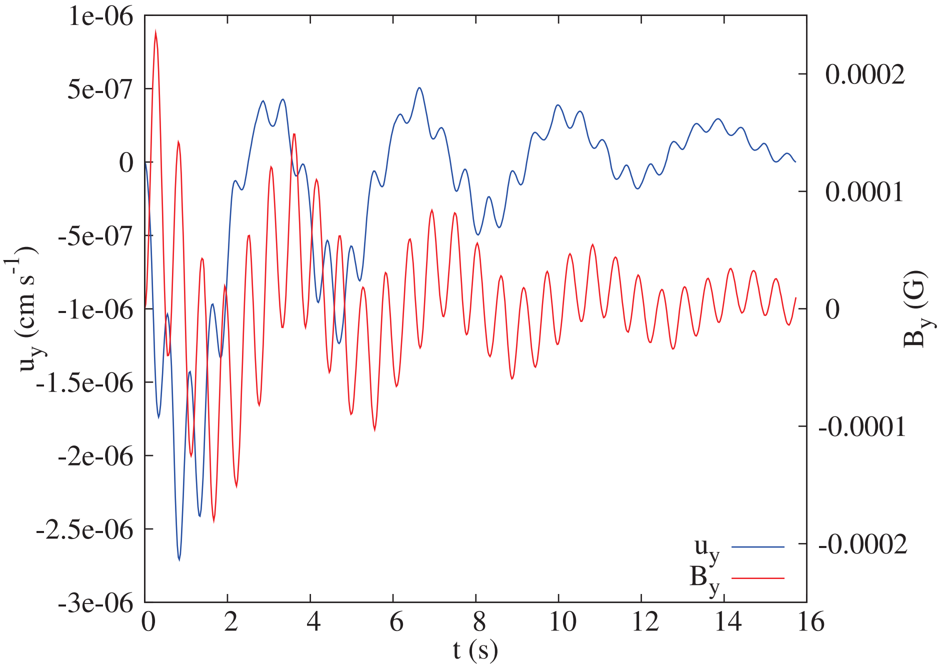

Figure 3.10: Typical evolution of u_y (in blue) and B_y (in red) through time for a random cell in the box (here $x = 0.378906265 = 48.5/128,\ y = 0.00390625 = 0.5/128,\ z = 0.49609375 = 63.5/128$). $k = 7$ cm^{-1}, $\eta_{\rm H} = 5 \times 10^{-3}$ cm^2 s^{-1}.

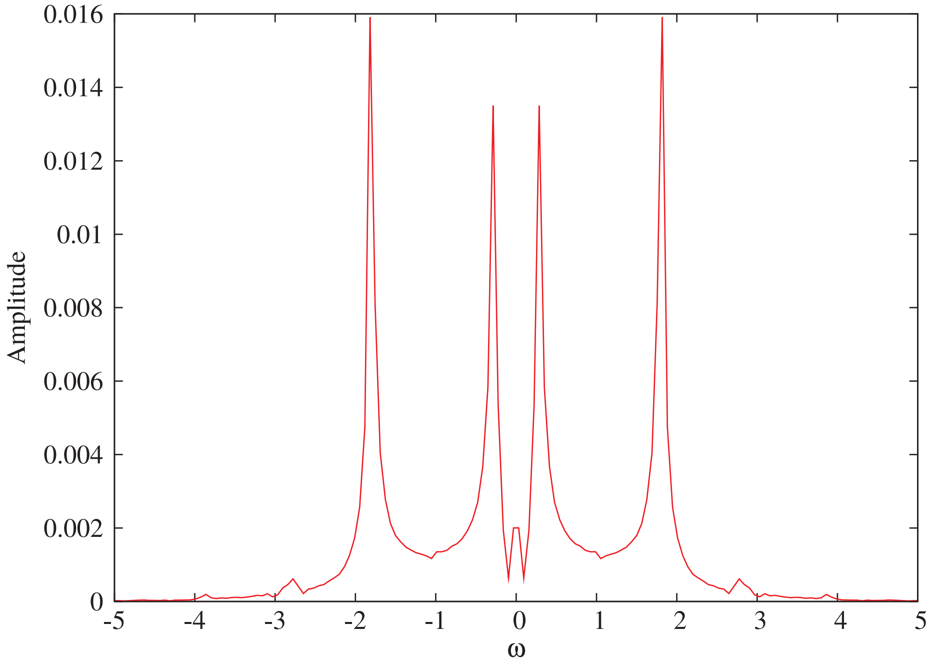

Figure 3.11: Fourier transform of $B_y(t)$ for a random cell in the box (here $x = 0.378906265 = 48.5/128,\ y = 0.00390625 = 0.5/128,\ z = 0.49609375 = 63.5/128$). $k = 7$ cm^{-1}, $\eta_{\rm H} = 5 \times 10^{-3}$ cm^2 s^{-1}.

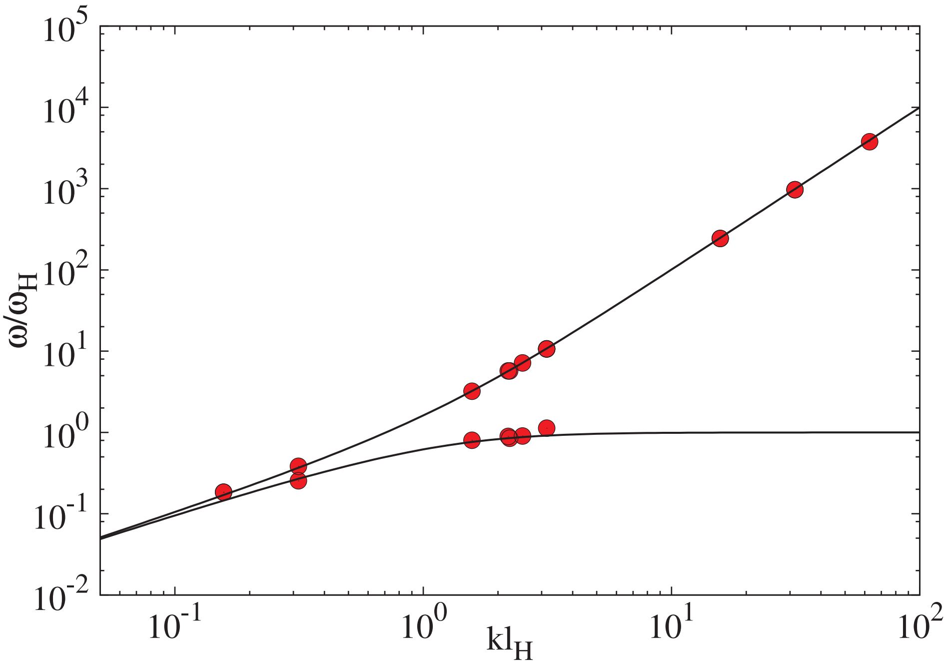

Figure 3.12: Correspondence between the theoretical dispersion relation of the whistler waves (solid line), and the main oscillation frequencies of the magnetic field (circles).

3.3.2 Numerical dissipation and order of the scheme

The numerical error made when we approximate the equations on finite resolution systems creates a dissipation. For instance, this means that in the case of the Hall effect, the whistler waves dissipate continuously as they propagate through the system. For a numerical scheme to be viable, this error/dissipation should decrease when the resolution increase.

Figure 3.13 represents the temporal evolution of the transverse magnetic field B_y at a random location in the simulation box (here $x = y = 32.5/128$, $z = 63.5/128$), for $k = 10$ and $k = 8$ cm^{-1} with $\eta_H = 0.005$ cm^2 s^{-1}. Beside its expected sinusoidal variation, the field is also damped over time. This damping is the numerical dissipation due to the finite resolution of the grid. The transverse magnetic field can then be estimated as

$$B_y(t) = f(t)e^{-at}, \tag{3.70}$$

where $f(t)$ is the periodic contribution and e^{-at} the damping, with a the damping coefficient in s^{-1}. In order to propagate the whistler waves in the best possible way, this coefficient needs to be as low as possible. To achieve this, we want to make sure our scheme is at the highest possible order in space, meaning that $a \propto \Delta x^n$, with n the order of the scheme. The higher is n, the more efficiently the dissipation decreases with the resolution. We can control the order of the convergence by choosing the slope limiter. We performed the same simulations than the previous section, with $k = 5$ cm^{-1}, $\eta_H = 0.005$ cm^2 s^{-1}, and with the slope limiters *minmod*, *moncen*, *Van Leer* ($\beta = 1.5$) and 3D unsplit, for resolutions of $\Delta x = \frac{1}{32}$, $\frac{1}{64}$ and $\frac{1}{128}$ cm. The resulting damping rates a are summarized in Table 3.1 and Figure 3.14. Similarly to Tóth et al. (2008) and Lesur et al. (2014), we find that the *minmod* limiter is only first order, while the *moncen*, *Van Leer* and 3D unsplit limiters show second order accuracy.

A second order scheme as MUSCL appears to be necessary to treat the Hall effect. The characteristic whistler speed scales as $1/\Delta x$, which lowers the order of the scheme by one. The

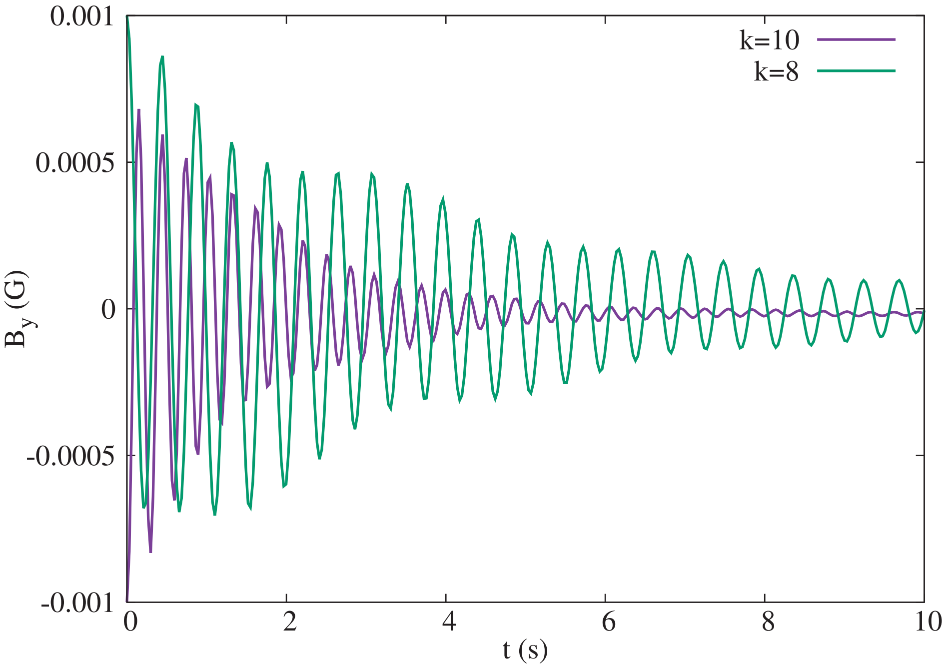

Figure 3.13: Magnetic field B_y in a random cell (here $x = 0.378906265 = 48.5/128$, $y = 0.00390625 = 0.5/128$, $z = 0.49609375 = 63.5/128$) as a function of time, for $k = 10$ cm^{-1} (purple line) and $k = 8$ cm^{-1} (green line).

Table 3.1: Numerical damping rate in s^{-1} as a function of the slope limiter and the resolution level.

Resolution Slope limiter	$\frac{1}{32}$ cm	$\frac{1}{64}$ cm	$\frac{1}{128}$ cm
No limiter	2.85	2.65	2.55
Minmod	1.3	0.5	0.26
Moncen	0.64	0.14	0.031
Van Leer	0.80	0.18	0.04
Unsplit 3D	0.64	0.14	0.031

test results show that without a TVD slope, the numerical dissipation does not decrease with the resolution, and the scheme is inconsistent.

Tóth et al. (2008) shows that for a second order slope limiter, the numerical dissipation scales as $\frac{\partial^4 U}{\partial x^4}$. It means that at a given number of points per l_{H} the damping rate increases as k^4. We evaluated the damping rate for $\eta_{\mathrm{H}} = 0.005$ cm^2 s^{-1} at a fixed resolution of $\Delta x = \frac{1}{128}$ cm and $k = 5,\ 7,\ 8,\ 10,\ 20$ cm^{-1}. We used the moncen slope limiter since it is second order. Figure 3.15 shows the very satisfying results alongside a scaling in k^4 for comparison. Such a behaviour indicates that smaller wavelengths are substantially more affected by the numerical dissipation than the larger ones.

3.3.3 Grid refinement

We examine here the behaviour of whistler waves on non-regular grids. The setup of previous tests is kept, but we refine the grid on specific locations. We take again $k = 5$ cm^{-1} and $\eta_{\mathrm{H}} = 0.005$ cm^2 s^{-1}, with the moncen slope limiter. The test is plan parallel as previously, with

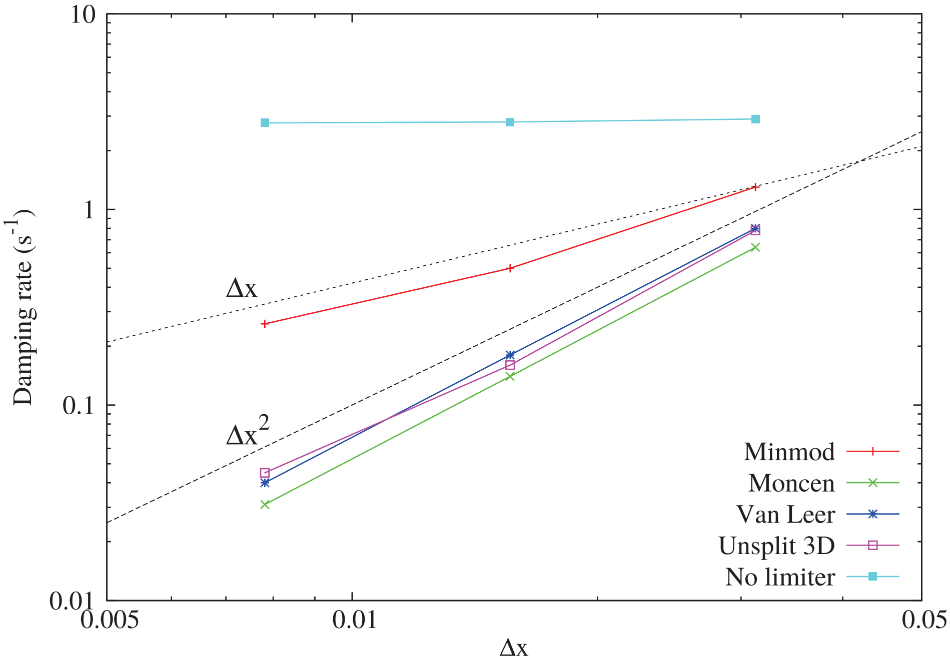

Figure 3.14: Numerical damping rates as a function of resolution for different slope limiters, and Δx and Δx^2 scalings for comparison.

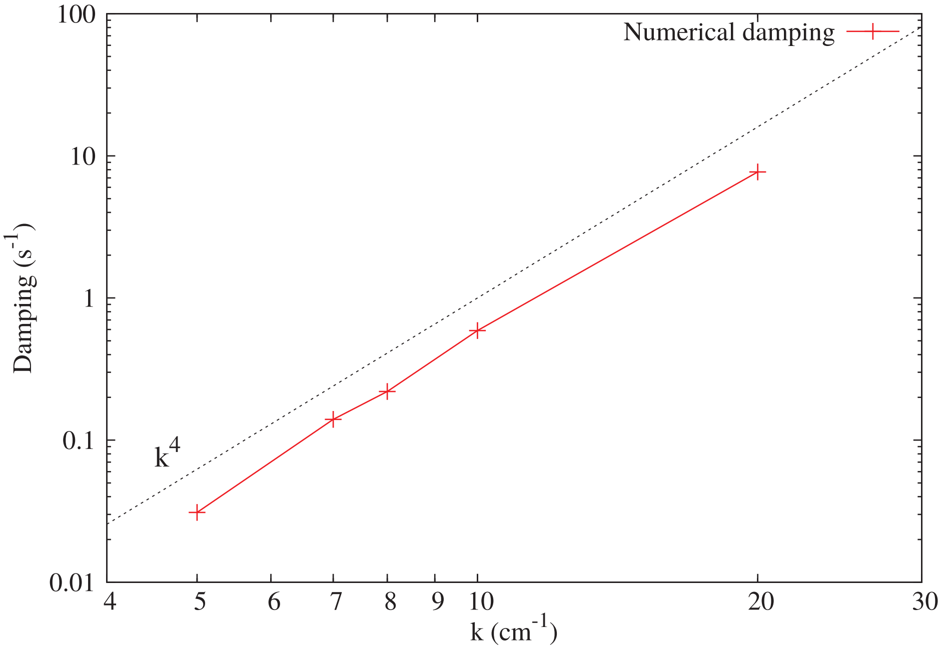

Figure 3.15: Numerical damping rates versus wave number k. Solid line: numerical results, dashed line: k^4 scaling.

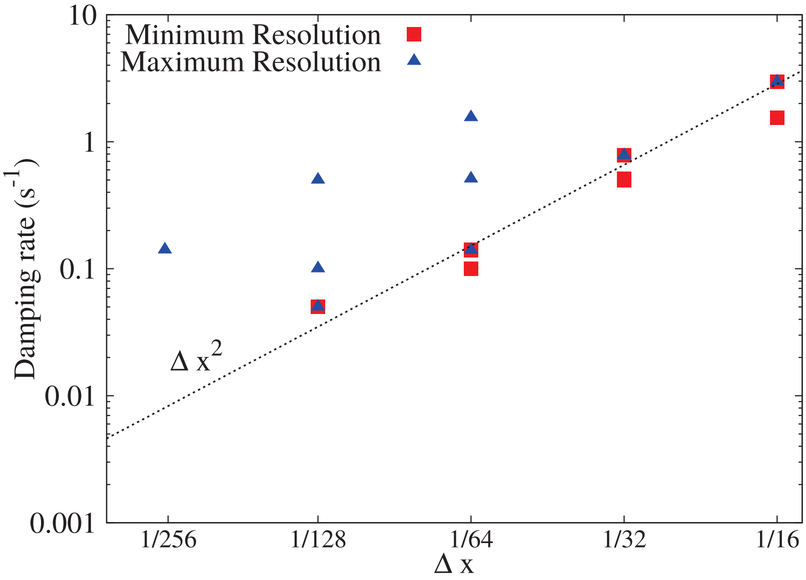

Figure 3.16: Damping coefficient of the whistler wave as a function of the maximum resolution (blue triangles) and minimum resolution (red squares) of the grid. The superimposed points are the regular grids, and the dashed lines represents the least-square fit in Δx^2 of the regular grids.

two or three different levels of refinement, with the maximum resolution in the center around $x = 0$ and gradually decreasing on each side. With two resolutions, the AMR level is $\ell = \ell_0$ for $-0.25 < x < 0.25$, and $\ell = \ell_0 - 1$ everywhere else $(-0.5 < x < 0.5)$. For three resolutions, it is $\ell = \ell_0$ in $-0.125 < x < 0.125$, $\ell = \ell_0 - 1$ in $-0.25 < x < 0.25$ and $\ell = \ell_0 - 2$ in the rest of the box. We choose $\ell_0 = 5, 6, 7$ for two AMR levels and $\ell_0 = 7, 8$ for three levels. The whistler wave propagates along the x-axis.

Figure 3.16 shows the damping rates of the whistler waves as a function of the maximum (blue triangles) and minimum (red squares) resolution for the five above-described runs and for regular grids with refinement levels from 4 to 7. The damping in regular grids follows the same Δx^2 scaling as in the previous test. However, non-regular grids produce a higher damping rate that does not always scale down with the maximum resolution. Instead, the damping rate seems only affected by the minimum resolution. While the AMR is an efficient tool to capture small scale phenomena at a relatively low cost, it does not seem adapted for the propagation of whistler waves, whose dissipation depends only on the smaller resolution they cross.

3.3.4 Shock test

Now that the precision and order of the scheme have been verified, we test the Hall effect in a more physical situation. We consider a unidimensional isothermal shock in a Hall-dominated regime in presence of Ohmic and ambipolar diffusion, as in Falle (2003) and Wurster et al. (2016). The sound speed and x-magnetic field are constant, with $c_{\rm s} = \sqrt{\frac{P}{\rho}} = 0.1$ cm s^{-1}, $B_x = 1$ G, and we use the resistivities $\eta_\Omega = 10^{-9}$, $\eta_{\rm H} = -2 \times 10^{-2} B$ and $\eta_{\rm AD} = 3.5 \times 10^{-3} \frac{B^2}{\rho}$ cm^2 s^{-1}.

The left and right states are defined by

$$\rho_{\mathrm{L}} = 1.7942 \text{ g cm}^{-3} \quad , \rho_{\mathrm{R}} = 1.0 \text{ g cm}^{-3}, \tag{3.71}$$

$$P_{\mathrm{L}} = 0.017942 \text{ dyn cm}^{-2} \quad , P_{\mathrm{R}} = 0.01 \text{ dyn cm}^{-2}, \tag{3.72}$$

$$u_{\mathrm{L}} = (-0.9759, -0.6561, 0.0) \text{ cm s}^{-1} \quad , u_{\mathrm{R}} = (-1.751, 0.0, 0.0) \text{ cm s}^{-1}, \tag{3.73}$$

$$B_{\mathrm{L}} = (1.0, 1.74885, 0.0) \text{ G} \quad , B_{\mathrm{R}} = (1.0, 0.6, 0.0) \text{ G}. \tag{3.74}$$

Initially, the left state spans $x \in [0;0.3]$ while the region $x \in]0.3;1]$ is in the right state. We put the discontinuity at $x = 0.3$ to let the fluid oscillate in the low density zone. The boundaries are periodic in the y and z-directions, and are fixed with the left and right states in the x-direction. The box has a 1 cm size. We use the AMR instead of a fixed resolution in order to gain computation time while keeping a good precision in the sensitive zones. The minimum resolution is 1/32 cm, and we refine the grid to keep the magnetic field variation lower than 5% in one cell, up to a resolution of 1/256 cm.

The initial discontinuity is progressively smoothed and converges towards a particular shape that is the steady-state profile of the shock.

We find the analytical profile of the shock by cancelling all derivatives except $\frac{\partial}{\partial x}$ in equations (3.65)-(3.68). This yields

$$\frac{d\rho u_x}{dx} = 0, \tag{3.75}$$

$$\frac{d}{dx}\begin{pmatrix} u_x B_y - u_y B_x \\ u_x B_z - u_z B_x \end{pmatrix} = \frac{d}{dx}\begin{pmatrix} \left[\eta_\Omega + \eta_{\mathrm{AD}}\left(1 - \frac{B_z^2}{B^2}\right)\right]\frac{dB_y}{dx} + \left[\eta_{\mathrm{H}}\frac{B_x}{B} + \eta_{\mathrm{AD}}\frac{B_y B_z}{B^2}\right]\frac{dB_z}{dx} \\ \left[-\eta_{\mathrm{H}}\frac{B_x}{B} + \eta_{\mathrm{AD}}\frac{B_y B_z}{B^2}\right]\frac{dB_y}{dx} + \left[\eta_\Omega + \eta_{\mathrm{AD}}\left(1 - \frac{B_y^2}{B^2}\right)\right]\frac{dB_z}{dx} \end{pmatrix}, \tag{3.76}$$

$$\frac{d((\rho u_x)u_x + \rho c_{\mathrm{s}}^2 + B^2/2)}{dx} = 0, \tag{3.77}$$

$$\frac{d((\rho u_x)u_y - B_x B_y)}{dx} = 0, \tag{3.78}$$

$$\frac{d((\rho u_x)u_z - B_x B_z)}{dx} = 0, \tag{3.79}$$

and $\frac{dB_x}{dx} = 0$ to satisfy the divergence-free condition. Integrating the equation (3.76) gives two coupled differential equations in B_y and B_z. Isolating the derivatives yields

$$\frac{\partial B_y}{dx} = \frac{M_1 R_{22} - M_2 R_{12}}{R_{11} R_{22} - R_{21} R_{12}}, \tag{3.80}$$

$$\frac{\partial B_z}{dx} = \frac{M_2 R_{11} - M_1 R_{21}}{R_{11} R_{22} - R_{21} R_{12}}, \tag{3.81}$$

with

$$M = \begin{pmatrix} u_x B_y - u_y B_x - u_{\mathrm{y},0} B_x + u_{\mathrm{x},0} B_{\mathrm{y},0} \\ u_x B_z - u_z B_x - u_{\mathrm{z},0} B_x + u_{\mathrm{x},0} B_{\mathrm{z},0} \end{pmatrix} \tag{3.82}$$

and

$$R = \begin{pmatrix} \eta_\Omega + \eta_{\mathrm{AD}}(1 - \frac{B_z^2}{B^2}) & \eta_{\mathrm{H}}\frac{B_x}{B} + \eta_{\mathrm{AD}} B_y B_z \\ -\eta_{\mathrm{H}}\frac{B_x}{B} + \eta_{\mathrm{AD}} B_y B_z & \eta_\Omega + \eta_{\mathrm{AD}}(1 - \frac{B_y^2}{B^2}). \end{pmatrix} \tag{3.83}$$

Equations (3.80) and (3.81) are integrated using a Runge-Kutta scheme. We then use the constant quantities $Q = \rho u_x$ and $K = Q u_{\mathrm{x},0} + \frac{Q}{u_{\mathrm{x},0}} c_{\mathrm{s}}^2 + \frac{B_0^2}{2}$ to compute the density and speed profiles

$$u_x = \frac{1}{2Q}\left(K - \frac{B^2}{2} - \sqrt{\left(K - \frac{B^2}{2}\right)^2 - 4Q^2c_\mathrm{s}^2}\right), \tag{3.84}$$

$$u_y = u_{\mathrm{y},0} + \frac{B_x(B_y - B_{\mathrm{y},0})}{Q}, \tag{3.85}$$

$$u_z = u_{\mathrm{z},0} + \frac{B_x(B_z - B_{\mathrm{z},0})}{Q}. \tag{3.86}$$

$$\rho = \frac{Q}{u_x} \tag{3.87}$$

Figure 3.17 displays both the numerical equilibrium state and the analytical solution of the above equations. The agreement between the two results is very good with a difference lower than 1% at shock interface. The larger error in outer regions is due to the low resolution. For comparison, figure 3.18 shows the shock profile for u_z and B_z (which have the larger errors) for a simulation box with a constant level of refinement of 6 (versus a level 5 of refinement in the boundary regions for the AMR case). It shows that the error near the boundaries becomes small at this resolution. Unfortunately, in perspective of the computational cost increasing with the resolution, one has to choose between minimizing the error in this region or accurately describe the shock profile.

3.4 Comparison to other codes

Our implementation of the Hall effect in `RAMSES` is adapted from Lesur et al. (2014). They modify the 1D Riemann solver of the eulerian code PLUTO (Mignone et al. 2007) while we have included the Hall effect into the constrained transport (2D) scheme, which has never been done. Both code use a second order evolution scheme (Runge-Kutta for PLUTO), and converge at the same order.

The approach is similar to Tóth et al. (2008) for the BASTRUS code (Tóth et al. 2006). They however implement the Hall effect explicitly in an implicit code. It comes with numerical difficulties concerning the calculation of the preconditionner, but since the implicit schemes are unconditionnally stables, they are not strictly bound to the whistler speed to choose their time-step. This emancipation results in a faster computation because larger time-steps are allowed. Moreover, the scheme order is increased by one since the whistler speed decreases it by the same amount. The drawback is a less precise approximation as the shortest whistler waves cannot be correctly propagated.

The Hall effect in the eulerian code ZeusTW (Stone & Norman 1992; Krasnopolsky et al. 2010) is implemented according to Sano & Stone (2002). The term $(\nabla \times \mathbf{B}) \times \mathbf{B}$ is evolved at $t^{n+1/2}$ using a finite difference scheme to evaluate the curls in an explicit way. The resulting emf is then added to the ideal emf $\mathbf{u} \times \mathbf{B}$ into a modified constrained transport method. The test in Sano & Stone (2002) show that the dispersion relation of the Hall effect is verified, but we have not found any information about the order of the scheme.

Lagragean codes cannot use the constrained transport method due to their nature. In the SPH code PHANTOM (Wurster et al. 2014; Price et al. 2017a), the three non-ideal MHD terms are implemented in the same manner as source terms. Their tests with the ambipolar diffusion show second order convergence, but no information is given on this subject concerning the Hall effect. They however recover the theoretical dispersion relation, and perform the shock-test described in section 3.3.4 with results fitting the expected profile within 3%.

Summary

We have successfully implemented the Hall effect in `RAMSES` with an original implementation. Our scheme, based on a modification of the HLL Riemann solver, propagates the whistler waves

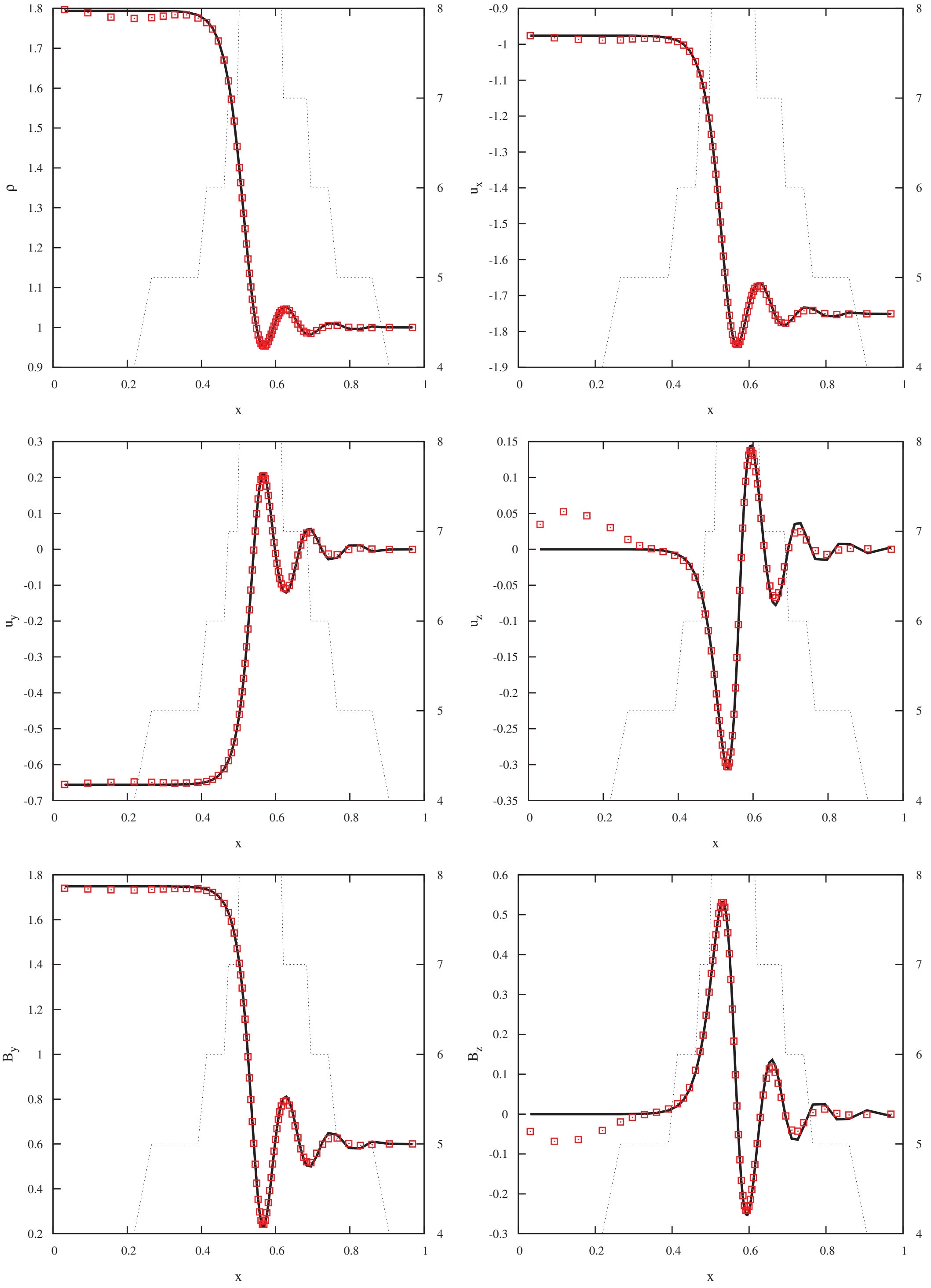

Figure 3.17: Comparison between the analytical solution of the standing shock (solid black line) and the numerical result (red squares). The AMR level is represented as the dashed black line. From top to bottom: ρ and u_x, u_y and u_z, B_y and B_z.

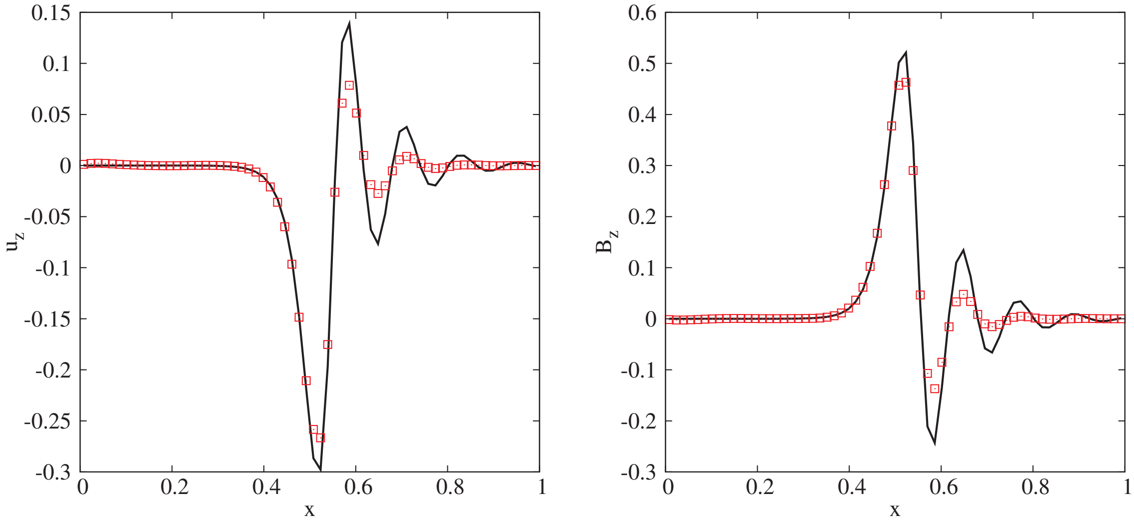

Figure 3.18: Same as figure 3.17 for the variables u_z (left panel) and B_z (right panel), and a constant level of refinement of 6.

at the frequencies predicted by the dispersion relation (1.88) and shows a second order accuracy in space. We also obtain very satisfying results on a 1D shock test with AMR and four levels of refinement. Comparing the precision of the scheme with other codes is complicated since the authors often show only one test without commenting on the order of convergence.

In the next chapter, we perform star formation simulations with the Hall effect to study its role in this context.

Chapter 4

The Hall effect in star formation

This chapter presents my results on core-collapse simulations with all non-ideal MHD effects. We first run a test case of a dense core without rotation, and analyze the Hall-induced rotation. We then study the impact of the Hall effect on a rotating cloud at various magnetic field strengths and orientations. The goal is to qualitatively retrieve and extent the results of Tsukamoto et al. (2015), Wurster et al. (2016), and to compare with the most recent work of Tsukamoto et al. (2017).

4.1 Model and initial conditions

We solve the full set of non-ideal MHD equations in conservative form, with gravity as a source term (as implemented in `RAMSES`)

$$\frac{\partial \rho}{\partial t} + \nabla \cdot [\rho \mathbf{u}] = 0, \tag{4.1}$$

$$\frac{\partial \rho \mathbf{u}}{\partial t} + \nabla \cdot \left[\rho \mathbf{u}\mathbf{u} + \left(P + \frac{B^2}{2}\right)\mathbb{I} - \mathbf{B}\mathbf{B}\right] = -\rho \nabla \Phi, \tag{4.2}$$

$$\frac{\partial E_{\mathrm{tot}}}{\partial t} + \nabla \cdot [(E_{\mathrm{tot}} + P_{\mathrm{tot}})\mathbf{u} - (\mathbf{u} \cdot \mathbf{B})\mathbf{B} - \mathbf{E}_{\mathrm{NIMHD}} \times \mathbf{B}] = -\rho \mathbf{u} \cdot \nabla \Phi, \tag{4.3}$$

$$\frac{\partial \mathbf{B}}{\partial t} - \nabla \times (\mathbf{u} \times \mathbf{B} + \mathbf{E}_{\mathrm{NIMHD}}) = 0, \tag{4.4}$$

$$\nabla \cdot \mathbf{B} = 0. \tag{4.5}$$

with

$$\mathbf{E}_{\mathrm{NIMHD}} = -\eta_{\Omega} \nabla \times \mathbf{J} - \eta_{\mathrm{H}}(\mathbf{J}) \times \mathbf{B} + \eta_{\mathrm{AD}} (\mathbf{J} \times \mathbf{B}) \times \mathbf{B}.$$

We are mainly interested in the impact of non-ideal MHD on the collapse. For this reason, we use a fitted equation of state (Vaytet et al. 2013) instead of radiative hydrodynamics, so as to speed up the calculations. The EOS mimics the evolution of the temperature with density in a star forming environment (see figure 1.1). The fluid is considered as a perfect gas.

Unless stated otherwise, we use `RAMSES` in 3D with the modified HLL solver described in previous chapter and the minmod slope limiter[1]. Our initial condition is a uniform sphere at 10 K defined by its mass and thermal to gravitational energy ratio

$$\alpha = \frac{5 R k_{\mathrm{B}} T}{2 G M \mu m_{\mathrm{H}}}, \tag{4.6}$$

which determines its radius and density. The sphere undergoes a solid rotation around an axis, which is characterized by the rotational on gravitational energy ratio

$$\beta = \frac{R^3 \Omega^2}{3 G M}. \tag{4.7}$$

---

[1] Due to issues with the ambipolar diffusion.

The matter lies in a medium at rest, also at 10 K with a density contrast of 100. This kind of setup has been proposed by Boss & Bodenheimer (1979) and is now a standard initial condition for protostellar collapses. Our refinement criterion imposes at least 8 points per Jeans length, for a minimum resolution at $\ell = 5$ (32^3). The simulation box has a length equal to four times the sphere radius, and we impose periodic boundary conditions.

We also perform simulations with turbulence because most dense cores are agitated with turbulent motions. Only the initial velocity field changes from the standard case. There is no global rotation (so $\beta = 0$), but random motions with a Kolmogorov power spectrum and random phases, with a Mach number of 1. Turbulence sets a random distribution of angular momentum that does not necessarily add up to 0 globally. For more details on the mathematics of the turbulence, refer to Levrier (2004).

We call the "formation of the first core" the time at witch the maximum density in the box reaches 10^{-13} g cm^{-3}. Finally, we use the criteria of Joos et al. (2012) to define the rotationally supported disks.

- $\rho > 3.8 \times 10^{-15}$g cm^{-3},
- $u_\theta > 2u_z$,
- $u_\theta > 2u_r$,
- $\frac{\rho u_\theta^2}{2} > 2\frac{P}{\gamma-1}$.

The second and third conditions ensure that the velocity is dominated by its azimuthal component (i.e. the fluid is rotating), and the last condition guarantees that the fluid is supported against gravity by its rotational rather than its thermal energy. In the presence of non-ideal MHD effects, the thermal pressure overcomes the magnetic pressure in the disk region (Masson et al. 2016), which is measured by the plasma beta $\beta_{\text{plasma}} = P_{\text{thermal}}/P_{\text{magnetic}}$.

4.2 Test case: a non-rotating cloud

4.2.1 Initial conditions and physical parameters

We first simulate a collapse without initial rotation as Krasnopolsky et al. (2011). We expect the cloud to start rotating due to the twisting of the magnetic field lines by the Hall effect as theorized in section 1.3.4.3.

Our initial condition is a sphere at rest of $M = 1.5$ M$_\odot$ with a radius of $R = 3700$ au, which yields a ratio $\alpha = 0.25$. The magnetic field is homogeneous in the whole box with $B_0 = B_z = 35.4$ μG, or $\mu \approx 7$. We neglect the ambipolar and Ohmic diffusions, so we solve the system (4.1)-(4.5) with $\eta_\Omega = \eta_{\text{AD}} = 0$. For this test case, the Hall resistivity does not follow our chemical table, and is set at a constant value $\eta_{\text{H}} = 10^{20}$ cm^2 s^{-1}. We use here the 3D unsplit slope limiter described in section 3.1.3.

4.2.2 Results

A differential rotation of the cloud starts along the initial magnetic field, with an increased intensity over time. Figure 4.1 shows the radial profile of azimuthal velocity u_θ in the plane $z = 0$ at the formation of the first core at $t_c = 29.266$ kyr, and at two later times. For comparison, we have also represented the Keplerian velocity, at which the rotational support is in equilibrium with the gravitational attraction. Using the second Newton law, the Keplerian velocity is calculated as

$$u_{\text{Kepler}}(\mathbf{r}) = \left[r \left(\sum_{\substack{i=1,\text{ncells} \\ \mathbf{r}_i \neq \mathbf{r}}} \frac{Gm_i}{\|\mathbf{r}_i - \mathbf{r}\|^3} (\mathbf{r}_i - \mathbf{r}) \right)_r \right]^{\frac{1}{2}} . \tag{4.8}$$

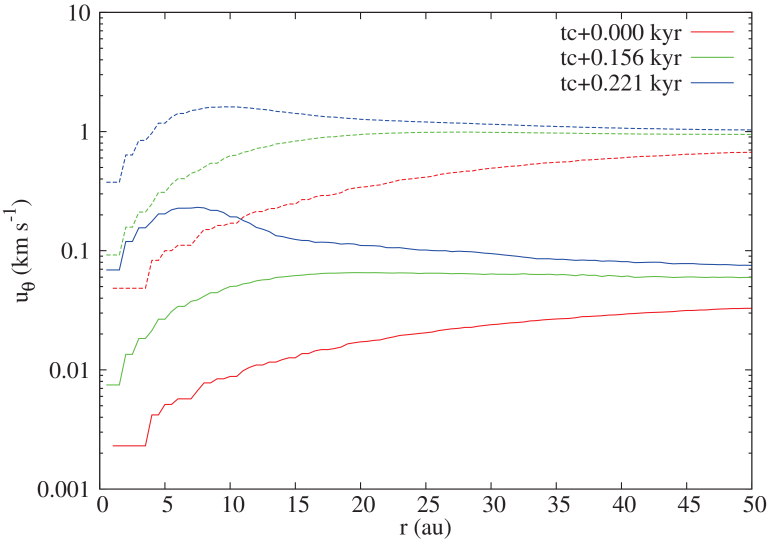

Figure 4.1: Azimuthal velocity profile (solid lines) in the plane $z = 0$ at three times, early after the formation of the first core. The dashed lines represent the Keplerian velocity.

for each cell in our discretized system (assuming the center of mass is at the origin). All radial profiles are azimuthally averaged. The fluid rotation velocity remains far below the Keplerian velocity at these early stages, with $u_\theta \approx 0.1 v_{\text{Kepler}}$.

The toroidal magnetic field that generates this rotation is strongest in the core, with $B_\theta \approx 3 \times 10^{-3}$G $\approx 0.7\mathbf{B}_z$. The relative twisting is however the strongest 200 au above and below the mid-plane, as seen in figure 4.2 which represents B_θ/B. A lot of angular momentum is created in the disk while the Alfvén waves transport its negative counter-part along the field lines. This negative angular momentum is transfered in the regions above and below the disk, thus setting a backward rotation in the fluid, as seen in the maps of azimuthal velocity of figure 4.3. The momentum of the core and disk are therefore compensated by the counter-rotation of an hourglass-shaped envelope of 1000 au in height and diameter. With a similar setup, Krasnopolsky et al. (2011) and Li et al. (2011) obtained the same kind of envelopes.

We then compare the azimuthal velocity u_θ of the fluid to the Hall speed and to the Keplerian velocity in figure 4.4 at later stages, 0.550 and 0.872 kyr after the first core formation[2]. The Hall speed is defined accordingly to section 1.3.4.3

$$\mathbf{u}_{\text{Hall}} = \eta_{\text{H}} \frac{\mathbf{J}}{\|\mathbf{B}\|}. \tag{4.9}$$

In the inner regions, the rotation speed is equal to the Keplerian velocity and superior to the Hall speed. The centrifugal force overcomes gravity, which results in a positive radial velocity of the fluid and the formation of a ring-shaped core. All the velocities drop outside the Larson core, beyond 30 au, and the fluid is roughly rotating at the Hall velocity, as seen in figure 4.5. The two value do not perfectly match but differ by less than 50%. In the absence of every other forces but the Lorentz force, the two velocities should correspond, but in this case, gravity and thermal pressure also influence these variables, preventing a perfect match. The coupling is effective up to $r \approx 160$ au, down to a density of $\rho \approx 10^{-14}$ g cm^{-3}. As predicted by theory, the region we could define as the pseudo-disk (as in section 1.3.3) is rotating at the Hall velocity.

The Hall effect then redistribute the angular momentum, but what about the magnetic flux ? Figure 4.6 shows the magnetic field as a function of density in the box for this simulation and its counter-part without the Hall effect, when they both reach a maximum density of $\rho =$

---

[2] Careful, contrarily to figure 4.1, this one is not in log scale.

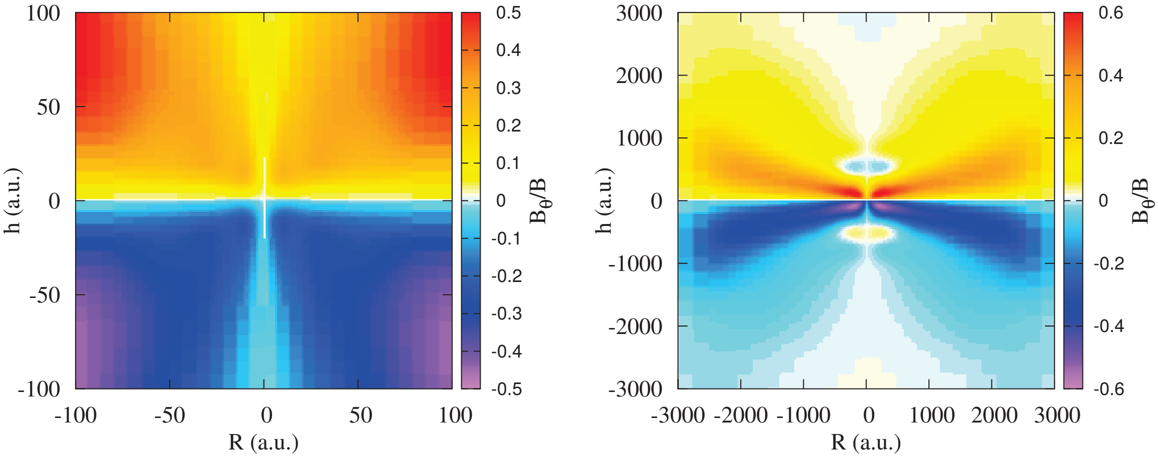

Figure 4.2: Toroidal magnetic field B_θ on the plane $x = 0$ at two different zooms, 0.221 kyr after the formation of the first core.

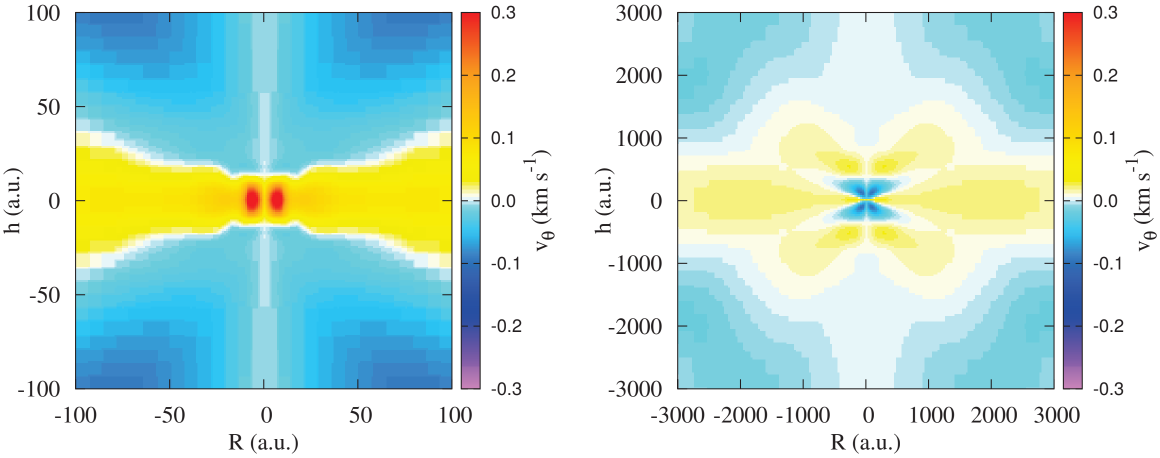

Figure 4.3: Azimuthal velocity map (in km s^{-1}) on the plane $x = 0$ at two different zooms, 0.221 kyr after the formation of the first core.

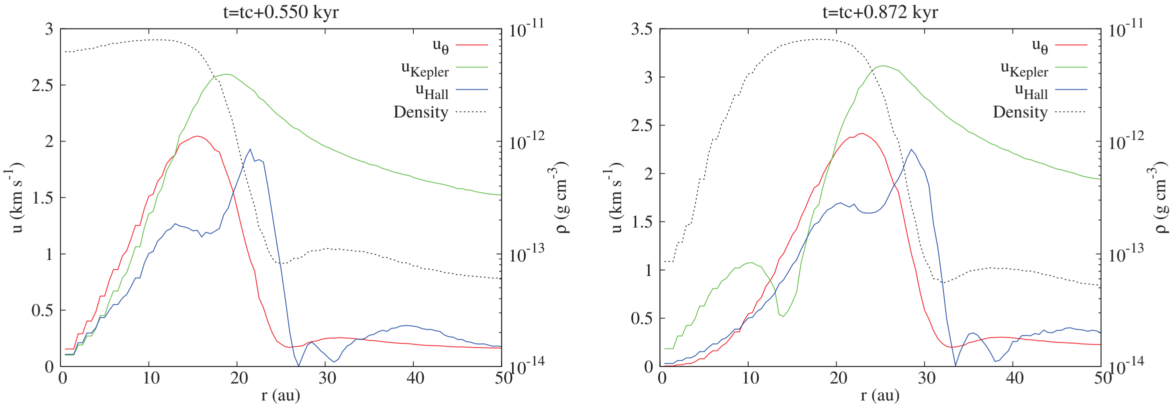

Figure 4.4: Radial profiles ($z = 0$, azimuthal averaging) of the azimuthal velocity (red curve), the Hall speed (blue curve) and the Keplerian velocity (green curve) at $t = t_\mathrm{c} + 0.550$ and $t = t_\mathrm{c} + 0.872$ kyr (left and right panel). The black dotted line represents the density profile (right axis).

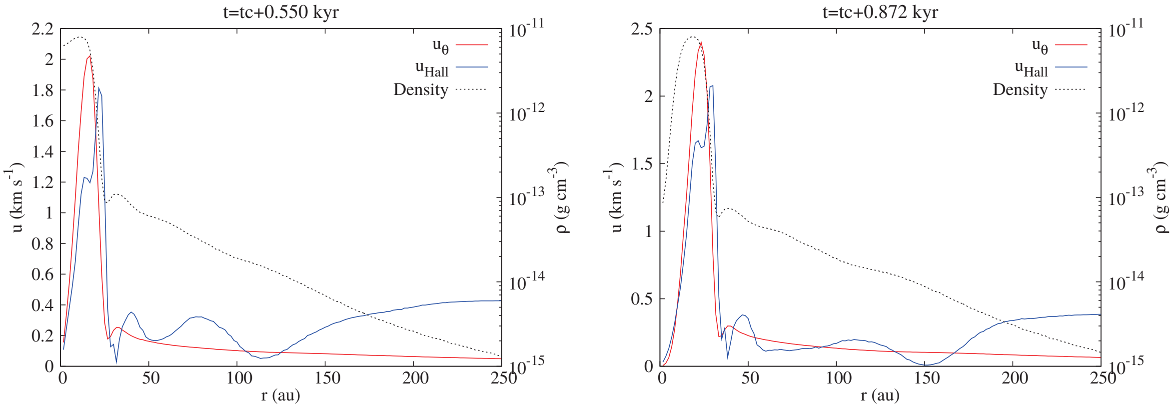

Figure 4.5: Same as figure 4.4, at larger radius and without the Keplerian velocity.

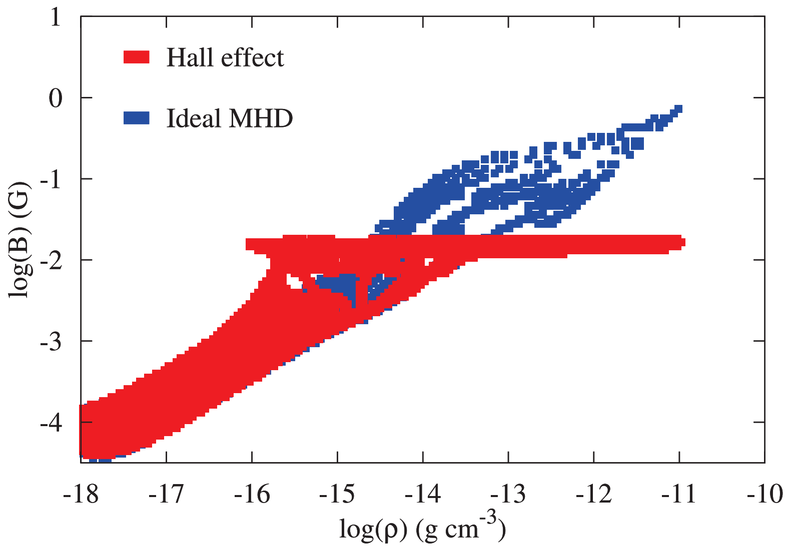

Figure 4.6: Magnetic field as a function of density for the simulation with and without Hall (red and blue domains respectively). The snapshot is taken when the maximum density reaches 10^{-10} g cm^{-3}.

10^{-11} g cm^{-3}. The magnetic field in ideal MHD already reaches 1 G, while it is bounded to 10^{-2} G with the Hall effect. On the contrary, the two magnetic fields are very similar at densities below 10^{-15}-10^{-14} g cm^{-3}, confirming that the Hall effect becomes relevant above these densities. Masson et al. (2016) found a comparable "plateau" using the ambipolar diffusion, which redistributes the flux and yields a similar profile for the magnetic field. Both effects then act to regulate the flux in the Larson core stage.

4.2.3 The angular momentum issue

We introduce here some notations useful to the following discussion. We note **L** the angular momentum vector

$$\mathbf{L} = \sum_{i=1,\mathrm{ncell}} m_i \mathbf{r}_i \times \mathbf{u}_i, \tag{4.10}$$

where m_i, $\mathbf{r}_i$ and $\mathbf{u}_i$ represent the mass, the position vector and the velocity vector of cell i. The system being nearly axisymmetric, the main component of this vector is L_z, that can also be calculated as

$$L_z = \sum_{i=1,\mathrm{ncell}} m_i r_{\mathrm{c},i} v_{\theta,i}, \tag{4.11}$$

with r_c the cylindrical radius and u_θ the azimuthal velocity. From this, we define the "positive" and "negative" momenta L_z^+ and L_z^- as follow

$$L_z^+ = \sum_{i,v_{\theta,i}>0} m_i r_{\mathrm{c},i} v_{\theta,i}, \tag{4.12}$$

$$L_z^- = \sum_{i,v_{\theta,i}<0} m_i r_{\mathrm{c},i} v_{\theta,i}. \tag{4.13}$$

$$\tag{4.14}$$

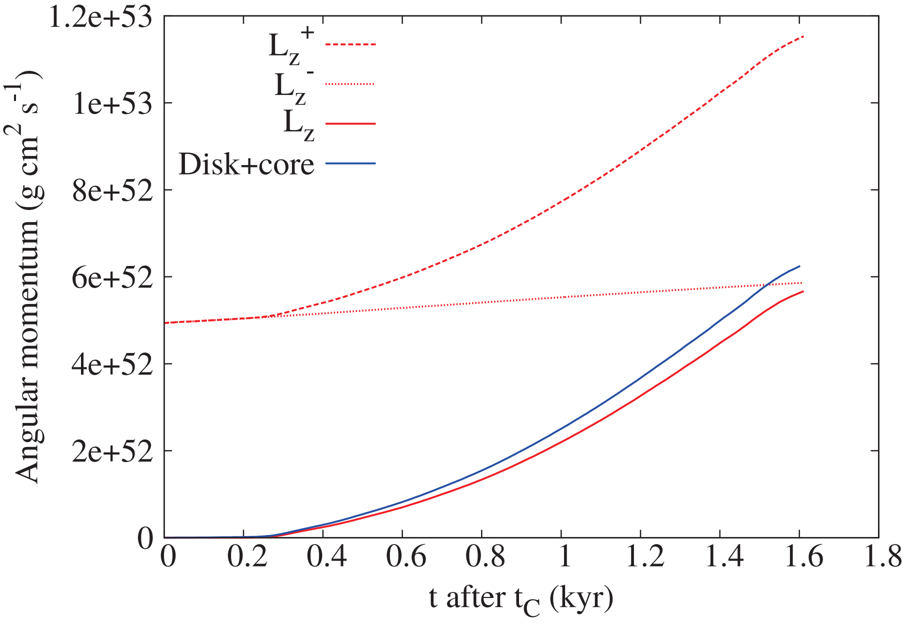

Figure 4.7: Positive L_z^+ and negative L_z^- angular momentum evolution after the formation of the first Larson core, in red dashed and dotted line respectively. The red solid line is the total angular momentum L_z, and the blue line is the angular momentum of the core+disk region.

We therefore have $L_z^+ + L_z^- = Lz \cong \|\mathbf{L}\|$.

There is initially no angular momentum in this system. L_z^+ thus represents the "positive" rotation created by the Hall effect, balanced by the "negative" rotation L_z^-, and we have $\|L_z^+\| \approx \|L_z^-\|$. L_z does not exactly equal 0 because of the finite precision of the numerical schemes, but this is not an issue if L_z remains small (typically, compared with L_z^+ and L_z^-). However, this condition breaks in our simulation.

In the left panel of figure 4.7, we have plotted the evolution of L_z^+ and L_z^- during the simulation after the formation of the first Larson core, as well as their sum L_z. From $t = t_c + 0.230$ kyr, the positive momentum skyrockets and doubles its value by $t = t_c + 1.600$ kyr, while the negative momentum increases by less than 15%. The total angular momentum L_z then increases as well and reaches the value of L_z^-. It is therefore not conserved in the simulation box.

Krasnopolsky et al. (2011) encoutered a non-conservation of angular momentum in their very similar simulation. They attribute this phenomenon to torsional Alfvén waves leaving the simulation box. It is however not the case here since the boundary conditions are periodic. The blue curve of figure 4.7 represents the angular momentum of the disk (as defined in 4.1) and the core ($\rho > 10^{-13}$ g cm^{-3}). This angular momentum shows the same evolution as the excess of angular momentum in the simulation box, with $L_z \approx 0.85 L_{\mathrm{core+disk}}$. This strongly suggests that the problem takes its origin in the central region. The same issue arises for outflow boundary conditions and other slope limiters as represented in figure 4.8.

From the Shannon theorem (Shannon 1949), we can state that at a given resolution Δx, only wavelengths larger than $2\Delta x$ can propagate. The AMR therefore poses a fundamental problem. Figure 4.9 represents a map of the size of the grid cells, in the plane $x = 0$, with isodensities in black contours. At the center of the simulation box, the cell size is 2 a.u. (level 13 of AMR), but the resolution drops by a factor 4 at a radius of 100 a.u. and a factor 32 at a radius of 500 a.u.. Let us consider a short whistler wave ($\lesssim$ 100 a.u.) generated at the center of the box and propagating outwards. By traveling a distance of merely a few times its wavelength, it enters a region in which it cannot be described, and is therefore dissipated. Only the waves with a wavelength larger than twice the minimum resolution ($\Delta x \approx$ 500 a.u.) can propagate in the

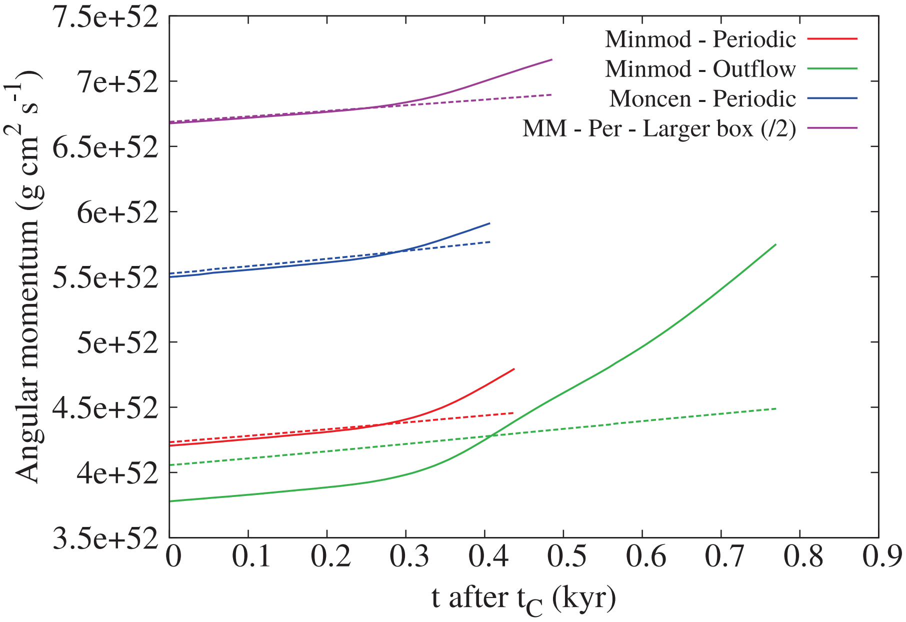

Figure 4.8: Positive L_z^+ (solid lines) and negative L_z^- (dashed lines) angular momentum evolution after the formation of the first Larson core for several simulation parameters. Red curves: minmod slope limiter, green curves: outflow boundary conditions, blue curves: moncen slope limiter, purple curves: simulation box length twice as large (the value of the angular momentum has been divided by two to the improve readability of the graph).

whole simulation box, which corresponds to $\lambda > 1000$ a.u., or a quarter of the dense core's initial radius. Additionally, the short wavelengths are dissipated much faster than the large ones (the damping rate scales as k^4, see figure 3.15) and the numerical dissipation scales with the lower resolution rather than the highest (see figure 3.16). The scenario is then the following. The Hall effect twists the field lines in the plane of the pseudo-disk which generates a rotation in the positive direction. The associated magnetic perturbations propagate outwards which creates rotation in the negative direction in further regions. However, these whistler waves are dissipated prematurely due to the three effects described before, which leads to a deficit of counter-rotation, hence increasing the total angular momentum.

This issue appears even in the presence of ambipolar and Ohmic diffusion. Figure 4.10 shows the evolution of the angular momentum of the same setup, with $\eta_\Omega = \eta_{\rm AD} = 10^{20}$ cm^2 s^{-1}. The right panel represents the temporal variation of each positive momentum. The divergence occurs ~ 400 years after the first Larson core formation, which is a short 100 years delay compared with the reference case. The increase of momentum also shows a sharper initial increase. While the two diffusive effects influence the dynamics of the collapse, their respective electric field, $\mathbf{E}_{\rm AD} \propto \eta_{\rm AD}(\mathbf{J}\times\mathbf{B})\times\mathbf{B}$ and $\mathbf{E}_\Omega \propto \eta_\Omega \mathbf{J}$ are both perpendicular to the Hall magnetic field $\mathbf{E} \propto \mathbf{J}\times\mathbf{B}$, so they do not counter-act the rotation of the field lines induced by the Hall effect. The ambipolar and Ohmic diffusion also dissipate the magnetic energy, which may be however be at the origin of the short delay. However, unless the Hall resistivity is several orders of magnitudes lower than the ambipolar and Ohmic resistivities, the two later effects do not seem to damp naturally the short whistler waves faster than the numerical scheme.

In the following simulations, we monitor the angular momentum to attest the validity of our results.

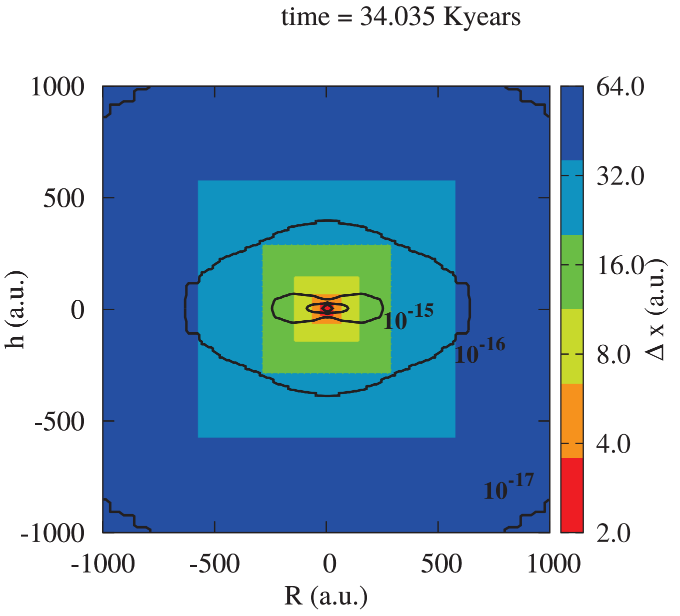

Figure 4.9: Mapping of cell sizes in the simulation (slice $x = 0$).

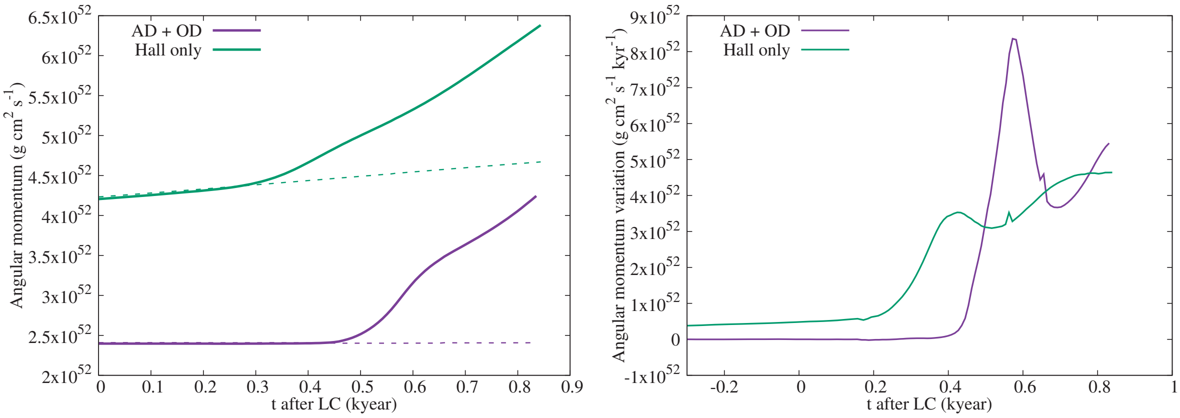

Figure 4.10: Left panel: Angular momentum evolution in the standard case (green curves) and with ambipolar and Ohmic diffusion (purple curves). Right panel: temporal variations of the positive angular momenta.

Table 4.1: Magnetic field strength and orientation used in the simulations.

μ	$\widehat{\mathbf{B},\mathbf{\Omega}}$	Name
4	0°	M4-00
4	40°	M4-40
4	90°	M4-90
4	140°	M4-140
4	180°	M4-180
4	Turbulence	M4TURB
2	0°	M2-00
2	40°	M2-40
2	90°	M2-90
2	140°	M2-140
2	180°	M2-180
2	Turbulence	M2TURB

4.3 Influence of the magnetisation

We now study the impact of the Hall effect on star formation in more realistic situations. The Hall effect modifies the magnetic braking, and we show in what extent in two sets of simulations, at two different magnetisations. From this point, the abundance table is used to compute all the non-ideal MHD resistivities.

4.3.1 Simulation setup

Our initial sphere has a radius of 2650 au for a total mass of 1 $M_\odot$. The thermal and rotational energy ratios are respectively $\alpha = 0.27$ and $\beta = 0.011$, which yields a density of $\rho = 7.62 \times 10^{-18}$ g cm^{-3} and an angular velocity of 2.65×10^{-13} rad s^{-1}. The magnetic field is uniform in the whole box along the z-direction. Its strength, defined by the mass-to-flux ratio, and the angle it forms with the rotation axis $\mathbf{\Omega}$ are the varying parameters and are summarized in table 4.1. The angle is in the $x-z$ plane, so that $\mathbf{\Omega} = \Omega \sin(\widehat{\mathbf{B},\mathbf{\Omega}})\mathbf{e_x} + \Omega \cos(\widehat{\mathbf{B},\mathbf{\Omega}})\mathbf{e_z}$. We use all three non-ideal MHD effects and the resistivity table computed with our chemical code (see chapter 2).

4.3.2 Results

We treat the $\mu = 4$ simulations first because they reproduce the setup of Tsukamoto et al. (2017).

4.3.2.1 $\mu = 4$

The characteristic times of the $\mu = 4$ simulations are summarized in table 4.2, but we first consider the two aligned and anti-aligned simulations M4-00 and M4-180.

The top row of figure 4.11 displays maps of density and velocity for these two setups, taken in the plane $z = 0$ and 0.450 kyr after the formation of the first Larson core. The two orientations generate very dissimilar results from each other, whereas the same simulations without the Hall effect are identical (M4-00 without Hall plotted in the bottom panel for comparison). As explained in section 1.3.4.3, the Hall effect is not symmetric by the change of sign of $\mathbf{B}$. Therefore, the direction of its associated azimuthal velocity depends on the sign of the magnetic field B_z and the Hall resistivity η_H. In both simulations, $\eta_\mathrm{H} < 0$ for $\rho < 10^{-13}$ g cm^{-3}. Hence, $\eta_\mathrm{H} B_z < 0$ in the parallel case M4-00, so the angular velocity generated by the Hall effect counter-acts and slows the initial rotation. Conversely, $\eta_\mathrm{H} B_z > 0$ for the anti-parallel case M4-180, so the Hall effects enhances the rotation of the fluid.

Table 4.2: Characteristic times (in kyr) and resolution of the simulations $\mu = 4$. "nH" stands for "no Hall".

Run	First core (t_c)	Second collapse	End time of the run	Maximum resolution (au)
M4-00	27.049	$27.526 = t_c + 0.477$	$27.556 = t_c + 0.505$	0.040 (level 18)
M4-40	27.100	Not reached	$27.471 = t_c + 0.371$	0.080 (level 17)
M4-90	27.200	Not reached	$27.557 = t_c + 0.357$	0.040 (level 18)
M4-140	27.104	Not reached	$27.541 = t_c + 0.437$	0.323 (level 15)
M4-180	27.131	Not reached	$27.836 = t_c + 0.705$	0.161 (level 16)
M4TURB	29.360	Not reached	$29.960 = t_c + 0.600$	0.323 (level 15)
M4-00 (nH)	27.113	$27.510 = t_c + 0.397$	$27.563 = t_c + 0.451$	0.323 (level 15)

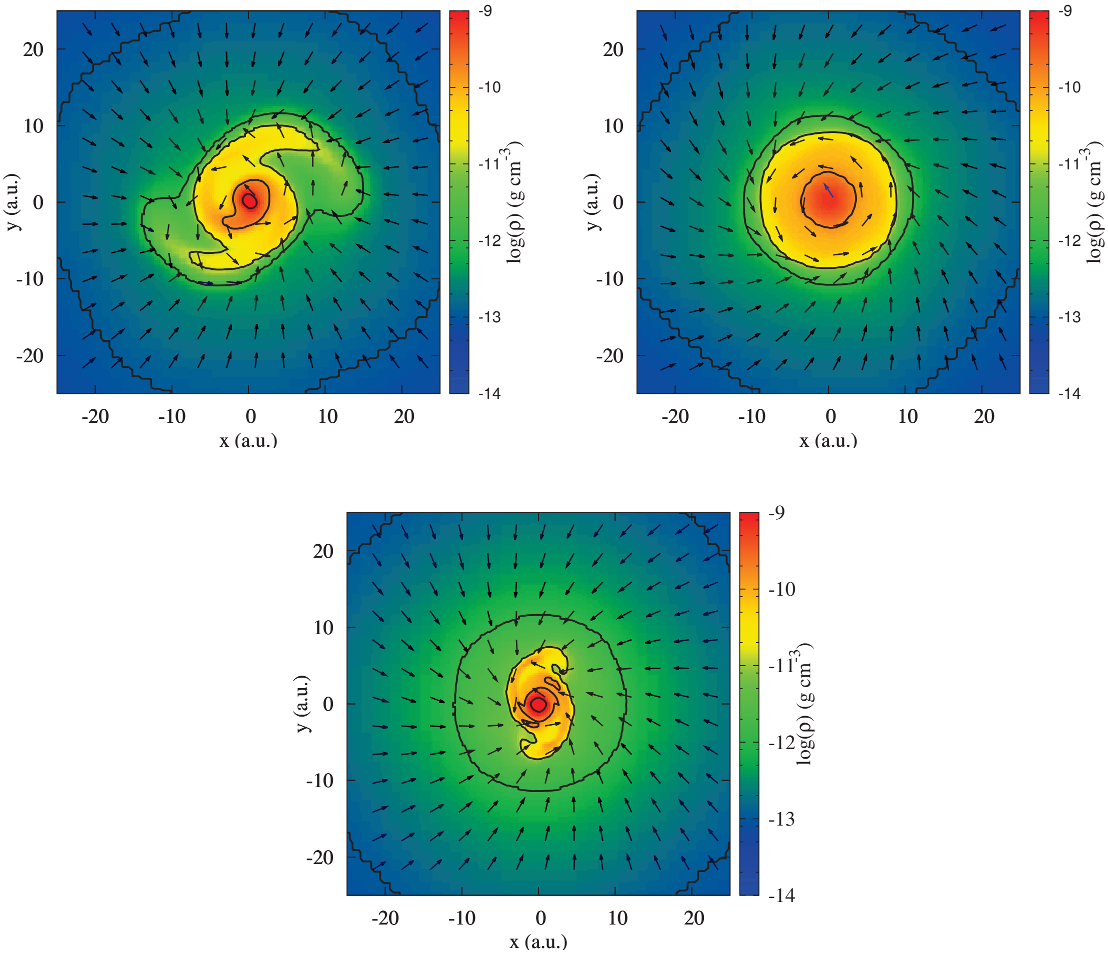

Figure 4.11: Density and velocity maps for simulations M4-00 (top left) and M4-180 (top right), 0.450 kyr after the formation of the first Larson core, with (top row) and without (bottom) the Hall effect. The contours represent isodensities at $10^{[-13,-12,-11,-10,-9]}$ g cm^{-3}.

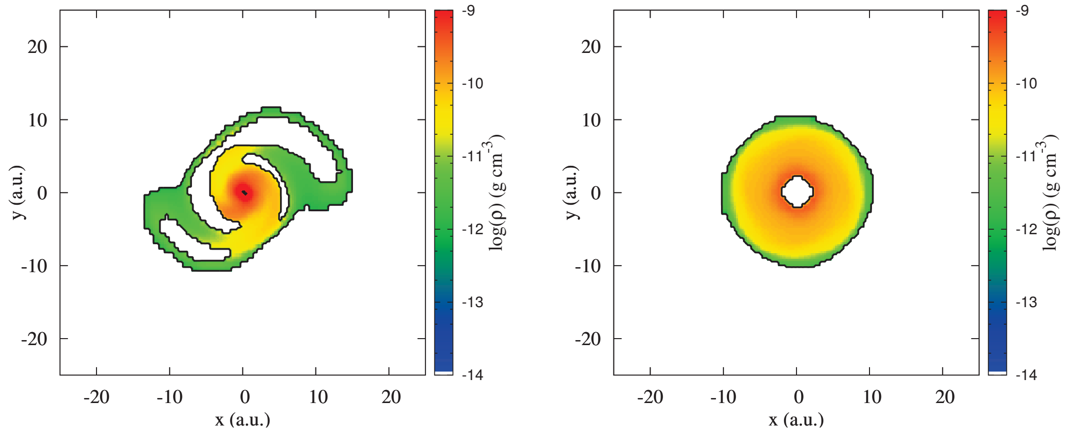

Figure 4.12: Density map of the disk for simulations M4-00 (left column) and M4-180 (right column), 0.450 kyr after the formation of the first Larson core.

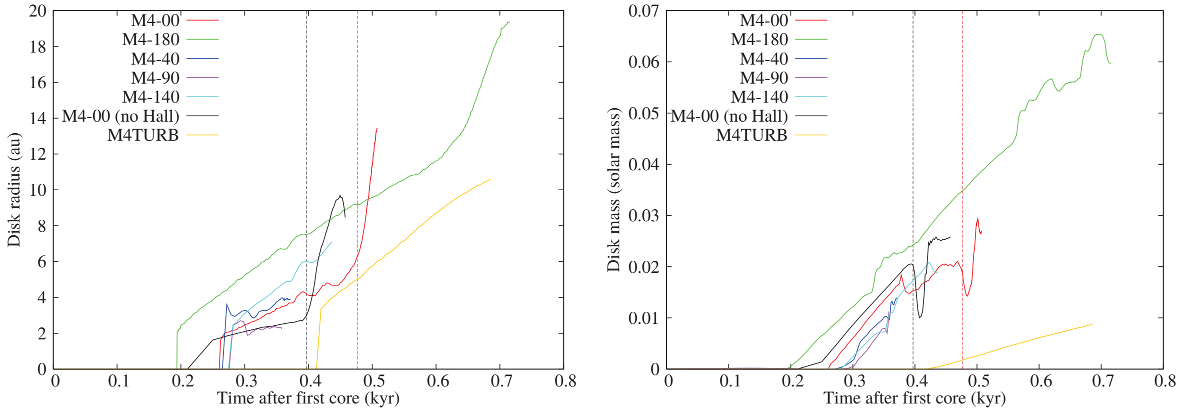

Figure 4.13: Evolution of the disk radius (top panel) and its mass (bottom panel) after the formation of the first Larson core. The colors represent the different simulations (see legend). The vertical lines indicate the start of the second collapse for M4-00 and M4-00.

Figure 4.12 highlights the presence of rotationally supported disk, using the disk criteria of Joos et al. (2012) (see 4.1). Both maps show a disk with a radius of $r_{\text{disk}} \lessapprox 10$ au at this time. The evolution of their radius and mass after the first core formation is plotted in figure 4.13, alongside the tilted setups. The vertical red and black lines indicate at which time M4-00 with and without Hall starts their second collapse. The rapid infall of the gas at this moment boosts the disk's growth in both situations for a short time. Meanwhile, the disk in M4-180 grows rapidly and steadily. According to the first Larson core formation times of table 4.2, the Hall effect does not seem to bring a significant rotational support in the isothermal stage of the collapse. It however plays a major role afterwards in the core. The slower rotation of M4-00 leads to a smaller disk and accelerates the collapse, while in simulation M4-180, the second collapse is delayed and the disk is expanding.

It is however interesting to note that M4-00 starts its second collapse after its counterpart without the Hall effect, whereas the global rotation is slowed down. This is due to η_{H} becoming positive in the inner part of the core. In figure 4.14, we have represented the value of η_{H} in the central region, with its change of sign indicated by the red line, and the black line circumscribing the limit of the disk as previously defined. In both simulations, the resistivity is negative in most

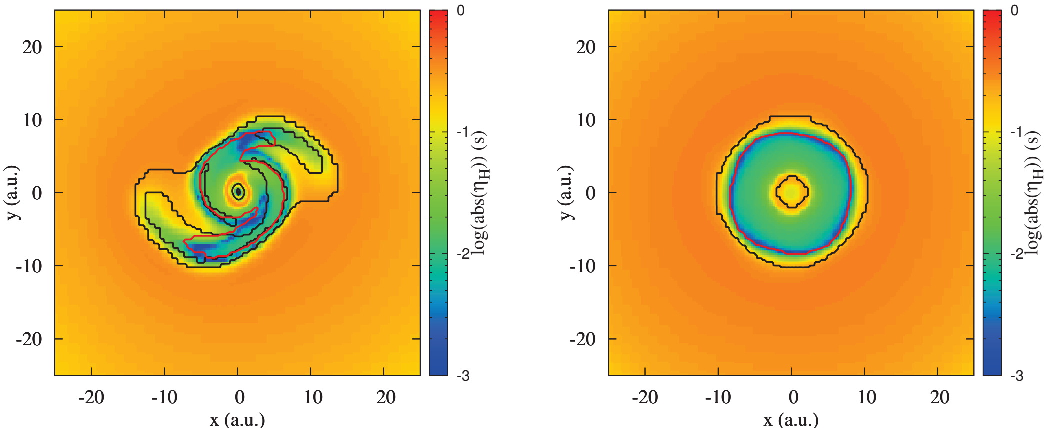

Figure 4.14: Value of $|\eta_{\rm H}|$ for M4-00 (left panel) and M4-180 (right panel). The black line shows the limit of the disk, and the red line encloses the region in which $\eta_{\rm H} < 0$. The rotation is counter-clockwise.

of the box, and positive in the inner regions of the disk, with an amplitude one or two orders of magnitude lower than in its vicinity. A slight change of behaviour of the azimuthal velocity can then be expected. To confirm this hypothesis, we run a simulation with an identical setup as M4-00, only we prevent the resistivity from becoming positive and set its value at 0 instead. Figure 4.15 shows the evolution of the maximum density with time for this simulation and the standard M4-00. With an always negative resistivity, the first core does not take time to "settle" and quickly collapses. Hence, despite the resistivity being one to two orders of magnitude lower in the inner region, the Hall effect possess enough strength to provide small rotational support. In M4-180 though, the change of sign does not seem to prevent the expansion of the disk. 800 years after the first core formation, the core has not started its second collapse.

Figure 4.16 exhibits maps of azimuthal velocity at $t = t_{\rm c} + 0.450$ kyr on the plane $x = 0$. In M4-180, the accretion of angular momentum in the equatorial plane leads to the creation of counter-rotating envelopes despite the initial rotation of the cloud, as in (Tsukamoto et al. 2015). In the opposite way, the core of M4-00 is surrounded by fast-rotating fluid as positive angular momentum is transported away from the center. We also notice two thin layers of negative angular velocity, carrying a low amount of angular momentum ($\sim 7 \times 10^{48}$ g cm^2 s^{-1}, 100 times lower than the core), which coincide with the border of the pseudo-disk.

Figure 4.17 compares the azimuthal velocity to the Keplerian and Hall velocities at $t = t_{\rm c} + 0.250$ and $t = t_{\rm c} + 0.450$ kyr. In both systems, the Hall speed drops to almost 0 in the inner 10 au because the resistivity in this region is very low. In the same radii range, the rotation velocity of M4-180 is almost perfectly Keplerian, hence providing support for the disk. Further from the center, the azimuthal velocity gets closer to the Hall speed as seen in figure 4.18. As in the test case, the pseudo-disk is rotating at roughly the theoretical Hall speed. The excess of u_θ in M4-180 in $r \in [100 : 250]$ au (about the order of 40%) is probably due to the initial enhanced rotation. For both simulations, the Hall influence area stops at $r \approx 250$ au and $\rho \approx 10^{-14}$ g cm^{-3}.

We compare the rotation speed with the case without Hall effect, plotted in green dashed line. As expected, the speed is lower in M4-00 and higher in M4-180. The difference goes up to ~ 0.1 km s^{-1}, which is a variation of 50 to 100 % from the case without Hall. The azimuthal velocities then share the same profile beyond $r \approx 300$ au, proving that at this point the Hall-effect becomes negligible.

Cross-sections of the pseudo-disks are represented in figure 4.19 in the plane $y = 0$, with the

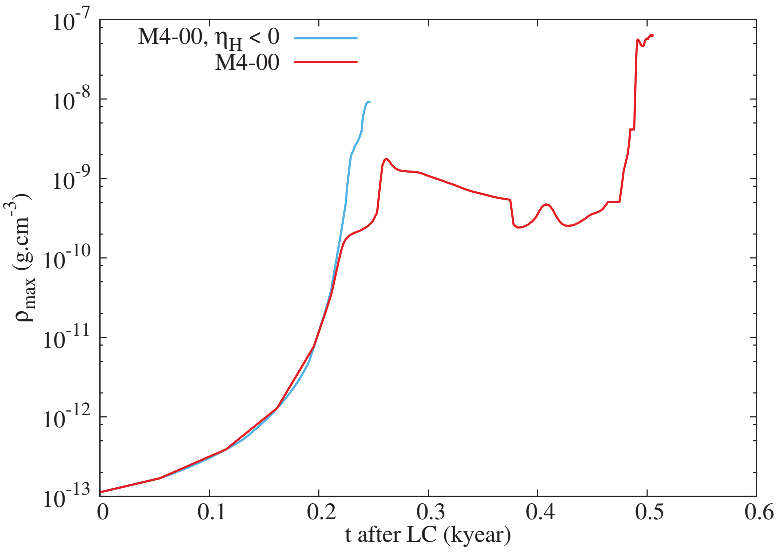

Figure 4.15: Evolution of the maximum density with respect to time in simulation M4-00 (blue line) and in the same simulation with a bounded Hall resistivity (red line).

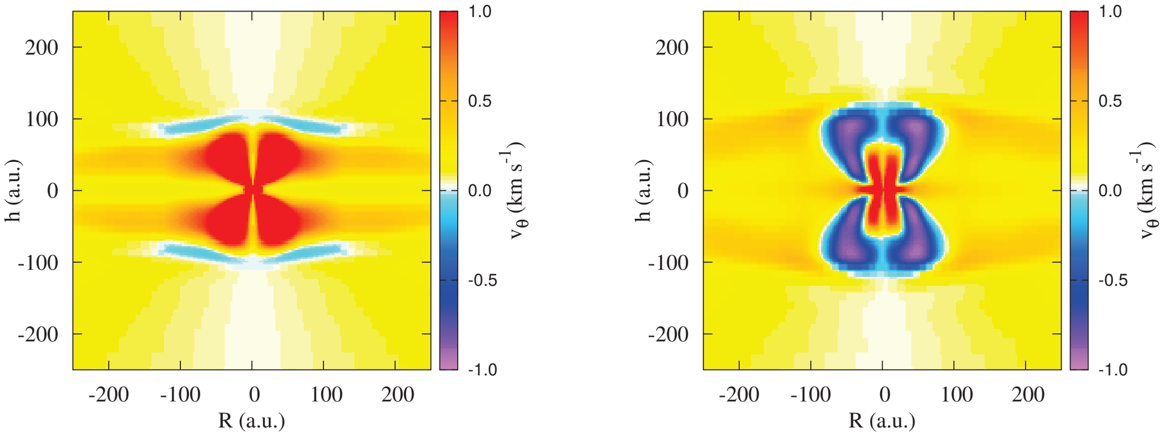

Figure 4.16: Azimuthal velocity maps on $x = 0$ plane at $t = t_c + 0.450$ kyr, for M4-00 (left) and M4-180 (right).

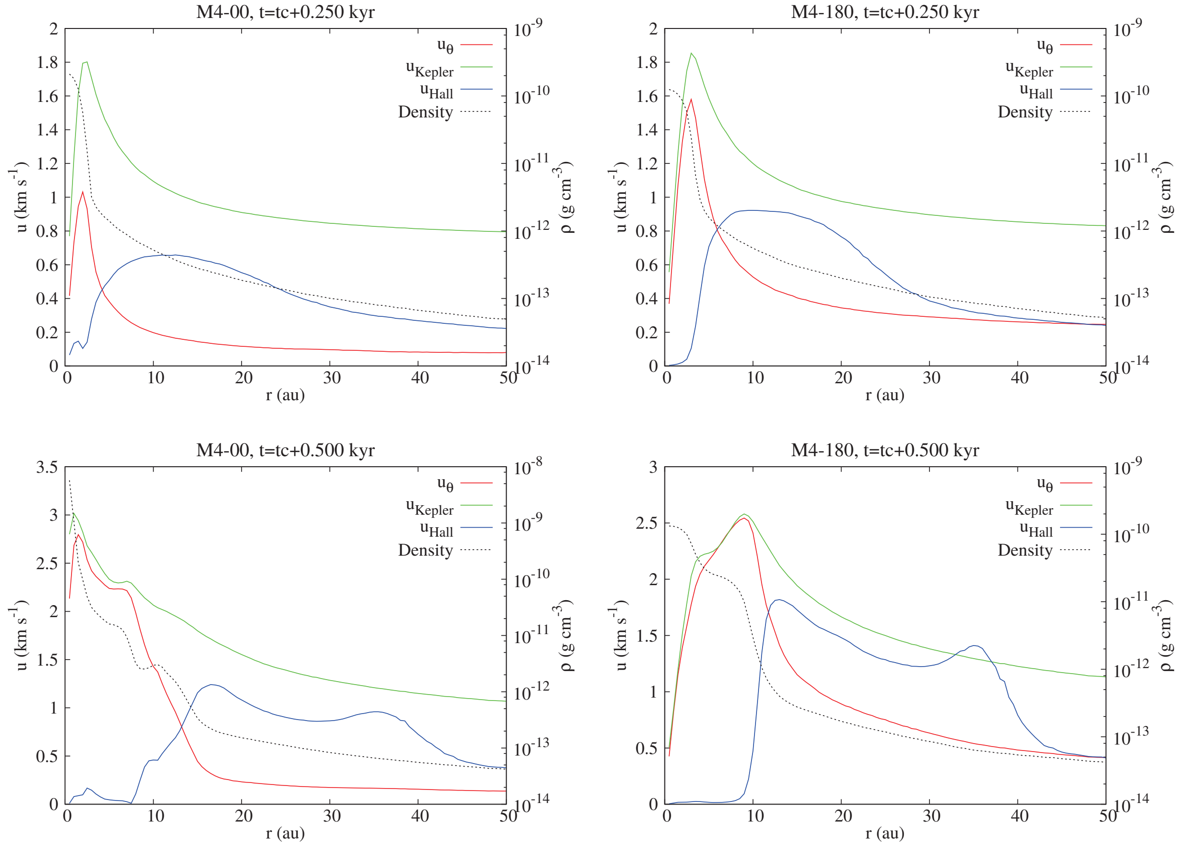

Figure 4.17: Profiles of azimuthal velocity (red curves), Hall velocity (light blue curves), Keplerian velocity (darker blue curves) and density (dotted black curves) at times $t = t_c + 0.250$ and $t = t_c + 0.450$ kyr (top and bottom panels), for M4-00 (left column) and M4-180 (right column).

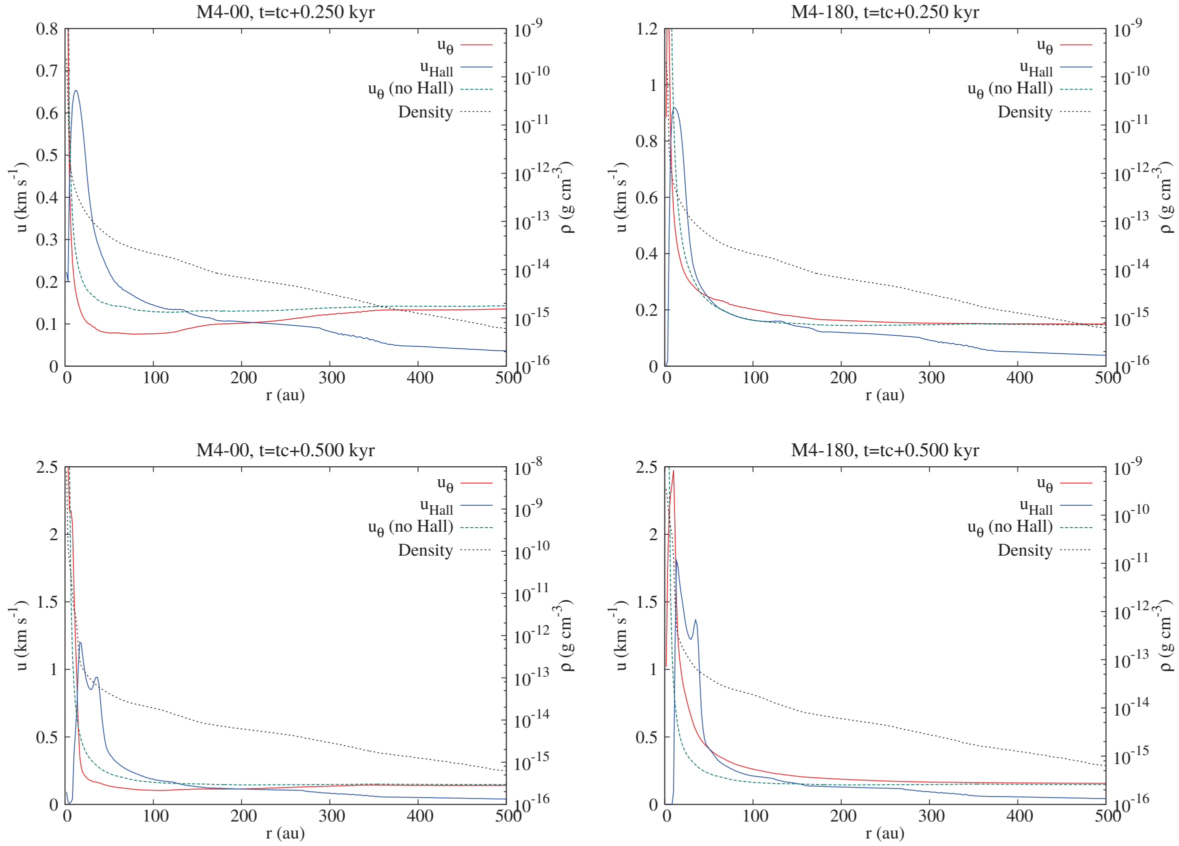

Figure 4.18: Same as figure 4.17, at larger radius and without the Keplerian velocity.

white arrows indicating the direction of the magnetic field, and the red arrow pointing in the direction of the disk's angular momentum. Despite the Hall effect losing its intensity at $\rho < 10^{-14}$ g cm^{-3}, the pinching of the field lines is already strong from $\rho = 10^{-15}$ g cm^{-3}. Away from the first core, the three pseudo-disks are very similar. This suggests that the Hall effect has a very low impact on the structure of the pseudo-disk .

In the two above-discussed cases, $\Omega_{\rm ini}$ and $\eta_{\rm H}\mathbf{B}_{\rm ini}$ are either parallel or anti-parallel. Whether they are slowed or accelerated, the disks have the same rotation axis as the initial cloud. This may change in tilted setups where two different angles of rotation are in competition. One could expect a disk axis in an intermediate state, being closer of $\Omega_{\rm ini}$ or $\eta_{\rm H}\mathbf{B}_{\rm ini}$ depending on the strength of each rotation. We take snapshots of these tilted simulations when their maximum density reaches $\rho = 3 \times 10^{-10}$ g cm^{-3}, about 0.300 kyr after the first core formation.

Left panel of figure 4.20 shows the evolution of the angle of the rotation axis of the inner core region ($r < 10$ au) with respect to the magnetic field for M4-40, M4-90, M4-140 and M4TURB. Dashed lines represent the initial angle of the rotation. The M4-40 and M4-90 disks stay roughly aligned with their initial rotation axis. On the other hand, the disk of M4-140 tends to anti-align itself with the magnetic field, in the privileged direction of the Hall effect's induced rotation. Right panel of figure 4.20 displays the norm of the angular momentum of the disk and the core ($\rho > 10^{-13}$ g cm^{-3}). As we could expect, M4-180 has the highest value. We note that M4-40 and M4-90 show a lower angular momentum than M4-00. What happens is an intermediate state between M4-00 rotating clockwise, and M4-180 rotating counter-clockwise, where the Hall effect and the initial rotation almost cancel each other, leading to a slow-rotating disk. The effect is even more striking with M2-40 (see next section). M4-140 being the most "Hall-friendly" case, due to its alignment, it forms the larger disk among the tilted setups.

We represent the cross-section of the pseudo-disk and the magnetic field in figure 4.21 for these tilted setups. The maps are slices of the planes containing the vector normal to the pseudo-disk $\mathbf{n}$ and the z axis (which is the vertical axis). We determine $\mathbf{n}$ the same way as Tsukamoto et al.

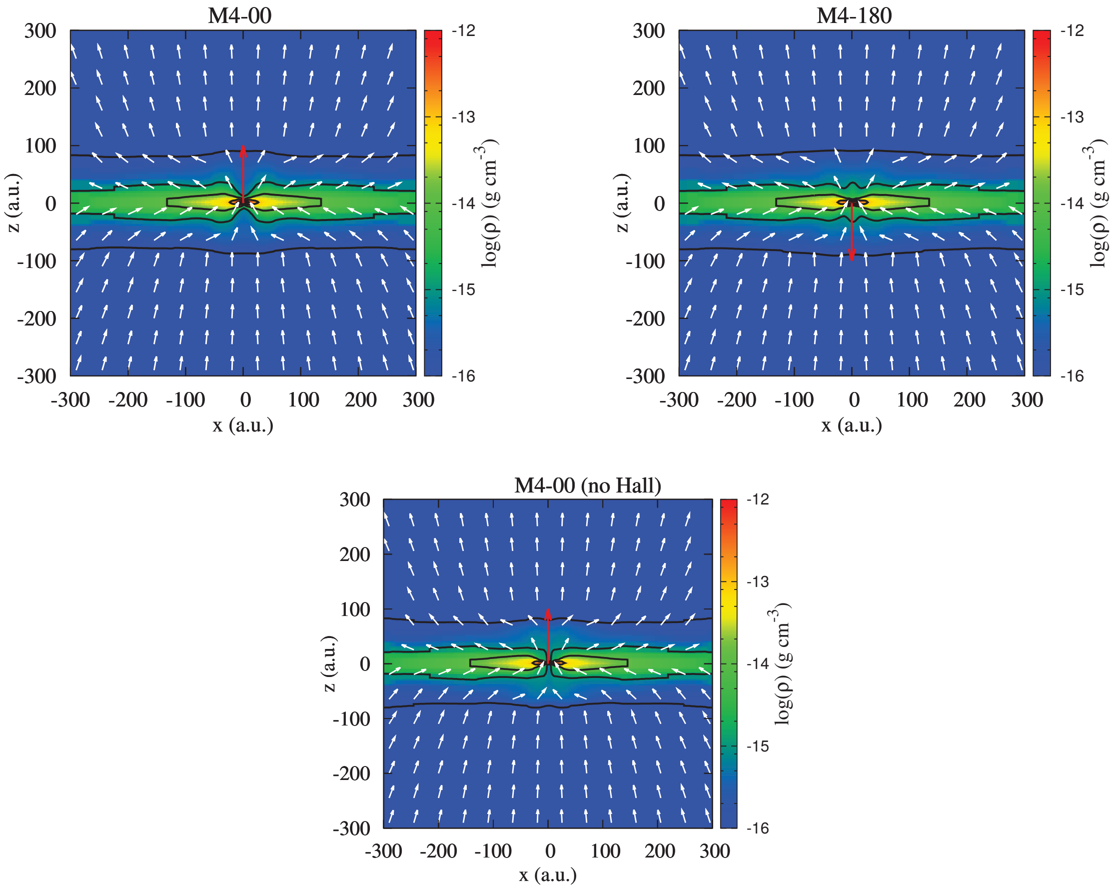

Figure 4.19: Density maps at the pseudo-disk scale for M4-00 (top left), M4-180 (top right), and M4-00 without the Hall effect (bottom) at $t = t_c + 0.450$ kyr. The white arrows represent the direction of the magnetic field, and the black contours are isodensities at $\rho = 10^{[-16,-15,-14,-13]}$ g cm^{-3}. The red arrow represents the direction of the disk's angular momentum.

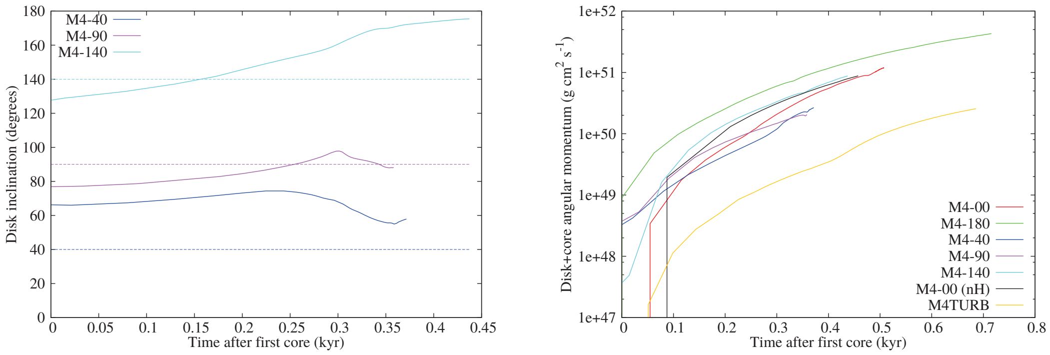

Figure 4.20: Left panel: Evolution of the angle between the inner angular momentum ($r < 10$ au) and the initial magnetic field for the non-aligned simulations. The dashed line represents the initial angle. Right panel: Norm of the angular momentum for the disk and core region ($\rho > 10^{-13}$ g cm^{-3}) for every $\mu = 4$ simulations.

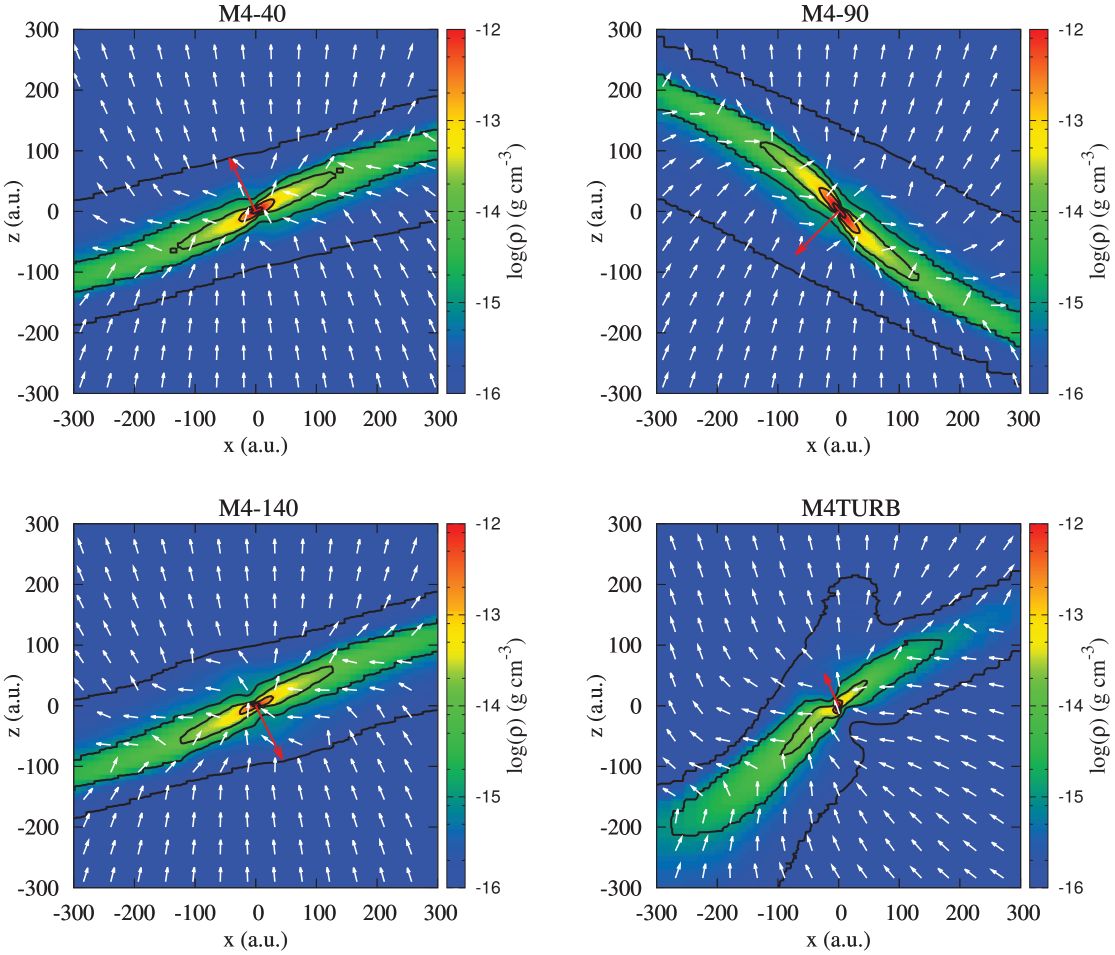

Figure 4.21: Same as figure 4.19 for the M4-40, M4-90, M4-140 and M4TURB cases, at $t = t_\mathrm{c} + 0.350$ kyr.

(2017) by computing the inertia momentum matrix

$$\mathbb{I} = \int_{\rho > 10^{-15}\mathrm{g\ cm^{-3}}} \mathbf{r} \otimes \mathbf{r} \rho d\tau, \tag{4.15}$$

with $d\tau$ the volume element, then taking the eigenvector associated to the smallest eigenvalue of the matrix[3]. There again, the pinching of the magnetic field is the negligible below densities of few 10^{-15} g cm^{-3}. M4-40 and M4-140 show symmetries in their orientation and shape. In both cases, the inner disk ($\rho > 10^{-13}$ g cm^{-3}) seems roughly aligned with the pseudo-disk, while the misalignment is more pronounced in M4-90. The turbulent case shows a smaller and non-symmetrical pseudo-disk.

While the disk is structured by rotational support, the pseudo-disk depends on the magnetic field, so we can expect a different orientation. Figure 4.22 displays the polar angle $\varphi = \widehat{\mathbf{n}, \mathbf{e_z}}$, and the azimuthal angle $\theta = \widehat{\mathbf{n}, \mathbf{e_x}}$ of the pseudo-disk, as a function of $\widehat{\mathbf{B}, \mathbf{\Omega}}$ (the left panel summarizes the notations). The dashed line represents the simulations without the Hall effect.

While the two rotation axises in competition lie in the $x - z$ plane, it is interesting to see that the resulting pseudo-disk is strongly tilted toward the $y-$axis. Actually, this inclination is due to the initial rotation. $\mathbf{\Omega}$ can be decomposed into two components Ω_x and Ω_z. Ω_z participates in the rotation of the pseudo-disk that naturally forms perpendicularly to the magnetic field, and that is all what happens in M4-00 and M4-180. Here, Ω_x generates a rotation of the fluid around the $x-$axis, hence pivoting the plane in which the gas settles.

---

[3] The eigenvalues of $\mathbb{I}$ are always real because the matrix is symmetric.

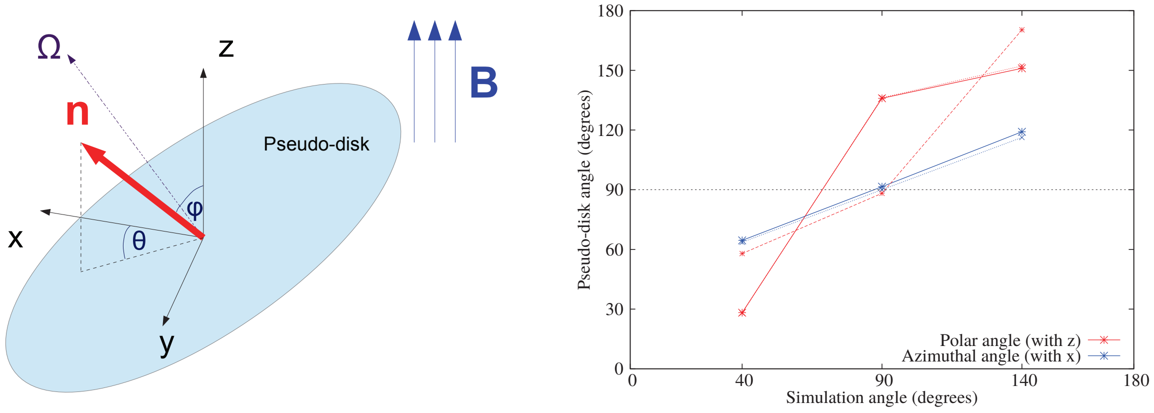

Figure 4.22: Left panel: scheme of the pseudo-disk inclination. Right panel: Polar angle φ (red line) and azimuthal angle θ (blue line) of the pseudo-disk and the disk (solid and dashed line) for the $\mu = 4$ simulations. The dotted lines represent the pseudo-disk without the Hall effect.

The tilting of the pseudo-disk is independent from the presence of the Hall effect at this magnetisation. M4-90 shows the greatest inclination angle in both directions, which is not surprising given that it has the highest rotation velocity around the $x-$axis, or simply by an argument of symmetry that is demonstrated by the similarities between M4-40 and M4-140. The turbulent pseudo-disk, not represented in this plot, have inclinations of $\varphi = 35°$ and $\theta = 58°$ with the Hall effect, and $\varphi = 29°$ and $\theta = 62°$ without. Given the random assignation of the angular momentum, there is nothing special about the azimuthal angle, but the polar angle is the highest of all.

So far, the polar angle of the pseudo-disk does not seem to influence the disk, whose inclination stays close to the initial global rotation.

We investigate the presence of counter-rotating envelopes in the intermediate cases. In figure 4.23, we plot the speed perpendicular to the plane of the map, similarly to Tsukamoto et al. (2017). We perform a slice of the plane containing the vector $\mathbf{n}$ and the initial rotation vector $\mathbf{\Omega}$, and represent the speed of the gas along the normal vector of the plane $\mathbf{n}_{\text{slice}} = \mathbf{n} \times \mathbf{\Omega}$. The yellow-red regions go toward the "front" of the plane, and the blue regions go "behind" the plane. We chose this representation because it is more complicated to discern structures in these configurations, given that the gas does not necessarily rotates in the plane of the pseudo-disk. M4-90 and M4-140 both present a counter-rotating envelope, with a dimension (radius and height) of roughly 50 and 70 au respectively. As expected, the more the rotation is enhanced by the Hall effect, the larger and faster the counter-rotating regions. M4-40 does not form such structure and the azimuthal velocity inside the isodentity $\rho = 10^{-14}$ g cm^{-3} is extremely low. Nonetheless, the rotation of the pseudo-disk seems well-structured within a width of 50 au above and below its mid plane. M4TURB is represented in figure 4.24 along with the case without the Hall effect[4]. It seems to present counter-rotation similar to the other cases, with two envelopes of comparable size on each side of a coherent disk. The random motion of the gas makes difficult to determine in what extent these envelopes have been formed by the Hall effect, but their presence makes no doubt. Furthermore, a very coherent disk appears, circled by the isodensity $\rho = 10^{-14}$ g cm^{-3}. Such well-bounded structure does not appear without the Hall effect. Outside the pseudo-disk, the two maps bear close resemblance.

Figure 4.25 compares the azimuthal velocity profile into the pseudo-disk to the expected Hall speed. The rotation of the pseudo-disk is far below the Hall speed in M4-40 and M4-90. In M4-40, the velocity increases at larger radius due to the initial rotation, but in M4-90, the initial velocity is perpendicular to the pseudo-disk and cannot contribute to its rotation. On the other

---

[4] Careful, the color scale has been changed to increase the contrast.

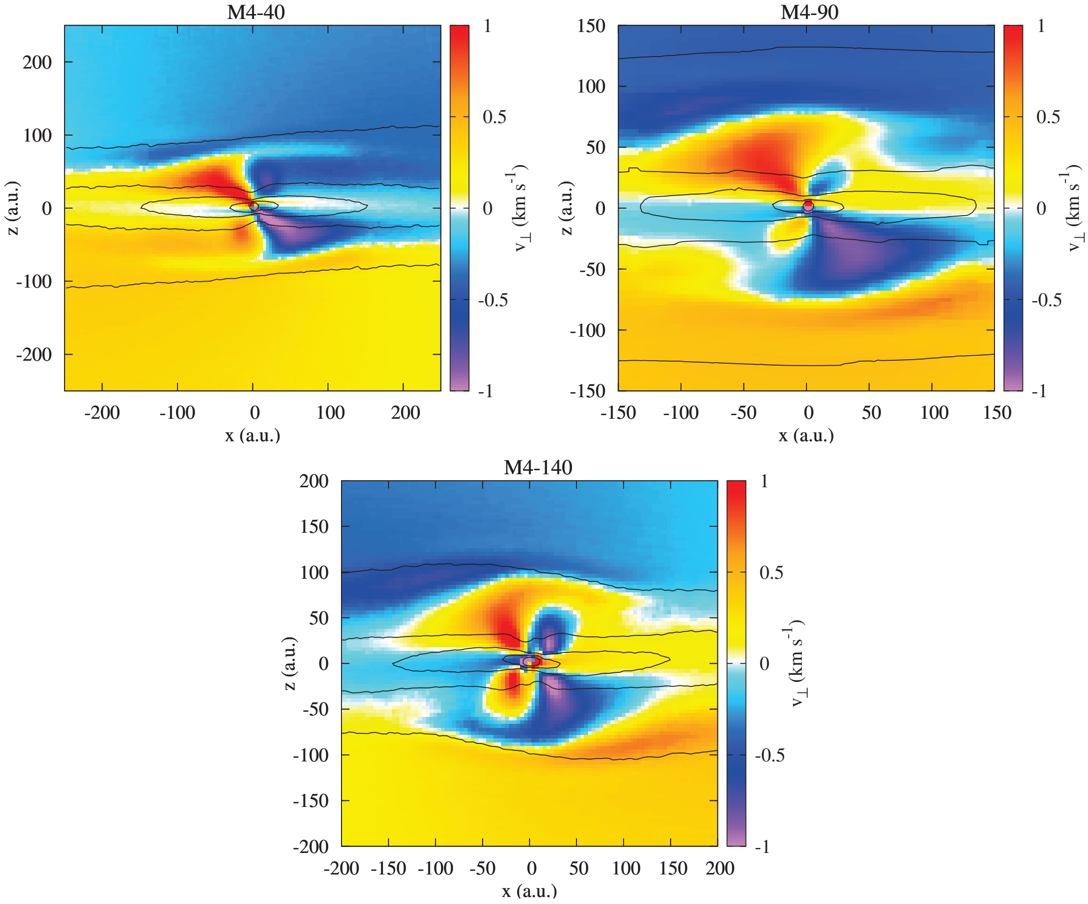

Figure 4.23: Velocity of the fluid coming "out" from the plane (yellow colors) and coming "in" (blue colors) for the tilted setups of $\mu = 4$ simulations at $t = tc + 0.350$ kyr. Top left: M4-40, top right: M4-90, bottom: M4-140.

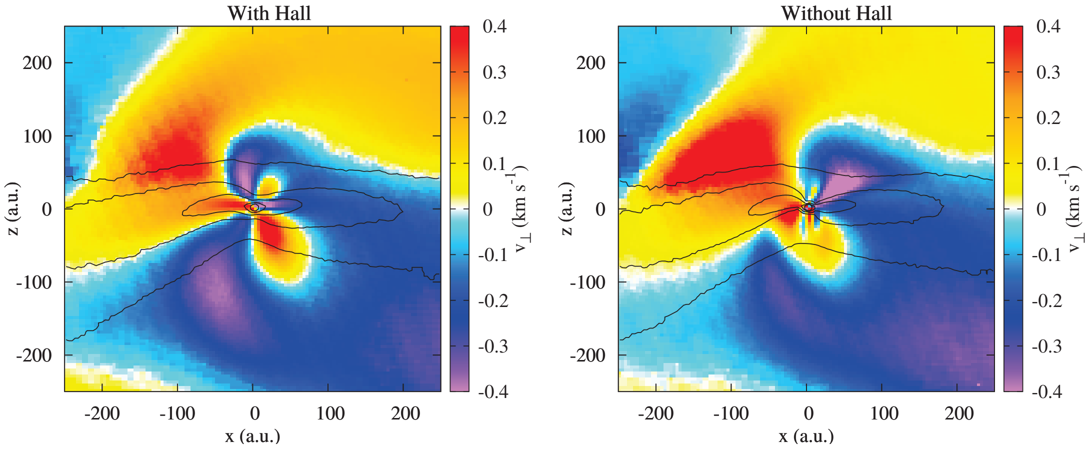

Figure 4.24: Velocity of the fluid coming "out" from the plane (yellow colors) and coming "in" (blue colors) for M4TURB, with and without the Hall effect (left and right panels) $t = tc + 0.400$ kyr.

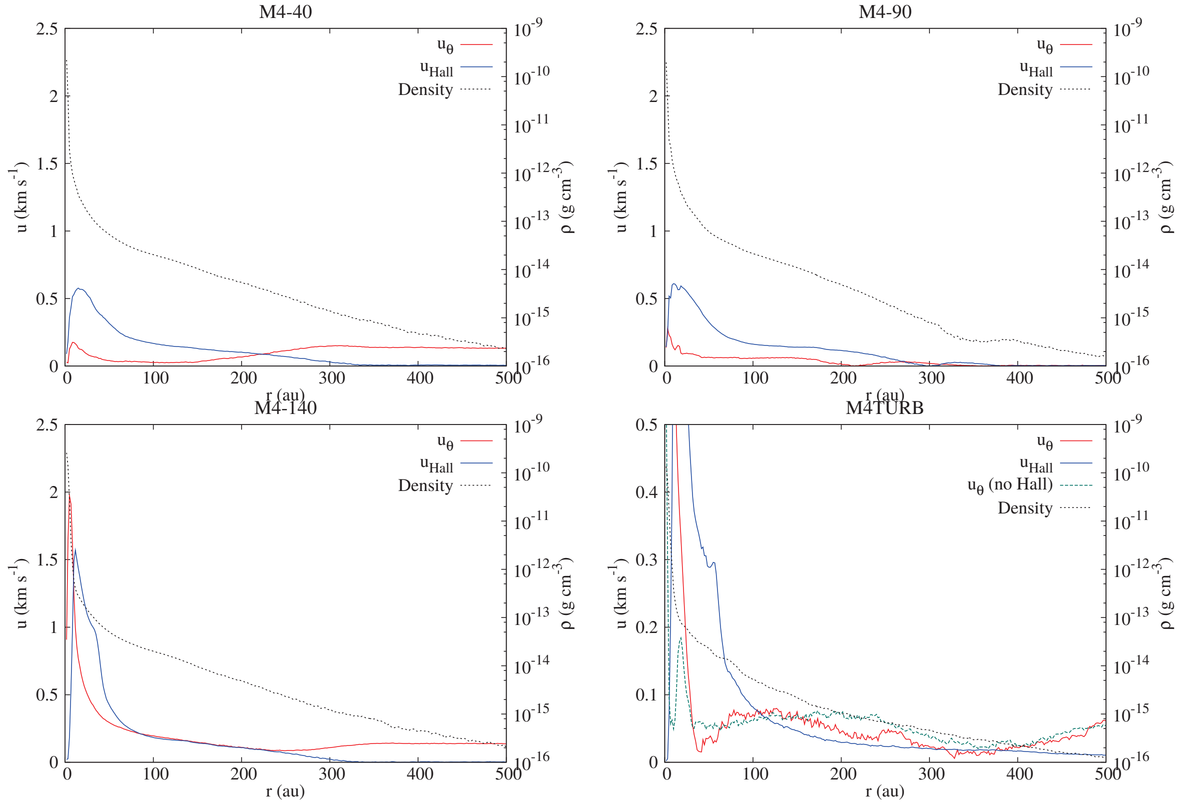

Figure 4.25: Azimuthal velocity and Hall velocity profiles in the pseudo-disk, in red and blue respectively. The dashed line represents the density. Top left: M4-40, top right: M4-90, bottom left: M4-140, bottom right: M4TURB.

hand, M4-140 does have a velocity profile fitting the theoretical Hall speed across 150 au. The turbulent case shows seemingly the best agreement. As already seen in the perpendicular velocity maps, the Hall effect appears to have structured the turbulent motions in the disk into a coherent azimuthal velocity. However, the speeds at stake are small, and the u_θ is not significantly closer to the Hall speed than without the Hall effect (green dashed line). Moreover, the two profiles coincide the most at densities at which the influence Hall effect is almost negligible.

The angular momentum problem described in 4.2 arises also in these simulations. Figure 4.26 shows the excess of angular momentum L_z alongside the angular momentum contained in the disk region. The divergence starts around $t = t_c + 0.300$ kyr, with an increase of $\approx 2.5 \times 10^{51}$ g cm^2 s^{-1} kyr^{-1} for every simulation. The test case showed quantitatively the same evolution. While the disk in M4-40, M4-140 and M4-180 largely overcome the creation of angular momentum, it is not the case in M4-00 and M4-90, where both values are close to each other. The disk in M4TURB, the momentum of the disk is even lower than the increasing of momentum. In every case, it is then not possible to draw quantitative conclusions despite the similarity with other studies.

4.3.2.2 A stronger magnetic field, $\mu = 2$

This series of proto-stellar collapses is identical to the former, but takes place in a strongly magnetised medium. Table 4.3 summarizes the characteristic times of the simulations. The delay of ~ 7 kyr of the first core formation, compared to the previous cases, is due to the higher value of the magnetic pressure.

Figure 4.27 presents density and velocity maps of M2-00, M2-180 and M2-00 (nH) at $t = t_c + 0.400$ kyr. The stronger magnetic braking leads to the formation of very concentrated cores.

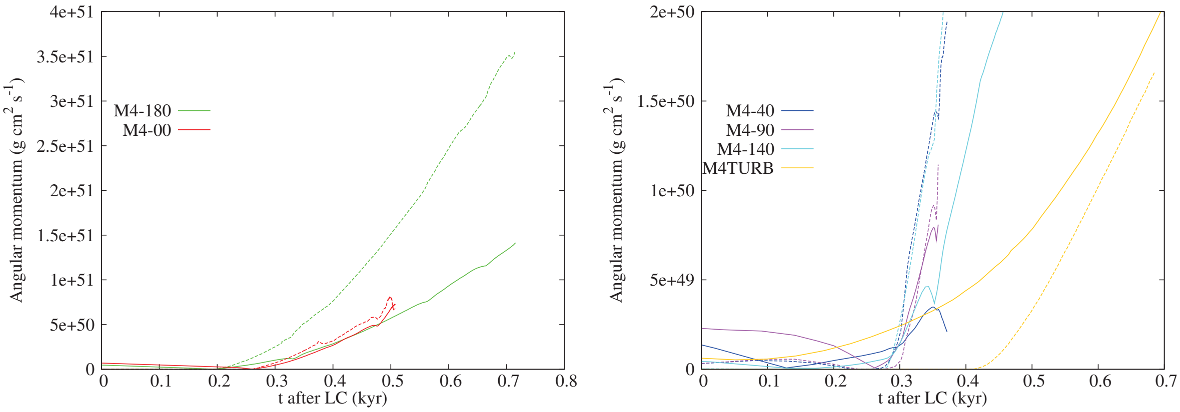

Figure 4.26: Comparison between the excess of angular momentum L_z (solid line) and the angular momentum of the disk region (dashed line) in the $\mu = 4$ simulations.

Table 4.3: Characteristic times (in kyr) of the simulations $\mu = 2$.

Run	First core (t_c)	Second collapse	End time of the run	Maximum resolution (au)
M2-00	34.498	Not reached	$34.896 = t_c + 0.398$	0.162 (level 16)
M2-40	34.547	$34.844 = t_c + 0.297$	$34.853 = t_c + 0.306$	0.020 (level 19)
M2-90	34.817	Not reached	$35.220 = t_c + 0.403$	0.162 (level 16)
M2-140	34.618	Not reached	$34.990 = t_c + 0.372$	0.324 (level 15)
M2-180	34.598	Not reached	$35.130 = t_c + 0.632$	0.162 (level 16)
M2TURB	34.006	Not reached	$34.445 = t_c + 0.439$	0.324 (level 15)
M2-00 (nH)	34.146	Not reached	$34.607 = t_c + 0.461$	0.080 (level 17)

In the aligned case, the switch of sign of the Hall effect for $\rho > 10^{-11}$ g cm^{-3} creates an additional support against the collapse, resulting in a slightly more extended core than without the Hall effect.

Figure 4.28 compares the various growths of the disk mass and radius for all the $\mu = 2$ simulations. In every case, the disk appears about 300 years after the first core formation, and its mass evolution seems nearly independent from the orientation. The radius increase for the different orientations reflects nonetheless what we could expect, with M2-180 and M2-140 creating the largest disks, and M2-90 and M2-00 the smallest (then denser) ones. The change of sign of the Hall effect in M4-00 provides a small support allowing the disk to grow larger than without the Hall effect by about 50%. Overall, the disks are twice as small as in $\mu = 4$.

The only notable exception is M2-40, which does not form a disk. This is a more dramatic case than M4-40, whose central region has the lowest angular momentum among the $\mu = 4$ simulations. The rotation almost stops for two reasons. First, since 40° is an acute angle, the Hall effect strengthens the magnetic braking at this orientation. M2-00 experiences a stronger braking but conserve more angular momentum, which is counter-intuitive. This is due to the initial rotation axis. In M2-00, the fluid enters the pseudo-disk with a given amount of azimuthal velocity, but in M2-40, this velocity is reduced by a factor of roughly $1/\cos(40°) \approx 1.3$. This projected component of $\mathbf{\Omega}$ does not allow the fluid to enter the pseudo-disk with a sufficient azimuthal velocity. It is therefore accreted into the core carrying a low amount of angular momentum. The total amount of angular momentum of the core+disk region, plotted in figure 4.29, confirms these observations. The very low rotational support in M2-40 leads to its fast second collapse, merely 0.300 kyr after the first core formation, far earlier than M2-00 which has not reached this phase by $t = t_c + 0.400$ kyr.

Overall, the rotation is slower than for $\mu = 4$. The angular momentum in the central region is at most at the same order of magnitude as M4-00, one of the slowest rotating core in the

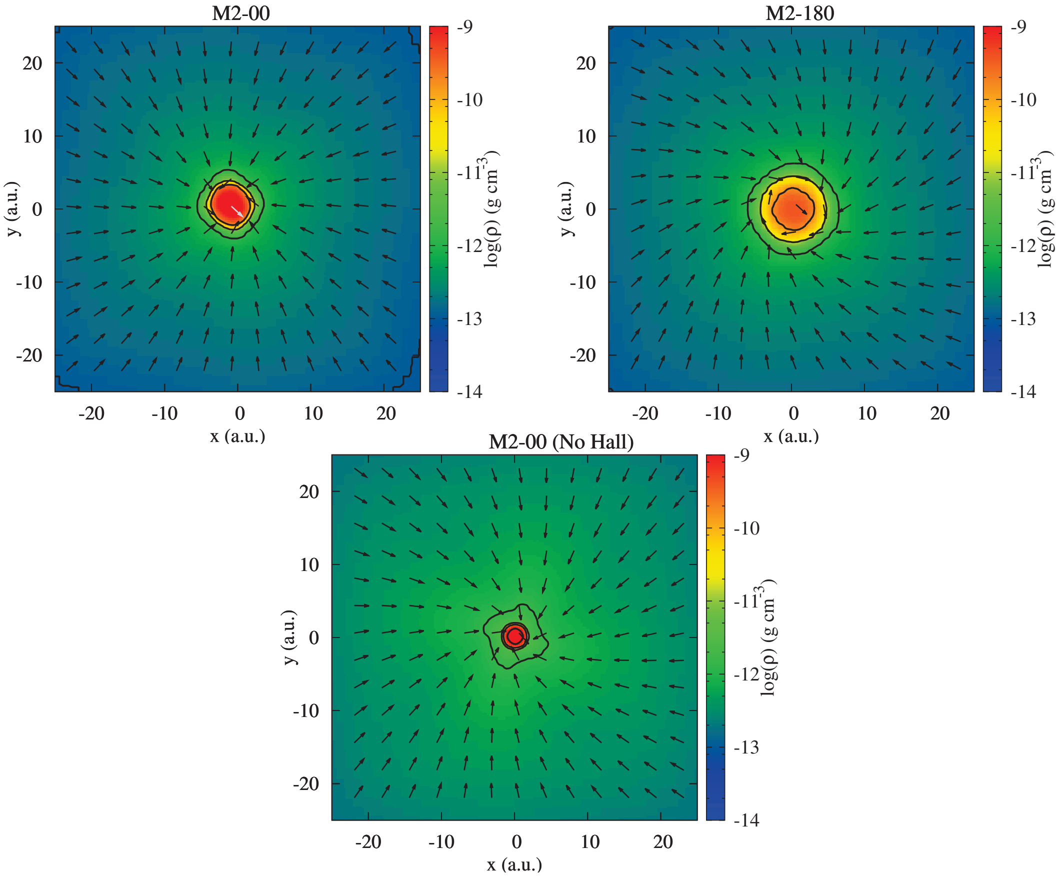

Figure 4.27: Density and velocity maps of M2-00 (top left), M2-180 (top right) and M2-00 without Hall (bottom) at $t = t_c + 0.400$ kyr.

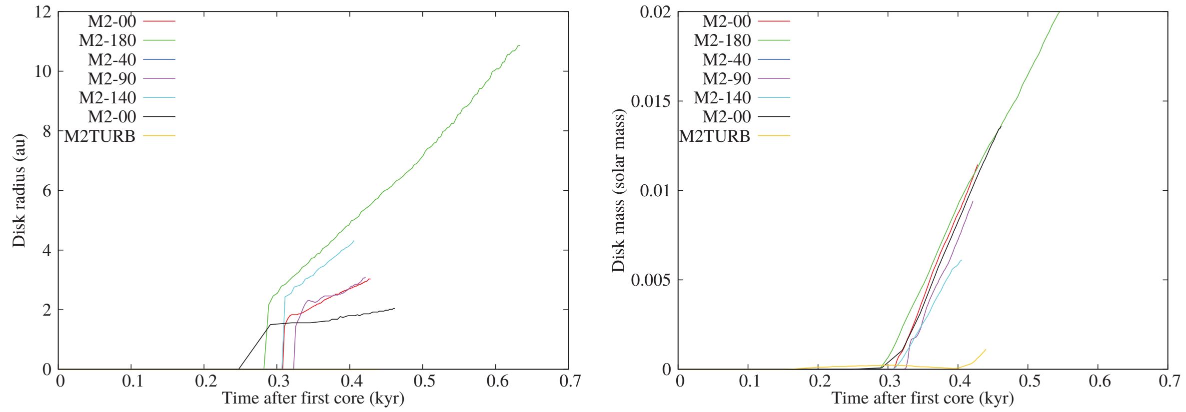

Figure 4.28: Evolution of the radius of the disk (top panel) and its mass (bottom panel) after the formation of the first Larson core. Simulations M2-00 (red line), M2-90 (dark blue line), M2-140 (purple line), M2-180 (grey line) and M2-00 without line (black line).

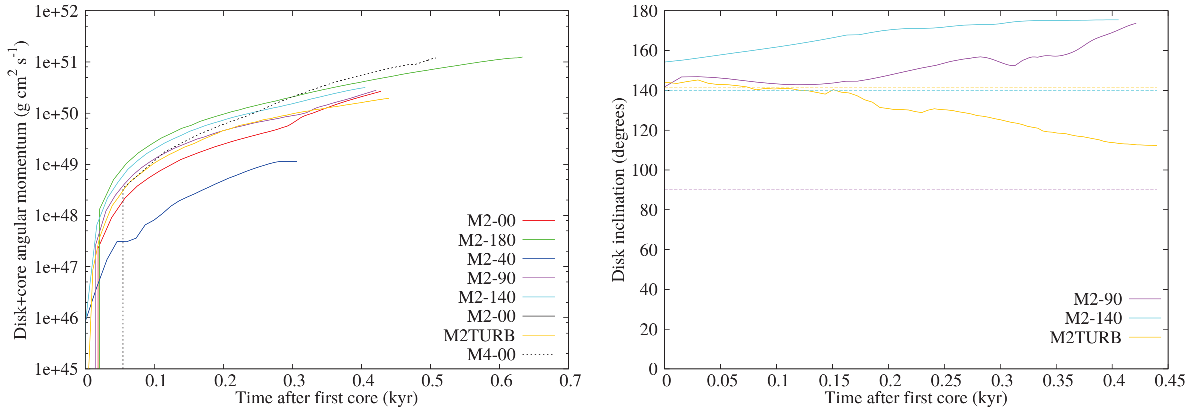

Figure 4.29: Left: Norm of the angular momentum for the disk and the core region ($\rho > 10^{-13}$ g cm^{-3}) for every $\mu = 2$ simulation, and M4-00 for comparison. Right: Angle between the disk and the global magnetic field, for tilted setups: M2-90 (90°, pink line), M2-140 (140°, blue line) at $t = t_c + 0.300$ kyr.

set $\mu = 4$. The Hall effect cannot weaken the braking enough to create a substantial rotational support, which produce less massive, smaller disks, with roughly a factor 2 compared to $\mu = 4$.

The inclination angle formed by the disk with the global magnetic field is displayed in the right panel of figure 4.29, for M2-90 and M2-140 at $t = t_c + 0.300$ kyr. Their angle approaches 180°, which is the privileged direction of the Hall effect. We do not represent the angle of M2-40 due to its almost nullified rotation.

At larger scale, the angle of the pseudo-disk is plotted in figure 4.30 for those three orientations. In all cases, the amplified magnetic braking reduce the angular momentum of the fluid able to tilt the disk, hence resulting in a smaller polar angle (the dotted black lines are for $\mu = 4$). The Hall effect still has no influence on the inclination of the pseudo-disk. For M4-90 and M4-140, the pseudo-disk is quasi anti-aligned with the initial magnetic field. This may explain the orientation of the circumstellar disk. The Hall effect does not change the orientation of the pseudo-disk, but generates an azimuthal acceleration in its mid-plane. The fluid then falls onto the central region with a velocity mostly contained within this plane, thus setting a privileged direction of rotation, with an axis perpendicular to the pseudo-disk. The higher the magnetisation, the

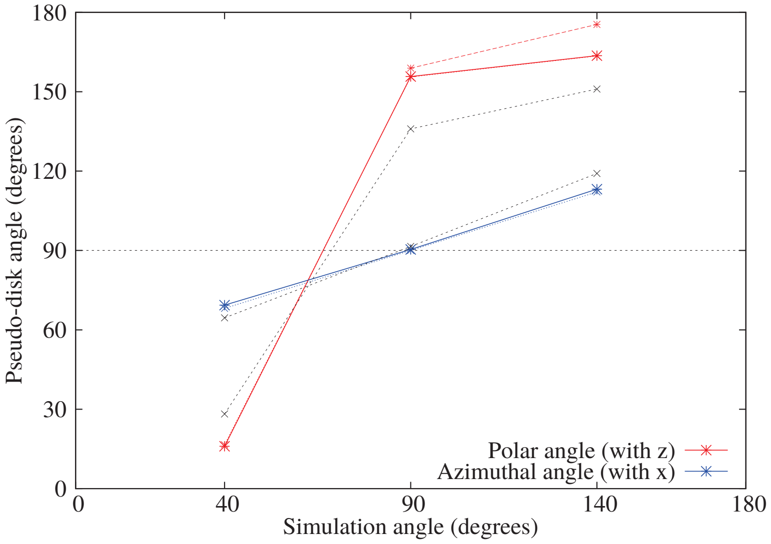

Figure 4.30: Same as 4.22. The black dashed lines represent the $\mu = 4$ pseudo-disks.

stronger the Hall-induced rotation. This explains why the disk orientation is decorrelated from the pseudo-disk for $\mu = 4$ but not in $\mu = 2$. In this later case, the magnetic field is so strong that the pseudo-disk's polar angle is less influenced by the dynamics of the fluid, and the circumstellar disks is aligned with the pseudo-disk. In other words, in strong magnetisation, the Hall effect can "straighten" the disk. In M2TURB, the angle is $\theta = 15°$ (12° without the Hall effect), which is far lower than the 58° in M4TURB. Comparing this angle with the angle of the disk would not be very conclusive, given that the disk is barely developed.

Since every pseudo-disk look alike at various orientations, we only display M2-00 and M2TURB in figure 4.31, 0.300 kyr after the first core formation. The slice planes are chosen the same way as previously, using equation (4.15). The shape of the pseudo-disk is quite different from a lower magnetisation, with an inflated outer region, rather than a plane profile with a small bulge in the middle. The only notable difference concerns the size of the first Larson core (red regions on the map), with M2-90 and M2TURB harbouring the largest with 100 and 150 au in diameter. The turbulent case is nearly indistinguishable from the non-turbulent one, meaning that the magnetic field is strong enough to smooth the density profile and form a pseudo-disk as flat as the others.

Figure 4.32 compares the fluid azimuthal velocity to the Hall speed. Contrarily to the lower magnetised case, no pseudo-disk follows the theoretical rotation speed (M2-180 and M2-140 are the closer though). In the inner 100 au, the rotation speed is lower, then higher than the Hall speed in every simulation. The only exception is M2-40. The Hall velocity in this pseudo-disk is twice as small as in the other cases ($\lesssim 5 \times 10^{-2}$ km s^{-1} for $r > 100$ au), which increases the ratio despite a lower u_θ. Nevertheless, the rotation of the pseudo-disk is impacted by the Hall effect in the same extent as $\mu = 4$. The Hall effect does increase or decrease the rotation velocity by ~ 0.1 km s^{-1}, from 50% to 100% in relative value, in the two extreme cases M2-00 and M2-180. The point at which the azimuthal velocity surpasses the Hall speed, around $r = 150$ au, corresponds to a density $\rho = 10^{-14}$ g cm^{-3}.

The azimuthal velocity maps of these simulations at are presented in figure 4.33 at $t = t_c + 0.300$ kyr. In the same way as $\mu = 4$, the isodensity $\rho = 10^{-14}$ g cm^{-3} contains a coherent rotation in every case, including M2TURB (which is not the case without the Hall effect). In M2-40, the velocity is almost nullified in this region. This explains why no disk could be formed because the Larson core accretes mainly in the pseudo-disk. The angular momentum transported by the fluid is therefore too low to build-up into a rotationally supported disk. Counter-rotating

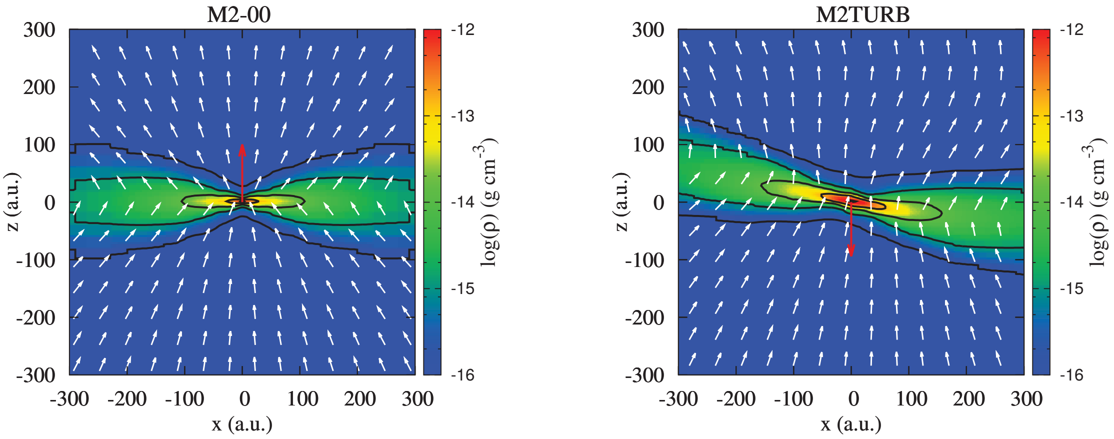

Figure 4.31: Cross-sections of the pseudo-disk for M2-00 (left) and M2TURB (right). The white arrows represent the direction of the magnetic field and the red arrows the angular momentum of the disk.

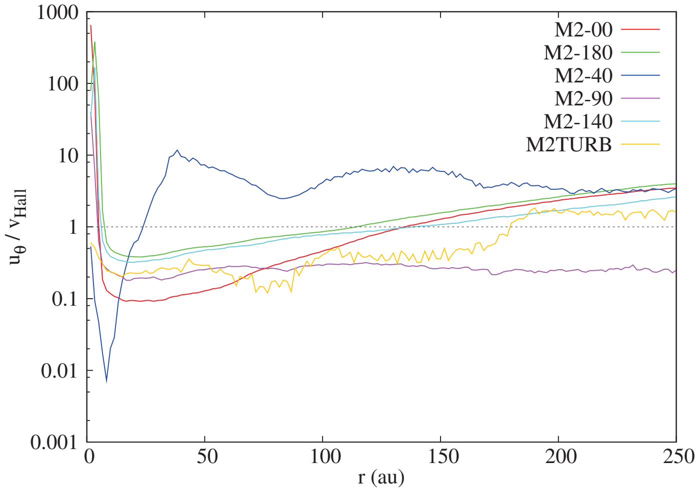

Figure 4.32: Ratio between the azimuthal velocity and the Hall speed in the plane of the pseudo-disk (azimuthal mean), for every $\mu = 2$ simulation.

envelopes appear in the same cases as previously, and with larger dimensions. Their size reach 100 au in height and radius for the tilted setups, and up to 250 au for M2-180. For both μ, the envelopes are contained within the height of the pseudo-disk, except in M2-180 where they expand far higher, and M2TURB, despite the difficulty to determine their exact extent.

This set of simulations also presents an increasing of the angular momentum, as shown in figure 4.34. This time, the disk in the 90° setup exceeds the increasing of momentum, but not in M2-00 and M2TURB.

4.4 Discussion

We form a disk in nearly every simulation. Their apparition coincide with the begining of the non-conservation of angular momentum, therefore we cannot attest the validity of most results but we present those who seem reasonable. The size varies with the initial conditions because the Hall effect acts on the rotational support in different ways depending on the angle. On the other hand, the mass evolution seems independent of the angle. The disk mass grows at a rate of $\sim 1.3 \times 10^{-4}$ M$_\odot$/yr for $\mu = 4$, and $\sim 7.4 \times 10^{-5}$ M$_\odot$/yr for $\mu = 2$. Masson et al. (2016) noticed this effect in very similar simulations including only the ambipolar diffusion, despite a factor 2 to 5 between disk sizes. We can then extend their observations by stating that, probably until the second collapse, both the inclination and the Hall effect have almost no influence on the disk's mass, only on its radius. Wurster et al. (2016) performed simulations with a similar thermal support $\alpha = 0.27$, and a lower rotational energy with $\beta = 0.005$. They observed that in aligned setups ($\mathbf{\Omega} \cdot \mathbf{B} > 0$), a disk was formed only for a very low magnetisation at $\mu = 10$. However, to speed up the calculations, they used sink particles of radius $r = 6.7$ au, which is the same size or larger than the disks we form in aligned configurations for $\mu = 2$ and $\mu = 4$. Therefore, we can not determine whether their observation of the disk's absence is due to their numerical resolution and/or their initial condition, or if our disk is the result of the non-conservation of angular momentum.

Counter-rotation was previously observed in ideal MHD simulations. Without non-ideal processes to dissipate the magnetic flux, the pile-up of the magnetic field in the core creates a magnetic braking so strong that the gas stops and rotates backward (Galli et al. 2006; Mellon & Li 2009; Krasnopolsky et al. 2010; Masson et al. 2016). However, this catastrophic braking takes essentially place into the core and the disk, where the flux is the most intense, resulting in a counter-rotating core and a small or non-existent disk. While these results are regarded as physically doubtful, the actions of the Hall effect suggests that counter-rotating envelopes do exist (Krasnopolsky et al. 2011; Wurster et al. 2016; Tsukamoto et al. 2017). Only, they take place outside the core and allow the formation of rotationally supported disks. Our envelopes appear before the divergence of the angular momentum, so we can reasonably confirm this result.

We qualitatively recover the results of Tsukamoto et al. (2017) concerning the influence of the angle on the size and orientation of the circumstellar disk. We also form counter-rotating envelopes for the same inclinations, though our envelopes are smaller by a factor 2. Despite the very similar setups, we see three possible origins to these differences. First, their model to compute the resistivities is different from ours, and a variation in η_{H} induces a modification of the Hall effect strength in the same extent. Another possibility concerns the time at which the snapshots are taken. Tsukamoto et al. (2017) evolve all their simulations beyond the second collapse, while we generally stop before that point. In M4-180 for instance, the envelope grows in height at a constant rate of ~ 115 au/kyr with a roughly constant radius of 90 au. If this rate stays constant, at least during the first core adiabatic contraction, advancing the simulation by 1 kyr could then grow envelopes twice as big. Finally, these small sizes may be explained by the lack of "negative rotation" due to the diverging angular momentum. If the whistler waves are dissipated before delivering their information, the Hall effect may accelerate the disk and the core without a full compensation by the envelopes. Wurster et al. (2016) also finds counter-rotating envelopes in anti-aligned simulations. Their rotation speed is however relatively low compared to M4-180 and M2-180. We link that to their different resistivities. They solve the electrons,

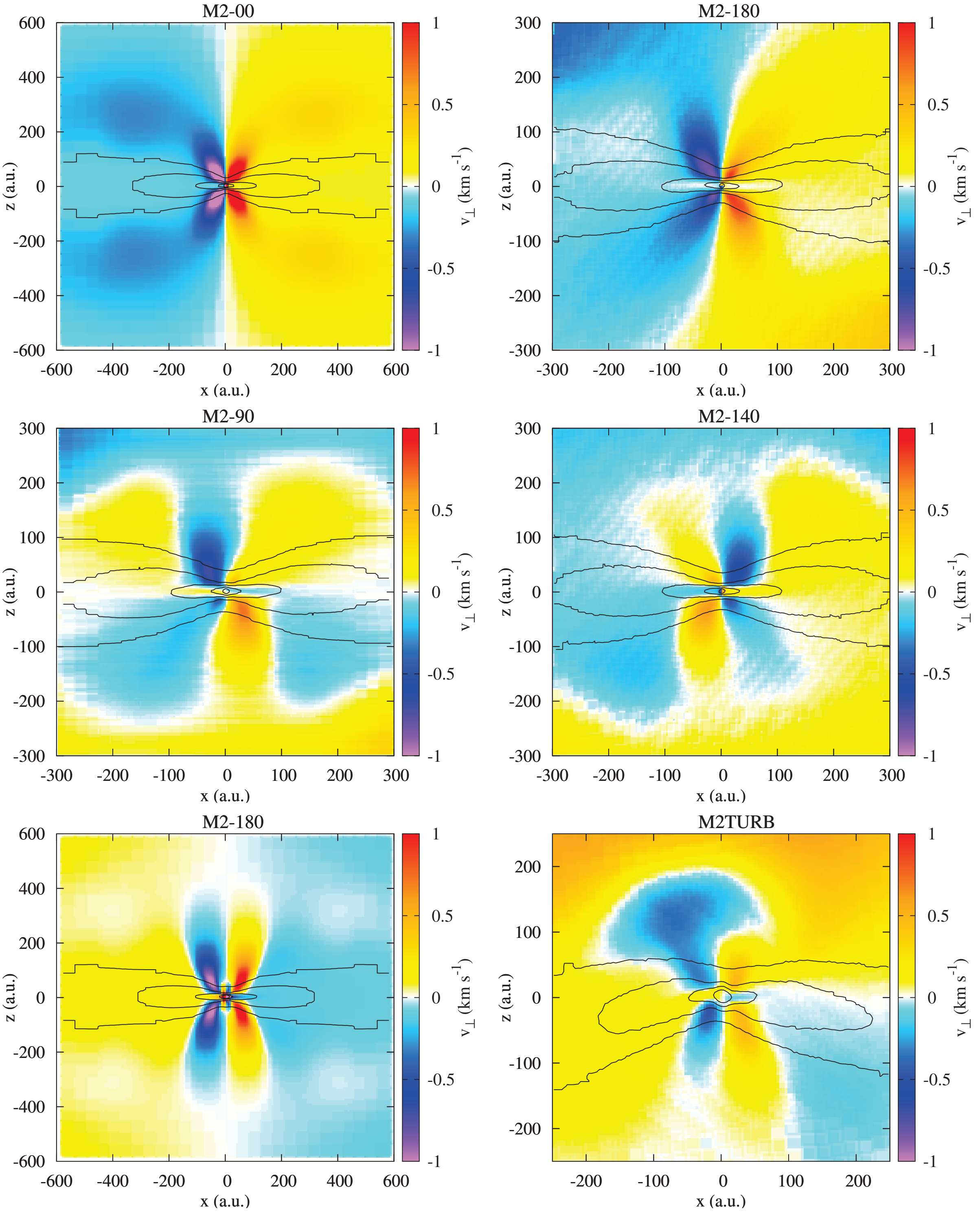

Figure 4.33: Velocity of the fluid coming "out" from the plane (yellow colors) and coming "in" (blue colors) for the $\mu = 2$ simulations. Top left: M2-00, top right: M2-40, middle left: M2-90, middle right: M2-140, bottom left: M2-180, bottom right: M2TURB.

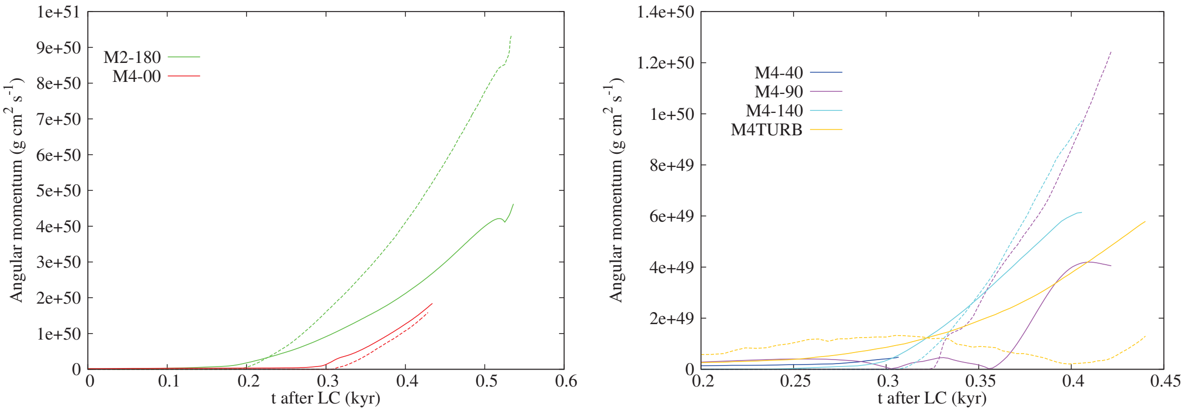

Figure 4.34: Comparison between the excess of angular momentum L_z (solid line) and the angular momentum of the disk region (dashed line) for the $\mu = 2$ simulations.

ions and grains equilibrium abundances with a different model from us (Wurster 2016), which yields Hall resistivities one order of magnitude lower than the values calculated with our code. The Hall effect is therefore less "active" in their simulation, which leads to less pronounced counter-rotation.

We do not find counter-rotation in the mid-plane of the pseudo-disk as Tsukamoto et al. (2017) do for their 0° and 45° angles. This phenomenon is due to the enhanced magnetic braking generating enough azimuthal acceleration to stop and reverse the fluid rotation. Our less advanced simulation time and the angular momentum divergence may also be in cause here, and we do not exclude the fact that this might happen.

In the neighborhood of the central objects, magnetic forces may launch jets of matter along the axis of rotation called *outflows* (Blandford & Payne 1982). These structures have been observed in several MHD simulations during the life of the first core (Seifried et al. 2012; Masson et al. 2016; Tomida et al. 2015), but do not appear in ours. The advancement of the simulation may be in cause, or simply the setup because Wurster et al. (2016) observed them in simulations in which the magnetic braking is enhanced. Since the outflows originate from the toroidal magnetic field around the rotation axis, this is not surprising because in parallel configurations, the Hall effect twists even more the field lines. On the contrary, in anti-parallel configurations, the toroidal field is weakened. It would be interesting to study in what extent the Hall effect enhances or prevent outflows, or if it can generates a strong enough toroidal field to launch one without initial rotation. Since outflows remove angular momentum from the core, it is of prime interest for the question of its regulation during star formation.

We therefore retrieve most results of Tsukamoto et al. (2015), Tsukamoto et al. (2017) and Wurster et al. (2016) about the role of the Hall effect in star formation. However, they do not mention this problem of angular momentum. The implementation of Wurster et al. (2016) propagates the whistler waves at the right frequencies and pass the steady-shock test, but there is no additional information about the accuracy or the order of their scheme. Despite the difference in the nature of the code (SPH) and the implementation, their simulations also contain various levels of resolution (the size of the SPH kernel) and should therefore equally meet a premature dissipation of whistler waves. As we currently understand the problem, the only solution to prevent it seems to perform simulations on regular grids. However, given the fact that protostellar collapses involve several orders of magnitude of characteristic lengths (from the dense core, ≈ 3000 a.u. to the second Larson core, ≈ 1 a.u.), precise results require a high resolution. In our case, to satisfy the Truelove et al. (1997) condition, we would need at least $\approx \left(2^{13}\right)^3 = 2^{39} \approx 10^{12}$ cells in our simulations, a computational cost far too heavy for any computer.

4.5 Conclusion

During protostellar collapses, the Hall effect induces a rotation parallel to the electric current, in the plane of the pseudo-disk created by the pinching of the magnetic field lines. The magnetic braking is strengthened or weakened depending on the orientation of the magnetic field, and rotation is generated even if there is no initial velocity. By conservation of angular momentum, regions of counter-rotation form above and below the plane of the pseudo-disk.

However, few hundreds of years after the formation of the first Larson core, the angular momentum of the system increases for every simulation. Based on the tests of the Hall effect and on the Shannon theorem, there is strong evidence suggesting that this non-conservation originates from the premature dissipation of whistler waves on AMR grids. The angular momentum generated in the core and the disk is not fully compensated by counter-rotation.

Drawing quantitative conclusions of our simulations is therefore difficult at stages later than this angular momentum divergence. Prior to this point, we can nonetheless assume that the Hall effect is well described and that its impact on the dynamics of the collapse is correct.

The most notable signature of the Hall effect are the counter-rotating envelopes. The Hall effect is the only non-ideal MHD process able to form such structure. They are situated in the vicinity of the protostar, and their extent is correlated with the strength and inclination of the global magnetic field. Angles larger than 90° tend to form larger disks with surrounding counter-rotative envelopes, while a stronger magnetic field leads to smaller disks but larger envelopes. Planets are therefore directly affected as the Hall effect modifies their environment of formation. The fact that the magnetic braking is strengthened for acute angles, while we seek to temper it through non-ideal MHD, suggests either that this configuration is rare, or that the Hall effect has a lower impact on real protostellar collapses than in our simulations (e.g. with a lower resistivity).

This is of prime interest for observations of young YSOs. The correlation between the magnetic field strength, its direction, the size of the disk, the counter-rotating envelopes and the chemical composition is a mean to test the physics at stake. Detecting the above-mentioned structures would be a serious evidence of the importance of the Hall effect during star formation. On the contrary, the absence of counter-rotating envelopes in anti-aligned magnetic field configurations would indicate a negligible impact of the Hall effect. Both situations would indirectly bring constraints on the chemical composition of the object through a rough estimation of the Hall resistivity. For nearby objects, the ALMA telescope should have the necessary resolution to detect the Hall-induced structures and the direction of the magnetic field.

Chapter 5

Conclusion

After an introduction on the physics of star formation, we did a brief review of the contemporary issue of the domain. Nowadays, the regulations of the angular momentum and the magnetic flux are subject to the most extensive studies. In this work, we sought answers through the prism of non-ideal MHD, particularly the Hall effect.

First, we focused on the chemical environment of star-forming clouds. We have successfully designed a code solving the chemical equilibrium in relevant thermodynamical conditions in order to compute the non-ideal MHD resistivities. The chemical abundances and resistivities are notably influenced by the cosmic-ray ionisation rate and the grain population. However, there is no current model able to perfectly describe the evolution of grains through the stellar life cycle. The MRN size distribution introduced by (Mathis et al. 1977) is currently widely accepted for the Interstellar Medium, but grains undergo many interactions as charge transfer, coagulation or fragmentation as their environment change (Ormel et al. 2009). This complex chemistry affects the gas composition as the heart of many chemical reactions, the surface of the grains, is modified. It also influences the non-ideal MHD resistivities in a not easily predictable way. Moreover, it is not obvious that the size distribution remains the same in dense cores and during proto-stellar collapses, as we already know that the dust to gas ratio is inhomogeneous in proto-planetary disks (Dipierro et al. 2016). Advanced models of grains, coupled with hydrodynamical simulations following the dust density should bring interesting information about the chemistry and the resistivities during star formation. We have generated a large table of chemical abundances across a wide range of density, temperature and cosmic-ray ionisation rate that we now use in numerical simulations. In further work, we will extend this table by varying the grain population, as its distribution or the dust-to-gas ratio.

We have then implemented the Hall effect in the eulerian code `RAMSES`. To do this, we have directly modified the Riemann solver that computes the magnetic flux of ideal MHD. The tests showed that our implementation is valid and that the code can manage the dispersive nature of the Hall effect. However, despite the excellent results on regular grids, we observe that the whistler waves are quickly dissipated on grids with several levels of AMR. Their numerical damping depends on the lowest resolution instead of the highest.

Finally, we used `RAMSES` to simulate the gravitational collapse of pre-stellar cores, and study the role of the Hall effect in the redistribution of the angular momentum. We found that rotation is spontaneously generated in non-rotating core, and that the magnetic braking is either strengthened or weakened. Counter-rotating regions, that compensate the rotation generated in the plane of the pseudo-disk, are a very distinctive feature of the Hall effect. We however do not know their fate. Is this negative momentum carried outside the core, leaving a large and fast rotating disk ? Or does it fall back onto the disk at the Class I or Class II stage, canceling the positive impulse that was given at earlier times ? This would require more advanced simulations, from the dense core to the Class II protostar, when the whole the envelope has been accreted.

To our knowledge, no such simulation has been performed to this day, as it would require heavy numerical ressources.

Few hundreds of years after the formation of the first Larson core, a premature dissipation of whistler waves leads to a non-conservation of the total angular momentum. No mention of such problem has been found in litterature, including in recent studies of protostellar collapses with SPH codes, but there is no evidence showing that the angular momentum is indeed conserved in these simulations. We retrieve most of their results despite the angular momentum divergence, so we do not know to what extent the results of theses studies are valid. The PHANTOM code has been released recently (Price et al. 2017b), and reproducing the simulations is a necessary step to understand more deeply this issue.

Meanwhile, we can not determine the exact influence of the Hall effect on star formation at later stages than the first Larson core formation. Nonetheless, its impact on the distribution of angular momentum make them of special interest for binary systems (Wurster et al. 2017). The enhancement of rotation in quasi-misaligned configurations would facilitate the fragmentation of the disk or the first core and the ejection of a second object. On the contrary, it can also inhibit this fragmentation by lowering the centrifugal force. Quantifying its ability to change the outcome of the process (e.g. formation of a wide binary instead of a tight binary) would be a valuable result.

Many studies on the impact of non-ideal MHD on star formation still need to be done in the upcoming years. Coupled with observations, they should bring much needed information on questions that have been waiting clear-cut answers for decades.

List of Figures

Bibliography

Allen, A., Shu, F. H., & Li, Z.-Y. 2003, Astrophys. J. , 599, 351

ALMA Partnership, Brogan, C. L., Pérez, L. M., et al. 2015, Astrophys. J., Lett. , 808, L3

Alves, J., Lada, C., & Lada, E. 2001, The Messenger, 103, 1

André, P. 2002, in EAS Publications Series, Vol. 3, EAS Publications Series, ed. J. Bouvier & J.-P. Zahn, 1 38

André, P., Ward-Thompson, D., & Barsony, M. 1993, Astrophys. J. , 406, 122

André, P., Ward-Thompson, D., & Motte, F. 1996, A&A, 314, 625

Balbus, S. A. 2009, ArXiv e-prints

Balbus, S. A. & Terquem, C. 2001, Astrophys. J. , 552, 235

Berger, M. J. & Oliger, J. 1984, Journal of Computational Physics, 53, 484

Black, D. C. & Scott, E. H. 1982, Astrophys. J. , 263, 696

Blandford, R. D. & Payne, D. G. 1982, MNRAS, 199, 883

Bless, R. C. & Savage, B. D. 1972, Astrophys. J. , 171, 293

Bonnor, W. B. 1956, MNRAS, 116, 351

Boss, A. P. & Bodenheimer, P. 1979, Astrophys. J. , 234, 289

Chandrasekhar, S. & Fermi, E. 1953, Astrophys. J. , 118, 113

Choi, E., Kim, J., & Wiita, P. J. 2009, Astrophys. J., Suppl. Ser. , 181, 413

Commerçon, B., Hennebelle, P., Audit, E., Chabrier, G., & Teyssier, R. 2010, A&A, 510, L3

Compiègne, M., Verstraete, L., Jones, A., et al. 2011, A&A, 525, A103

Courant, R., Friedrichs, K., & Lewy, H. 1928, Mathematische Annalen, 100, 32

Crutcher, R. M., Roberts, D. A., Troland, T. H., & Goss, W. M. 1999, Astrophys. J. , 515, 275

Desch, S. J. & Mouschovias, T. C. 2001, Astrophys. J. , 550, 314

Desch, S. J. & Turner, N. J. 2015, Astrophys. J. , 811, 156

Dipierro, G., Laibe, G., Price, D. J., & Lodato, G. 2016, MNRAS, 459, L1

Draine, B. T. & Sutin, B. 1987, Astrophys. J. , 320, 803

Duffin, D. F. & Pudritz, R. E. 2008, MNRAS, 391, 1659

Ebert, R. 1955, Zeitschrift für Astrophysik, 37, 217

Evans, C. R. & Hawley, J. F. 1988, Astrophys. J. , 332, 659

Falle, S. A. E. G. 2003, MNRAS, 344, 1210

Fermi, E. 1949, Physical Review, 75, 1169

Fromang, S., Hennebelle, P., & Teyssier, R. 2006, A&A, 457, 371

Fujii, Y. I., Okuzumi, S., & Inutsuka, S.-i. 2011, Astrophys. J. , 743, 53

Galli, D., Lizano, S., Shu, F. H., & Allen, A. 2006, Astrophys. J. , 647, 374

Galli, D. & Shu, F. H. 1993, Astrophys. J. , 417, 243

Gillett, F. C., Forrest, W. J., & Merrill, K. M. 1973, Astrophys. J. , 183, 87

Gillis, J., Mestel, L., & Paris, R. B. 1974, Astrophys. and Space Science, 27, 167

Girart, J. M., Rao, R., & Marrone, D. P. 2006, Science, 313, 812

Godunov, S. K. 1959, Math. Sbornik

Golub, G. H. & van Loan, C. F. 1983, Matrix Computations, Johns Hopkins Series in the Mathematical Sciences No. 1 (The Johns Hopkins University Press)

Goodman, A. A., Barranco, J. A., Wilner, D. J., & Heyer, M. H. 1998, Astrophys. J. , 504, 223

Goodman, A. A., Benson, P. J., Fuller, G. A., & Myers, P. C. 1993, Astrophys. J. , 406, 528

Hall, J. S. 1951, Astrophys. J. , 56, 40

Harten, A. 1983, Journal of Computational Physics, 49, 357

Harten, A., Lax, P., & Van Leer, B. 1983, SIAM Review, 25

Hennebelle, P., Commerçon, B., Chabrier, G., & Marchand, P. 2016, Astrophys. J., Lett. , 830, L8

Hennebelle, P. & Fromang, S. 2008, A&A, 477, 9

Hennebelle, P. & Teyssier, R. 2008, A&A, 477, 25

Hiltner, W. A. 1951, Astrophys. J. , 114, 241

Ilgner, M. & Nelson, R. P. 2006, A&A, 445, 205

Jeans, J. H. 1902, Philosophical Transactions of the Royal Society of London Series A, 199, 1

Joos, M., Hennebelle, P., & Ciardi, A. 2012, A&A, 543, A128

Khokhlov, A. 1998, Journal of Computational Physics, 143, 519

Kitamura, Y., Sunada, K., Hayashi, M., & Hasegawa, T. H. 1993, Astrophys. J. , 413, 221

Kleiner, S. C. & Dickman, R. L. 1985, Astrophys. J. , 295, 466

Kolmogorov, A. N. 1941, Akademiia Nauk SSSR Doklady, 32, 16

Krasnopolsky, R., Li, Z.-Y., & Shang, H. 2010, Astrophys. J. , 716, 1541

Krasnopolsky, R., Li, Z.-Y., & Shang, H. 2011, Astrophys. J. , 733, 54

Krishna Swamy, K. S. & O'dell, C. R. 1968, Astrophys. J., Lett. , 151, L61

Kunz, M. W. & Lesur, G. 2013, MNRAS, 434, 2295

Kunz, M. W. & Mouschovias, T. C. 2009, Astrophys. J. , 693, 1895

Kunz, M. W. & Mouschovias, T. C. 2010, MNRAS, 408, 322

Lada, C. J. & Wilking, B. A. 1984, Astrophys. J. , 287, 610

Larson, R. B. 1969, MNRAS, 145, 271

Larson, R. B. 1981, MNRAS, 194, 809

Lenzuni, P., Gail, H.-P., & Henning, T. 1995, Astrophys. J. , 447, 848

Lesur, G., Kunz, M. W., & Fromang, S. 2014, A&A, 566, A56

Levrier, F. 2004, A&A, 421, 387

Li, Z.-Y. 1998, Astrophys. J. , 497, 850

Li, Z.-Y., Krasnopolsky, R., & Shang, H. 2011, Astrophys. J. , 738, 180

Londrillo, P. & del Zanna, L. 2004, Journal of Computational Physics, 195, 17

Mac Low, M., Norman, M. L., Konigl, A., & Wardle, M. 1995, Astrophys. J. , 442, 726

Machida, M. N., Inutsuka, S., & Matsumoto, T. 2006, Astrophys. J., Lett. , 647, L151

Machida, M. N., Inutsuka, S., & Matsumoto, T. 2007, Astrophys. J. , 670, 1198

Machida, M. N., Inutsuka, S., & Matsumoto, T. 2008, Astrophys. J. , 676, 1088

Machida, M. N., Inutsuka, S., & Matsumoto, T. 2009, Astrophys. J., Lett. , 704, L10

Marchand, P., Masson, J., Chabrier, G., et al. 2016, A&A, 592, A18

Masson, J., Chabrier, G., Hennebelle, P., Vaytet, N., & Commercon, B. 2016, A&A, 587, A32

Masson, J., Teyssier, R., Mulet-Marquis, C., Hennebelle, P., & Chabrier, G. 2012, Astrophys. J., Suppl. Ser. , 201, 24

Mathis, J. S., Rumpl, W., & Nordsieck, K. H. 1977, Astrophys. J. , 217, 425

Matsumoto, T. & Tomisaka, K. 2004, Astrophys. J. , 616, 266

McElroy, D., Walsh, C., Markwick, A. J., et al. 2013, A&A, 550, A36

Mellon, R. R. & Li, Z. 2009, Astrophys. J. , 698, 922

Mestel, L. & Spitzer, Jr., L. 1956, MNRAS, 116, 503

Mignone, A., Bodo, G., Massaglia, S., et al. 2007, Astrophys. J., Suppl. Ser. , 170, 228

Miyoshi, T. & Kusano, K. 2005, Journal of Computational Physics, 208, 315

Mouschovias, T. C. 1977, Astrophys. J. , 211, 147

Mouschovias, T. C. 1991, Astrophys. J. , 373, 169

Mouschovias, T. C. & Spitzer, Jr., L. 1976, Astrophys. J. , 210, 326

Nakano, T. 1984, Fundamentals of Cosmic Physics, 9, 139

Nakano, T., Nishi, R., & Umebayashi, T. 2002, Astrophys. J. , 573, 199

Nishi, R., Nakano, T., & Umebayashi, T. 1991, Astrophys. J. , 368, 181

Okuzumi, S. 2009, Astrophys. J. , 698, 1122

Ormel, C. W., Paszun, D., Dominik, C., & Tielens, A. G. G. M. T. 2009, A&A, 502, 845

O'Sullivan, S. & Downes, T. P. 2006, in Astronomical Society of the Pacific Conference Series, Vol. 359, Numerical Modeling of Space Plasma Flows, ed. G. P. Zank & N. V. Pogorelov, 178

Padovani, M. & Galli, D. 2011, A&A, 530, A109

Padovani, M. & Galli, D. 2013, in Advances in Solid State Physics, Vol. 34, Cosmic Rays in Star-Forming Environments, ed. D. F. Torres & O. Reimer, 61

Padovani, M., Galli, D., & Glassgold, A. E. 2013, A&A, 549, C3

Padovani, M., Hennebelle, P., & Galli, D. 2014, ASTRA Proceedings, 1, 23

Pinto, C. & Galli, D. 2008, A&A, 484, 17

Pinto, C. & Galli, D. 2009, Three-Fluid Magnetohydrodynamics in Star Formation, ed. Tsinganos, K., Ray, T., & Stute, M., 597 599

Pinto, C., Galli, D., & Bacciotti, F. 2008, A&A, 484, 1

Pneuman, G. W. & Mitchell, T. P. 1965, icarus, 4, 494

Press, W. H., Teukolsky, S. A., Vetterling, W. T., & Flannery, B. P. 2007, Numerical Recipes 3rd Edition: The Art of Scientific Computing, 3rd edn. (New York, NY, USA: Cambridge University Press)

Price, D. J. & Bate, M. R. 2007, Astrophys. and Space Science, 311, 75

Price, D. J., Wurster, J., Nixon, C., et al. 2017a, ArXiv e-prints

Price, D. J., Wurster, J., Nixon, C., et al. 2017b, PHANTOM: Smoothed particle hydrodynamics and magnetohydrodynamics code, Astrophysics Source Code Library

Sano, T., Miyama, S. M., Umebayashi, T., & Nakano, T. N. 2000, Astrophys. J. , 543, 486

Sano, T. & Stone, J. M. 2002, Astrophys. J. , 570, 314

Savage, B. D. & Jenkins, E. B. 1972, Astrophys. J. , 172, 491

Seifried, D., Pudritz, R. E., Banerjee, R., Duffin, D., & Klessen, R. S. 2012, MNRAS, 422, 347

Semenov, D., Henning, T., Helling, C., Ilgner, M., & Sedlmayr, E. 2003, A&A, 410, 611

Semenov, D., Wiebe, D., & Henning, T. 2004, A&A, 417, 93

Shannon, C. 1949, Proceedings of the Institute of Radio Engineers, 37, 10

Shu, F. H. 1977, Astrophys. J. , 214, 488

Shu, F. H., Lizano, S., & Adams, F. C. 1987, in IAU Symposium, Vol. 115, Star Forming Regions, ed. M. Peimbert & J. Jugaku, 417 433

Srinivasan, B. & Shumlak, U. 2011, Physics of plasma, 18, 092113

Stone, J. M. & Norman, M. L. 1992, Astrophys. J., Suppl. Ser. , 80, 753

Teyssier, R. 2002, A&A, 385, 337

Teyssier, R., Fromang, S., & Dormy, E. 2006, Journal of Computational Physics, 218, 44

Tilley, D. A. & Balsara, D. S. 2011, MNRAS, 415, 3681

Tomida, K., Okuzumi, S., & Machida, M. N. 2015, Astrophys. J. , 801, 117

Toro, E. F. 2009, Riemann Solvers and Numerical Methods for Fluid Dynamics, third edition edn.

Toth, G. 1994, Astrophys. J. , 425, 171

Tóth, G., De Zeeuw, D. L., Gombosi, T. I., & Powell, K. G. 2006, J. Comput. Phys., 217, 722

Tóth, G., Ma, Y., & Gombosi, T. I. 2008, Journal of Computational Physics, 227, 6967

Troland, T. H. & Crutcher, R. M. 2008, Astrophys. J. , 680, 457

Truelove, J. K., Klein, R. I., McKee, C. F., et al. 1997, Astrophys. J., Lett. , 489, L179

Tsukamoto, Y. 2016, Publications of the Astron. Soc. of Australia, 33, e010

Tsukamoto, Y., Iwasaki, K., Okuzumi, S., Machida, M. N., & Inutsuka, S. 2015, Astrophys. J., Lett. , 810, L26

Tsukamoto, Y., Okuzumi, S., Iwasaki, K., Machida, M. N., & Inutsuka, S.-i. 2017, ArXiv e-prints

Umebayashi, T. & Nakano, T. 1990, MNRAS, 243, 103

Valdivia, V. & Hennebelle, P. 2014, A&A, 571, A46

van Leer, B. 1976, in Computing in Plasma Physics and Astrophysics, ed. D. Biskamp

Vaytet, N., Chabrier, G., Audit, E., et al. 2013, A&A, 557, A90

Wurster, J. 2016, Publications of the Astron. Soc. of Australia, 33, e041

Wurster, J., Price, D., & Ayliffe, B. 2014, MNRAS, 444, 1104

Wurster, J., Price, D. J., & Bate, M. R. 2016, MNRAS, 457, 1037

Wurster, J., Price, D. J., & Bate, M. R. 2017, MNRAS, 466, 1788

York, D. G., Drake, J. F., Jenkins, E. B., et al. 1973, Astrophys. J., Lett. , 182, L1

Zipf, G. 1936, The Psychobiology of Language

Zipf, G. 1949, Human Behavior and the Principle of Least Effort